

Solar-driven water electrolysis

Citation for published version (APA):

Pinto Branco, B. F. (2023). *Solar-driven water electrolysis: new multijunction solar cells and electrolysis materials*. [Phd Thesis 1 (Research TU/e / Graduation TU/e), Chemical Engineering and Chemistry]. Eindhoven University of Technology.

Document status and date:

Published: 19/09/2023

Document Version:

Publisher's PDF, also known as Version of Record (includes final page, issue and volume numbers)

Please check the document version of this publication:

- A submitted manuscript is the version of the article upon submission and before peer-review. There can be important differences between the submitted version and the official published version of record. People interested in the research are advised to contact the author for the final version of the publication, or visit the DOI to the publisher's website.
- The final author version and the galley proof are versions of the publication after peer review.
- The final published version features the final layout of the paper including the volume, issue and page numbers.

[Link to publication](#)

General rights

Copyright and moral rights for the publications made accessible in the public portal are retained by the authors and/or other copyright owners and it is a condition of accessing publications that users recognise and abide by the legal requirements associated with these rights.

- Users may download and print one copy of any publication from the public portal for the purpose of private study or research.
- You may not further distribute the material or use it for any profit-making activity or commercial gain
- You may freely distribute the URL identifying the publication in the public portal.

If the publication is distributed under the terms of Article 25fa of the Dutch Copyright Act, indicated by the "Taverne" license above, please follow below link for the End User Agreement:

www.tue.nl/taverne

Take down policy

If you believe that this document breaches copyright please contact us at:

openaccess@tue.nl

providing details and we will investigate your claim.

Solar–driven water electrolysis: new multijunction solar cells and electrolysis materials

PROEFSCHRIFT

ter verkrijging van de graad van doctor aan de Technische Universiteit
Eindhoven, op gezag van de rector magnificus prof.dr. S.K. Lenaerts, voor een
commissie aangewezen door het College voor Promoties, in het openbaar te
verdedigen op dinsdag 19 september 2023 om 11:00 uur

door

Bruno Filipe Pinto Branco

geboren te Pragal, Portugal

Dit proefschrift is goedgekeurd door de promotoren en de samenstelling van de promotiecommissie is als volgt:

voorzitter: prof.dr. Ž. Tomović
1^e promotor: prof.dr.ir. R.A.J Janssen
2^e promotor: prof.dr.rer.nat. K.A. Friedrich (University of Stuttgart)
leden: prof.dr. E. Klemm (University of Stuttgart)
 prof.dr. R. van de Krol (Technische Universität Berlin)
 dr.ir. M.T. de Groot
adviseur: dr. V. Atanasov (University of Stuttgart)

Het onderzoek of ontwerp dat in dit proefschrift wordt beschreven is uitgevoerd in overeenstemming met de TU/e Gedragscode Wetenschapsbeoefening.

**Solar–driven water electrolysis: new
multijunction solar cells and electrolysis
materials**

Bruno Filipe Pinto Branco

Printed by Proefschrift specialist.

Cover design by Tijana Čulum and Kostadin Petrov.

Translation of Summary in Dutch by Lana Kessels.

Translation of Summary in German by Nicolas Daub.

Translation of Summary in Portuguese by Bruno Branco.

A catalogue record is available from the Eindhoven University of Technology Library.

ISBN: 978–90–386–5810–0

The research described in this thesis has received funding from the European Union’s Horizon 2020 Research and Innovation Programme under the Marie Skłodowska–Curie grant agreement No. 765376 (eSCALED) and the NWO Spinoza award.

Table of Contents

Chapter 1 Introduction	1
1.1. Global energy consumption	2
1.2. Renewable energy storage	4
1.3. Solar-driven water electrolysis	6
1.4. Thesis aim and outline	8
1.5. References	12
Chapter 2 Design and optimization of a lab-scale water electrolysis setup	17
2.1. Introduction	18
2.2. Materials	23
2.3. Voltage losses in water electrolysis	29
2.4. Water electrolysis setup scheme	35
2.5. Cell clamping torque	36
2.6. Oil bath and inlet cell temperature study	38
2.7. Porous transport layers for water electrolysis	40
2.8. Membrane-electrode assembly storage under inert atmosphere	43
2.9. Titanium flow field and removal of the back O-ring	44
2.10. Conclusion	46
2.11. Experimental section	49
2.12. References	50
Chapter 3 Efficient continuous light-driven water electrolysis using an electrochemical flow cell and a perovskite/silicon tandem solar cell	59
3.1. Introduction	60
3.2. Water electrolysis in an electrochemical flow cell	63
3.3. Monolithic perovskite/c-silicon tandem solar cell	65
3.4. Light-driven water electrolysis	67
3.5. Conclusion	69
3.6. Experimental section	70
3.7. References	74
Chapter 4 All-perovskite tandem solar cells for solar-driven water electrolysis	79
4.1. Introduction	80
4.2. All-perovskite tandem solar cells: 1 cm ² active area	81
4.3. Solar-driven water electrolysis with all-perovskite tandem solar cell	85
4.4. One-step procedure for narrow-bandgap perovskite solar cell	89
4.5. Conclusion	101
4.6. Experimental section	102
4.7. References	106
Chapter 5 Proton exchange membranes for water electrolysis	111
5.1. Introduction	112
5.2. Ionomers and their blend membranes	116
5.3. Water electrolysis with blend membranes	118
5.4. Conclusion	125

5.5.	Experimental section	127
5.6.	References	128
Chapter 6	Preparation of membranes–electrode assemblies by screen printing	131
6.1.	Introduction	132
6.2.	Screen printing patterns	135
6.3.	Slit screen printed graphite electrodes	137
6.4.	Small screen printed graphite electrodes	139
6.5.	Conclusion	141
6.6.	Experimental section	142
6.7.	References	144
Chapter 7	Life cycle assessment of an artificial leaf: new and standard materials	149
7.1.	Introduction	150
7.2.	Objectives	153
7.3.	Products	153
7.4.	Life cycle assessment	153
7.5.	Conclusion	172
7.6.	References	174
	Summary	177
	Samenvatting	181
	Zusammenfassung	185
	Resumo	189
	Curriculum Vitae	193
	Acknowledgements	195

Chapter 1

Introduction

Abstract

The growing global energy consumption driven by a continuously increasing population and global economic growth have led the world into an energy and environmental crisis. The development and implementation of zero-carbon emission solutions has become indispensable to revert the consequences from the extensive use of fossil fuels since the industrial era. Harvesting solar energy and directly using it to convert water to hydrogen and oxygen arises as one of those solutions. This chapter provides a brief introduction to the different solar-driven water electrolysis technologies, especially focusing on the independent coupling of photovoltaics and water electrolysis cells. Current material requirements and associated costs are highlighted, providing an insight on the difficult implementation of this technology. Lastly, a general overview of the eSCALED project as well as the aim and outline of this thesis are explained. Shortly, this thesis describes the evaluation of proton exchange membranes developed in eSCALED and printing methodologies for membrane-electrode assemblies. It also demonstrates the first example of a two terminal perovskite/crystalline silicon (PVK-Si) and all-perovskite multijunction solar cells coupled to a water electrolysis flow cell operating under normal sunlight, reaching solar-to-hydrogen efficiencies of 21.5% and 18.6%, respectively. The system with the PVK-Si multijunction solar cell reached the highest reported STH for a system operating without sunlight concentration. Finally, this thesis describes the environmental profile of the developed materials in working solar-driven water electrolysis device using life cycle analysis, providing feedback on where future research should focus to decrease the environmental impacts.

1.1. Global energy consumption

The global energy consumption has more than tripled in the last 50 years and almost doubled during my lifetime (**Figure 1.1a**).¹ Fast growing global population and economic growth have been major drivers for the steep increase in energy consumption.² The energy consumption per capita of a country is intimately connected with its gross domestic product (GDP) per capita, with higher GDP per capita directly associated with larger energy consumption (Figure 1.1b). Additionally, the fast and substantial economic growth of largely populated countries like China and India has had a substantial contribution to the global rise in energy consumption, due to an increase in the energy consumption per capita.^{3,4}

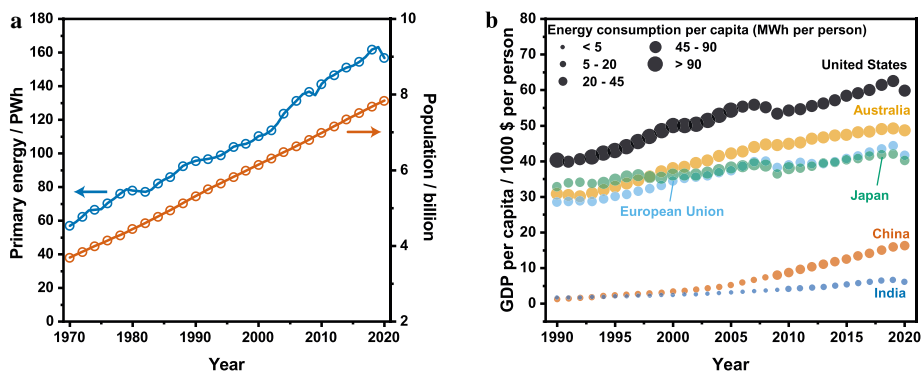


Figure 1.1: Energy, population and economic growth indicators. a) Global primary energy consumption and population growth since 1970. b) Gross domestic product evolution in different countries and European Union over the years. The size of the marker represents the energy consumption per capita for each analyzed country and region. Data retrieved from the database maintained by Our World in Data (ourworldindata.org).

Despite the increasing share of renewable energy sources (solar, wind, hydropower, and biomass) over the years, the majority of energy (82% in 2021) is still generated by fossil fuels (coal, oil, and gas) as illustrated in **Figure 1.2a**. The energy sector is the main contributor for greenhouse gases emissions (GHG), with 64% of the total emissions (32 billion ton CO₂ eq.) (Figure 1.2b). The excessive use of fossil fuels are a primary driver of global warming that represents one of humanity largest and most–immediate issues of our lifetimes.⁵

The global average temperature is tightly connected with GHG. In fact, without the GHG effect, Earth’s global average surface temperature would be around -18°C , below water’s melting point (0°C at 1 atm) and thus, the existence of life would be impossible.⁶ However, the continuously increasing anthropogenic GHG concentration has intensified this effect, resulting in an

increase of global average temperature of about 1 K since the start of the industrial era (Figure 1.2c).

Although seemingly small, such temperature rise may lead to severe environmental consequences that include more recurrent and harsher droughts, heatwaves, and sea level rising due to the melting of the polar ice caps. Hence, reducing global GHG emissions and mitigate climate change impacts became a major global target. On December 2015, at the Paris Conference, 196 parties agreed on a legally binding international treaty on climate change, now known as the Paris Agreement.⁷ The main target of the agreement is to limit the increase in global average temperature to well below 2 °C above pre-industrial levels within this century, while pursuing a value below 1.5 °C.

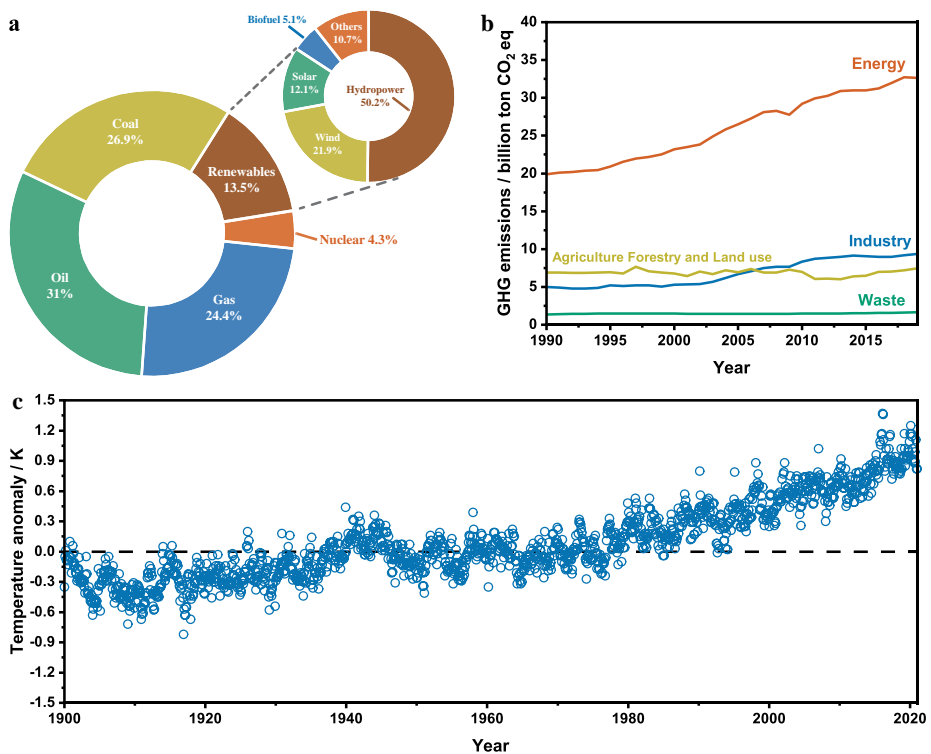


Figure 1.2: Energy sources and global warming indicators. a) Share of energy consumption generated from different energy sources in 2021. b) Total greenhouse gas emissions by sector. Non-CO₂ gases are weighed by the amount of global warming they cause over a 100-year timescale. c) Combined land–surface air and sea–surface water temperature anomaly given as the deviation from the 1951–1980 mean. Data retrieved from the database maintained by Our World in Data (ourworldindata.org).

A drastic reduction in GHG emissions is evidently required to achieve the ambitious targets set in the Paris agreement. The GHG emissions should peak before 2025 and decrease 43% by 2050 to limit the increase in global average temperature to 1.5 °C.⁷ Such target can only be reached by a transition from a fossil fuel-based energy supply to renewable energy sources in all major sectors.^{8,9} Consequently, the development, support, and implementation of current and new zero-carbon solutions are vital to meet the carbon-neutrality targets.

1.2. Renewable energy storage

Solar energy is the most abundant energy source, exceeding by far all other energy sources, non-renewables or renewables. The Sun supplies about 1.2×10^{17} W to Earth's surface, which corresponds to a yearly energy supply of 1.05×10^{21} Wh.¹⁰ This represents an energy supply ~9000 times larger than the current energy demand, or in other words, one hour of sunlight would be enough to cover the global demand.^{11,12} According to the Renewables 2022 report from the International Energy Agency, the photovoltaics power capacity is expected to surpass the hydropower capacity by 2024, and coal by 2027, becoming the largest installed electricity capacity globally.¹³ It is then clear that solar energy plays a significant role in the energy crisis and the decarbonization of energy.

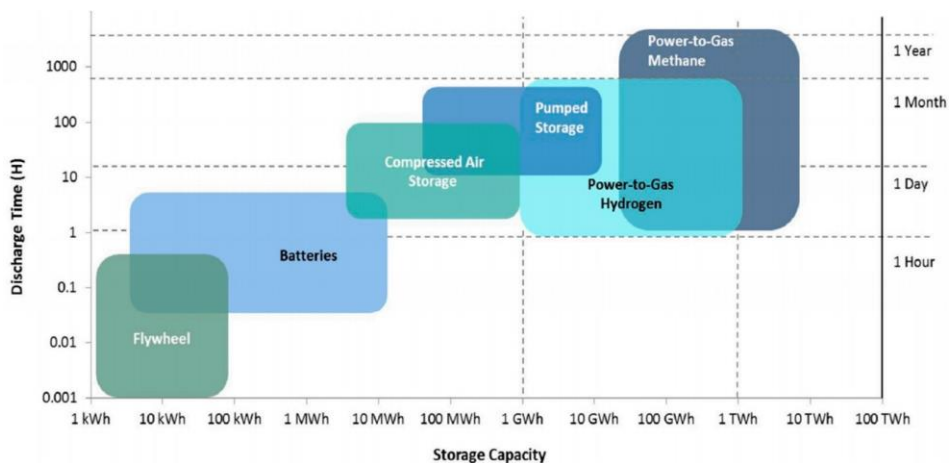
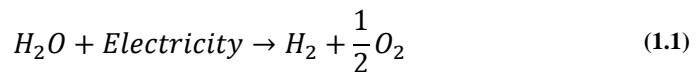


Figure 1.3: Current energy storage technologies based on discharge time and storage capacity. Reprinted from Applied Energy, 287, Dohyung Jang, Hyun-Seok Cho, Sanggyu Kang, Numerical modelling and analysis of the effect of pressure on the performance of an alkaline water electrolysis system, 116554, 2021, with permission from Elsevier.¹⁸

In contrast to fossil fuels, solar energy – and most renewable energy sources – are particularly limited by their unpredictability and intermittency. The

supply of solar energy is affected by the diurnal nature of solar irradiation, geography, and weather conditions. Therefore, an additional expansion of the renewable energy grid relies on finding suitable energy storage methods (**Figure 1.3**).^{14–16} Chemical energy carriers arise as the most promising and viable energy storage technology resulting from their long term and large energy capacity. These chemical energy carriers are also referred to as solar fuels when the renewable energy source is solar energy.^{17,18}

Molecular hydrogen (H₂) is widely regarded as an important energy vector because it is a clean chemical fuel, i.e. carbon dioxide free combustion, with high energy density (120 MJ kg⁻¹), and it can be easily stored as compressed gas.¹⁹ Furthermore, hydrogen serves as a major feedstock in the chemical industry to produce other value-added products.²⁰ Hydrogen production is possible through water electrolysis that consists in splitting water (H₂O) into H₂ and oxygen (O₂) in an electrochemical cell using an external electricity source (**Eq. 1.1**).²¹ The external electricity source should be preferentially from a renewable energy source to provide carbon-neutral hydrogen production (green hydrogen).



Hydrogen produced through water electrolysis represented only 4% of the global hydrogen production in 2021 while the remaining 96% are produced by fossil fuel-based processes (grey hydrogen), such as steam reforming and coal gasification. However, only about 1% of the global hydrogen was produced by water electrolysis powered by renewable energy sources.²⁰ The predominant use of fossil fuel-based processes result in considerable CO₂ emissions, with a total of 900 Mton CO₂ (9.7 kg CO₂ kg H₂⁻¹) in 2021, highlighting the importance of an energy transition from fossil fuels to renewables.²² The operational expenditure (OPEX), related to electricity consumption, is the main cost contributor in water electrolysis and thus, the higher cost of renewable energy sources in comparison to fossil fuels result in the small share of green hydrogen.²³ To increase the commercial competitiveness of green hydrogen, the energy requirement of water electrolysis and costs of sustainable electricity from solar or any renewable energy source, must drop.

The development and utilization of highly efficient and cost-effective materials for renewable energy conversion and storage is crucial to reach carbon neutrality. For example, commercially available photovoltaic modules based on crystalline silicon (c-Si) have an energy-intensive production process.²⁴ Emerging technologies, such as perovskite solar cells, hold promising performances that are comparable with c-Si while providing cheap and scalable

options in the photovoltaic market.²⁵ For the water electrolysis cell, the most active materials include platinum (Pt), ruthenium (Ru), iridium (Ir), and titanium (Ti), which are all highly expensive metals. This will be further explored in chapters 3 to 6 of this thesis.

1.3. Solar-driven water electrolysis

Solar-driven water electrolysis takes inspiration from Nature's photosynthesis where chloroplasts harness solar energy to convert water and CO₂ into oxygen and sugars. Hence, it is regularly referred to as artificial photosynthesis.^{11,26–28} It can be carried out using three distinct systems depending on how the combination of the photoabsorber and electrochemical components is done: photocatalytic particles (PC),^{29–31} photoelectrochemical (PEC),^{27,32–35} and coupled photovoltaic–electrochemical (PV–EC) systems.³⁶

The simplest PC system involves the use of photocatalytic particles that usually consist of semiconductor particles (photoabsorber) surface-functionalized with co-catalysts for the hydrogen and oxygen evolution reactions. Stability in the aqueous media and semiconductors with adequate bandgaps are some of the many requirements for a PC system. The absence of an applied bias causes difficult charge carrier collection. Moreover, backward reactions occur more easily due to the lack of product separation, resulting in the lowest efficiency of the three methods.¹²

The PEC system consists of an electrochemical cell where one or both electrodes function as the photoabsorber. Additionally, the use of an electrochemical reactor enables the spatial separation of the electrolysis products. This system was first demonstrated by Honda and Fujishima in 1972 with a titanium dioxide (TiO₂) electrode acting both as photoabsorber and anode externally wired to a platinum cathode in a different compartment.³³ Metal oxide semiconductors are the most common photoelectrodes and are frequently combined with other electrocatalysts to enhance the performance. Recently, more efficient semiconductors commonly used for photovoltaics, such as silicon (Si) and perovskite for example, have also been implemented as photoelectrodes in combination with a wide range of electrocatalysts.^{37,38} However, the monolithic nature of the photoelectrodes demands a simultaneous optimization of both the photoabsorber and the electrocatalytic component, hindering highly efficient systems.

The most efficient and, actually, commercialized system is the PV–EC that combines photovoltaic cells and water electrolysis cells independently through external wiring, enabling individual optimization of the components.

Water electrolysis and photovoltaics are two already mature technologies and their integration immediately allows higher solar to hydrogen efficiencies (STH, **Eq. 1.2**) to be reached than the previously described systems.³⁹ In contrast to PC and PEC, the photoactive component is not immersed in the aqueous electrolyte, preventing faster degradation. Commonly, commercial PV–EC systems make use of power electronics such as DC–DC converters to ensure sufficient voltage is provided to the water electrolysis cell, complicating the balance of plant. Directly connecting both components would thereby simplify the balance of plant and avoid additional electrical losses, due to power electronics.⁴⁰

$$\text{STH} = \frac{1.23 I_{\text{op}} \eta_{\text{far}}}{A_{\text{sc}} P_{\text{in}}} \quad (1.2)$$

where I_{op} is the operating current density in A, η_{far} the (dimensionless) faradaic efficiency of the water electrolysis reactions, A_{sc} the solar cell area in m^2 and P_{in} the irradiance in W m^{-2} .⁴¹

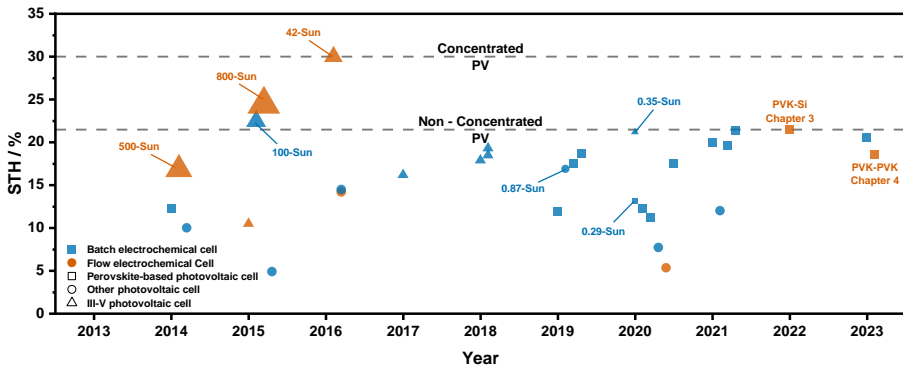


Figure 1.4: Solar-to-hydrogen (STH) efficiency across different types of water electrolysis cells driven by perovskite-based, III–V based or other photovoltaic devices. Other photovoltaic devices include: c–Si single-junction in series, organic multijunction and CuInGaSe (CIGS) single-junctions in series. The color of the marker distinguishes batch (blue) or flow (orange) electrochemical cells, the shape indicates perovskite-based (square), III–V based (triangle) or other photovoltaic devices (circle), and the size emphasizes illumination intensity. Unless specified, all devices are operated at approx. 1–Sun equivalent light intensity. The dash lines represent the record STH obtained with and without light concentration techniques.^{8,39,44–66}

Figure 1.4 summarizes the STH obtained in recent laboratory-scale PV–EC systems. At laboratory-scale, solar-driven water electrolysis is frequently conducted in batch electrochemical cells combined with a photovoltaic device. These studies focus mainly on the use of earth-abundant and cheap electrocatalysts and their performance. Cox et al. combined nickel borate (NiB_i) and NiMoZn as oxygen and hydrogen evolution catalysts and coupled them with

four c-Si single-junction solar cells connected in series to reach a STH of 10% at an operating voltage of approximately 2 V.³⁹ More recently, Wang et al. reported also two nickel-based catalysts with comparable performance to a Ir/Pt catalyst combination and integrated them with a perovskite-silicon tandem solar cell that enabled an STH > 20%. This was the first time that a STH > 20% was reached while using earth-abundant catalysts and a solar cell that was not composed of III-V semiconductors.⁸ Despite, such systems having already achieved high STH (> 20%), the large associated ohmic losses with batch electrochemical processes, makes these less relevant from a large-scale point of view. Instead, industrial water electrolysis is operated with electrochemical flow cells, i.e. operate under continuous water flow, that have a zero-gap configuration to minimize such losses.^{42,43}

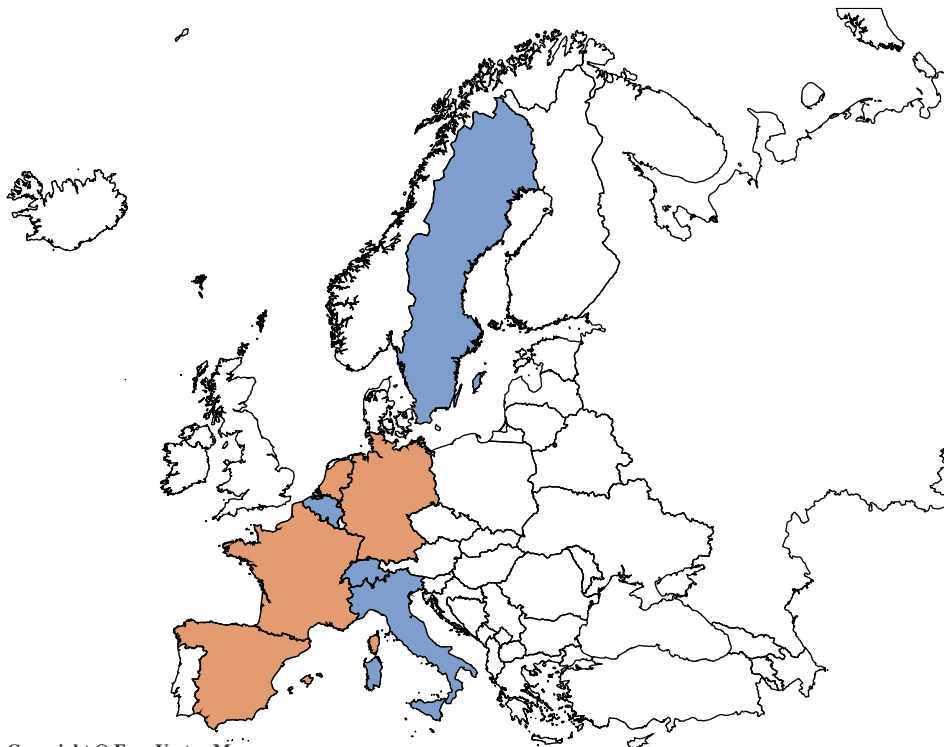
The higher current outputs enabled by electrochemical flow cells is then generally matched by expensive III-V semiconductor multijunction solar cells operated under concentrated light conditions to maximize the STH. For example, Nakamura et al. combined up to five electrochemical flow cells and three concentrator modules based on InGaP/GaAs/Ge triple-junction solar cells. Platinum was used both as hydrogen and oxygen evolution catalyst. The concentrator modules enabled a 800-Sun equivalent light illumination, resulting in a STH of 24.4%.⁶³ Similarly, the highest STH up to now (~30%) was reached for a InGaP/GaAs/GaInNAsSb triple-junction solar cell operated under 42-Sun equivalent light intensity, integrated with a Ir/Pt catalyst combination for the anode/cathode sub-cells in two series-connected flow cells.⁶⁵

These highly efficient systems are all based on high-cost materials and operate under concentrated solar light, hampering their implementation at large-scale. Hence, the integration of cost-effective material in both components (PV + EC) while maintaining high STH is fundamental to greatly increase their economic viability and also, applicability in indirect sunlight.

1.4. Thesis aim and outline

The work developed throughout this thesis was conducted as part of the “European School on Artificial Leaf: Electrodes & Devices (eSCALED)” project under a Marie Skłodowska-Curie Actions (MSCA) funding programme. The eSCALED project aimed to structure early-stage research training at European level, expanding the European innovation capacity to prepare an artificial leaf, i.e. a device that accomplishes artificial photosynthesis. The project consisted of 14 early-stage researchers (ESR) distributed across 12 European academic and industrial research groups from 8 countries (**Figure 1.5**) that allowed to combine the most recent knowledge on catalysis, photovoltaics, and polymer chemistry.

Throughout the duration of the project, the ESRs had the opportunity to move between countries and work with the different academic and industrial partners for periods of a minimum of three months.



Copyright © Free Vector Maps.com

Figure 1.5: Map of Europe with the countries from the partners involved in the eSCALED project marked in color. The orange color represents the countries where the work from this thesis was developed (Spain, Germany, France, and The Netherlands). In blue are the remaining countries that participated in eSCALED (Belgium, Italy, Sweden, and Switzerland). Based on a design from freevectormaps.com.

The ESRs were collectively responsible for developing cheap and earth-abundant materials for water electrolysis, electrocatalytic CO₂ reduction, and photovoltaics. These materials involved molecular catalysts, natural/artificial hydrogenase enzymes, new fluorinated proton-exchange membranes, microporous electrodes, and perovskite semiconductors. Ultimately, the materials should be combined using cost-effective and scalable processes to elaborate the ambitious artificial leaf.

Efficient solar-driven water electrolysis presently depends on expensive perfluorinated polyelectrolytes, noble metal or metal oxide electrocatalysts, and the use of expensive III-V multijunction solar cells to provide the required energy

to drive the reaction. This thesis focuses on testing new proton-exchange membranes developed by other ESRs from the eSCALED project, printing methodologies for membrane-electrode assembly preparation, and perovskite-based solar cells to enable efficient STH conversion using cost-effective materials.

In chapter 2, a water electrolysis setup and cell were firstly optimized to ensure reproducible and comparable results to literature when using state-of-the-art materials. The influence of the cell clamping torque, cell temperature, flow field's material, porous transport layer (PTL) material, and storage environment were studied and optimized to decrease ohmic losses, improve reaction kinetics and the overall stability of the electrolysis cell. This allowed to set the benchmark for the new electrolysis materials and preparation methodology investigated in later chapters.

In chapter 3 and chapter 4, two multijunction solar cells based on perovskite semiconductors were developed to carry out water electrolysis under 1-Sun equivalent light intensity. Two terminal multijunction solar cells grant an increased open-circuit voltage (V_{oc}) that can conduct electrochemical water splitting while also increasing the power conversion efficiency (PCE) above the limit of series-connected single-junction cells. The multijunction solar cells combine either a wide-bandgap perovskite semiconductor with a narrow-bandgap crystalline silicon (c-Si) in a perovskite-silicon (PVK-Si) tandem solar cell (chapter 3) or two perovskite semiconductors with complementary bandgaps in an all-perovskite tandem solar cell (chapter 4). The PVK-Si tandem solar cell reaches a V_{oc} above 1.75 V, high enough to split water and the cell provides high current densities that enable a STH conversion of 21.5% when using state-of-the-art catalysts and membranes. This STH value is presently the highest reported value for a system operating without sunlight concentration. The system also represents the first example of a two terminal PVK-Si multijunction cell coupled to flow electrochemical cell operating in normal sunlight.

The V_{oc} of the PVK-Si tandem solar cell might not be enough to achieve efficient water electrolysis in case more earth-abundant, but less efficient catalysts are used in water electrolysis, where higher overpotentials arise. All-perovskite tandem solar cells provide a higher V_{oc} , reaching almost 2.0 V. This widens the voltage range for operating water electrolysis but at the expense of some drop in current density. Nonetheless, perovskite-based tandem solar cells reach close to 19% STH conversion using a comparatively inexpensive semiconductor and low processing costs and state-of-the-art catalysts and membranes. Furthermore, this chapter describes the optimization of a narrow-

bandgap perovskite solar cell based on a one-step deposition procedure to possibly boost the PCE of the all-perovskite tandem solar cell and STH of the coupled system. Additives in the perovskite precursor solution and top surface treatments of the perovskite film allowed to reach a maximum PCE of 18.6%, a 3.1% increase over the previous procedure. This optimization combined with further improvements on the wide-bandgap sub-cell may elevate the PCE of the all-perovskite tandems above 26% and STH to almost 20%.

In chapter 5, proton exchange membranes (PEMs) made of sulfonated derivatives of polypentafluorostyrene and poly(arylene thioether)s were compared to Nafion in terms of electrolysis performance and hydrogen permeability. These PEMs had better ionic transport properties than Nafion but it was found that Nafion outperforms most of the new membranes in terms of energy and faradaic efficiency. The new membranes have larger water uptake and swelling ratios, which increase mass transfer losses at the electrodes whilst allowing more hydrogen to crossover. Thus, new ionomers for PEMs should combine high ion transport properties and low water uptakes to avoid excessive gas permeation and energy losses.

The high capital cost resulting from the use of titanium as base material for PTLs and bipolar plates, decreases the economic viability of water electrolysis. The emerging field of printed electronics can provide a suitable answer for high throughput and low-cost manufacturing of electrodes. In chapter 6, graphite-based electrodes were directly printed on Nafion with diverse patterns that allowed proton transport that resulted in successful water electrolysis. Further improvements on the ink formulation and other patterns would clearly benefit the efficiency of these electrodes, while using minimal amount of materials.

In chapter 7, a life cycle assessment (LCA) of a solar-assisted water electrolysis device that integrates the new materials (PEM and molecular catalysts developed in eSCALED project) was conducted and compared with a device using state-of-the-art materials. The environmental impact described by LCA covers a broad range of impacts upon the environment and also, cumulative energy demand. All the environmental impacts from raw material extraction (cradle) to manufacture (gate) of the devices were considered and used to identify the most environmentally critical processes and materials. Overall, the eSCALED device presents larger environmental impact than the state-of-the-art device, which is mostly associated to the low efficiency and thus, inability to operate at high current densities. Moreover, the identification of the most environmental

impactful processes led to a better understanding of the environmental burden of the devices and where to improve them in the future.

1.5. References

1. International Energy Agency (IEA). Global Energy and CO₂ Status report. <https://www.iea.org/geco/> (2019).
2. Sapountzi, F. M., Gracia, J. M., Weststrate, C. J., Fredriksson, H. O. A. & Niemantsverdriet, J. W. Electrocatalysts for the generation of hydrogen, oxygen and synthesis gas. *Prog. Energy Combust. Sci.* **58**, 1–35 (2017).
3. Ritchie, H., Roser, M. & Rosado, P. Energy. <https://ourworldindata.org/energy> (Accessed on February 27th, 2023).
4. GDP per capita. <https://ourworldindata.org/grapher/gdp-per-capita-worldbank?tab=chart>. (Accessed on March 4th, 2023)
5. Chang, X., Wang, T. & Gong, J. CO₂ Photo-reduction: Insights into CO₂ activation and reaction on surfaces of photocatalysts. *Energy Environ. Sci.* **9**, 2177–2196 (2016).
6. Kweku, D., Bismark, O., Maxwell, A., Desmond, K., Danso, K., Oti-Mensah, E., Quachie, A. & Adormaa, B. Greenhouse Effect: Greenhouse Gases and Their Impact on Global Warming. *J. Sci. Res. Reports* **17**, 1–9 (2018).
7. The Paris Agreement. <https://unfccc.int/process-and-meetings/the-paris-agreement>. (Accessed on February 24th, 2023)
8. Wang, Y., Sharma, A., Duong, T., Arandiyani, H., Zhao, T., Zhang, D., Su, Z., Garbrecht, M., Beck, F. J., Karuturi, S., Zhao, C. & Catchpole, K. Direct Solar Hydrogen Generation at 20% Efficiency Using Low-Cost Materials. *Adv. Energy Mater.* **11**, 2101053 (2021).
9. Nogalska, A., Zukowska, A. & Garcia-Valls, R. Atmospheric CO₂ capture for the artificial photosynthetic system. *Sci. Total Environ.* **621**, 186–192 (2018).
10. Crabtree, G. W. & Lewis, N. S. Solar energy conversion. *Phys. Today* **60**, 37–42 (2007).
11. Gust, D., Moore, T. A. & Moore, A. L. Solar Fuels via Artificial Photosynthesis. *Acc. Chem. Res.* **42**, 1890–1898 (2009).
12. Kim, J. H., Hansora, D., Sharma, P., Jang, J. W. & Lee, J. S. Toward practical solar hydrogen production-an artificial photosynthetic leaf-to-farm challenge. *Chem. Soc. Rev.* **48**, 1908–1971 (2019).
13. International Energy Agency (IEA). *Renewables* 2022. <https://www.iea.org/reports/renewables-2022> (2022).
14. Jang, D., Cho, H. & Kang, S. Numerical modeling and analysis of the effect of pressure on the performance of an alkaline water electrolysis system. *Appl. Energy* **287**, 116554 (2021).
15. Buffo, G., Marocco, P., Ferrero, D., Lanzini, A. & Santarelli, M. Power-to-X and power-to-power routes. in *Solar Hydrogen Production* 529–557 (Elsevier, 2019).
16. Cheng, W.-H., Richter, M. H., Sullivan, I., Larson, D. M., Xiang, C., Brunschwig, B. S. & Atwater, H. A. CO₂ Reduction to CO with 19% Efficiency in a Solar-Driven Gas Diffusion

- Electrode Flow Cell under Outdoor Solar Illumination. *ACS Energy Lett.* **5**, 470–476 (2020).
17. Davoudi, S., Khalili-Garakani, A. & Kashefi, K. Power-to-X for Renewable-Based Hybrid Energy Systems. in *Power Systems* 23–40 (Springer Science and Business Media Deutschland GmbH, 2022).
 18. ISPT. *Power to Ammonia*. <http://www.ispt.eu/media/ISPT-P2A-Final-Report.pdf> (2017).
 19. Park, J. E., Kang, S. Y., Oh, S.-H. H., Kim, J. K., Lim, M. S., Ahn, C.-Y. Y., Cho, Y.-H. H. & Sung, Y.-E. E. High-performance anion-exchange membrane water electrolysis. *Electrochim. Acta* **295**, 99–106 (2019).
 20. International Renewable Energy Agency (IRENA). Hydrogen. <https://www.irena.org/Energy-Transition/Technology/Hydrogen>. (Accessed on February 27th, 2023)
 21. van Trooswijk, A. P. & Deiman, J. R. Sur Une Manière de Décomposer l’Eau En Air Inflammable et En Air Vital. *Obs. Phys.* **35**, 369–384 (1789).
 22. International Energy Agency (IEA). *Hydrogen Supply*. <https://www.iea.org/reports/hydrogen-supply> (Accessed on February 27th, 2023)
 23. Schuler, T., Schmidt, T. J. & Büchi, F. N. Polymer Electrolyte Water Electrolysis: Correlating Performance and Porous Transport Layer Structure: Part II. Electrochemical Performance Analysis. *J. Electrochem. Soc.* **166**, F555–F565 (2019).
 24. Čulík, P., Brooks, K., Momblona, C., Adams, M., Kinge, S., Maréchal, F., Dyson, P. J. & Nazeeruddin, M. K. Design and Cost Analysis of 100 MW Perovskite Solar Panel Manufacturing Process in Different Locations. *ACS Energy Lett.* **7**, 3039–3044 (2022).
 25. Almora, O., Baran, D., Bazan, G. C., Cabrera, C. I., Erten-Ela, S., Forberich, K., Guo, F., Hauch, J., Ho-Baillie, A. W. Y., Jacobsson, T. J., Janssen, R. A. J., Kirchartz, T., Kopidakis, N., Loi, M. A., Lunt, R. R., Mathew, X., McGehee, M. D., Min, J., Mitzi, D. B., *et al.* Device Performance of Emerging Photovoltaic Materials (Version 3). *Adv. Energy Mater.* **13**, 2203313 (2023).
 26. Barber, J. Biological solar energy. *Philos. Trans. R. Soc. A Math. Phys. Eng. Sci.* **365**, 1007–1023 (2007).
 27. Reece, S. Y., Hamel, J. A., Sung, K., Jarvi, T. D., Esswein, A. J., Pijpers, J. J. H. & Nocera, D. G. Wireless Solar Water Splitting Using Silicon-Based Semiconductors and Earth-Abundant Catalysts. *Science*. **334**, 645–648 (2011).
 28. Nocera, D. G. The Artificial Leaf. *Acc. Chem. Res.* **45**, 767–776 (2012).
 29. Cook, R. L., MacDuff, R. C. & Sammells, A. F. Photoelectrochemical Carbon Dioxide Reduction to Hydrocarbons at Ambient Temperature and Pressure. *J. Electrochem. Soc.* **135**, 3069–3070 (1988).
 30. Sasaki, Y., Nemoto, H., Saito, K. & Kudo, A. Solar Water Splitting Using Powdered Photocatalysts Driven by Z-Schematic Interparticle Electron Transfer without an Electron Mediator. *J. Phys. Chem. C* **113**, 17536–17542 (2009).
 31. Chowdhury, F. A., Trudeau, M. L., Guo, H. & Mi, Z. A photochemical diode artificial photosynthesis system for unassisted high efficiency overall pure water splitting. *Nat.*

- Commun.* **9**, 1707 (2018).
32. Halmann, M. Photoelectrochemical reduction of aqueous carbon dioxide on p-type gallium phosphide in liquid junction solar cells. *Nature* **275**, 115–116 (1978).
 33. Fujishima, A. & Honda, K. Electrochemical Photolysis of Water at a Semiconductor Electrode. *Nature* **238**, 37–38 (1972).
 34. Kang, U., Park, H., Choi, S. K., Ham, D. J., Ji, S. M., Choi, W., Han, D. S. & Abdel-Wahab, A. Photosynthesis of formate from CO₂ and water at 1% energy efficiency via copper iron oxide catalysis. *Energy Environ. Sci.* **8**, 2638–2643 (2015).
 35. Zhang, J. Z., Warnan, J., Nowaczyk, M. M., Reisner, E., Kornienko, N., Sokol, K. P., Robinson, W. E., Ruff, A., Warnan, J., Kornienko, N., Nowaczyk, M. M., Ruff, A., Zhang, J. Z. & Reisner, E. Bias-free photoelectrochemical water splitting with photosystem II on a dye-sensitized photoanode wired to hydrogenase. *Nat. Energy* **3**, 944–951 (2018).
 36. Nguyen, P. D., Duong, T. M. & Tran, P. D. Current progress and challenges in engineering viable artificial leaf for solar water splitting. *J. Sci. Adv. Mater. Devices* **2**, 399–417 (2017).
 37. Bhattacharjee, S., Rahaman, M., Andrei, V., Miller, M., Rodríguez-Jiménez, S., Lam, E., Pornrungrroj, C. & Reisner, E. Photoelectrochemical CO₂-to-fuel conversion with simultaneous plastic reforming. *Nat. Synth.* **2**, 182–192 (2023).
 38. Abdi, F. F., Han, L., Smets, A. H. M., Zeman, M., Dam, B. & van de Krol, R. Efficient solar water splitting by enhanced charge separation in a bismuth vanadate-silicon tandem photoelectrode. *Nat. Commun.* **4**, 2195 (2013).
 39. Cox, C. R., Lee, J. Z., Nocera, D. G. & Buonassisi, T. Ten-percent solar-to-fuel conversion with nonprecious materials. *Proc. Natl. Acad. Sci.* **111**, 14057–14061 (2014).
 40. Tembhumne, S., Nandjou, F. & Haussener, S. A thermally synergistic photoelectrochemical hydrogen generator operating under concentrated solar irradiation. *Nat. Energy* **4**, 399–407 (2019).
 41. Walter, M. G., Warren, E. L., McKone, J. R., Boettcher, S. W., Mi, Q., Santori, E. A. & Lewis, N. S. Solar water splitting cells. *Chem. Rev.* **110**, 6446–6473 (2010).
 42. Godula-Jopek, A. *Hydrogen Production: by Electrolysis*. (Wiley-VCH Verlag GmbH & Co., 2015).
 43. Koper, M. T. M. Thermodynamic theory of multi-electron transfer reactions: Implications for electrocatalysis. *J. Electroanal. Chem.* **660**, 254–260 (2011).
 44. Young, J. L., Steiner, M. A., Döscher, H., France, R. M., Turner, J. A. & Deutsch, T. G. Direct solar-to-hydrogen conversion via inverted metamorphic multi-junction semiconductor architectures. *Nat. Energy* **2**, 17028 (2017).
 45. Hsu, S.-H., Miao, J., Zhang, L., Gao, J., Wang, H., Tao, H., Hung, S.-F., Vasileff, A., Qiao, S. Z. & Liu, B. An Earth-Abundant Catalyst-Based Seawater Photoelectrolysis System with 17.9% Solar-to-Hydrogen Efficiency. *Adv. Mater.* **30**, 1707261 (2018).
 46. Cheng, W.-H., Richter, M. H., May, M. M., Ohlmann, J., Lackner, D., Dimroth, F., Hannappel, T., Atwater, H. A. & Lewerenz, H.-J. Monolithic Photoelectrochemical Device for Direct Water Splitting with 19% Efficiency. *ACS Energy Lett.* **3**, 1795–1800 (2018).

47. Kuang, Y., Kenney, M. J., Meng, Y., Hung, W. H., Liu, Y., Huang, J. E., Prasanna, R., Li, P., Li, Y., Wang, L., Lin, M. C., McGehee, M. D., Sun, X. & Dai, H. Solar-driven, highly sustained splitting of seawater into hydrogen and oxygen fuels. *Proc. Natl. Acad. Sci. U. S. A.* **116**, 6624–6629 (2019).
48. Chen, H., Song, L., Ouyang, S., Wang, J., Lv, J. & Ye, J. Co and Fe Codoped WO_{2.72} as Alkaline-Solution-Available Oxygen Evolution Reaction Catalyst to Construct Photovoltaic Water Splitting System with Solar-To-Hydrogen Efficiency of 16.9%. *Adv. Sci.* **6**, 1900465 (2019).
49. Park, H., Park, I. J., Lee, M. G., Kwon, K. C., Hong, S.-P., Kim, D. H., Lee, S. A., Lee, T. H., Kim, C., Moon, C. W., Son, D.-Y., Jung, G. H., Yang, H. S., Lee, J. R., Lee, J., Park, N.-G., Kim, S. Y., Kim, J. Y. & Jang, H. W. Water Splitting Exceeding 17% Solar-to-Hydrogen Conversion Efficiency Using Solution-Processed Ni-Based Electrocatalysts and Perovskite/Si Tandem Solar Cell. *ACS Appl. Mater. Interfaces* **11**, 33835–33843 (2019).
50. Gao, J., Sahli, F., Liu, C., Ren, D., Guo, X., Werner, J., Jeangros, Q., Zakeeruddin, S. M., Ballif, C., Grätzel, M. & Luo, J. Solar Water Splitting with Perovskite/Silicon Tandem Cell and TiC-Supported Pt Nanocluster Electrocatalyst. *Joule* **3**, 2930–2941 (2019).
51. Shi, Y., Hsieh, T.-Y. Y., Hoque, M. A., Cambarau, W., Narbey, S., Gimbert-Surinäch, C., Palomares, E., Lanza, M., Llobet, A., Gimbert-Suriñach, C., Palomares, E., Lanza, M. & Llobet, A. High Solar-to-Hydrogen Conversion Efficiency at pH 7 Based on a PV-EC Cell with an Oligomeric Molecular Anode. *ACS Appl. Mater. Interfaces* **12**, 55856–55864 (2020).
52. Li, Z., Wu, S., Zhang, J., Lee, K. C., Lei, H., Lin, F., Wang, Z., Zhu, Z. & Jen, A. K. Y. Y. Hybrid Perovskite-Organic Flexible Tandem Solar Cell Enabling Highly Efficient Electrocatalysis Overall Water Splitting. *Adv. Energy Mater.* **10**, 2000361 (2020).
53. Lee, M., Turan, B., Becker, J. P., Welter, K., Klingebiel, B., Neumann, E., Sohn, Y. J., Merdzhanova, T., Kirchartz, T., Finger, F., Rau, U. & Haas, S. A Bias-Free, Stand-Alone, and Scalable Photovoltaic–Electrochemical Device for Solar Hydrogen Production. *Adv. Sustain. Syst.* **4**, 2000070 (2020).
54. Luo, J., Im, J. H., Mayer, M. T., Schreier, M., Nazeeruddin, M. K., Park, N. G., Tilley, S. D., Fan, H. J. & Grätzel, M. Water photolysis at 12.3% efficiency via perovskite photovoltaics and Earth-abundant catalysts. *Science*. **345**, 1593–1596 (2014).
55. Karuturi, S. K., Shen, H., Sharma, A., Beck, F. J., Varadhan, P., Duong, T., Narangari, P. R., Zhang, D., Wan, Y., He, J., Tan, H. H., Jagadish, C. & Catchpole, K. Over 17% Efficiency Stand-Alone Solar Water Splitting Enabled by Perovskite-Silicon Tandem Absorbers. *Adv. Energy Mater.* **10**, 2000772 (2020).
56. Bayrak Pehlivan, İ., Atak, G., Niklasson, G. A., Stolt, L., Edoff, M. & Edvinsson, T. Electrochromic solar water splitting using a cathodic WO₃ electrocatalyst. *Nano Energy* **81**, 3–6 (2021).
57. Wang, M., Shi, B., Zhang, Q., Li, X., Pan, S., Zhao, Y. & Zhang, X. Integrated and Unassisted Solar Water-Splitting System by Monolithic Perovskite/Silicon Tandem Solar Cell. *Sol. RRL* **6**, 2100748 (2022).
58. Datta, K., Branco, B., Zhao, Y., Zardetto, V., Phung, N., Bracesco, A., Mazzarella, L., Wienk, M. M., Creatore, M., Isabella, O. & Janssen, R. A. J. Efficient Continuous Light-Driven Electrochemical Water Splitting Enabled by Monolithic Perovskite-Silicon

- Tandem Photovoltaics. *Adv. Mater. Technol.* **8**, 2201131 (2023).
59. Pan, S., Li, R., Wang, J., Zhang, Q., Wang, M., Shi, B., Wang, P., Zhao, Y. & Zhang, X. Floating Seawater Splitting Device Based on NiFeCrMo Metal Hydroxide Electrocatalyst and Perovskite/Silicon Tandem Solar Cells. *ACS Nano* **17**, 4539-4550 (2023).
 60. Rau, S., Vierrath, S., Ohlmann, J., Fallisch, A., Lackner, D., Dimroth, F. & Smolinka, T. Highly Efficient Solar Hydrogen Generation-An Integrated Concept Joining III-V Solar Cells with PEM Electrolysis Cells. *Energy Technol.* **2**, 43-53 (2014).
 61. Verlage, E., Hu, S., Liu, R., Jones, R. J. R. R., Sun, K., Xiang, C., Lewis, N. S. & Atwater, H. A. A monolithically integrated, intrinsically safe, 10% efficient, solar-driven water-splitting system based on active, stable earth-abundant electrocatalysts in conjunction with tandem III-V light absorbers protected by amorphous TiO₂ films. *Energy Environ. Sci.* **8**, 3166-3172 (2015).
 62. Bonke, S. A., Wiechen, M., MacFarlane, D. R. & Spiccia, L. Renewable fuels from concentrated solar power: towards practical artificial photosynthesis. *Energy Environ. Sci.* **8**, 2791-2796 (2015).
 63. Nakamura, A., Ota, Y., Koike, K., Hidaka, Y., Nishioka, K., Sugiyama, M. & Fujii, K. A 24.4% solar to hydrogen energy conversion efficiency by combining concentrator photovoltaic modules and electrochemical cells. *Appl. Phys. Express* **8**, (2015).
 64. Esiner, S., Willems, R. E. M. M., Furlan, A., Li, W., Wienk, M. M. & Janssen, R. A. J. Photoelectrochemical water splitting in an organic artificial leaf. *J. Mater. Chem. A* **3**, 23936-23945 (2015).
 65. Jia, J., Seitz, L. C., Benck, J. D., Huo, Y., Chen, Y., Ng, J. W. D., Bilir, T., Harris, J. S. & Jaramillo, T. F. Solar water splitting by photovoltaic-electrolysis with a solar-to-hydrogen efficiency over 30%. *Nat. Commun.* **7**, 13237 (2016).
 66. Schüttauf, J.-W., Modestino, M. A., Chinello, E., Lambelet, D., Delfino, A., Dominé, D., Faes, A., Despeisse, M., Bailat, J., Psaltis, D., Moser, C. & Ballif, C. Solar-to-Hydrogen Production at 14.2% Efficiency with Silicon Photovoltaics and Earth-Abundant Electrocatalysts. *J. Electrochem. Soc.* **163**, F1177-F1181 (2016).

Chapter 2

Assembly and optimization of a lab-scale setup for water electrolysis

Abstract

A proton exchange membrane water electrolysis setup and cell were assembled and optimized using state-of-the-art materials with a target maximum potential at 1 A cm^{-2} of 1.80 V. Assembling a setup and cell that yield reproducible and comparable results to literature when using state-of-the-art materials was deemed important as one of the aims of this thesis is to evaluate new proton exchange membranes. The optimization of the setup and cell included testing different cell clamping torques, inlet cell temperatures, type of porous transport layers, sample storage environment, and materials as flow fields. The optimized version of the setup achieved the target current density (1 A cm^{-2}) at 1.63 V, far exceeding the initial goal. The electrolysis cell was assembled using a clamping torque of 0.8 Nm and consisted of a polypropylene support with titanium flow fields, a ~260 mm porous titanium transport layer (PTL) at the anode, a carbon PTL with microporous layer at the cathode, ruthenium(IV) oxide as oxygen and platinum as hydrogen evolution catalyst, and a Nafion NRE-212 proton exchange membrane. Deionized water was pumped to the cell at a flow rate of 10 mL min^{-1} at $\sim 60 \text{ }^\circ\text{C}$ through each inlet.

2.1. Introduction

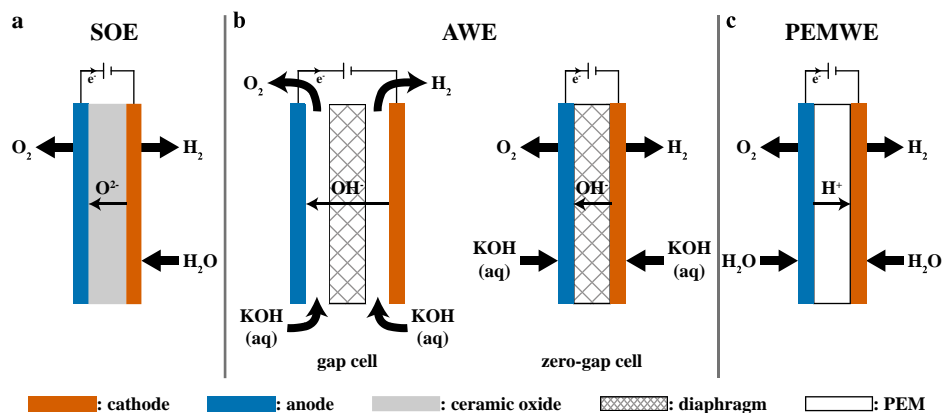
Water electrolysis was first observed in 1789 by Adriaan van Paets van Troostwijk and Jan Rudolph Deiman when they used an electrostatic generator to apply an electric discharge between two gold (Au) electrodes under water.^{1,2} About a decade later William Nicholson and Anthony Carlisle, while testing the recently invented voltaic pile, connected two copper (Cu) electrodes immersed in water to the pile, and observed a small stream of gas bubbles evolving from the electrodes, i.e., water electrolysis. Later the same year, Johann Wilhelm Ritter carried out a similar experiment to Nicholson and Carlisle, but this time, he was able to collect the evolved gases (H_2 and O_2) separately.³ In spite of these early encouraging developments, water electrolysis at industrial scale was only implemented in 1888, pioneered by a Russian engineer Dmitry Lachinov. More than 400 industrial electrolysis units were in operation at the start of the 20th century.⁴

Nowadays, there are three commercially available water electrolysis technologies that differ primarily on the used electrolyte, namely alkaline water electrolysis (AWE), proton exchange membrane water electrolysis (PEMWE), and solid oxide electrolysis (SOE). AWE and PEMWE operate at low temperatures ($T < 90$ °C) and use hydroxide ions (OH^-) and protons (H^+) as ionic charge carriers, respectively, while SOE operates at high temperatures ($T > 700$ °C) and the ionic charge carriers are oxygen ions (O^{2-}). The main characteristics of each technology are summarized in **Table 2.1**.^{3,5,6}

The most recent and least mature technology, still at lab-scale, is SOE that uses steam as water source as a result of the high operating temperatures and O^{2-} conductors, primarily yttria stabilized zirconia (YSZ) – **Figure 2.1a**. Since it was first reported in the 1980s, SOE has attracted a lot of attention, because the high operating temperature sharply decreases the thermodynamic potential and enhances reaction kinetics, enabling efficiencies close to 100% to be reached at current densities of practical interest (~ 1 A cm^{-2}).⁷ This could potentially lead to lower capital costs and energy demands if the required heat can be generated renewably or be supplied from waste heat.⁸ But, the high temperature oxygen produced at the anode is highly corrosive, and it easily degrades cell components. A solution to mitigate this problem is to dilute the formed oxygen with air, but that introduces extra energy costs and complexity to the balance of plant.^{9,10} Long-term sealing at such high temperatures is difficult to achieve, especially at elevated pressures. The high cost and low power modules in comparison to low temperature electrolysis limits SOE to niche applications.¹¹

Table 2.1: Comparison between different water electrolysis technologies.^{3,5,6,12,13}

	AWE	PEMWE	SOE
Technology status	Mature	Commercial	Lab-scale, R&D, demonstrators
Charge carrier	OH^-	H^+	O^{2-}
Temperature / °C	< 90	< 90	700 – 1000
Electrolyte	25–30 wt% KOH	Solid (perfluorosulfonic acid)	$\text{Y}_2\text{O}_3\text{-ZrO}_2$, $\text{Sc}_2\text{O}_3\text{-ZrO}_2$, MgO-ZrO_2 , CaO-ZrO_2
Anode	Ni, Fe, Co-based	Ir/Ru oxide	$\text{La}_x\text{Sr}_{1-x}\text{MnO}_3$ + Y-stabilized ZrO_2 (LSM-YSZ)
Cathode	Ni-based	Pt	Ni-YSZ
Separator	Porous diaphragm (e.g. Zirfon®)	Polymer membrane (e.g. Nafion)	Ceramic
Pressure / bar	1 – 200	1 – 350	1 – 5
Current density range / A cm^{-2}	0.2 – 0.5	0 – 3	0 – 2
Cell voltage / V	1.8 – 2.4	1.8 – 2.2	1.48 – 1.7
Capacity / $\text{Nm}^3 \text{h}^{-1}$	1 – 500	1 – 250	1
Durability / $\times 1000 \text{ h}$	100	10 – 50	0.5 – 23
H₂O specification	liquid	> 10 MΩ cm	steam


Figure 2.1: Operation principles and usual cell configurations. a) Solid oxide (SOE). b) Alkaline (AWE). c) Proton exchange membrane (PEM) water electrolysis.

Alkaline water electrolysis is the most mature of the three technologies, having been used in the first industrial electrolysis cells mentioned previously, and it has evolved to installations up to the megawatt (MW) range. Generally, in AWE, the electrodes are immersed in a liquid electrolyte, usually an aqueous solution of ~30 wt% KOH, and they are separated by a porous separator (diaphragm) that is permeable to water and OH^- .¹⁴ A large advantage of AWE is that the alkaline environment allows the use of a wide range of cost-effective

electrocatalysts, mainly based on transition metals such as iron (Fe), cobalt (Co), nickel (Ni), and their oxides.^{15–17} Despite not being as active as their noble metal counterparts, these catalysts are still chosen for AWE due to their abundance and their relatively high activity and stability in alkaline environment. The use of such catalysts results in decreased capital costs when compared with the other technologies. In the early days, AWE was operated in gap-cells, i.e., there is a small gap between the electrode and the separator (Figure 2.1b), however, this limited the maximum operating current density. In this configuration, at high current densities, the evolved gas can form a non-conductive film covering the electrode surface, resulting in increased resistance and therefore, higher energy consumption. More modern AWE cells have adopted a zero-gap configuration (Figure 2.1b) that consists of porous electrodes pressed against the diaphragm, minimizing the inter-electrode distance and ohmic resistance.¹⁸ Also, in such configuration, the gaseous products are released at the backside of the porous electrodes.¹⁹

Despite the large experience and advantages of this technology, AWE still has a few issues that require improvement. The first major issue in AWE is low operating current density, mainly caused by low ionic conduction across the liquid electrolyte and diaphragm. The use of a liquid electrolyte can additionally lead to the presence of stray currents, i.e., currents that flow through an element or elements other than the intended anode-cathode couple. Therefore, stray currents reduce the faradaic efficiency as not all current density is used in the electrochemical process and may induce corrosion of those elements.^{20,21} Another issue related to the use of a liquid electrolyte is the inability to operate at high differential pressure. Operating under differential pressure is advantageous because it increases the hydrogen purity by decrease of oxygen crossover while reducing the compression requirements of the produced hydrogen and avoiding handling of high pressure oxygen. Moreover, the combination of these two issues result in bulkier and heavier cell stacks, meaning that AWE plants will need more space to be deployed, which adds to the total capital cost.^{22,23} In addition to not being ionic conductive, the diaphragm also does not fully avoid gas crossover, causing decreased efficiency and the need for safety precautions. Excessive gas crossover can lead to concentrations of H₂ (> 4 mol%) at the anode or O₂ (> 6 mol%) at the cathode above the lower explosivity limits, especially at low current densities.^{24,25} The International Standard on hydrogen production by water electrolysis has defined a maximum of 2 mol% of hydrogen in oxygen, meaning that at such concentration, an emergency shutdown is initiated.²⁶ To avoid frequent shutdowns, an alarm value below 2 mol% is generally implemented in industrial electrolysis systems.²⁷ The efficiency can also drop as the crossed over

oxygen may react with the evolved hydrogen at the cathode, forming water. Furthermore, this makes AWE less suitable for intermittent power operation, as provided by renewable energy sources, since operation at low power availability and thus, low current densities, needs to be avoided.^{28,29} The optimization of the operating parameters, advancements in materials and the use of protective currents during shutdown can help to overcome this challenging issue.³⁰

The third water electrolysis technology, PEMWE was introduced in 1960s by General Electric as a result of the advent of proton-conductive polymers (ionomers).^{31–33} Recently, electrolysis plants on the order of 100s of kW or MW have arisen with many multiple MW installations planned until 2025.³⁴ Currently, Europe's largest PEMWE plant is located in Wesseling (Germany) with a capacity of 10 MW as part of the REFHYNE project funded by the European Commission's Fuel Cells and Hydrogen Joint Undertaking, while the world's largest is located in Quebec (Canada) with a capacity of 20 MW lead by Air Liquide.^{35,36} This technology consists of a solid proton exchange membrane (PEM), acting simultaneously as electrolyte and gas separator, in direct contact with the porous electrodes composing what is commonly called membrane-electrode assembly (MEA) as illustrated in Figure 2.1c. The electrodes are composed of porous transport layers, normally titanium (Ti) at the anode and carbon (C) at the cathode, and electrocatalysts based on platinum-group metals (PGM). A brief description of each PEMWE cell component is provided in following sections.

The replacement of the liquid electrolyte and diaphragm by a single component, the ion exchange membrane, solves most of the issues discussed earlier related to AWE. The use of a solid electrolyte avoids the use of corrosive and highly concentrated liquid electrolytes, allowing the use of merely deionized water as feed. PEMs are usually very thin (~ 20–200 μm) and provide high proton conductivity, leading to lower ohmic resistances. Hence, much higher current densities in the range of a few A cm^{-2} are achievable at the same potential, decreasing the operational costs of electrolysis and allowing a more compact and lighter design.³⁷ In contrast to AWE, PEMWE may operate under high pressure, both in balanced and differential modes, with reports demonstrating PEMWE systems up to 350 bar.^{38,39} Furthermore, the lower permeability of PEMs avoids safety issues related to gas mixing in the cell and it results in higher hydrogen purity. The possibility of operating at low current densities, combined with the lower footprint, makes PEMWE more suitable for decentralized systems and thus for intermittent power operation as supplied by renewable energy sources.^{19,40}

Naturally, the benefits of PEMWE are accompanied by some drawbacks, mainly related with the acidic environment provided by the PEM. Such harsh environment limits the use of possible materials for catalysts, porous transport layers (PTL) and bipolar plates (BPP) to highly expensive materials.⁴¹ Electrocatalysts are generally based on platinum group metals such as ruthenium (Ru), iridium (Ir), and platinum (Pt) for high activity and stability while anodic porous transport layers and the bipolar plates are made of Ti. Also, the proton exchange membranes, which are typically perfluoro sulfonated acid ionomers, have high costs. All these culminate in high capital costs for PEMWE (900 € kW⁻¹) in comparison to AWE (600 € kW⁻¹) as estimated in a technical report by the Joint Research Centre (JRC) of the European Union for a 100 MW hydrogen plant.¹¹ Therefore, most current research related to PEMWE is focused on developing new and less expensive materials that could provide higher or similar efficiencies to state-of-the-art ones and on finding better operational conditions that result in lower energy demands. This current research trend leads to the widely held belief that PEMWE will surpass AWE as the main water electrolysis technology in a near future due to better operational flexibility and predicted cost drop.^{42–49} Nevertheless, in field of AWE, there is a growing interest in moving from a porous separator to an anion exchange membrane (AEM) that could possibly combine some of the advantages of AWE and PEMWE. However, most of the AEM show much less ion conductivity and lower efficiency for water electrolysis than PEM.^{15,16,50–56}

PEMWE was chosen as water electrolysis technology to use for the remainder of this chapter and consequently, this thesis. PEMWE seems the most suitable choice as it has easier balance of plant than SOE at lab-scale and it can provide a safer and a higher efficiency process than AWE, despite the higher associated material costs. Moreover, this thesis intends to integrate a water electrolysis cell with a renewable energy source, i.e., solar cells, further supporting the choice of PEMWE over AWE.

In the following sections, a brief summary of the state-of-the-art materials for PEMWE carried out followed by a description of the main voltage losses in water electrolysis. Subsequently, the assembly and optimization of a proton exchange water electrolysis setup is described as well as the associated results. The target to consider the setup optimized to proceed to test new materials, i.e., PEMs, in the next chapters was set at obtaining a current density of 1 A cm⁻² below 1.8 V. These values were chosen as they are typical values obtained for lab-scale state-of-the-art PEMWE.^{6,41,42,49,57–61}

2.2. Materials

A PEMWE cell consists of a MEA sandwiched between PTLs that enable transport of water and gas to and from the catalyst layer, and provide electrical conductivity to the BPPs as illustrated in **Figure 2.2**. During operation, liquid water can be supplied to either only at the anode or both sides. At the anode, water is oxidized, producing electrons, protons, and oxygen. The oxygen is transported out of the catalyst layer through the PTL to the anode outlet. The protons move through the PEM to the cathodic catalyst layer where they can be reduced by electrons from the external circuit to hydrogen that exits at the cathode outlet.⁶ In the following sections, a brief description of the main components of a PEMWE cell will be given. These sections intend to introduce the typical materials and describe their advantages and disadvantages.

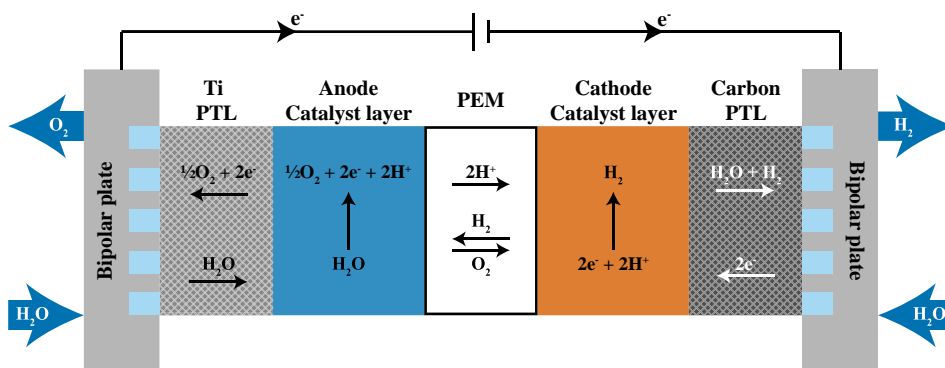


Figure 2.2: Schematic illustration of a proton exchange membrane water electrolysis cell. Based on the scheme from ref.⁴².

2.2.1. Catalysts

Well performing electrocatalysts are essential for efficient and large-scale water electrolysis. A material is considered a good electrocatalyst when it provides high catalytic activity for the target reaction at low overpotentials, has high electrochemical active area, high electrical conductivity, and is chemically and electrochemically stable. The high electrochemical active area promotes the accessibility to reactants and removal of the products, allowing a reduction of the required catalyst amount. The catalyst should also be able to withstand the harsh environment created by the low pH of the electrolyte (chemical stability) and the high overpotentials, i.e., corrosion resistant (electrochemical stability). Furthermore, commercialization of water electrolysis also depends on the capital costs of the system and thus, the catalyst material should be preferably inexpensive to facilitate the scale up of the system.^{5,62}

The acidic environment in PEMWE narrows the choice of appropriate catalysts to platinum group metals (PGM). McCrory et al. evaluated the catalytic activities of several mixed non-noble (Ni, Co, Fe, Mo based) and noble metal (Ir, Ru, Pt) electrocatalysts for both the oxygen evolution reaction (OER) and the hydrogen evolution reaction (HER).⁶³ For OER, they found that Ir and Ru had overpotentials of ~ 0.3 V (at 10 mA cm^{-2}) while the non-noble electrocatalysts showed equivalent activity and stability to the glassy carbon background (~ 1.1 V at 10 mA cm^{-2}) – **Figure 2.3**, top right. Under the oxidative conditions of OER in acidic environment, the metal electrocatalysts tend to form an oxide layer, causing a reduction in electrocatalytic activity due to decreased electron conductivity in comparison to the bare metal.^{64,65} However, for Ru and Ir, the respective oxides (RuO_2 and IrO_2) show better activity for OER ($\text{RuO}_2 > \text{IrO}_2$) as they have excellent electron conductivity in the order of 10s kS cm^{-1} .⁶⁶ Even though RuO_2 is more active and more abundant than IrO_2 , the latter is the main choice in state-of-the-art PEMWE as RuO_2 suffers from poor stability because it easily corrodes and dissolves under high anodic potentials, forming RuO_4 and losing activity.^{67,68} Currently, catalyst loadings at the anode are considerably high ($\approx 2 \text{ mg}_{\text{PGM}} \text{ cm}^{-2}$) due to the slow kinetics of OER. Ru and Ir are two of the scarcest metals on Earth, around 1 ppb, only produced as by-products of Ni or Pt mining.^{62,69} The limited availability of these combined with the increasing demand of these metals can lead to great capital costs, hindering the implementation of PEMWE on a commercial scale.

Pt-based materials have been the benchmark for HER in PEMWE over the years because of the lower overpotential (-0.04 V at 10 mA cm^{-2}) as shown in Figure 2.3. Initially, Pt black was used as the standard HER catalyst but, due to the experience in PEM fuel cell technology, researchers have started to use Pt supported on carbon black. The carbon black supports have good electronic conductivity, provide high surface area for dispersion of the catalyst and are reasonably stable in both acidic and basic electrolyte. These characteristics positively affect the electrochemical active area, catalytic layer conductivity and stability of the metallic catalyst.^{5,70} Together with the extremely fast kinetics of Pt for HER, low amounts of material of metal can be used without losing overall performance as standard loadings range from 0.5 to $1 \text{ mg}_{\text{Pt}} \text{ cm}^{-2}$. Interestingly, further reduction of this loading has been already shown down to 0.025 mg cm^{-2} without loss of performance.⁷¹

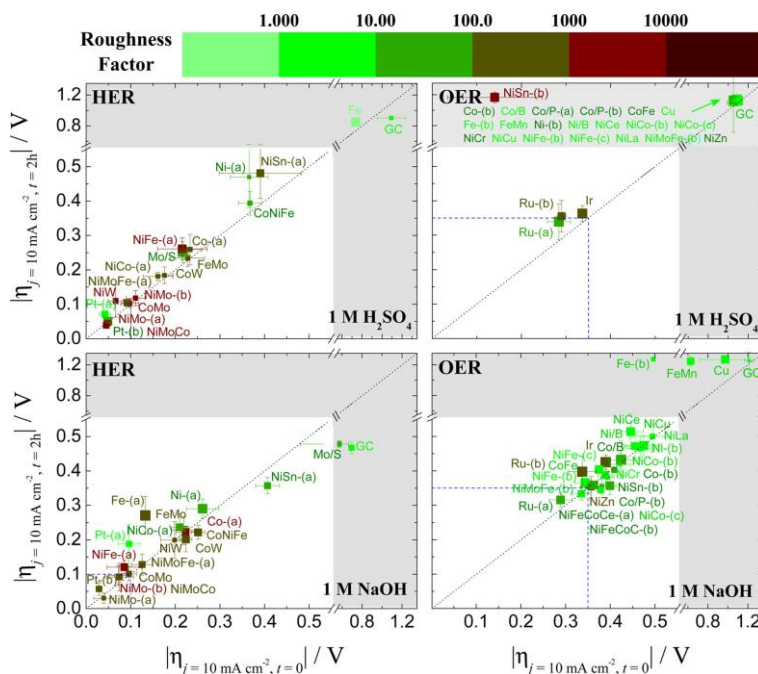


Figure 2.3: Plots of catalytic activity, stability, and electrochemically active surface area for HER (left) and OER (right) electrocatalysts in acidic (top) and alkaline (bottom) solutions. The x-axis is the overpotential required to achieve 10 mA cm^{-2} per geometric area at time $t = 0$. The y-axis is the overpotential required to achieve 10 mA cm^{-2} per geometric area at time $t = 2 \text{ h}$. The diagonal dashed line is the expected response for a stable catalyst that does not change in activity during 2 h constant polarization. The color of the each point represents the roughness factor (RF) of the catalyst with a bin size of 1 order of magnitude with light green representing $\text{RF} = 1$, and dark red representing $\text{RF} > 10^4$. The size of each point is inversely proportional to the standard deviation in the ECSA measurements. The region of interest for benchmarking is the unshaded white region of the plot where the overpotential required to achieve 10 mA cm^{-2} per geometric area at time $t = 0$ and $t = 2 \text{ h}$ is less than 0.55 V . There is a break and change in scale in both axes at overpotentials $> 0.55 \text{ V}$, and the corresponding region of the plot is shown in gray. Catalysts whose activity and stability measurements fall inside this gray area are outside the region of interest for benchmarking, but their activity and stability measurements are included for completeness. The blue boxed regions are the target regions for HER and OER catalysis under the given conditions. Reprinted with permission from Journal of the American chemical Society, 137 (13), Charles C. L. McCrory, Suho Jung, Ivonne M. Ferrer, Shawn M. Chatman, Jonas C. Peters, and Thomas F. Jaramillo, “Benchmarking Hydrogen Evolving Reaction and Oxygen Evolving Reaction Electrocatalysts for Solar Water Splitting Devices”, 4347-4357. Copyright 2015 American Chemical Society.⁶³

Nonetheless, Pt is still considerably expensive and despite being less of an economic burden than Ir or Ru, it is still important to focus research efforts to either further reduce these loadings or completely replace it with non-noble catalysts. In their study, McCrory et al. found that NiMo-(a) and NiMoCo had

similar initial activity to Pt and showed good stability over 25 h at a constant current density of 10 mA cm^{-2} . However, during a cycling experiment (> 20000 cycles, > 50 h) between -0.1 and 0.1 V versus reversible hydrogen electrode (RHE), the magnitude of the overpotential of NiMo-(a) at 10 mA cm^{-2} increased to values above 0.4 V. At $-0.1 \text{ V}_{\text{RHE}}$, current densities on the order of 100 mA cm^{-2} are reached, which suggests that the long-term stability of NiMo-(a) is significantly affected by operation at higher current densities. This set of experiments was not carried out for NiMoCo. Other alternative non-noble metal catalysts have also been shown to be quite active and stable for HER, but only a small number of studies have actually focused on integrating a few of these catalysts in a PEMWE cell.^{45,47–49,72}

For the development of the work presented below and subsequent chapters, RuO_2 and Pt supported on carbon nanoparticles (40 wt% Pt/C) were chosen as oxygen and hydrogen evolution catalysts, respectively. RuO_2 was chosen over IrO_2 , despite lower stability, as it is more active and cheaper, 53.04 €/g RuO_2 vs 417.04 €/g IrO_2 ,^{73,74} and our studies did not involve thorough stability tests. For the cathode side, Pt was chosen as the benchmark material due to the low overpotential for HER (-0.04 V at 10 mA cm^{-2}) and high stability in acidic environment, which allow lower material expenditure than with non-noble metal alternatives.

2.2.2. Proton exchange membrane (PEM)

The PEM is responsible for transporting the protons (H^+) formed during the OER on the anode to the cathode for the HER and for separating the two compartments as a permeation barrier. The PEM needs to be chemically and mechanically stable, show high proton conductivity and low gas permeability to ensure excellent performance and long-term stability. It is common to add a small amount of ionomer to the catalyst solution prior to deposition of the catalyst on the PEM. The ionomer, which is usually the same as the membrane, is used to improve the proton transport within the catalyst layer and to function as a binder, providing mechanical stability.^{75,76} However, excessive amounts of ionomer will also sharply decrease the electronic conductivity and porosity in the catalyst layer and thus, there is an optimum ionomer content depending on the fabrication and operation conditions.⁷⁷

The reference PEM material for water electrolysis has been perfluorosulfonic acid (PFSA) membranes for many years with Nafion membranes developed by DuPont set as the benchmark for efficient PEM.⁵⁷ These membranes are composed of a tetrafluoroethylene (TFE) backbone that provides excellent chemical and mechanical stability and vinyl ether side chains

terminated by sulfonic acid groups that provide high proton conductivities (**Figure 2.4**). However, the complex synthesis of Nafion leads to high manufacturing costs, further contributing to the large investment required for PEMWE.⁷⁸ This has led to a significant effort in the last few years to develop membranes based on different polymeric materials that could potentially show similar or better performances than Nafion at lower economic cost.^{57,59,79,80} In chapter 5 of this thesis, a few alternatives based on partially fluorinated polymers are investigated and compared with a state-of-the-art Nafion membrane.

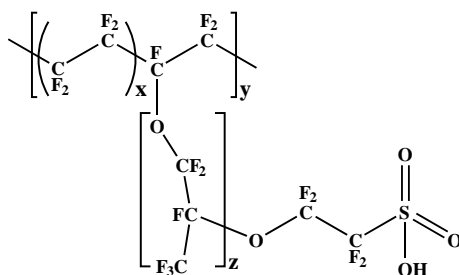


Figure 2.4: Polymer structure for Nafion membranes.

2.2.3. Porous transport layers (PTL)

The PTLs have two main purposes related to the pores and the solid structure. The pores enable the transport of water and gas to and from the catalyst layer while the solid structure provides heat and charge transport between the electrode and the bipolar plates.³⁴ The PTLs further provide mechanical support to the MEA, particularly when the electrolysis cell is operated under differential pressure.⁸¹ Therefore, the development and optimization of PTLs has to consider important aspects such as porosity, pore size distribution, tortuosity, permeability, and thickness. It is found that generally the most relevant of these properties are the porosity and pore size distribution.^{61,82–84}

On the cathode, based on the knowledge of PEM fuel cells (PEMFC), carbon-based materials such as carbon paper or cloths are commonly used. Nonetheless, operating conditions are distinct for PEMFC and PEMWE, and thereby, optimal performance may require a different set of properties, which due to larger issues at the anode side, has not been the focus of PEMWE research.³⁹ On the anode, the low pH due to the PEM combined with the high overpotential and presence of oxygen prevents the use of C and it narrows the number of materials that can be used. Most typically, the PTLs at the anode side are instead made of porous Ti in the form of sintered powders, fibers, or meshes.

There has been an extensive research effort related to the porosity and pores sizes as well as manufacturing techniques of Ti–PTLs to ensure optimal performance.^{61,83–88} For example, Ito et al. showed that electrolysis performance is enhanced by decreasing the pore size down to 10 μm , independently of the porosity as long as it is over 50%.⁸⁴ Lopata et al. tested sintered Ti–PTLs with different average pore diameter (33–160 μm) but similar porosity and two different Ir loadings (0.085 vs 0.595 $\text{mg}_{\text{Ir}} \text{cm}^{-2}$). Interestingly, they found that the PTL average pore diameter affected the performance much more for the lower Ir loading, caused by an increased contact resistance at larger pore diameters.⁶¹ This shows that the interplay between the PTLs and the catalyst layer also needs to be considered to achieve better water electrolysis performance at reduced catalyst loadings.

2.2.4. Bipolar Plates (BPP)

The bipolar plates, also referred as flow fields, commonly have a channel structure that evenly distributes water over the entire active area and removes the evolved gases. The effect of several channel configurations has already been studied and parallel channels seem to show better water electrolysis performance due to enhanced water distribution and lower pressure drop.^{89–91} Other essential properties for BPPs are excellent electric and thermal conductivity and mechanical stability to provide uniform pressure distribution as they also used to separate single cells in PEMWE cell stacks.

Similarly to the PTLs, carbon–based materials cannot be used and BPPs for PEMWE must be made of Ti as it has low permeability, high thermal and electrical conductivity, and excellent mechanical stability.⁹² Despite those good properties, Ti also tends to oxidize under high positive overpotentials at low pH, forming a passive oxide layer. Such passivation layer will clearly increase the contact resistance between the BPP and the PTLs, resulting in decreasing performance over time. This issue can be overcome by depositing noble metal coatings, e.g., Au and Pt. The additional coating, combined with the already high price of Ti and machining of the flow channels, sharply increase the cost of the BPP. With these flow fields, the BPP is the largest cost contributor for the PEMWE electrolysis stack while the stack itself accounts for more than half of the capital costs. Replacing Ti by cheaper materials is therefore crucial for a PEMWE cost–reduction. Alternative materials such as stainless steel have been studied but they also require a protective coating.^{93–95} Moreover, additive manufacturing techniques such as 3D printing have been introduced as an alternative to lower the costs and weight.⁹⁶

In this thesis, the bipolar plates were initially made out of Cu coated with thin films of Ni and Au as protective layers with parallel channels. Later, these were replaced by Ti without any coating as the coating on Cu was being removed over time, leaving the Cu surface exposed. The bipolar plates were encased in an acrylonitrile butadiene styrene (ABS) 3D printed support that was later changed to polypropylene (PP) because of the better temperature resistance of PP.

2.3. Voltage losses in water electrolysis

The cell voltage, E_{cell} in V, of a PEM water electrolysis cell is defined by adding the distinct voltage losses related to thermodynamics, ohmic, kinetics and mass transfer (Eq. 2.1) as illustrated by Figure 2.5. All voltage and current values are taken as positive.

$$E_{\text{cell}} = E_{\text{rev}} + E_{\Omega} + \eta_{\text{OER}} + \eta_{\text{HER}} + \eta_{\text{mt}} \quad (2.1)$$

In Eq. 2.1, E_{rev} is the thermodynamic potential of the water splitting reaction, E_{Ω} the ohmic overpotential related to the electrode and membrane resistances, η_{OER} and η_{HER} are the kinetic overpotentials for the OER and HER, respectively, and η_{mt} is the mass transfer overpotential. Each voltage loss will be described in detail in the following sections.

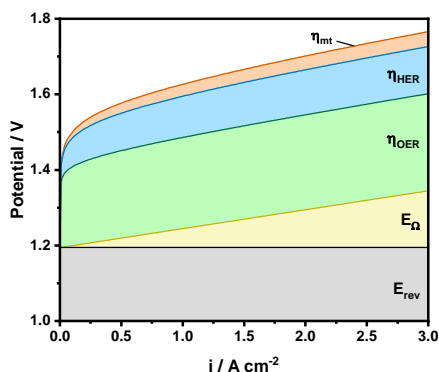


Figure 2.5: Schematic illustration of the contributions of various potential losses (overpotentials) to the cell potential.

2.3.1. Thermodynamics of water electrolysis

The molar reaction enthalpy, ΔH , represents the difference between the total reactant and total product molar enthalpies. At standard temperature and pressure (STP), that is $T^0 = 298.15$ K and $P^0 = 1$ bar, the reaction enthalpy, ΔH^0 , for the water splitting reaction is $285.84 \text{ kJ mol}^{-1}$.¹⁹ The standard Gibbs free energy, ΔG^0 , for this reaction is $237.22 \text{ kJ mol}^{-1}$ at standard temperature and

pressure (**Eq. 2.2**).¹⁹ The positive value indicates that water splitting is endergonic and thus, requires an external energy source to carry out the reaction.

$$\Delta H = \Delta G + T\Delta S \quad (2.2)$$

where T is the absolute temperature and ΔS is the change in molar entropy of the system ($\Delta S^0 = 165 \text{ J (K mol)}^{-1}$).¹⁹

The ΔG^0 represents the minimum electrical work required to split water into hydrogen and oxygen in the presence of an external heat source while ΔH^0 corresponds to the total energy required in absence of a heat source. The associated electrical potentials can be calculated by **Eq. 2.3** and **2.4**.

$$E_{\text{rev}}^0 = \left| -\frac{\Delta G^0}{nF} \right| = 1.229 \text{ V} \quad (2.3)$$

$$E_{\text{H}}^0 = \left| -\frac{\Delta H^0}{nF} \right| = 1.481 \text{ V} \quad (2.4)$$

where E_{rev}^0 is the standard reverse cell potential, E_{H}^0 is the enthalpic potential, n is the number of electrons involved in the reaction ($n = 2$ for water electrolysis) and F is Faraday's constant (96485 C mol^{-1}). The E_{H} defines the potential at which the water splitting reaction occurs without production or consumption of heat. Typically, in electrolysis processes, the reversible cell potential and enthalpic potential are considered positive as they represent an applied potential.

The reversible cell potential can be estimated using the Nernst equation as a function of temperature, pressure and the activities of each species involved in the reaction as calculated by **Eq. 2.5**.

$$E_{\text{rev}} = E_{\text{rev},T}^0 + \frac{RT}{nF} \ln \left(\frac{a_{\text{H}_2} \times (a_{\text{O}_2})^{0.5}}{a_{\text{H}_2\text{O}}} \right) \quad (2.5)$$

where $E_{\text{rev},T}^0$ is the temperature dependent reversible cell potential at standard pressure, R is the universal gas constant, and a_{H_2} , a_{O_2} and $a_{\text{H}_2\text{O}}$ are the activities of hydrogen, oxygen, and liquid water, respectively. The $E_{\text{rev},T}^0$ can be calculated by the following empirical relation (**Eq. 2.6**) as reported by Bratsch, which is valid up to $100 \text{ }^\circ\text{C}$.⁹⁷

$$E_{\text{rev},T}^0(\text{V}) = 1.229 - 0.0008456 \times (T(\text{K}) - 298.15) \quad (2.6)$$

The $a_{\text{H}_2\text{O}}$ is 1 whereas the a_{H_2} and a_{O_2} are defined as the ratio between the fugacity (f_{H_2} and f_{O_2}) and the standard pressure ($P^0 = 1 \text{ bar}$). Assuming that

H_2 and O_2 are ideal gases, the fugacity can be considered the same as the gas partial pressures, P_{H_2} and P_{O_2} . During water electrolysis, the gas phase is a binary mixture of the evolved gas, either H_2 or O_2 , and saturated water vapor, meaning that the absolute pressure P_{abs} is the sum of the partial pressure of the evolved gas and the vapor pressure of water.^{23,98} Hence, the a_{H_2} and a_{O_2} can be determined by **Eq. 2.7**, considering that the water electrolysis process is carried out under balanced pressure.

$$a_e = \frac{f_e}{P^0} = \frac{P_e}{P^0} = \frac{P_{abs} - P_{H_2O}}{P^0} \quad (2.7)$$

where f_e and P_e are the fugacity and partial pressure of gas e and P_{H_2O} is the vapor pressure of water. The vapor pressure of water can be described by the Antoine equation (**Eq. 2.8**) with the following Antoine constants, $A = 4.6543$, $B = -1435.2$ K and $C = -64.848$ K, and P_{H_2O} and T in bar and K, respectively.^{61,99,100}

$$P_{H_2O}(\text{bar}) = 10^{A + \frac{B}{C+T(K)}} \quad (2.8)$$

Hence, by substituting Eq. 2.7 and 2.8 in Eq. 2.5, the reversible cell potential for variable temperature and pressure can be calculated as follows:

$$E_{rev} = E_{rev,T}^0 + \frac{RT}{2F} \ln \left(\left(\frac{P_{abs}(\text{bar}) - 10^{A + \frac{B}{C+T(K)}}}{P^0(\text{bar})} \right)^{1.5} \right) \quad (2.9)$$

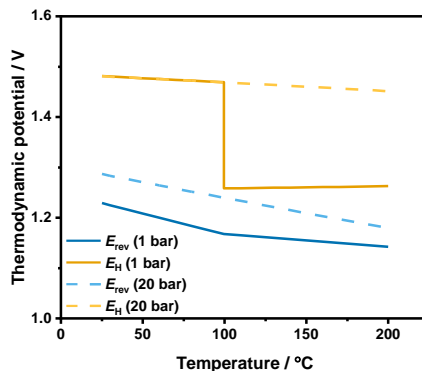


Figure 2.6: Energy required to split water over a large range of operating temperatures at 1 bar and 20 bar. Values calculated from refs.^{19,97,98,101}. The different slope in E_{rev} and sudden decrease in E_H at 1 bar at 100 °C are related to the phase change of water from liquid to gas.

Figure 2.6 shows the temperature and pressure dependence of the reversible cell potential and enthalpic potential. Operating water electrolysis at higher temperatures is thermodynamically beneficial as it decreases the energy required to carry out the reactions. However, these effects are less significant than kinetic effects. In contrast, an increase in pressure has the opposite effect, especially for the E_{rev} . However, by operating at higher pressures, direct storage of hydrogen is possible without further compression, simplifying the balance of plant. Also, additional drying steps are less energy consuming due to the lower water content in the evolved gas.

2.3.2. Ohmic overpotential

The ohmic overpotential (E_{Ω}) is directly related to the proton conductivity of the PEM (σ_{PEM} in S cm^{-1}), and the resistivities of the porous transport layer and the flow fields ($R_{\text{PTL-FF}}$) and also, the interface between FF | PTL | catalyst layer (CL) (R_{int}). The ohmic resistance (R_{Ω} in $\Omega \text{ cm}^2$) is the sum of the mentioned resistances and it is typically quantified by electrochemical impedance spectroscopy (EIS) as the high frequency intersection of the real axis on a Nyquist plot. The E_{Ω} is commonly modelled according to Ohm's law as shown by **Eq. 2.10**.¹⁰²

$$E_{\Omega} = iR_{\Omega} = i \left(\frac{\delta_{\text{PEM}}}{\sigma_{\text{PEM}}} + R_{\text{PTL-FF}} + R_{\text{int}} \right) \quad (2.10)$$

where i is the current density in A cm^{-2} and δ_{PEM} is the thickness of the PEM in cm. The ohmic overpotential has small impact in the cell voltage at low current densities but it starts to prevail over the kinetics overpotential at high current densities as illustrated in Figure 2.5.

The proton conductivity of the PEM is the major contributor of the ohmic overpotential. Several approaches have been used to model the proton conductivity of PEM, mainly Nafion, especially to model voltage losses of fuel cells.^{103,104} Springer et al. developed an empirical correlation to calculate the proton conductivity of Nafion 117 as function of the hydration number λ and the temperature – **Eq. 2.11**. The hydration number λ is the ratio between the number of water molecules and the number of functional groups, i.e. $-\text{SO}_3\text{H}$ for Nafion ($\text{mol H}_2\text{O mol SO}_3\text{H}^{-1}$).

$$\sigma_{\text{Nafion}} (\text{S cm}^{-1}) = (0.005139\lambda - 0.00326)e^{1268 \left(\frac{1}{303} - \frac{1}{T(\text{K})} \right)} \quad (2.11)$$

The hydration number λ depends on temperature and relative humidity. However, there is a lack of consensus on how they affect this number. Springer

et al. considers $\lambda = 16.8$ at 80 °C and $\lambda = 22$ at 100 °C while more recently, Kreuer et al. reported that for Nafion immersed in water, this number is around $\lambda = 20$ for a temperature range from 30 °C to 100 °C.^{104,105} In this chapter, all PEMWE experiments were carried at temperatures between 50 °C and 60 °C and the hydration number of Nafion will be considered as $\lambda = 20$ leading to a proton conductivity of Nafion $\sigma_{\text{Nafion}} = 129$ to 145 mS cm⁻¹ according to Eq. 2.11.

The electrical resistance of the bipolar plates and the porous transport $R_{\text{PTL-FF}}$ can be estimated by measuring the potential drop across FF and PTL at different current densities using the setup shown in **Figure 2.7**. The FF and PTL are considered to be pure resistors and therefore, Ohm's law can be applied.

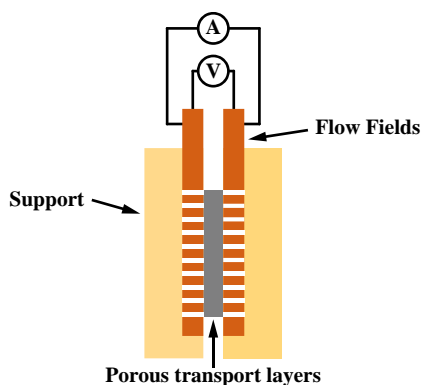


Figure 2.7: Schematic illustration of the setup used to measure the electrical resistance measurement of flow fields and porous transport layers.

2.3.3. Kinetic overpotential

The kinetic overpotential describes the electrochemical kinetics behavior, hence representing the activation energy required for electron transfer at the electrode–electrolyte interface. This overpotential is typically modelled for each electrode using the Butler–Volmer equation (**Eq. 2.12**) that describes the kinetics of charge transfer at an electrode–electrolyte interface.

$$i = i_0 \left(e^{\frac{\alpha_a F}{RT} \eta} - e^{-\frac{\alpha_c F}{RT} \eta} \right) \quad (2.12)$$

where i_0 is the exchange current density and α_a and α_c are the charge transfer coefficients for the anodic and cathodic reaction at the electrode–electrolyte interface, respectively. The exchange current density i_0 represents the current at which both cathodic processes and anodic processes are occurring at equal rates at the electrode–electrolyte interface and it depends on the used electrocatalyst.

The charge transfer coefficients describe the symmetry of the energy barrier.^{19,106,107}

Accurately modelling the kinetic overpotential can be quite challenging as this overpotential depends on a variety of parameters. Temperature, catalyst material, electroactive area, processing, and morphology are parameters that contribute to this overpotential as they influence the exchange current density. For this reason, the values of the exchange current density reported in literature vary over several orders of magnitude.^{6,107} Some authors have attempted to minimize these effects by replacing the exchange current density i_0 in Eq. 2.12 by an apparent exchange current density $i_{0,\text{app}}$ that is function of the electrode roughness factor r_f and an Arrhenius relation describing the temperature dependence – **Eq. 2.13**.^{61,107–111} The roughness factor is further defined as the ratio between the electrochemical active surface area (ECSA) and the geometric area of the electrode A – **Eq. 2.14**.

$$i_{0,\text{app}} = r_f i_{0,\text{ref}} e^{-\frac{E_a}{R} \left(\frac{1}{T} - \frac{1}{T_{\text{ref}}} \right)} \quad (2.13)$$

$$r_f = \frac{\text{ECSA}}{A} \quad (2.14)$$

where $i_{0,\text{ref}}$ is the exchange current density at the reference temperature T_{ref} and E_a is the activation energy for the electrode reaction, e.g., water oxidation at the anode. Nonetheless, Eq. 2.13 still requires an empirically determined E_a and $i_{0,\text{ref}}$ to be able to determine the apparent exchange current density, and subsequently the kinetic overpotential.

The HER on Pt has an exchange current density around $i_{0,\text{HER}} = 1 \text{ mA cm}^{-2}$ which is several orders of magnitude larger than the exchange current densities found for oxygen evolution reaction catalysts ($i_{0,\text{OER}} < 10^{-4} \text{ mA cm}^{-2}$). The high exchange current density results in low overpotentials and the Butler–Volmer equation can be linearized – **Eq. 2.15**.^{76,106} Bernt et al. have shown that the HER kinetic overpotential was less than 15 mV at current densities up to 3 A cm^{-2} even for Pt loadings down to 0.025 mg cm^{-2} .⁷¹ Hence, the contribution of HER kinetics is commonly neglected and only the OER overpotential is quantified.

$$\eta_{\text{HER}} = i \frac{RT}{F(\alpha_a + \alpha_c) i_{0,\text{HER}}} \quad (2.15)$$

The Butler–Volmer equation is simplified to the Tafel equation when the overpotential becomes sufficiently large, which means that for the OER

overpotential, the first term prevails, i.e., the oxidation current, and it is calculated as follows:^{61,106}

$$\eta_{\text{OER}} = \frac{RT}{\alpha_a F} \ln \left(\frac{i_{\text{OER}}}{i_{0,\text{OER}}} \right) = \frac{2.303RT}{\alpha_a F} \log \left(\frac{i_{\text{OER}}}{i_{0,\text{OER}}} \right) = b \log \left(\frac{i_{\text{OER}}}{i_{0,\text{OER}}} \right) \quad (2.16)$$

The Tafel slope b indicates the overpotential necessary to increase the current density tenfold and it is also associated with the reaction mechanism of the catalyst being used. At low current densities, up to 100 mA cm^{-2} , the mass transfer limitations can be neglected and the experimental ohmic free potential ($E_{iR \text{ free}} = E_{\text{cell}} - E_{\Omega}$) can be fitted to the Tafel equation. The Tafel slope contains important information regarding the mechanism, hinting to the possible rate determining step (r.d.s) of the electrochemical reaction.⁶²

2.3.4. Mass transfer overpotential

The mass transfer overpotential η_{mt} considers the mass transfer limitations that occur in the electrolysis cell, particularly at high current densities. The mass flow through porous electrodes in water electrolysis is commonly reported as a diffusion phenomenon, described by Fick's law. In water electrolysis, water is transported from the channels across the porous transport layers to the catalyst layer, where the reactions take place, and subsequently, H_2 and O_2 are transported out of the catalyst layer. This reaction product removal has the highest influence as a concentration increase at the catalytic active sites results in slowing down the reaction kinetics.¹⁰² This overpotential can be estimated by combining the Nernst equation and Fick's law for each electrode as defined by Marangio et al. – **Eq. 2.17**.¹⁰²

$$\eta_{\text{mt}} = \frac{RT}{nF} \ln \left(\frac{C_{e,\text{int}}}{C_{e,\text{int},0}} \right) \quad (2.17)$$

where $C_{e,\text{int}}$ and $C_{e,\text{int},0}$ are the concentrations of either O_2 or H_2 at the membrane-electrode interface at the operating condition and at a reference condition, respectively. Frequently, the influence of this overpotential is much smaller than the kinetics and ohmic overpotential in the operating current ranges studied and many reports consider it negligible.^{107,112}

2.4. Water electrolysis setup scheme

Figure 2.8 shows a scheme of the finalized PEM water electrolysis setup built during this work. The feed water ($\rho > 18 \text{ M}\Omega \text{ cm}$) is bubbled with N_2 gas to promote the removal of the evolved gases and avoid atmospheric CO_2 dissolution. The water is pumped by a peristaltic pump at a rate of 10 mL min^{-1} through a

home-built serpentine heater immersed in an oil bath before it reaches the cell. The evolved gases and water are recirculated to feeding bottles, where the gases are released to the atmosphere. The hydrogen line is also connected to a compact gas chromatograph CGC 4.0 (Global Analyzer Solutions–Interscience B.V.) for gas analysis. The water inlet temperature control is provided by the oil bath. Thermocouples (TE in Figure 2.8) are placed at both inlets and outlets of the cell. The lines between the heater and the cell inlet and outlets are wrapped in glass fiber tape to decrease heat loss. In addition, a by-pass between the inlets and outlets at each side of side was added to allow preheating the feed water while the electrolysis cell is disconnected from the setup.

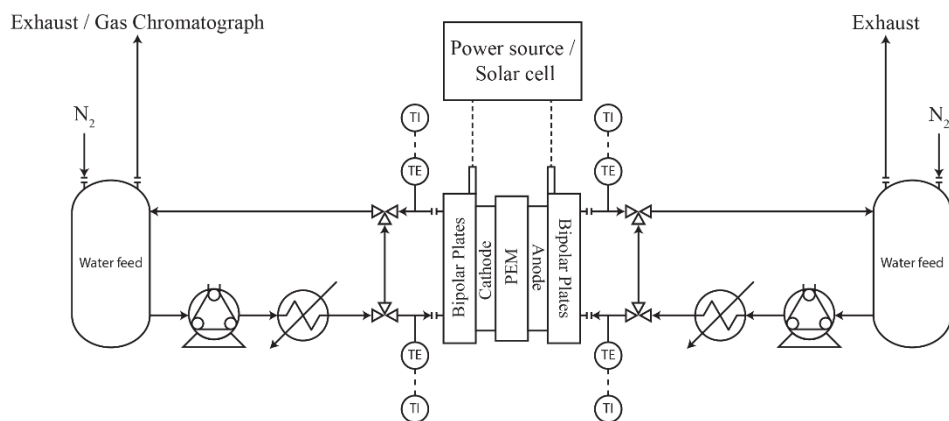


Figure 2.8: Scheme of the proton exchange water electrolysis setup assembled. TE: temperature element, TI: temperature indicator.

2.5. Cell clamping torque

For the initial experiments on the newly built setup, temperature control was done only at the oil bath where the serpentine heat exchanger was immersed. The anode inlet temperature was measured by taping a hot-plate thermocouple to the stainless steel tubing near the inlet. Subsequent iterations of the setup included thermocouples in both inlets and outlets to measure the temperature. Furthermore, the water feed was not purged. Regarding the electrolysis cell, it was made of 3D printed ABS and a Cu fluid diffuser with parallel channels electrocoated with Ni and Au (**Figure 2.9**). The ABS support had a 1 mm indentation where the fluid diffuser slid in. On the anode side, a 1 mm thick Ti-PTL and an ethylene propylene diene monomer rubber (EPDM) gasket were used while on the cathode, a carbon PTL (C-PTL) without microporous layer (MPL) and a polytetrafluoroethylene (PTFE) film were used. The polyimide film between the Ti-PTL and the MEA had two functions: prevent the Ti from puncturing the membrane when closing the cell and define the active area as 4 cm².

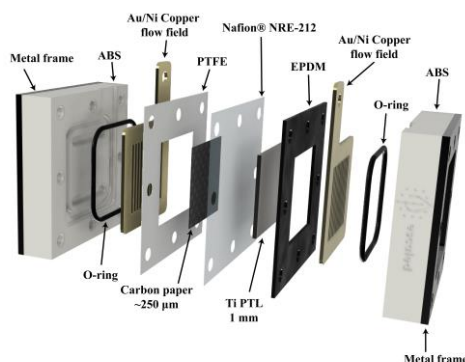


Figure 2.9: Electrolysis cell assembly with 1 mm Ti, EPDM gasket, ABS support, and Au/Ni coated Cu fluid diffuser.

The first experiments focused on testing the cell clamping torque used to close the electrolysis cell. The clamping torque can be easily tuned by the bolt torque method where the bolts are tightened with different torques.^{113,114} The applied torque directly affects the thicknesses of the C-PTL and the membrane, and the interfacial contact between the catalyst layer and membrane, impacting the ohmic resistance of the electrochemical cell. Higher compression leads to lower thickness, which should intuitively mean less ohmic resistance, and improved water electrolysis performance. However, the obtained potential rose when the torque was increased from 1 Nm to 1.6 Nm as shown by the polarization curves in **Figure 2.10a**.

Excessive torque can damage the C-PTL fibers, and thus, the impact of the clamping torque on the C-PTL was further analyzed by scanning electron microscopy (SEM) as shown in Figure 2.10b–d. It is important to note that the C-PTLs depicted in Figure 2.10c–d were only used to study the effect of pressure and that no water electrolysis experiments were carried out. The C-PTL clamped with a torque of 1 Nm has a comparable morphology as the pristine sample, presenting barely any damage. In contrast, for higher clamping pressures, the damage of the fibers is clear, with many broken fibers. Studies have shown that the broken fibers induce loss of porosity as they can occupy the free pores. This possibly hinders the formed gases escape, leading to an increase of the mass transfer resistance.^{114–116} The clamping torque also affects the PEM, particularly the proton conductivity. By increasing the torque, the water content of the PEM reduces and thus, the proton conductivity of the PEM also drops (Eq. 2.11).¹¹⁷ The proton conductivity drop is assumed to counteract the effect of better interfacial contact between the catalyst layer and the PEM as reported by Borgardt et al.¹¹⁵ These two factors, broken fibers and lower proton conductivity,

have most probably contributed to the lower performance with a torque of 1.6 Nm. Therefore, subsequent experiments were conducted with bolt torque of 1 Nm.

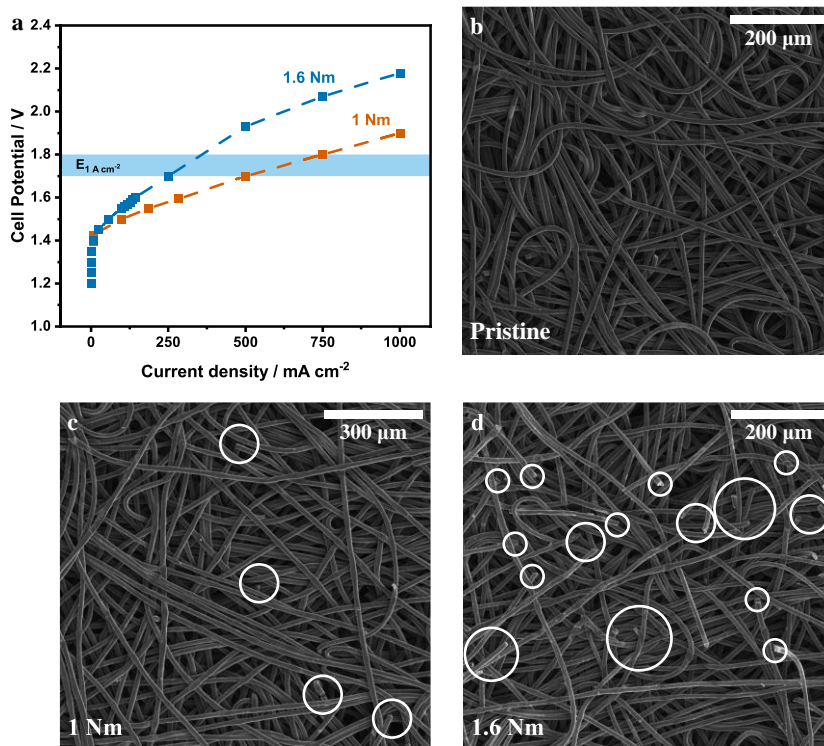


Figure 2.10: Electrolysis cell clamping torque study. a) Polarization curve for different applied compressions. The different compressions were set by varying the applied torque on the bolts. $F_{an} = F_{cat} = 10 \text{ mL min}^{-1}$, $T_{oil \text{ bath}} = 75 \text{ }^{\circ}\text{C}$, $T_{an, in} \approx 50 \text{ }^{\circ}\text{C}$. The blue shaded area delimits the target potential at 1 A cm^{-2} . b) SEM picture of a Pristine E30 gas diffusion layer. c) After applying 1 Nm. d) After applying 1.6 Nm.

2.6. Oil bath and inlet cell temperature study

Generally, proton exchange water electrolysis cells are operated at $80 \text{ }^{\circ}\text{C}$ to decrease the thermodynamic potential and ensure that the proton conductivity of the membrane, normally Nafion, is as high as possible without damaging it. The cell temperature only reaches approximately $50 \text{ }^{\circ}\text{C}$, as measured by a thermocouple tapped just before the anode inlet, when the oil bath is set to $75 \text{ }^{\circ}\text{C}$ as shown in the clamping torque experiment. Therefore, the oil bath temperature was set to $100 \text{ }^{\circ}\text{C}$, which allowed a cell inlet temperature $\sim 60 \text{ }^{\circ}\text{C}$. The polarization curves of the MEAs tested at $T_{oil \text{ bath}} = 100 \text{ }^{\circ}\text{C}$ are compared with the polarization curve of the MEA at 1 Nm in **Figure 2.11a**.

The first MEA at $T_{\text{oil bath}} = 100\text{ }^{\circ}\text{C}$ shows an unexpected drop in current densities at all cell potentials, reaching 1 A cm^{-2} at 2.2 V , in comparison to the best previous MEA. Initially, this was attributed to the cumulative damage observed on the flow fields (FFs) from this and the previous water electrolysis experiments as presented in Figure 2.11b. The removal of the Au/Ni coating at the anode exposes the Cu underneath, enabling it to be oxidized and thus, increasing the resistance over time. Moreover, part of the lost coating seems to have been transferred to the MEA (Figure 2.11b). The additional metal (Au and Ni) and their respective ions on the surface of the MEA may bind to the sulfonate sites of the Nafion membrane and ionomer present in the catalyst layer, reducing the number of active sulfonic acid groups available for charge transfer at the membrane-catalyst interface and for proton conduction through the membrane.^{118,119}

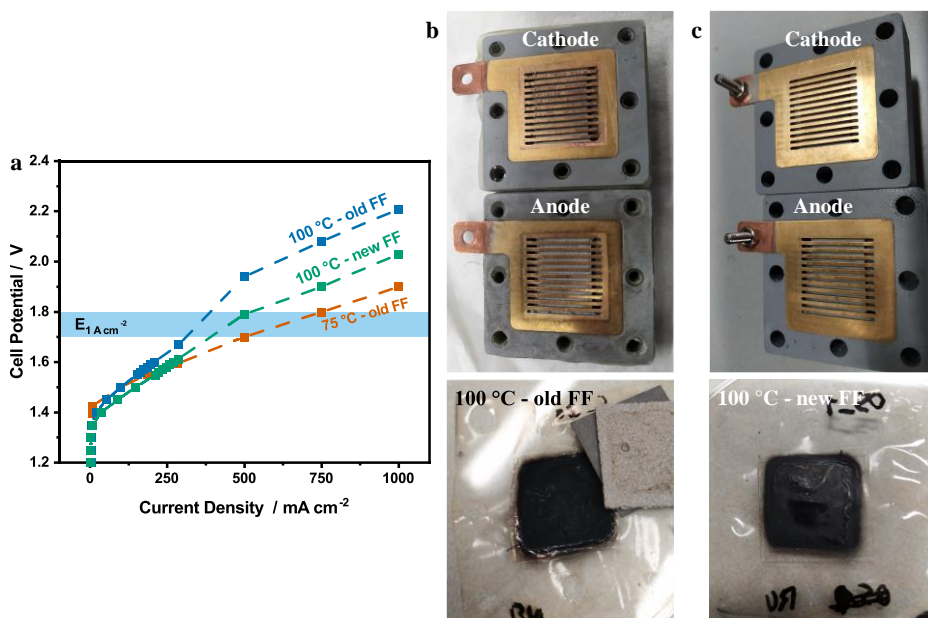


Figure 2.11: Oil bath temperature study. a) Polarization curves of the MEAs tested with $T_{\text{oil bath}} = 75\text{ }^{\circ}\text{C}$ and $100\text{ }^{\circ}\text{C}$ with old and new FF. b) Pictures after the polarization curves of the old FFs and first MEA tested at $T_{\text{oil bath}} = 100\text{ }^{\circ}\text{C}$. c) Same for the new FFs and second MEA tested at $T_{\text{oil bath}} = 100\text{ }^{\circ}\text{C}$.

When replacing the Cu-FF by pristine ones, there was indeed an enhancement of the water electrolysis performance, and in particular, barely any damage on the FF and coating transfer to the MEA were observed (Figure 2.11c). However, the current density was still lower than the MEA tested at $T_{\text{oil bath}} = 75\text{ }^{\circ}\text{C}$. This implies that there must be an additional reason for the worse

performance of the MEAs at $T_{\text{oil bath}} = 100\text{ }^{\circ}\text{C}$. The feeding water was never replaced up to this point and it seems reasonable to assume that the Au/Ni coating removed in the previous experiments was also present in the feeding water. Hence, as mentioned above, it is possible that these impurities may hinder the performance of the Nafion membrane and ionomer, despite the higher temperature. To avoid this issue, in following experiments, the water feed was always replaced in between experiments.

This study also revealed the need to reduce the heat loss between the serpentine heater and the electrolysis as using oil bath temperatures of $75\text{ }^{\circ}\text{C}$ to $100\text{ }^{\circ}\text{C}$ only resulted in operating temperatures of approximately $50\text{ }^{\circ}\text{C}$ and $60\text{ }^{\circ}\text{C}$, respectively. This large heat loss between the outlet of the serpentine and the inlet of the electrolysis cell was circumvented, to some extent, by wrapping the stainless steel tubes with glass fiber tape. This enabled the use of an oil bath temperature of $75\text{ }^{\circ}\text{C}$ to reach inlet temperatures around $60\text{ }^{\circ}\text{C}$. Despite the lower heat loss, preliminary experiments with such insulation indicated that it was still not possible to reach $80\text{ }^{\circ}\text{C}$ at the electrochemical cell inlets with oil bath temperatures up to $100\text{ }^{\circ}\text{C}$. Consequently, it was decided that subsequent experiments were going to be carried out at $60\text{ }^{\circ}\text{C}$ ($T_{\text{oil bath}} = 75\text{ }^{\circ}\text{C}$), which is also very commonly used for PEMWE.

2.7. Porous transport layers for water electrolysis

The next step in the optimization, after minimizing the effect of some external parameters to the electrolysis cell, was to reduce potential losses due to the cell materials, e.g., PTLs and electrical connections. The resistance of the PTLs and FFs was measured according to Figure 2.7 and the results are summarized in **Figure 2.12**. The electrical connection between the measuring equipment and the cell (via the Cu–FF) was enhanced by adding a carbon-based paste (C–paste) to the “*banana*” connector as shown by the resistance decrease in Figure 2.12.

These improvements of the PTLs and the FFs were implemented in the subsequent PEMWE testing. Furthermore, the clamping torque to close cell was decreased to 0.8 Nm , to partially reduce the delamination of the Au/Ni coating off the Cu–FF. The testing procedure was changed to include a conditioning step before any electrochemical characterization and the following characterization was done in galvanostatic mode. The new procedure comprised of three different stages based on the work of Bernt et al.⁷¹ The first was the conditioning stage that consisted of flowing water through the cell for 1 h to allow temperature stabilization and allow the membrane to fully swell, followed by 30 s steps at 10, 20, 40, 50, and 100 mA cm^{-2} , and 30 min at 250 mA cm^{-2} . The current

conditioning is useful to clean the catalyst layer of unbound particles that could be covering potential active sites. The second stage started with EIS at 10, 50, and 100 mA cm⁻², followed by five polarization curves with 2 min current steps between 1 and 375 mA cm⁻² and then, EIS again at the same current densities. The conditioning steps and EIS were carried out using a PGSTAT30 while the polarization curves were performed with a Keithley 2600 SMU since it can reach higher currents than the PGSTAT30. The third stage was the measurement at high current densities ($J > 375$ mA cm⁻²) with the aid of a power source to provide the intended current between 500 and 1500 mA cm⁻² and the Keithley SMU to measure the output potential. This change of measurement equipment is frequently noticed in the polarization curves by a slightly higher than expected potential increase. The average of the last three polarization curves and the EIS at 100 mA are shown in **Figure 2.13a** and b. Two MEAs were similarly prepared and tested with this method.

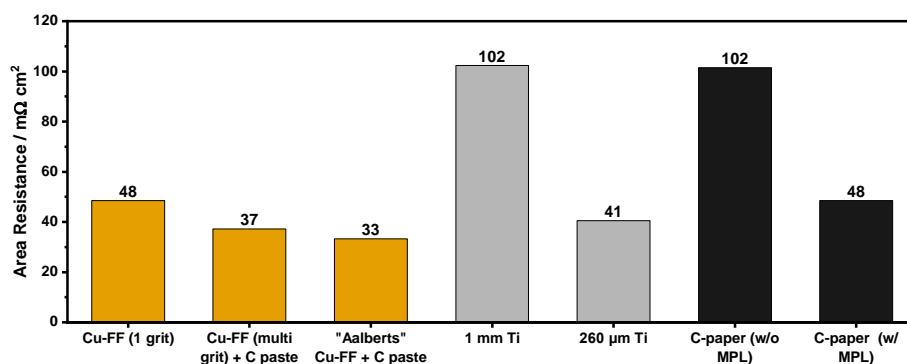


Figure 2.12: Contact resistance of different FFs (yellow bars) and PTLs (grey: Ti, black: carbon paper). The Cu-FF and Cu-FF + C paste were electrocoated in-house with Ni and then Au. The “Aalberts” Cu-FF + C paste were coated with Au professionally by Aalberts N.V. The Ti-PTLs and the carbon paper without microporous layer (C paper w/o MPL) were measured using the Cu-FF (1 grit) while the carbon paper with MPL (C paper w/ MPL) was measured using the Cu-FF (multi grit) + C paste.

The potential was improved at every current density for both tested MEAs in comparison to the previous best, indicating that some potential losses were mitigated. Furthermore, the potentials at 1 A cm⁻² are 1.84 and 1.81 V, are just slightly above the set target of 1.80 V. From the EIS data, the R_{Ω} and R_{ct} were calculated by fitting a modified simplified Randles equivalent electrical circuit (EEC) – Figure 2.13c. The ohmic resistance is around 0.14 Ω cm² for both samples and it is comparable to typical literature values.¹²⁰ A lower R_{ct} is found for the MEA_difPTL – 2 sample (~ 0.25 Ω cm²), agreeing with the earlier on-set observed in the polarization curves. The distinct R_{ct} for these samples and the

variation observed in the polarization curves are assigned to a slightly different catalyst loading.

Using the R_{Ω} , iR -free Tafel plots could be constructed from the polarization curves as presented in Figure 2.13d, by subtracting the ohmic overpotential E_{Ω} , calculated according to Eq. 2.10. The Tafel slopes were calculated by fitting Eq. 2.16 between 1 and 100 mA cm^{-2} and they are shown in Figure 2.13d. Assuming that the cathodic kinetic overpotential can be neglected, these values should fully correspond to the Tafel slope of RuO_2 . In literature, a wide range of Tafel slopes can be found for RuO_2 , varying from 40 to 60 mV dec^{-1} .^{121,122} The found values are inside this interval, further supporting that the cathodic kinetic overpotential can be neglected and that the reaction mechanism is similar to what is found in literature.

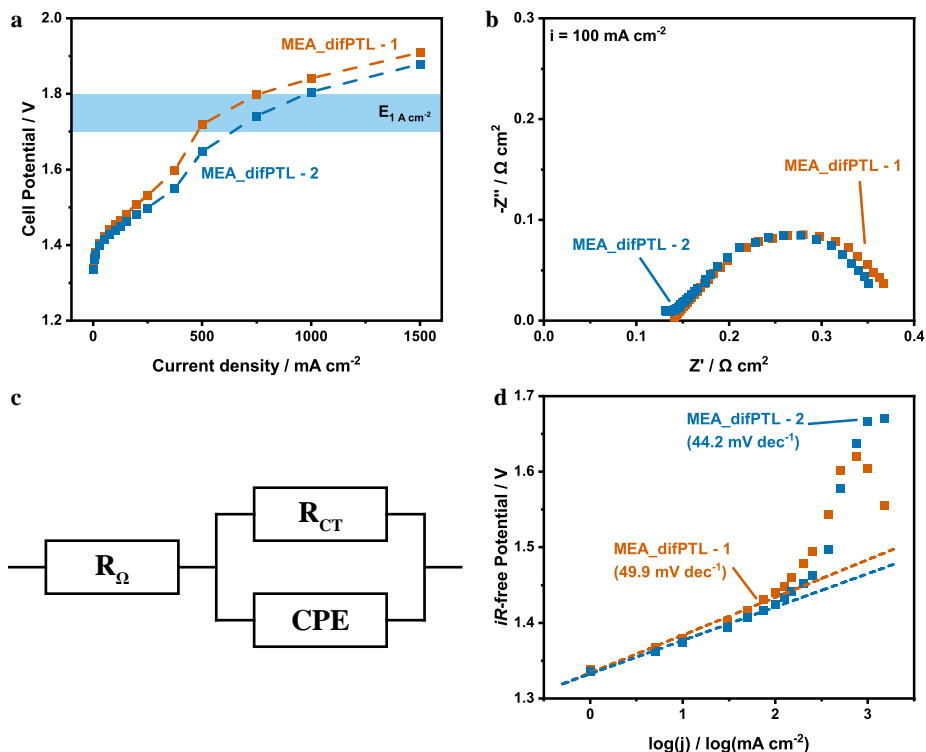


Figure 2.13: Electrochemical characterization of two MEAs with thin Ti-PTL and C-PTL with microporous layers. a) Polarization curves. b) Electrochemical impedance spectroscopy carried out before the polarization curves at 100 mA cm^{-2} . c) Equivalent electrical circuit used for EIS fitting, consisting of R_{Ω} (Eq. 2.10), the charge transfer resistance (R_{ct}), and a constant phase element (CPE). d) Tafel plot. The dashed lines represent the fittings according to Eq. 2.16.

2.8. Membrane-electrode assembly storage under inert atmosphere

The MEAs prepared up to this point were always stored in ambient atmosphere and it was noticed that the Nafion PEM would become yellow/brown as a result of organics pick-up. This effect is mentioned by several suppliers, who recommend to store Nafion in air-tight bags, but also state that this darkening is not expected to affect the membrane.¹²³ A few reports and Nafion suppliers suggest to soak the membrane in dilute nitric acid to clean the dark spots prior to catalyst deposition. In contrast, the darkening of the membrane during the current experiments was only observed after the catalyst deposition (Pt + RuO₂). Hence, subsequent MEAs were stored under N₂ immediately after the catalyst deposition and until they were tested, resulting in the absence of visible dark spots over the membrane.

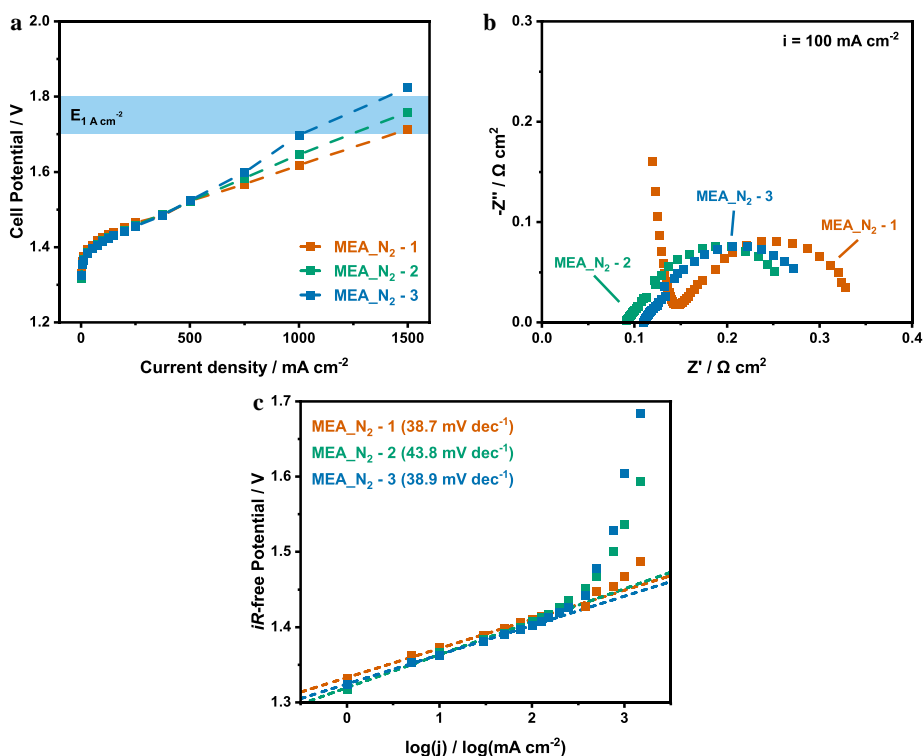


Figure 2.14: Electrochemical characterization of samples stored under N₂. a) Polarization curve, b) Electrochemical impedance spectroscopy carried out before the polarization curves at 100 mA cm⁻². c) Tafel plots. The dashed lines represent the fittings according to Eq. 2.16.

These MEAs were tested using the same galvanostatic procedure described previously and the EIS spectra were fitted to the EEC from Figure 2.13c. **Figure 2.14a** compares the polarization curves of three MEAs that were stored under N_2 . All MEAs outperformed previous MEAs and the cell potential at 1 A cm^{-2} was between 1.61 and 1.70 V, surpassing the initial target of 1.7–1.8 V. The EIS spectra (Figure 2.14b) provide some insight for such improvement. The ohmic resistance has a slight drop from $0.14\ \Omega\text{ cm}^2$ to about $0.10\ \Omega\text{ cm}^2$, except for one sample. Similarly, the R_{ct} decreased approximately to $0.2\ \Omega\text{ cm}^2$ in this set of MEAs. As the R_{ct} is typically related to the quality of the catalyst–membrane interface, such decrease hints to a better interface. It is likely that some of the proton exchange sites in both the membrane and the ionomer of the catalyst layer pick up organics when stored in air, rendering them unavailable and increasing both resistances.¹¹³ Hence, by storing the samples in N_2 atmosphere, this is avoided and more proton exchange sites are available for immediate transport of protons away from the catalytic active sites, leading to lower R_{ct} .⁴⁸ Furthermore, the iR -free potential was analyzed (Figure 2.14c) to calculate the Tafel slopes. Slightly lower but comparable Tafel slopes to previous MEAs are found for these samples, suggesting that the OER mechanism is unaffected by the storage approach.

2.9. Titanium flow field and removal of the back O–ring

Although, the set target for efficiency of the electrolysis setup and cell has been achieved, there are still remaining issues that need improvement, in particular, the Au/Ni coating on the FF. Throughout prior experiments, this coating presented a continuous issue as it would be removed and transferred to the PTLs and MEA during the experiments. Some improvement was previously observed when reducing the clamping torque down to 0.8 Nm and the Cu–FFs were sequentially polished with increasing grit size prior to the electrodeposition processes. Additionally, a few Cu–FFs were professionally electrocoated with Au by Aalberts N.V. These FF appeared to be more resistant to the polishing effect during the experiments, but still presented some damage after some testing (**Figure 2.15a**). These could be scrubbed carefully with abrasive soap to remove the dark spots, in contrast to the FF electrocoated in-house, where the coating would easily be polished away in just one cleaning. However, after several experiments and cleaning cycles, the coating would also be removed.

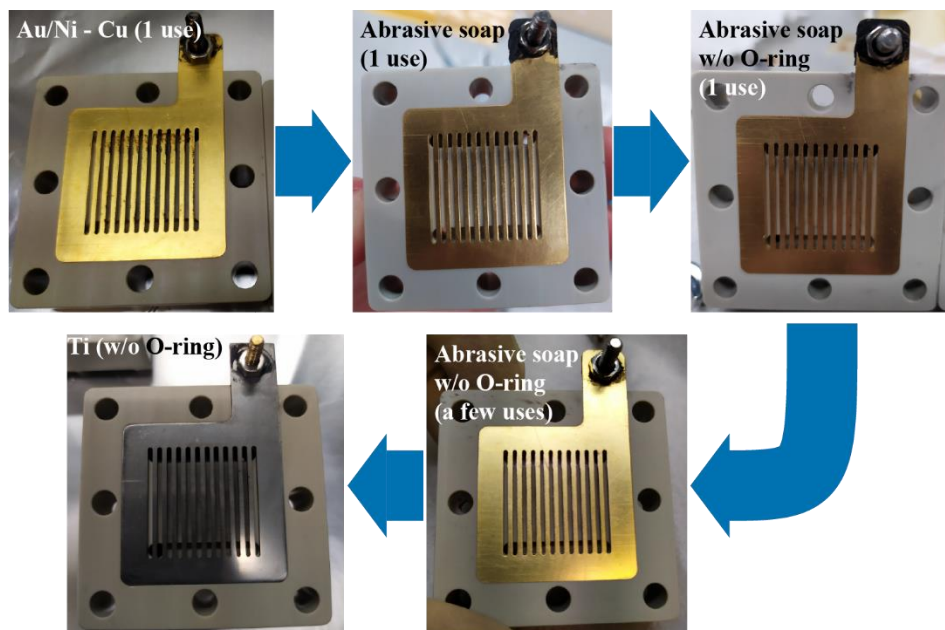


Figure 2.15: Representative FFs after PEMWE experiments.

A new approach consisted in removing the O-ring behind the FF. The O-ring puts additional pressure on the FF, and thus on the PTLs, since the O-ring is slightly larger than the indentation where it sits to ensure it insulates the cell. Nonetheless, the electrolysis cell was still leak-free during electrochemical characterization (**Figure 2.16a–b**) after removal of the O-ring. The absence of O-ring seems to have no effect on electrolysis performance as it shown by the identical polarization curve and ohmic resistance to when compared with the cell with O-rings were included in the electrolysis cell (**Figure 2.16a–b**). However, also with this approach, the coating starts to be scrubbed away after a few uses as shown in **Figure 2.15**.

A protective coating is mandatory for Cu-FFs to avoid corrosion ($E_{\text{Cu(II)/Cu(0)}}^0 = 0.34 V_{\text{SHE}}$), and as shown, such coating tends to be removed over time, leaving the underlying material exposed. Hence, the subsequent approach relied on replacing the coated Cu by bare Ti. Although, a thin oxide layer can also form on the surface of Ti, increasing the ohmic resistance over time, it is not regarded as a major concern when short duration electrolysis experiments are considered, as the ones presented in this thesis. Besides, the passivation layer protects the underlying Ti, and it can be easily polished off and cleaned between experiments as shown in **Figure 2.15**. The change to Ti-FFs, also without O-ring, had little impact on the performance of the electrolysis cell (**Figure 2.16a**).

The EIS shows a larger ohmic resistance than with the Au/Ni coated Cu-FFs, disagreeing with what is observed in the ohmic zone of the polarization curves (250 – 1500 mA cm⁻²). In addition, the stability was evaluated by a galvanostatic test at 250 mA cm⁻² for 16 h (Au/Ni coated Cu-FF) and 18 h (Ti-FF). The initial potential increase with Ti-FF probably arises by an increase in ohmic resistance due to the oxide formation on the Ti surface. After the surface is mostly covered by the oxide, the increase in resistance slows down. In contrast, the potential steadily increases with Au/Ni coated Cu-FFs, which may be ascribed to the flaking of the coating over time, exposing the Cu and enabling its oxidation. For longer measurement times, according to the potential increase rate, Au/Ni coated Cu-FF would most probably reach higher potentials than with the Ti-FF.

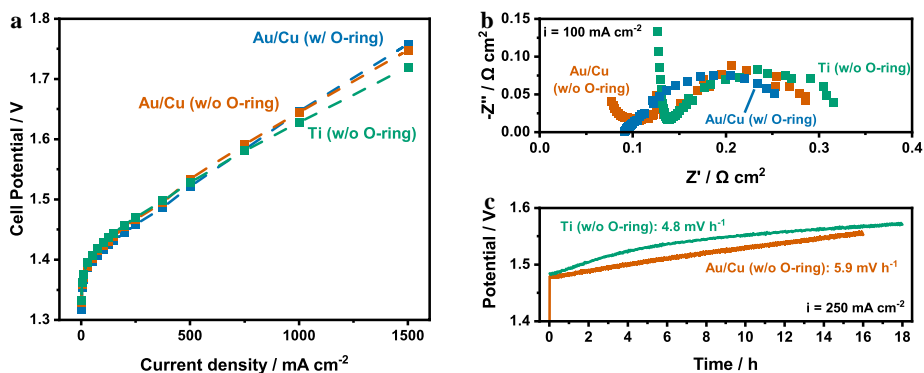


Figure 2.16: Electrochemical characterization of Ni/Au coated Cu-FFs with and without back O-ring and Ti-FF. a) Polarization curve. b) Electrochemical impedance spectroscopy at 100 mA cm⁻². c) Galvanostatic measurement at 250 mA cm⁻² over 16 h and 18 h.

2.10. Conclusion

In this chapter, the assembly and optimization of a proton exchange membrane water electrolysis setup was described. The target potential for this optimization was set at 1.80 V at 1 A cm⁻². The optimization involved testing different cell clamping torques, inlet cell temperatures, type of PTLs, sample storage environment, and materials as FFs. The initial cell assembly comprised Au/Ni coated Cu-FFs, a 1 mm Ti-PTL at the anode, a C-PTL without a microporous layer at the cathode. The Cu-FFs were encased in an ABS 3D printed support with a back O-ring to provide insulation to the cell. Also, the cell temperature was controlled by the oil bath where the serpentine heater was immersed and it was measured using thermocouple tapped to the anodic cell inlet. An oil bath temperature of 75 °C resulted in a cell inlet temperature around 50 °C.

The clamping torque influences the contact resistance of the cell with higher values typically resulting in lower resistances. However, between the tested clamping torques (1 and 1.6 Nm), the lowest value actually resulted in a better electrolysis performance. This result was mainly attributed to the damage done on the C-PTL, i.e. broken fibers, and to the decreased water content of the PEM at higher clamping torque. These counteracted the effect of better interfacial contact between the catalyst layer and the PEM expected at higher clamping torque. With 1 Nm, the potential at 1000 mA cm^{-2} was $\sim 1.9 \text{ V}$, 100 mV higher the target set for optimization.

Subsequently, the oil bath temperature was varied between 75 and 100 °C enabling cell temperatures of 50 and 60 °C. The higher temperature had worse water electrolysis performance ($E_{1 \text{ A cm}^{-2}} = 2.21 \text{ V}$) that was initially assigned to the cumulative damage on the FFs. The coating on the Cu-FFs was being removed over time, leaving the Cu underneath exposed and available to oxidize, increasing the contact resistance. Subsequently, the Cu-FFs were replaced to avoid these issues, and despite some improvement on the previous measurement at $T_{\text{oil bath}} = 100 \text{ °C}$, it was still worse than at 75 °C. This may be due to a contamination of the water feed by the Au and Ni coatings. Up to this point, the water feed had not been replaced, and it seems possible that the additional metal impurities contaminated both the catalyst layer and the proton exchange membrane. This would cause a drop in the proton conductivity of the ionomer, leading to a worse performance. Hence, the water feed was always replaced in the next experiments. This experiment further showed that there was a large heat loss between the serpentine heater and the cell inlet as there was a temperature difference of 25 and 40 °C for the two oil bath temperatures. This was also solved in later experiments by wrapping glass fiber tape around the stainless-steel tubes, allowing temperatures around 60 °C using an oil bath temperature of only 75 °C.

The next step involved trying thinner Ti-PTLs and a C-PTL with a microporous layer instead. Firstly, the contact resistances of the different PTLs were compared by evaluating the voltage drop across the FF | PTL | FF. Naturally, the thin (260 μm) Ti-PTL had less contact resistance and was chosen for PEMWE experiments. Similarly, the C-PTL with a microporous layer yielded less contact resistance than the one without and having the microporous layer, also improved the interface with the catalyst visually, as it does not delaminate as easily. Furthermore, a carbon-based paste was added to the “banana” connector to enhance the electrical connection between the cell and the measuring equipment. These improvements combined with a new testing procedure that included three stages (cell conditioning, measuring up to 375 mA cm^{-2} and measuring up to 1500 mA cm^{-2}) and a cell clamping torque of 0.8 Nm resulted in

lower potentials at every current density measured, failing to reach the set target of 1.80 V at 1000 mA cm⁻² by only 40 mV. The cell encasing initially made of ABS was also replaced by polypropylene due to the higher temperature resistance of the latter.

The storage of the prepared MEAs was done under atmospheric air and some dark brown spots were observed on the Nafion PEM. It is known that Nafion tends to become brown when in contact with air caused by pick-up of organics, although suppliers usually refer that it does not affect the membrane performance. To avoid this anyways, the samples were stored under N₂ right after the catalyst deposition, enabling spot-free MEAs. All three MEAs far surpassed the target potential, reaching 1000 mA cm⁻² between 1.61 and 1.70 V. EIS suggested that both the ohmic resistance and the charge transfer resistance were affected by those dark spots, dropped around 40 and 50 mΩ cm², respectively. This implies that ionomer present in the catalyst layer may also suffer from organics pick-up that could render proton exchange sites unavailable.

The target set initially was met with this last improvement on the storage environment but the issue regarding the damage on the Cu plates, with the Au/Ni protective coating being removed was still present. A few prospective solutions involving having the coating being professionally prepared, scrubbing the plates with abrasive soap after each experiment and removing the back O-ring were tested. These slightly decrease the observed damage but after some use, the coating would be polished away, revealing the bare Cu again. This was finally solved by replacing the Cu-FFs by Ti-FFs without any protective coating. Ti is more resistant to the harsh conditions in PEMWE than Cu, reducing the need of protective coating. The replacement of the flow fields had no effect on the polarization curves but a faster initial increase in potential during the galvanostatic measurement was observed. This is due to the formation of an oxide passivation layer on the surface of Ti, but after the surface is mostly covered by this layer, the potential stabilizes and after 18 h, the voltage increase rate is much slower than with the Au/Ni coated Cu-FFs.

In summary, the optimized water electrolysis cell thus comprised a polypropylene support with Ti-FFs, a ~260 mm Ti-PTL at the anode and a C-PTL with microporous layer at the cathode, RuO₂ as oxygen and Pt hydrogen evolution catalyst, and a Nafion NRE-212 as PEM. The cell is closed using a clamping torque of 0.8 Nm. Regarding the setup, the water feed is bubbled with N₂ and pumped (10 mL min⁻¹) through a serpentine heater immersed in an oil bath to control the temperature at the cell inlets, which is measured at both cell inlets and outlets. The optimization process described in this chapter had a rather

empirical approach as the main purpose was to obtain a water electrolysis cell and a setup that perform well, similar to literature work. Upon reaching this goal, other properties and materials such as PTLs' porosity, material and morphology, temperature, flow field layout and protective coatings, membranes (AEM or PEM) and electrocatalysts can be varied and studied more in depth.

2.11. Experimental section

Materials and membrane-electrode assembly preparation: All materials were used as received without purification. Nafion™ membrane NRE-212 was purchased from Ion Power. Pt/C (40 wt%) was purchased from Sigma Aldrich. RuO₂ (anhydrous, 99.9%) and Nafion dispersion (D-521) were purchased from Alfa Aesar. RuO₂ was stored inside inert atmosphere. 2-propanol was purchased from Biosolve. Ti porous sheets (1 mm, 18–21 μm pore size, 75–100 micron powder) were obtained by GKN Sinter Metals Filters. Ti fiber felt (0.2 – 0.3 mm, porosity: 53 – 56 %) was purchased from Fuel Cell Store. Carbon fiber non-woven fabric without (E30) and with microporous layer (H23 C2) were purchased from Quintech. All catalyst inks were prepared using water purified in Millipore system ($\rho > 18 \text{ M}\Omega \text{ cm}$).

The catalyst inks were prepared with 5 wt% solid content, with 3:1 ratio of catalyst to Nafion ionomer in a 2-propanol:water (4:1) mixture. For the RuO₂ ink, Nafion dispersion was first added, followed by 2-propanol:water. For the Pt/C ink, the catalyst power was first mixed with water to avoid combustion of the carbon particles and subsequently, the Nafion dispersion and 2-propanol were sequentially added. The inks were ultrasonicated for at least 10 min prior to catalyst deposition. The catalyst inks were manually spray-coated using a pneumatic airbrush (Aerotec) through a stainless-steel mask with a $2 \times 2 \text{ cm}^2$ opening on opposite sides of the membrane until the target loadings of 1 and 2 mg cm^{-2} for Pt and RuO₂ were reached, respectively. The catalyst loadings were calculated by weighing the membrane before and after spray coating. The deposition temperature was set to 85 °C to evaporate the solvent upon deposition and to avoid excessive membrane swelling.

PEM electrochemical cell setup: Water electrolysis tests were carried out in an in-house built PEM – electrolyzer cell ($5 \times 5 \text{ cm}^2$) using 3D printed ABS or high-impact polypropylene (PP) as support for the Au/Ni coated Cu or Ti current collectors (1 mm thick) with machined parallel FFs (1 mm wide, channel area: $2.25 \times 2.25 \text{ cm}^2$). Porous Ti and carbon fiber non-woven fabric were used as porous transport layers (PTL) at the anode and cathode, respectively. The MEA was pressed between the PTLs and the electrolyzer was sealed with PTFE ($5 \times 5 \text{ cm}^2$, 200 mm, from Polyfluor). When using the thicker Ti-PTL, an EPDM (1 mm, from Plazura®) gasket was used instead. Polyimide film (50 μm, from Wu Xi Shun Xuan New Materials Co., Ltd) was used between the Ti-PTL and the membrane to delimit the active area to 4 cm^2 . Millipore purified water ($\rho > 18 \text{ M}\Omega \text{ cm}$) was circulated using a peristaltic pump (Masterflex® L/S® Digital Miniflex®) into both anodic and cathodic compartment at 10 mL min^{-1} . Independent water lines and feeding bottles were used for each compartment. The water bottles were N₂-bubbled to prevent oxygen and hydrogen build-up.

Electrochemical Characterization: Potentiostatic polarization curve and electrochemical impedance spectroscopy (EIS) was performed using potentiostat PGSTAT30 (Autolab) equipped with a frequency response analyzer (FRA) module. Galvanostatic polarization curves and steady-state stability was performed using a 2-channel Keithley 2600 SMU controlled by LabVIEW 2600 SMU controlled by LabVIEW. The first channel was used to apply the current whereas the second

channel was used to measure the voltage across the PEM electrochemical cell. For current densities above 250 mA cm^{-2} , a power source ES015–10 was used to provide the intended current between 500 and 1500 mA cm^{-2} and the potential was either measured with the PGSTAT30 or the Keithley 2600 SMU. For the first used procedure, the potentiostatic polarization curve was recorded between 1.2 and 1.6 V with each potential step being held for 30 s. The test at $T_{\text{oil bath}} = 100 \text{ }^{\circ}\text{C}$, the water was circulated through the cell for 30 min to allow membrane swelling and equilibration prior to any measurements. For the second used procedure, water was circulated through the cell for 1 h to allow membrane swelling and equilibration prior to any measurements. Subsequently, the cell was conditioned by applying 10, 20, 50 and 100 mA cm^{-2} for 30 s and then 250 mA cm^{-2} for 30 min, followed by EIS with a frequency range of 10 kHz – 1 Hz at 10, 50 and 100 mA cm^{-2} . Five galvanostatic polarization curves were recorded from 1 to 375 mA cm^{-2} . Each current density step was held for 2 min to allow for potential stabilization and the last 10 s was taken as the potential value. The first two polarization curves were considered part of the conditioning process and thus, not included here. The polarization curves shown in this work with this method represent an average of the last three polarization curves. Steady-state stability was recorded while applying a current density of 250 mA cm^{-2} for either 16 or 18 h.

Physical Characterization: Scanning electron microscopy was carried out using a SEM Quanta 3D FEG (Thermo Fisher Scientific, USA) at an acceleration voltage of 5 kV.

2.12. References

1. van Trooswijk, A. P. & Deiman, J. R. Sur Une Manière de Décomposer l'Eau En Air Inflammable et En Air Vital. *Obs. Phys.* **35**, 369–384 (1789).
2. de Levie, R. The electrolysis of water. *J. Electroanal. Chem.* **476**, 92–93 (1999).
3. Grigoriev, S. A., Fateev, V. N., Bessarabov, D. G. & Millet, P. Current status, research trends, and challenges in water electrolysis science and technology. *Int. J. Hydrogen Energy* **45**, 26036–26058 (2020).
4. Chisholm, G. & Cronin, L. Hydrogen From Water Electrolysis. in *Storing Energy* 315–343 (Elsevier, 2016).
5. Sapountzi, F. M., Gracia, J. M., Weststrate, C. J., Fredriksson, H. O. A. & Niemantsverdriet, J. W. Electrocatalysts for the generation of hydrogen, oxygen and synthesis gas. *Prog. Energy Combust. Sci.* **58**, 1–35 (2017).
6. Carmo, M., Fritz, D. L., Mergel, J. & Stolten, D. A comprehensive review on PEM water electrolysis. *Int. J. Hydrogen Energy* **38**, 4901–4934 (2013).
7. Dönitz, W. & Erdle, E. High-temperature electrolysis of water vapor-status of development and perspectives for application. *Int. J. Hydrogen Energy* **10**, 291–295 (1985).
8. Riedel, M., Heddrich, M. P. & Friedrich, K. A. Analysis of pressurized operation of 10 layer solid oxide electrolysis stacks. *Int. J. Hydrogen Energy* **44**, 4570–4581 (2019).
9. Chen, K. & Jiang, S. P. Review—Materials Degradation of Solid Oxide Electrolysis Cells. *J. Electrochem. Soc.* **163**, F3070–F3083 (2016).
10. Schiller, G., Ansar, A., Lang, M. & Patz, O. High temperature water electrolysis using metal supported solid oxide electrolyser cells (SOEC). *J. Appl. Electrochem.* **39**, 293–301 (2009).

11. Dolci, F., Gryc, K., Eynard, U., Georgakaki, A., Letout, S., Kuokkanen, A., Mountraki, A., Ince, E., Shtjefni, D., Joanny, G., Eulaerts, O. & Grabowska, M. *Clean Energy Technology Observatory, Water electrolysis and hydrogen in the European Union: status report on technology development, trends, value chains and markets: 2022*. (Publications Office of the European Union, 2022).
12. Schefold, J., Brisse, A. & Poepke, H. 23,000 h steam electrolysis with an electrolyte supported solid oxide cell. *Int. J. Hydrogen Energy* **42**, 13415–13426 (2017).
13. GrInHy 2.0. <https://salcos.salzgitter-ag.com/en/grinhy-20.html>. (Accessed on March 27th, 2023)
14. Schalenbach, M., Kasian, O. & Mayrhofer, K. J. J. An alkaline water electrolyzer with nickel electrodes enables efficient high current density operation. *Int. J. Hydrogen Energy* **43**, 11932–11938 (2018).
15. Park, J. E., Kang, S. Y., Oh, S.-H. H., Kim, J. K., Lim, M. S., Ahn, C.-Y. Y., Cho, Y.-H. H. & Sung, Y.-E. E. High-performance anion-exchange membrane water electrolysis. *Electrochim. Acta* **295**, 99–106 (2019).
16. Wang, L., Weissbach, T., Reissner, R., Ansar, A., Gago, A. S., Holdcroft, S. & Friedrich, K. A. High Performance Anion Exchange Membrane Electrolysis Using Plasma-Sprayed, Non-Precious-Metal Electrodes. *ACS Appl. Energy Mater.* **2**, 7903–7912 (2019).
17. Pletcher, D., Li, X. & Wang, S. A comparison of cathodes for zero gap alkaline water electrolyzers for hydrogen production. *Int. J. Hydrogen Energy* **37**, 7429–7435 (2012).
18. Scharlau, A. Wasserstoff-Erzeugung durch Druckelektrolyse von Wasser. *Fette, Seifen, Anstrichm.* **62**, 185–189 (1960).
19. Godula-Jopek, A. *Hydrogen Production: by Electrolysis*. (Wiley-VCH Verlag GmbH & Co., 2015).
20. Pismenny, A. Stray current corrosion of carbon steel, electroplated nickel, and electroless nickel in alkaline environment. (University of Toronto, 2001).
21. Chen, Z., Koleva, D. & van Breugel, K. A review on stray current-induced steel corrosion in infrastructure. *Corros. Rev.* **35**, 397–423 (2017).
22. de Groot, M. T. & Vreman, A. W. Ohmic resistance in zero gap alkaline electrolysis with a Zirfon diaphragm. *Electrochim. Acta* **369**, 137684 (2021).
23. Jang, D., Cho, H. & Kang, S. Numerical modeling and analysis of the effect of pressure on the performance of an alkaline water electrolysis system. *Appl. Energy* **287**, 116554 (2021).
24. Schröder, V., Emonts, B., Janßen, H. & Schulze, H.-P. Explosion Limits of Hydrogen/Oxygen Mixtures at Initial Pressures up to 200 bar. *Chem. Eng. Technol.* **27**, 847–851 (2004).
25. Brauns, J. & Turek, T. Alkaline Water Electrolysis Powered by Renewable Energy: A Review. *Processes* **8**, 248 (2020).
26. International Organization for Standardization (ISO). *ISO 22734:2019 Hydrogen generators using water electrolysis - Industrial, commercial, and residential applications*. (2019).

27. de Groot, M. T., Kraakman, J. & Garcia Barros, R. L. Optimal operating parameters for advanced alkaline water electrolysis. *Int. J. Hydrogen Energy* **47**, 34773–34783 (2022).
28. Amireh, S. F., Heineman, N. N., Vermeulen, P., Barros, R. L. G., Yang, D., van der Schaaf, J. & de Groot, M. T. Impact of power supply fluctuation and part load operation on the efficiency of alkaline water electrolysis. *J. Power Sources* **560**, 232629 (2023).
29. Brauns, J. & Turek, T. Experimental evaluation of dynamic operating concepts for alkaline water electrolyzers powered by renewable energy. *Electrochim. Acta* **404**, 139715 (2022).
30. Abdel Haleem, A., Huyan, J., Nagasawa, K., Kuroda, Y., Nishiki, Y., Kato, A., Nakai, T., Araki, T. & Mitsushima, S. Effects of operation and shutdown parameters and electrode materials on the reverse current phenomenon in alkaline water analyzers. *J. Power Sources* **535**, 231454 (2022).
31. Russel, J., Nuttall, L. & Fickett, A. Hydrogen generation by solid polymer electrolyte water electrolysis. *Am. Chem. Soc. Div. Fuel Chem. Prepr.* **18**, 24–40 (1973).
32. Grubb, W. T. Ionic Migration in Ion-exchange Membranes. *J. Phys. Chem.* **63**, 55–58 (1959).
33. Grubb, W. T. Batteries with Solid Ion Exchange Electrolytes: I . Secondary Cells Employing Metal Electrodes. *J. Electrochem. Soc.* **106**, 275-278 (1959).
34. Thomassen, M. S., Reksten, A. H., Barnett, A. O., Khoza, T. & Ayers, K. PEM water electrolysis. in *Electrochemical Power Sources: Fundamentals, Systems, and Applications* 199–228 (Elsevier, 2022).
35. Shell starts up Europe’s largest PEM green hydrogen electrolyser. <https://www.refhyne.eu/shell-starts-up-europes-largest-pem-green-hydrogen-electrolyser/> (2021). (Accessed on November 22nd, 2022)
36. Inauguration of the world’s largest PEM electrolyzer to produce decarbonized hydrogen. <https://www.airliquide.com/stories/industry/inauguration-worlds-largest-pem-electrolyzer-produce-decarbonized-hydrogen> (2021). (Accessed on November 22nd, 2022)
37. Ito, H., Maeda, T., Nakano, A. & Takenaka, H. Properties of Nafion membranes under PEM water electrolysis conditions. *Int. J. Hydrogen Energy* **36**, 10527–10540 (2011).
38. Ayers, K. E., Anderson, E. B., Capuano, C., Carter, B., Dalton, L., Hanlon, G., Manco, J. & Niedzwiecki, M. Research Advances towards Low Cost, High Efficiency PEM Electrolysis. *ECS Trans.* **33**, 3–15 (2010).
39. Babic, U., Suermann, M., Büchi, F. N., Gubler, L. & Schmidt, T. J. Critical Review—Identifying Critical Gaps for Polymer Electrolyte Water Electrolysis Development. *J. Electrochem. Soc.* **164**, F387–F399 (2017).
40. Thorbjørnsen, K. F. K. Ir based catalysts for PEM water electrolysis prepared via galvanic displacement. (Norwegian University of Science and Technology, 2021).
41. Siracusano, S., Baglio, V., Van Dijk, N., Merlo, L. & Aricò, A. S. Enhanced performance and durability of low catalyst loading PEM water electrolyser based on a short-side chain perfluorosulfonic ionomer. *Appl. Energy* **192**, 477–489 (2017).
42. Bernt, M. P. Analysis of Voltage Losses and Degradation Phenomena in PEM Water Electrolyzers. (Technische Universität München, 2019).

43. Hoque, M. A., Gil-Sepulcre, M., de Aguirre, A., Elemans, J. A. A. W., Moonshiram, D., Matheu, R., Shi, Y., Benet-Buchholz, J., Sala, X., Malfois, M., Solano, E., Lim, J., Garzón-Manjón, A., Scheu, C., Lanza, M., Maseras, F., Gimbert-Suriñach, C. & Llobet, A. Water oxidation electrocatalysis using ruthenium coordination oligomers adsorbed on multiwalled carbon nanotubes. *Nat. Chem.* **12**, 1060–1066 (2020).
44. Matheu, R., Francàs, L., Chernev, P., Ertem, M. Z., Batista, V., Haumann, M., Sala, X. & Llobet, A. Behavior of the Ru-bda water oxidation catalyst covalently anchored on glassy carbon electrodes. *ACS Catal.* **5**, 3422–3429 (2015).
45. King, L. A., Hubert, M. K. A. A., Capuano, C., Manco, J., Danilovic, N., Valle, E., Hellstern, T. R., Ayers, K. & Jaramillo, T. F. A non-precious metal hydrogen catalyst in a commercial polymer electrolyte membrane electrolyser. *Nat. Nanotechnol.* **14**, 1071–1074 (2019).
46. Zhang, R., Van Straaten, G., Di Palma, V., Zafeiropoulos, G., Van De Sanden, M. C. M., Kessels, W. M. M., Tsampas, M. N. & Creatore, M. Electrochemical Activation of Atomic Layer-Deposited Cobalt Phosphate Electrocatalysts for Water Oxidation. *ACS Catal.* **11**, 2774–2785 (2021).
47. Sapountzi, F. M., Orlova, E. D., Sousa, J. P. S. S., Salonen, L. M., Lebedev, O. I., Zafeiropoulos, G., Tsampas, M. N., Niemantsverdriet, H. J. W. W., Kolen'ko, Y. V. & Kolen'ko, Y. V. FeP Nanocatalyst with Preferential [010] Orientation Boosts the Hydrogen Evolution Reaction in Polymer-Electrolyte Membrane Electrolyzer. *Energy & Fuels* **34**, 6423–6429 (2020).
48. Corrales-Sánchez, T., Ampurdanés, J. & Urakawa, A. MoS₂-based materials as alternative cathode catalyst for PEM electrolysis. *Int. J. Hydrogen Energy* **39**, 20837–20843 (2014).
49. Ng, J. W. D., Hellstern, T. R., Kibsgaard, J., Hinckley, A. C., Benck, J. D. & Jaramillo, T. F. Polymer Electrolyte Membrane Electrolyzers Utilizing Non-precious Mo-based Hydrogen Evolution Catalysts. *ChemSusChem* **8**, 3512–3519 (2015).
50. Xiao, L., Zhang, S., Pan, J., Yang, C., He, M., Zhuang, L. & Lu, J. First implementation of alkaline polymer electrolyte water electrolysis working only with pure water. *Energy Environ. Sci.* **5**, 7869 (2012).
51. Leng, Y., Chen, G., Mendoza, A. J., Tighe, T. B., Hickner, M. A. & Wang, C.-Y. Solid-State Water Electrolysis with an Alkaline Membrane. *J. Am. Chem. Soc.* **134**, 9054–9057 (2012).
52. Pavel, C. C., Cecconi, F., Emiliani, C., Santiccioli, S., Scaffidi, A., Catanorchi, S. & Comotti, M. Highly Efficient Platinum Group Metal Free Based Membrane-Electrode Assembly for Anion Exchange Membrane Water Electrolysis. *Angew. Chemie Int. Ed.* **53**, 1378–1381 (2014).
53. Pandey, T. P., Sarode, H. N., Yang, Y., Yang, Y., Vezzù, K., Noto, V. Di, Seifert, S., Knauss, D. M., Liberatore, M. W. & Herring, A. M. A Highly Hydroxide Conductive, Chemically Stable Anion Exchange Membrane, Poly(2,6 dimethyl 1,4 phenylene oxide)-b-Poly(vinyl benzyl trimethyl ammonium), for Electrochemical Applications. *J. Electrochem. Soc.* **163**, H513–H520 (2016).
54. Ren, X., Price, S. C., Jackson, A. C., Pomerantz, N. & Beyer, F. L. Highly Conductive Anion Exchange Membrane for High Power Density Fuel-Cell Performance. *ACS Appl. Mater. Interfaces* **6**, 13330–13333 (2014).

55. Yang, G., Hao, J., Cheng, J., Zhang, N., He, G., Zhang, F. & Hao, C. Hydroxide ion transfer in anion exchange membrane: A density functional theory study. *Int. J. Hydrogen Energy* **41**, 6877–6884 (2016).
56. Plevová, M., Hnát, J., Žitka, J., Pavlovec, L., Otmar, M. & Bouzek, K. Optimization of the membrane electrode assembly for an alkaline water electrolyser based on the catalyst-coated membrane. *J. Power Sources* **539**, 231476 (2022).
57. Siracusano, S., Baglio, V., Stassi, A., Merlo, L., Moukheiber, E. & Arico', A. S. Performance analysis of short-side-chain Aquivion® perfluorosulfonic acid polymer for proton exchange membrane water electrolysis. *J. Memb. Sci.* **466**, 1–7 (2014).
58. Lim, J. Y., Rahman, G., Chae, S. Y., Lee, K. Y., Kim, C. S. & Joo, O. S. Highly stable RuO₂/SnO₂ nanocomposites as anode electrocatalysts in a PEM water electrolysis cell. *Int. J. Energy Res.* **38**, 875–883 (2014).
59. Wei, G., Xu, L., Huang, C. & Wang, Y. SPE water electrolysis with SPEEK/PES blend membrane. *Int. J. Hydrogen Energy* **35**, 7778–7783 (2010).
60. Stähler, M., Stähler, A., Scheepers, F., Carmo, M. & Stolten, D. A completely slot die coated membrane electrode assembly. *Int. J. Hydrogen Energy* **44**, 7053–7058 (2019).
61. Lopata, J., Kang, Z., Young, J., Bender, G., Weidner, J. W. & Shimpalee, S. Effects of the Transport/Catalyst Layer Interface and Catalyst Loading on Mass and Charge Transport Phenomena in Polymer Electrolyte Membrane Water Electrolysis Devices. *J. Electrochem. Soc.* **167**, 064507 (2020).
62. Fabbri, E., Haberer, A., Waltar, K., Kötz, R. & Schmidt, T. J. Developments and perspectives of oxide-based catalysts for the oxygen evolution reaction. *Catal. Sci. Technol.* **4**, 3800–3821 (2014).
63. McCrory, C. C. L., Jung, S., Ferrer, I. M., Chatman, S. M., Peters, J. C. & Jaramillo, T. F. Benchmarking Hydrogen Evolving Reaction and Oxygen Evolving Reaction Electrocatalysts for Solar Water Splitting Devices. *J. Am. Chem. Soc.* **137**, 4347–4357 (2015).
64. Miles, M. H. & Thomason, M. A. Periodic Variations of Overvoltages for Water Electrolysis in Acid Solutions from Cyclic Voltammetric Studies. *J. Electrochem. Soc.* **123**, 1459–1461 (1976).
65. Damjanovic, A., Dey, A. & Bockris, J. O. Electrode Kinetics of Oxygen Evolution and Dissolution on Rh, Ir, and Pt-Rh Alloy Electrodes. *J. Electrochem. Soc.* **113**, 739–746 (1966).
66. Galizzioli, D., Tantardini, F. & Trasatti, S. Ruthenium dioxide: a new electrode material. I. Behaviour in acid solutions of inert electrolytes. *J. Appl. Electrochem.* **4**, 57–67 (1974).
67. Cherevko, S., Geiger, S., Kasian, O., Kulyk, N., Grote, J.-P., Savan, A., Shrestha, B. R., Merzlikin, S., Breitbach, B., Ludwig, A. & Mayrhofer, K. J. J. Oxygen and hydrogen evolution reactions on Ru, RuO₂, Ir, and IrO₂ thin film electrodes in acidic and alkaline electrolytes: A comparative study on activity and stability. *Catal. Today* **262**, 170–180 (2016).
68. Kötz, R., Lewerenz, H. J. & Stucki, S. XPS Studies of Oxygen Evolution on Ru and RuO₂ Anodes. *J. Electrochem. Soc.* **130**, 825–829 (1983).

69. Section 14: Geophysics, Astronomy and Acoustics. in *CRC Handbook of Chemistry and Physics* (ed. Rumble, J. R.) 17 (CRC Press/Taylor & Francis, 2022).
70. Ramli, Z. A. C. & Kamarudin, S. K. Platinum-Based Catalysts on Various Carbon Supports and Conducting Polymers for Direct Methanol Fuel Cell Applications: a Review. *Nanoscale Res. Lett.* **13**, 410 (2018).
71. Bernt, M., Siebel, A. & Gasteiger, H. A. Analysis of Voltage Losses in PEM Water Electrolyzers with Low Platinum Group Metal Loadings. *J. Electrochem. Soc.* **165**, F305–F314 (2018).
72. Giovanni, C. Di, Reyes-Carmona, Á., Coursier, A., Nowak, S., Grenèche, J., Lecoq, H., Mouton, L., Rozière, J., Jones, D., Peron, J., Giraud, M. & Tard, C. Low-Cost Nanostructured Iron Sulfide Electrocatalysts for PEM Water Electrolysis. *ACS Catal.* **6**, 2626–2631 (2016).
73. A10816 Ruthenium(IV) oxide, anhydrous, 99.9%. <https://www.alfa.com/en/catalog/A10816/>. (Accessed on November 24th, 2022)
74. A17849 Iridium(IV) oxide powder, 99%. <https://www.alfa.com/en/catalog/A17849/>. (Accessed on November 24th, 2022)
75. Goñi-Urtiaga, A., Presvytes, D. & Scott, K. Solid acids as electrolyte materials for proton exchange membrane (PEM) electrolysis: Review. *Int. J. Hydrogen Energy* **37**, 3358–3372 (2012).
76. Bernt, M. & Gasteiger, H. A. Influence of Ionomer Content in IrO₂/TiO₂ Electrodes on PEM Water Electrolyzer Performance. *J. Electrochem. Soc.* **163**, F3179–F3189 (2016).
77. Xu, W. & Scott, K. The effects of ionomer content on PEM water electrolyser membrane electrode assembly performance. *Int. J. Hydrogen Energy* **35**, 12029–12037 (2010).
78. Bosson, K., Marcasuzaa, P., Bousquet, A., Tovar, G. E. M., Atanasov, V. & Billon, L. para fluoro-thiol clicked diblock-copolymer self-assembly: Towards a new paradigm for highly proton-conductive membranes. *J. Memb. Sci.* **659**, 120796 (2022).
79. Chae, J. E., Lee, S. Y., Baek, S. Y., Song, K. H., Park, C. H., Kim, H.-J. & Lee, K.-S. High-performance multiblock PEMs containing a highly acidic fluorinated-hydrophilic domain for water electrolysis. *J. Memb. Sci.* **638**, 119694 (2021).
80. Siracusano, S., Pantò, F., Tonella, S., Oldani, C. & Aricò, A. S. Reinforced short-side-chain Aquivion® membrane for proton exchange membrane water electrolysis. *Int. J. Hydrogen Energy* **47**, 15557–15570 (2022).
81. Borgardt, E., Panchenko, O., Hackemüller, F. J., Giffin, J., Bram, M., Müller, M., Lehnert, W. & Stolten, D. Mechanical characterization and durability of sintered porous transport layers for polymer electrolyte membrane electrolysis. *J. Power Sources* **374**, 84–91 (2018).
82. Bromberger, K., Ghinaiya, J., Lickert, T., Fallisch, A. & Smolinka, T. Hydraulic ex situ through-plane characterization of porous transport layers in PEM water electrolysis cells. *Int. J. Hydrogen Energy* **43**, 2556–2569 (2018).
83. Lee, C. H., Banerjee, R., Arbabi, F., Hinebaugh, J. & Bazylak, A. Porous Transport Layer Related Mass Transport Losses in Polymer Electrolyte Membrane Electrolysis: A Review. in *ASME 2016 14th International Conference on Nanochannels, Microchannels, and*

Minichannels (American Society of Mechanical Engineers, 2016).

84. Ito, H., Maeda, T., Nakano, A., Hwang, C. M., Ishida, M., Kato, A. & Yoshida, T. Experimental study on porous current collectors of PEM electrolyzers. *Int. J. Hydrogen Energy* **37**, 7418–7428 (2012).
85. Grigoriev, S. A., Millet, P., Volobuev, S. A. & Fateev, V. N. Optimization of porous current collectors for PEM water electrolyzers. *Int. J. Hydrogen Energy* **34**, 4968–4973 (2009).
86. Zielke, L., Fallisch, A., Paust, N., Zengerle, R. & Thiele, S. Tomography based screening of flow field / current collector combinations for PEM water electrolysis. *RSC Adv.* **4**, 58888–58894 (2014).
87. Lettenmeier, P., Kolb, S., Sata, N., Fallisch, A., Zielke, L., Thiele, S., Gago, A. S. & Friedrich, K. A. Comprehensive investigation of novel pore-graded gas diffusion layers for high-performance and cost-effective proton exchange membrane electrolyzers. *Energy Environ. Sci.* **10**, 2521–2533 (2017).
88. Lettenmeier, P., Kolb, S., Burggraf, F., Gago, A. S. & Friedrich, K. A. Towards developing a backing layer for proton exchange membrane electrolyzers. *J. Power Sources* **311**, 153–158 (2016).
89. Ito, H., Maeda, T., Nakano, A., Hasegawa, Y., Yokoi, N., Hwang, C. M. M., Ishida, M., Kato, A. & Yoshida, T. Effect of flow regime of circulating water on a proton exchange membrane electrolyzer. *Int. J. Hydrogen Energy* **35**, 9550–9560 (2010).
90. Kazim, A., Liu, H. T. & Forges, P. Modelling of performance of PEM fuel cells with conventional and interdigitated flow fields. *J. Appl. Electrochem.* **29**, 1409–1416 (1999).
91. Nie, J. H., Chen, Y. T., Wu, J. F. & Veepuri, K. M. Explorations of Improving Flow Uniformity in the Bipolar Plate of a PEM Electrolysis Cell Using Different Designs. in *Volume 1: Symposia, Parts A and B* 725–732 (2008).
92. Millet, P. Degradation Processes and Failure Mechanisms in PEM Water Electrolyzers. in *PEM Electrolysis for Hydrogen Production* 219–242 (CRC Press/Taylor & Francis, 2016).
93. Gago, A. S., Ansar, S. A., Saruhan, B., Schulz, U., Lettenmeier, P., Cañas, N. A., Gazdzicki, P., Morawietz, T., Hiesgen, R., Arnold, J. & Friedrich, K. A. Protective coatings on stainless steel bipolar plates for proton exchange membrane (PEM) electrolyzers. *J. Power Sources* **307**, 815–825 (2016).
94. Langemann, M., Fritz, D. L., Müller, M. & Stolten, D. Validation and characterization of suitable materials for bipolar plates in PEM water electrolysis. *Int. J. Hydrogen Energy* **40**, 11385–11391 (2015).
95. Jung, H.-Y., Huang, S.-Y., Ganesan, P. & Popov, B. N. Performance of gold-coated titanium bipolar plates in unitized regenerative fuel cell operation. *J. Power Sources* **194**, 972–975 (2009).
96. Chisholm, G., Kitson, P. J., Kirkaldy, N. D., Bloor, L. G. & Cronin, L. 3D printed flow plates for the electrolysis of water: An economic and adaptable approach to device manufacture. *Energy Environ. Sci.* **7**, 3026–3032 (2014).
97. Bratsch, S. G. Standard Electrode Potentials and Temperature Coefficients in Water at 298.15 K. *J. Phys. Chem. Ref. Data* **18**, 1–21 (1989).

98. LeRoy, R. L., Bowen, C. T. & LeRoy, D. J. The Thermodynamics of Aqueous Water Electrolysis. *J. Electrochem. Soc.* **127**, 1954–1962 (1980).
99. Stull, D. R. Vapor Pressure of Pure Substances. Organic and Inorganic Compounds. *Ind. Eng. Chem.* **39**, 517–540 (1947).
100. Stull, D. R. Vapor Pressure of Pure Substances. Inorganic Compounds. *Ind. Eng. Chem.* **39**, 540–550 (1947).
101. Beaton, C. F. Steam tables. Heat Exchanger Design Handbook Multimedia Edition http://hedhme.com/content_map/?article_id=526. (Accessed on July 20th, 2022)
102. Marangio, F., Santarelli, M. & Calì, M. Theoretical model and experimental analysis of a high pressure PEM water electrolyser for hydrogen production. *Int. J. Hydrogen Energy* **34**, 1143–1158 (2009).
103. Choi, P., Jalani, N. H. & Datta, R. Thermodynamics and Proton Transport in Nafion. *J. Electrochem. Soc.* **152**, E123 (2005).
104. Springer, T. E., Zawodzinski, T. A. & Gottesfeld, S. Polymer Electrolyte Fuel Cell Model. *J. Electrochem. Soc.* **138**, 2334–2342 (1991).
105. Kreuer, K.-D. The role of internal pressure for the hydration and transport properties of ionomers and polyelectrolytes. *Solid State Ionics* **252**, 93–101 (2013).
106. Bard, A. J. & Faulkner, L. R. *Electrochemical Methods: Fundamentals and Applications, 2nd Edition*. (John Wiley & Sons, Incorporated, 2001).
107. García-Valverde, R., Espinosa, N. & Urbina, A. Simple PEM water electrolyser model and experimental validation. *Int. J. Hydrogen Energy* **37**, 1927–1938 (2012).
108. Datta, R., Martino, D. J., Dong, Y. & Choi, P. Modeling of PEM Water Electrolyzer. in *PEM Electrolysis for Hydrogen Production—Principles and Applications* 243–267 (CRC Press, 2016).
109. Liso, V., Savoia, G., Araya, S. S., Cinti, G. & Kær, S. K. Modelling and Experimental Analysis of a Polymer Electrolyte Membrane Water Electrolysis Cell at Different Operating Temperatures. *Energies* **11**, 3273 (2018).
110. Thampan, T., Malhotra, S., Zhang, J. & Datta, R. PEM fuel cell as a membrane reactor. *Catal. Today* **67**, 15–32 (2001).
111. Garbe, S., Futter, J., Schmidt, T. J. & Gubler, L. Insight into elevated temperature and thin membrane application for high efficiency in polymer electrolyte water electrolysis. *Electrochim. Acta* **377**, 138046 (2021).
112. Colbertaldo, P., Gómez Aláez, S. L. & Campanari, S. Zero-dimensional dynamic modeling of PEM electrolyzers. *Energy Procedia* **142**, 1468–1473 (2017).
113. Lee, W., Ho, C.-H., Van Zee, J. W. & Murthy, M. The effects of compression and gas diffusion layers on the performance of a PEM fuel cell. *J. Power Sources* **84**, 45–51 (1999).
114. Mason, T. J., Millichamp, J., Neville, T. P., El-kharouf, A., Pollet, B. G. & Brett, D. J. L. Effect of clamping pressure on ohmic resistance and compression of gas diffusion layers for polymer electrolyte fuel cells. *J. Power Sources* **219**, 52–59 (2012).
115. Borgardt, E., Giesenberg, L., Reska, M., Müller, M., Wippermann, K., Langemann, M.,

- Lehnert, W. & Stolten, D. Impact of clamping pressure and stress relaxation on the performance of different polymer electrolyte membrane water electrolysis cell designs. *Int. J. Hydrogen Energy* **44**, 23556–23567 (2019).
116. Moreno Soriano, R., Rojas, N., Nieto, E., de Guadalupe González-Huerta, R. & Sandoval-Pineda, J. M. Influence of the gasket materials on the clamping pressure distribution in a PEM water electrolyzer: Bolt torques and operation mode in pre-conditioning. *Int. J. Hydrogen Energy* **46**, 25944–25953 (2021).
117. Yun, S.-H. H., Shin, S.-H. H., Lee, J.-Y. Y., Seo, S.-J. J., Oh, S.-H. H., Choi, Y.-W. W. & Moon, S.-H. H. Effect of pressure on through-plane proton conductivity of polymer electrolyte membranes. *J. Memb. Sci.* **417–418**, 210–216 (2012).
118. Okada, T., Møller-Holst, S., Gorseth, O. & Kjelstrup, S. Transport and equilibrium properties of Nafion® membranes with H⁺ and Na⁺ ions. *J. Electroanal. Chem.* **442**, 137–145 (1998).
119. Zhang, L., Jie, X., Shao, Z. G., Wang, X. & Yi, B. The dynamic-state effects of sodium ion contamination on the solid polymer electrolyte water electrolysis. *J. Power Sources* **241**, 341–348 (2013).
120. Rakousky, C., Reimer, U., Wippermann, K., Carmo, M., Lueke, W. & Stolten, D. An analysis of degradation phenomena in polymer electrolyte membrane water electrolysis. *J. Power Sources* **326**, 120–128 (2016).
121. Lyons, M. E. G. & Floquet, S. Mechanism of oxygen reactions at porous oxide electrodes. Part 2 - Oxygen evolution at RuO₂, IrO₂ and Ir_xRu_{1-x}O₂ electrodes in aqueous acid and alkaline solution. *Phys. Chem. Chem. Phys.* **13**, 5314–5335 (2011).
122. Ma, Z., Zhang, Y., Liu, S., Xu, W., Wu, L., Hsieh, Y.-C. C., Liu, P., Zhu, Y., Sasaki, K., Renner, J. N., Ayers, K. E., Adzic, R. R. & Wang, J. X. Reaction mechanism for oxygen evolution on RuO₂, IrO₂, and RuO₂@IrO₂ core-shell nanocatalysts. *J. Electroanal. Chem.* **819**, 296–305 (2018).
123. Nafion® perfluorinated membrane - NRE-212. <https://www.sigmaaldrich.com/NL/en/product/aldrich/676470>. (Accessed on March 7th, 2023)
124. The Basic Physical and Chemical Properties of Nafion™ Polymer. <https://www.permapure.com/environmental-scientific/nafion-tubing/nafion-physical-and-chemical-properties/>. (Accessed on March 7th, 2023)

Chapter 3

Efficient continuous light-driven water electrolysis using an electrochemical flow cell and a perovskite/silicon tandem solar cell

Abstract

Voltage matching between the photovoltaic and electrochemical components is essential to reach high efficiencies in artificial photosynthesis. To exceed the thermodynamic potential for water-splitting of 1.23 V, photovoltaic cells are commonly series connected or employed in tandem configurations. The highest solar-to-hydrogen efficiency (STH) of 30% has been obtained using expensive triple-junction III-V semiconductor-based solar cells under 42-Sun concentrated light intensity when combined with a flow electrochemical cell. Perovskite-silicon tandem solar cells promise an efficient and cost-effective route to reduce cost and provide high efficiency in normal solar light. In this chapter, a first example is demonstrated of an integrated continuous flow electrochemical cell coupled to a monolithic perovskite-silicon tandem solar cell that in concert provide a light-driven electrochemical STH conversion efficiency exceeding 21% at 1-Sun equivalent light intensity and stable operation during three simulated day-night cycles.

The crystalline silicon sub-cell was fabricated in TU Delft (Yifeng Zhao, MSc.) while the perovskite sub-cell was fabricated in TU Eindhoven (Kunal Datta, PhD).

This chapter is partially reproduced from: Datta, K., Branco, B., Zhao, Y., Zardetto, V., Phung, N., Bracesco, A., Mazzarella, L., Wienk, M. M., Creatore, M., Isabella, O., Janssen, R. A. J., Efficient Continuous Light-Driven Electrochemical Water Splitting Enabled by Monolithic Perovskite-Silicon Tandem Photovoltaics. *Adv. Mater. Technol.* 2023, 8, 2201131

3.1. Introduction

Water electrolysis powered by solar energy is the most straightforward embodiment of artificial photosynthesis. The viability of an artificial photosynthesis reactor relies on appropriate matching of the water electrolysis and photoactive components. The solar-to-hydrogen efficiency (STH) (Eq. 3.1) directly influences the cost of the green hydrogen and the United States department of energy (DOE) defined a target STH of 20% using low-cost materials by 2020.¹

$$\text{STH} = \frac{1.23 I_{\text{op}} \eta_{\text{far}}}{A_{\text{sc}} P_{\text{in}}} \quad (3.1)$$

In Eq. 3.1, I_{op} is the average operating current in A, η_{far} is the (dimensionless) faradaic efficiency of the water electrolysis reactions, A_{sc} the solar cell area in m^2 , and P_{in} the irradiance in W m^{-2} .²

Typical lab-scale studies for artificial photosynthesis rely on 1- or 2-compartment batch electrochemical cells (Figure 3.1a) combined with a photovoltaic device. Batch electrochemical cells are generally used to test new catalyst materials in a well-controlled pH environment. In H-cells, the two compartments are separated by an ionomer membrane or a glass-frit, allowing product separation. Such batch electrochemical cells have high ohmic losses due to the large inter-electrode distance, in the order of mm, resulting in significant voltage losses, and thereby, rendering them unsuitable for large-scale applications. Instead, for such scale, electrochemical cells (EC) that operate with continuous water flow and a zero-gap configuration are adopted (Figure 3.1b).

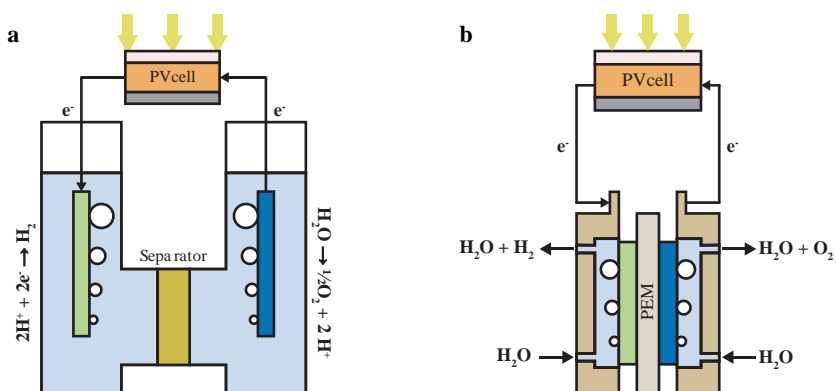


Figure 3.1: Electrochemical cell schematics. a) batch H-cell and b) continuous flow electrochemical cell-based devices. In this diagram the PV cell is a monolithic multijunction cell, but it can be replaced by series-connected single-junction cells.

Continuous flow electrochemical cells, hereinafter referred to as flow cells, can achieve much higher current outputs due to the use of thin solid-state electrolytes that have higher ionic conductivity than the liquid electrolytes commonly used in batch cells. Furthermore, the zero-gap configuration (Figure 3.1b), i.e., the electrodes are in direct contact with the solid electrolyte, allows an inter-electrode distance of a few hundredths of micrometers, further reducing ohmic losses.³ The constant water flow avoids accumulation of gaseous products, decreasing mass transfer limitations and improving the cell potential as well.⁴ For these reasons, flow cells coupled to III-V multijunction solar cells operated under concentrated light achieve high STH in artificial photosynthesis.⁵⁻⁷ For instance, the record STH (~30%) has been reported for a InGaP/GaAs/GaInNAsSb triple-junction solar cell operated at 42-Sun equivalent light intensity, coupled to a Ir/Pt catalyst combination for the anode/cathode sub-cells in two series-connected flow cells (Figure 1.4, chapter 1).⁷ This and other works have exceedingly surpassed the target STH set by the US DOE, but these devices are based on high-cost materials and operate under concentrated solar light, greatly reducing their economic viability and applicability in indirect sunlight.

The drawback of expensive semiconductor materials has led to a growing interest to shift to more cost-effective semiconductor materials. Lead halide perovskite-based solar cells promise a cost-effective route to increase the power conversion efficiency (PCE) due to the comparatively inexpensive material and processing costs associated with this type of material. Furthermore, the high luminescence quantum efficiency of such materials enable a high open-circuit voltage (V_{oc}) in devices. Kuang et al.⁸ and Luo et al.⁹ reported the use of Ni-based electrocatalysts combined with two series-connected perovskite solar cells, reaching an STH of 11.90% and 12.3%, respectively. The STH in these two reports is limited by the low current densities as a consequence of connecting the solar cells in series, because the output current is the same while the solar cell active area is multiplied by the number of connected cells. The use of more than one solar cell is nevertheless needed to surpass the relatively high potential required for water electrolysis (> 1.23 V at 25 °C). For an efficient artificial photosynthesis system, the photovoltage at the maximum power point (V_{mpp}) of the solar cell combination should exceed the required electrochemical potential ($V_{mpp} \geq 1.23$ V). V_{mpp} will be always lower than the open-circuit voltage (V_{oc}), which in turn will be lower than the bandgap energy (E_g) of the semiconductor. For example, for the highest PCE perovskite (FAPbI₃, where FA is formamidinium), $E_g = 1.48$ eV while $V_{oc} = 1.19$ V and $V_{mpp} \approx 1.00$ V. These single-junction voltages are clearly insufficient to meet the requirements for water electrolysis, and hence, series connections are needed.^{10,11}

However, simply connecting several cells in series is not the only approach to meet the voltage requirement. The potential requirement can be more efficiently reached by monolithically (two terminal, 2T) or mechanically (four terminal, 4T) stacking two or more semiconductor materials with complementary bandgaps in what is called a multijunction solar cell.¹² Incorporating multiple light absorber layers with cascaded bandgaps is an effective route to increase the PCE of solar cells above the efficiency limits of single-junctions.¹³ In these devices, the energy losses by thermalization of high-energy charge carriers and transmission of low-energy carriers are diminished by the multiple absorbers that are active in different areas of the solar spectrum. High-energy photons are absorbed by the wide-bandgap top cell whereas the transmitted low-energy photons are absorbed by the narrow-bandgap bottom cell as illustrated in **Figure 3.2a**.¹⁴ Because the V_{oc} of the wide-bandgap cell is higher than of the narrow-bandgap cell, losses are minimized and the photon energy is better conserved across the whole solar spectrum (Figure 3.2b). In a monolithic multijunction solar cell, $V_{oc,2T}$ is approximately the sum of the V_{oc} s of the sub-cells. A small V_{oc} loss in such devices is typical because the light intensity reaching the bottom cell is reduced due to filtering by the top cell.¹⁵ The current density of the monolithic tandem cell ($J_{sc,2T}$) corresponds to the short-current density (J_{sc}) of the sub-cell with lowest value, i.e., the current-limiting cell. In an optimized multijunction solar cell, $J_{sc,2T}$ will be approximately equal to the J_{sc} of the narrowest-bandgap sub-cell – as a single-junction – divided by the number of sub-cells. Hence, to match the requirements for water electrolysis and maximize the STH, the $V_{mpp,2T}$, and by extension $V_{oc,2T}$, should be designed to match the V_{op} while using as few as possible absorber materials to maximize $J_{sc,2T}$.

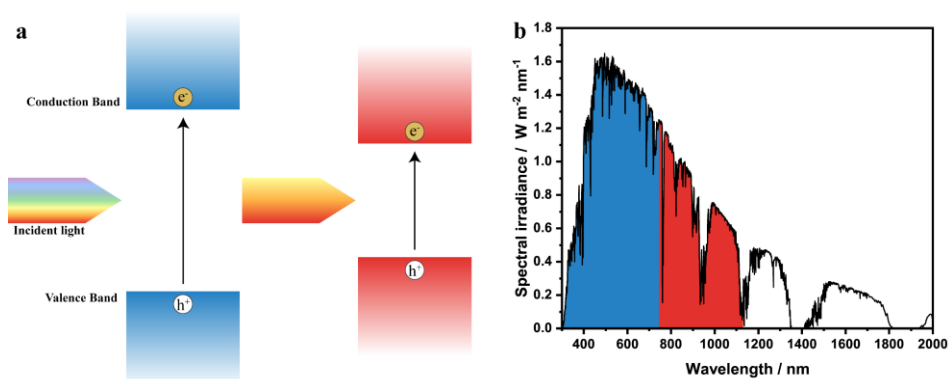


Figure 3.2: Multijunction solar cells. a) Schematic energy diagram of a multijunction solar cell. b) Standard solar irradiance (AM1.5G). The colored areas represent the spectral regions being absorbed by different light absorbers: $E_g = 1.67$ eV (blue) and 1.1 eV (red).

Perovskite semiconductors are considered particularly suitable for multijunction solar cells because their bandgap energy can be engineered by changing the perovskite composition. In the past three years, there have been a few studies that have employed lead halide perovskite multijunction solar cells. Most of these studies combine a wide-bandgap perovskite semiconductor with narrow-bandgap crystalline silicon (c-Si) bottom cell. These type of multijunction solar cells have recently achieved a PCE exceeding 30%.¹⁶ Such perovskite/c-Si tandems cells are especially interesting for artificial photosynthesis because their high V_{oc} , and thus, high V_{mpp} , enable a high current output at the required operating potential (> 1.23 V). In 2019, Park et al.¹⁷ and Gao et al.¹⁸ reported for the first time water electrolysis carried out by a monolithic perovskite/c-Si tandem, reaching a STH of 17.52% and 18.7%, respectively. In 2021, the 20% STH threshold was surpassed by Pan et al.¹⁹ by combining a perovskite/c-Si tandem cell with 27.26% PCE with Ni-based catalysts in alkaline electrolyte, enabling an operating current density of 17.33 mA cm⁻², corresponding to a STH of 21.32% under 1-Sun equivalent light intensity. Besides, the authors report an STH of 20.43% after > 8 h of continuous operation. These reports show that high STHs without light concentration can be achieved by more cost-effective solar cells such as perovskite/c-Si tandems (Figure 1.4, chapter 1), avoiding the use of III-V semiconductor-based multijunction solar cells. However, all publications, as well as the artificial photosynthesis devices using perovskite-based solar cells presented in Figure 1.4 (chapter 1), use batch electrochemical cells.

In this chapter, the first light-driven continuous flow water splitting device, powered by a 1 cm² monolithic perovskite-silicon tandem solar cell operated at 1-Sun equivalent light intensity is described. The good compatibility between the electrical behavior of the photovoltaic (PV) and EC components results in a STH efficiency of 21.5%, exceeding previously reported values at 1-Sun, together with stable operation during 72 h of diurnal operation.

3.2. Water electrolysis in an electrochemical flow cell

An electrochemical flow cell with an active area of 4 cm² was constructed based on a two-compartment design separated by a Nafion NRE-212 membrane (50 μ m dry thickness) spray coated with 1.2 mg cm⁻² Pt and 2.0 mg cm⁻² RuO₂ for hydrogen and oxygen evolution, respectively. The membrane-electrode assembly (MEA), along with titanium (anode) and carbon (cathode) porous transport layers (PTL), is pressed between two titanium plates with parallel flow fields that simultaneously act as current collectors and fluid distributors. **Figure 3.3a** shows the cross-section scanning electron microscopy (SEM) image of the

MEA. The thickness of Pt/C layer is about $30 \pm 2 \mu\text{m}$ while the RuO_2 layer has a thickness of $16 \pm 2 \mu\text{m}$ and thus, the total thickness of the MEA is approximately $100 \mu\text{m}$. The reduced inter-electrode distance grants decreased ohmic loss, and accordingly, higher currents can be more easily achieved in comparison to batch electrochemical cells.

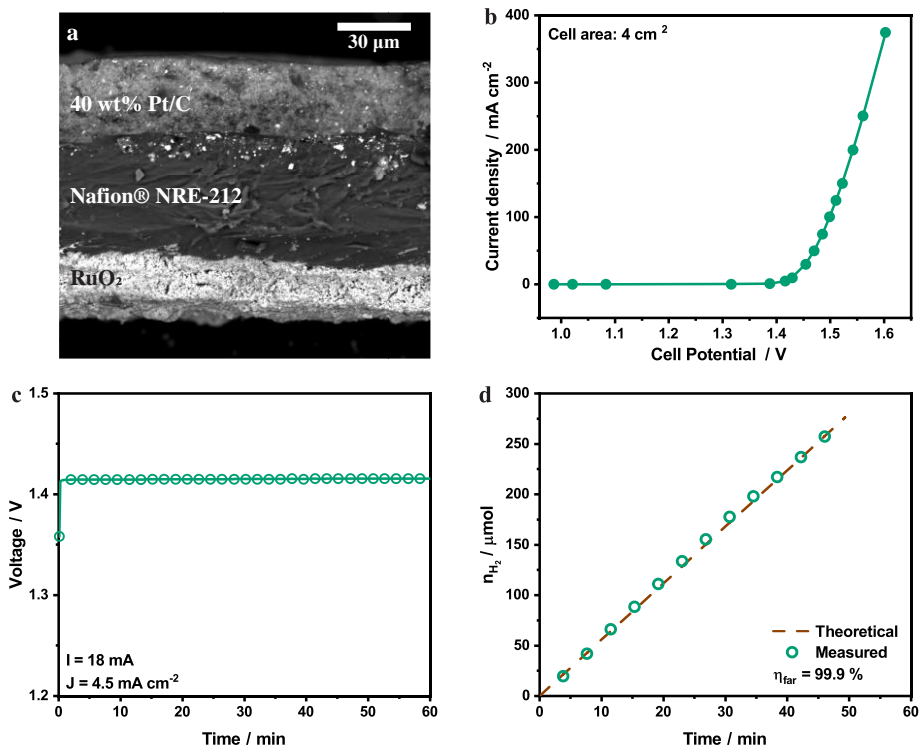


Figure 3.3: Electrochemical flow cell. a) Cross-section SEM image of a representative MEA. The hydrogen (Pt) and oxygen (RuO_2) evolution sides are identified. The bright spots on the membrane arise from sample preparation for SEM. b) Polarization curve of the electrochemical flow cell (active area = 4 cm^2 , Pt/Nafion NRE-212/ RuO_2) using ultrapure water at room temperature. c) Galvanostatic measurement at $I = 18.0 \text{ mA}$ for 1 h. d) Hydrogen quantification by gas chromatography under 1 h continuous operation with applied current of 18.0 mA .

In contrast to chapter 2 of this thesis, all electrochemical characterization was performed at room temperature to decrease unnecessary energy expenditure. The effect of temperature on the STH will be discussed later in **Section 3.4** of this chapter. Figure 3.3b shows the polarization curve of the EC at room temperature. Cell potentials below the thermodynamic potential for water electrolysis arise at low current densities ($0.01 - 0.5 \text{ mA cm}^{-2}$), which may be a consequence of the polarization of the electrolyte in the membrane and slow response to reach equilibrium conditions. The origin of this effect was not further

investigated but it has been observed in other literature work as well.^{20–23} A cell voltage of 1.42 V is measured at an applied current of 20 mA ($J_{\text{EC}} = 5 \text{ mA cm}^{-2}$); however, the potential only slightly increases to 1.60 V when the applied current is increased to 1500 mA ($J_{\text{EC}} = 375 \text{ mA cm}^{-2}$). This small increase in potential at a high current density range allows the solar-assisted water splitting system to operate within a narrow potential window, independent of solar illumination intensity, minimizing the degradation of the catalysts and electrodes.^{24,25} Furthermore, the EC cell is operationally stable when applying a constant current of 18.0 mA ($J_{\text{EC}} = 4.5 \text{ mA cm}^{-2}$) as shown in Figure 3.3c. Finally, hydrogen evolution, as quantified by in-line gas chromatography, was found to be similar to that determined theoretically (Figure 3.3d). As a result, under operating conditions, the flow EC has a faradaic efficiency (η_{far}) close to unity (0.999).

3.3. Monolithic perovskite/c-silicon tandem solar cell

Monolithic perovskite-silicon tandem solar cells (**Figure 3.4a**) were prepared using a wide-bandgap ($E_g \sim 1.67 \text{ eV}$) perovskite (nominally $\text{K}_{0.05}\text{Cs}_{0.05}(\text{FA}_{0.79}\text{MA}_{0.21})_{0.90}\text{Pb}(\text{I}_{0.79}\text{Br}_{0.21})_3$, in which MA is methyl ammonium) top-cell integrated with a silicon heterojunction (SHJ) bottom-cell. The perovskite top-cell was fabricated using an atomic layer deposited (ALD) NiO interlayer and a self-assembled monolayer (SAM) of [2-(9H-carbazol-9-yl)ethyl]phosphonic acid (2PACz) as hole-selective contact, and a thermally evaporated C_{60} layer as electron-selective contact. The perovskite/ C_{60} interface was treated with choline chloride to reduce interfacial defects and improve the V_{oc} of the perovskite sub-cell.^{26,27} The SHJ device platform was chosen as the bottom-cell because of the high achievable V_{oc} (0.70 V), which makes it commonly used in efficient perovskite-silicon tandem structures.²⁸ The perovskite top-cell and c-Si bottom-cell were monolithically integrated using an indium tin oxide (ITO) interconnection layer. Figure 3.4b shows the X-ray photoelectron spectra (XPS) in the oxygen (O1s) region of the ITO surface which allows quantifying the ratio between hydroxyl (-OH) and metal oxide (M-O) species at the ITO surface. As can be seen, transparent ITO electrodes on glass (commercial ITO) used to prepare single-junction solar cells have a -OH to M-O ratio of 0.61 (Figure 3.4c). In contrast, the -OH to M-O ratio of the ITO layer deposited in-house (sputtered ITO) has a lower -OH to M-O ratio of 0.57.

Tandem cells made using a 2PACz SAM directly on the sputtered ITO interlayer showed a $V_{\text{oc}}^{\text{tandem}}$ of 0.74 V (Figure 3.4d), i.e., close to $V_{\text{oc}}^{\text{c-Si}}$ of a SHJ single-junction device. The low $V_{\text{oc}}^{\text{tandem}}$ indicates a partial coverage of the 2PACz SAM, which binds to metal oxide surfaces through a phosphonic acid anchoring group, leading to a poorly-functioning hole-selective contact in the perovskite

top-cell.²⁹ This was solved by depositing a thin (≈ 8 nm) NiO layer on the sputtered ITO using ALD.³⁰ Subsequent XPS characterization showed that the $-\text{OH}$ to $\text{M}-\text{O}$ ratio increased from 0.57 for the ITO surface to 0.70 for the NiO surface. The increased hydroxyl surface concentration, and thereby improved 2PACz coverage, resulted in a significantly higher $V_{\text{oc}}^{\text{tandem}}$ of 1.78 V, approaching the sum of $V_{\text{oc}}^{\text{c-Si}}$ and $V_{\text{oc}}^{\text{perovskite}}$. A 1 cm^2 champion device with a stable PCE of 25.1% ($J_{\text{sc}} = 17.9\text{ mA cm}^{-2}$, $V_{\text{oc}} = 1.80\text{ V}$, and fill factor (FF) = 0.78) with minimal mismatch in J_{sc} between the two sub-cells (Figure 3.4e and Figure 3.4f) can therefore be prepared, aided by the ALD–NiO layer.

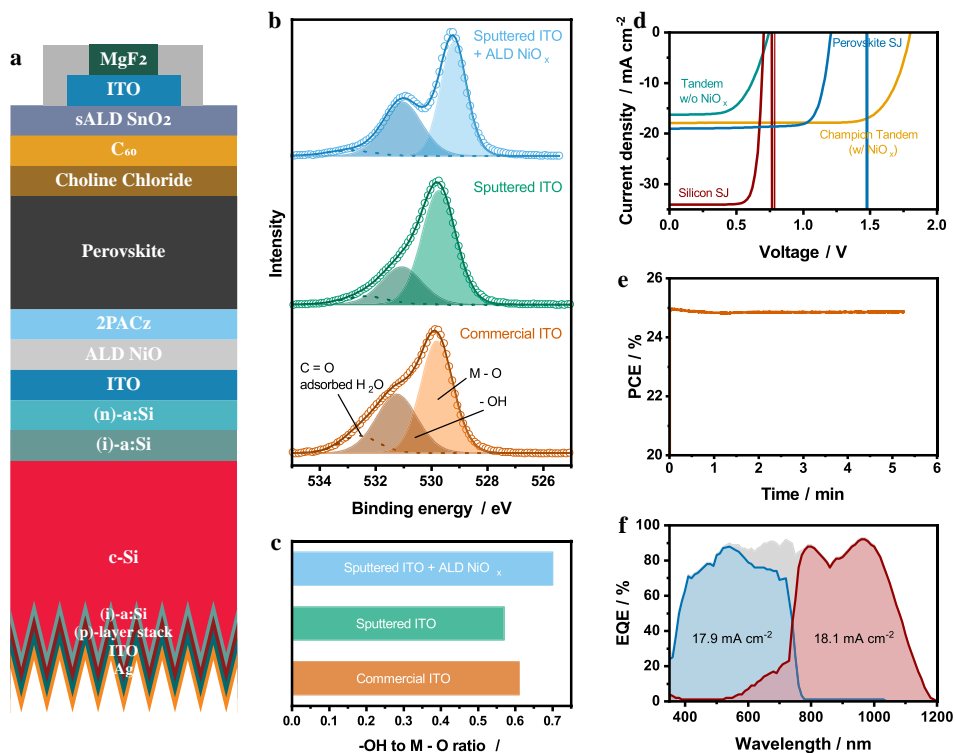


Figure 3.4: Monolithic perovskite–silicon tandem solar cell. a) Schematic of monolithic tandem device. b) X-ray photoelectron spectra (O1s) of commercial ITO, sputtered ITO, and sputtered ITO with an 8 nm–thick ALD–NiO interlayer. Spectral fits for metal oxide M–O and hydroxyl groups (–OH) are identified. c) –OH to M–O ratios derived from panel b). d) Current density versus voltage (J – V) curves of tandem solar cells without (w/o) or with (w/) ALD–NiO interlayer, and champion device. e) Maximum power point tracking data of perovskite–silicon tandem solar cell. f) External quantum efficiency (EQE) spectrum of perovskite–silicon tandem solar cell. The integrated J_{sc} for the perovskite (blue) and Silicon (red) sub-cells are indicated.

3.4. Light-driven water electrolysis

The electrochemical and photovoltaic cells were wire-connected into an integrated solar-assisted water splitting system. Here, the overlap between the polarization curve (EC) and current density versus voltage curve (PV) determines the operating point of the system (1.41 V and 17.5 mA) at 1-Sun equivalent light intensity (**Figure 3.5a**).^{20–23} The system was operated over 18 h of continuous illumination (**Figure 3.5b**), and subsequently simulating three 12 h diurnal cycles (**Figure 3.5c**). The system showed a stable output (STH) at the same potential as above (1.41 V) during 18 h of continuous illumination. The average output current of the solar cell was 18.0 mA, corresponding to a STH efficiency of 21.5% as calculated from Eq. 3.1. The solar-assisted water splitting system was also explored in multiple diurnal (12 h on-off) cycling.³¹ **Figure 3.5c** further shows stable current and potential during the 72 h measurement window with similar irradiation conditions, indicating that the system is able to operate through several day-night cycles without loss of performance.

Under these operating conditions, the system operated below the enthalpic potential for water splitting ($E_{\text{H}}^0 = 1.48$ V) and thus, the remaining energy (0.07 V) was provided by the water flowing in the electrochemical cell, cooling it. This water cooling could be especially useful for a scaled-up system, where heat integration is crucial. The water could possibly be used to cool down the solar cell, improving the stability of solar cell as it is known that solar cells tend to heat up under operation, inducing a loss of performance.^{32,33}

Additional considerations related to the area ratio of both components and the use of heated water to the electrolysis were also taken into account. The Tafel slope of the electrochemical system is 37.3 mV dec⁻¹ and the contact resistance is 369 mΩ cm². This would amount to about 27 mV increased potential if the area of the electrochemical and photovoltaic components were equal and increase the operating potential from 1.411 to 1.438 V and reduce the current from 17.5 to 17.3 mA cm⁻² (at 1-Sun intensity). This would lower the efficiency marginally from 21.5% to 21.3%. In the case of conducting water electrolysis at higher temperature, the STH would increase only to 21.6% as the operating current would increase to 17.6 mA cm⁻² (at 1-Sun intensity) while the potential would decrease to 1.359 V. It should be noted that this STH was calculated without considering the energy required to heat the water.

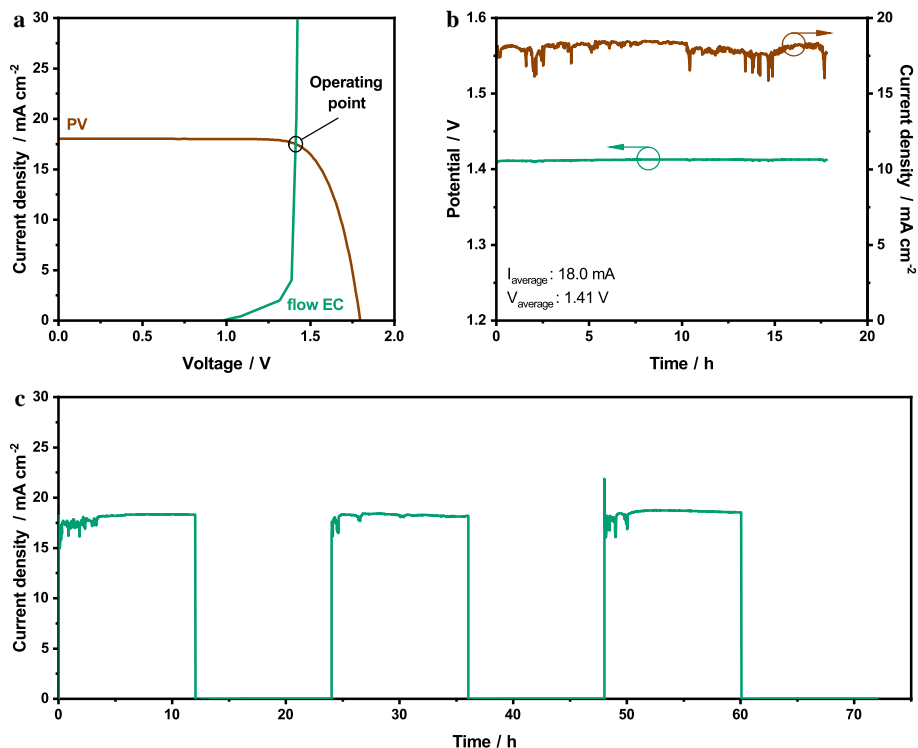


Figure 3.5: Continuous solar-assisted water splitting. a) Overlap of the J - V curve of the perovskite-silicon tandem solar cell with the polarization curve of the electrochemical flow cell. b) Solar-to-hydrogen conversion as a function of time using the integrated PV-EC system over 18 h continuous operation at approx. 1-Sun equivalent light intensity. c) Diurnal cycling of PV-EC system (12 h light and 12 h dark) for total 72 h at approx. 1-Sun equivalent light intensity. Fluctuations in the STH traces in panels b) and c) arise from fluctuations in lamp intensity during the operation.

Finally, the EC and PV units were characterized after the cumulative 90 h of operation. The polarization curve (EC) and current density versus voltage curves (PV) are nearly identical to the initial measurements (**Figure 3.6**), indicating that both systems retain their original performance, and that the operating potential of the integrated system remains unchanged. The shown stability is greater than most reports in literature with only a few reports showing system stabilities over 90 h.^{5,7,35-41,8,17,18,20-23,34} Nonetheless, the degradation of the individual components cannot be overlooked if the duration of the measurements is extended. For instance, some white spots arose on the perovskite/silicon tandem cell outside of the active area, suggesting some degradation has happened. It is thus reasonable to think that for longer measurement durations, these could affect the performance of the solar cell.

Efficient continuous light-driven water electrolysis using an electrochemical flow cell and a perovskite/silicon tandem solar cell

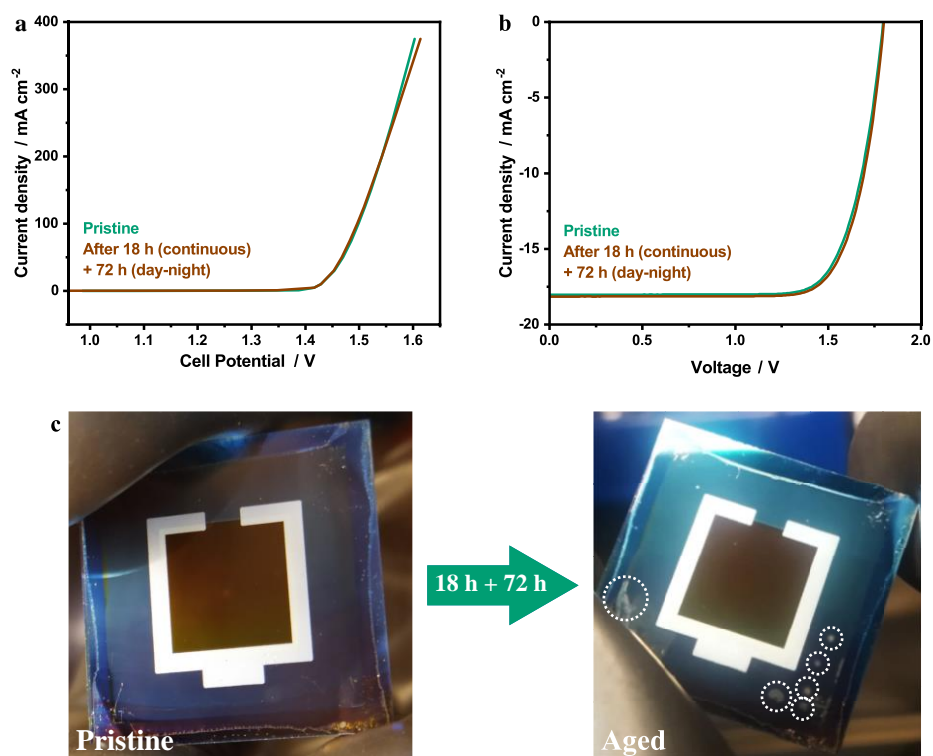


Figure 3.6: Stability of EC and PV systems. a) Polarization curve of electrochemical cell before and after 90 h of operation. b) J - V curves of perovskite-silicon tandem device before and after 90 h of operation. c) Photos of the perovskite-silicon tandem device before and after 90 h of operation.

3.5. Conclusion

This work describes an integrated solar-assisted water splitting system using a flow electrochemical cell and a monolithic perovskite-silicon tandem solar cell, delivering an STH of 21%. This STH is the highest reported for systems operating at approximately 1-Sun equivalent light intensity, and among the highest reported across a variety of combinations of EC and PV systems. Specifically, to the best of our knowledge, this work is the first to demonstrate an efficient flow electrochemical cell operated without any light concentration techniques. Light concentration techniques are typically employed for systems using flow electrochemical cells. However, in this work, this was not required as the monolithic perovskite-silicon tandem solar cell generates a high current (~18 mA) that allows the operation of the flow electrochemical cell at a stable operating potential over 1.4 V, which is close to the maximum power point of the solar cell. In addition, both the solar cell and the electrochemical cell maintained

their initial individual performances after 90 h of combined operation (continuous 18 h + intermittent 72 h), indicating excellent stability.

Despite the use of less abundant electrocatalysts, the high STH efficiency, the absence of light-concentration methods, and the use of low-cost monolithic perovskite-silicon tandem photovoltaics demonstrate a potential route to produce low-cost H₂.⁴² Moreover, optimizing the EC/PV area ratio can be beneficial in terms of material cost in practical applications while maintaining high STH. In this work, a reduction of the EC/PV area ratio from 4 to 1 would imply only a minor drop in STH (21.5% to 21.3%). Recent efforts to develop earth-abundant electrocatalytic materials for use in electrochemical cells can further be used to construct low-cost electrochemical systems, augmenting the economic viability of solar-assisted H₂ production.⁴³

3.6. Experimental section

Materials and membrane-electrode assembly preparation: All materials were used as received without purification. NafionTM membrane NRE-212 was purchased from Ion Power. Pt/C (40 wt%) was purchased from Sigma Aldrich. RuO₂ (anhydrous, 99.9%) and Nafion dispersion (D-521) were purchased from Alfa Aesar. RuO₂ was stored inside inert atmosphere. 2-propanol was purchased from Biosolve. All catalyst inks were prepared using water purified in Millipore system ($\rho > 18 \text{ M}\Omega \text{ cm}$).

The catalyst inks were prepared with 5 wt% solid content, with 3:1 ratio of catalyst to Nafion ionomer in a 2-propanol:water (4:1) mixture. For the RuO₂ ink, Nafion dispersion was first added, followed by 2-propanol:water. For the Pt/C ink, the catalyst power was first mixed with water to avoid combustion of the carbon particles and, subsequently, the Nafion dispersion and 2-propanol were sequentially added. The inks were ultrasonicated for at least 10 min prior to catalyst deposition. The catalyst inks were manually spray-coated using a pneumatic airbrush (Aerotec) through a stainless-steel mask with a $2 \times 2 \text{ cm}^2$ opening on opposite sides of the membrane until the target loadings of 1 and 2 mg cm⁻² for Pt and RuO₂ were reached, respectively. The catalyst loadings were calculated by weighing the membrane before and after spray coating. The deposition temperature was set to 85 °C to evaporate the solvent upon deposition and to avoid excessive membrane swelling.

Proton exchange membrane (PEM) electrochemical cell setup: Water electrolysis tests were carried out in an in-house built PEM-electrolyzer cell ($5 \times 5 \text{ cm}^2$) using high-impact polypropylene (PP) as end plates and titanium current collectors (1 mm thick) with machined parallel flow fields (1 mm wide, channel area: $2.25 \times 2.25 \text{ cm}^2$). Titanium fiber felt ($2.5 \times 2.5 \text{ cm}^2$, 0.2 – 0.3 mm, porosity: 53 – 56 %, from Fuel Cell Store) and carbon fiber non-woven fabric ($2.5 \times 2.5 \text{ cm}^2$, 255 μm , with MPL, H23 C2, from Quintech) were used as porous transport layers (PTL) at the anode and cathode, respectively. The MEA was pressed between the PTLs and the electrolyzer was sealed with PTFE ($5 \times 5 \text{ cm}^2$, 200 mm, from Polyflur) and closed using a compression force of 0.8 Nm. Polyimide film (50 μm , from Wu Xi Shun Xuan New Materials Co., Ltd) was used between the Ti PTL and the membrane to delimit the active area to 4 cm². Millipore purified water ($\rho > 18 \text{ M}\Omega \text{ cm}$) was circulated using a peristaltic pump (Masterflex® L/S® Digital Miniflex®) into both anodic and cathodic compartment at 10 mL min⁻¹. Independent water lines

Efficient continuous light-driven water electrolysis using an electrochemical flow cell and a perovskite/silicon tandem solar cell

and feeding bottles were used for each compartment. The water bottles were N₂-bubbled to prevent oxygen and hydrogen build-up.

Material and precursor solution preparation: All materials were used as received without purification and stored in inert atmosphere unless stated otherwise. [2-(9H-carbazol-9-yl)ethyl]phosphonic acid (> 98%), PbI₂ (> 99.99%), and PbBr₂ (> 98%) were purchased from TCI. Formamidinium iodide (FAI) (> 99.99%) and methylammonium bromide (MABr) (> 99.99%) were purchased from Greatcell Solar Materials. KI (ultra-dry, 99.998%) was purchased from Alfa Aesar. CsI (beads, 99.999%), choline chloride (> 99%), DMF (99.8%), DMSO (99.9%), 2-propanol, and anisole (99.7%) were purchased from Sigma Aldrich. C₆₀ (99.95%) was purchased from SES Research and bathocuproine (BCP, 99%) was purchased from Lumtec.

The 2PACz hole transport layer was dissolved in anhydrous ethanol at a concentration of 0.3 mg mL⁻¹ by sonication prior to use. To prepare the perovskite precursor solution, PbI₂ (691.5 mg mL⁻¹) and PbBr₂ (550.5 mg mL⁻¹) were each dissolved overnight at 60 °C in solvent mixtures containing DMF and DMSO in a volumetric ratio of 4:1. Stock solutions of CsI (389.7 mg mL⁻¹) in DMSO and KI (249.0 mg mL⁻¹) in DMF:DMSO (4:1 v/v) were prepared and stirred overnight at 60 °C. The solutions were cooled to room temperature, following which 936 μL PbI₂ was added to 199.9 mg FAI and 936 μL PbBr₂ was added to 133.1 mg MABr. The resulting solutions (FAPbI₃ and MAPbBr₃) were stirred at 60 °C for approx. 1 h and then cooled to room temperature. 752 μL FAPbI₃ and 200 μL MAPbBr₃ were mixed with 48 μL CsI and 48 μL KI; the resulting solution was stirred at 60 °C for approx. 1 h and cooled to room temperature prior to use. Choline chloride was dissolved in 2-propanol (1 mg mL⁻¹) and stirred overnight at 60 °C.

Single-junction solar cell preparation: Single-junction perovskite solar cells were prepared on glass/ITO substrates (Naranjo Substrates 15 – 17 Ω/sq.). The substrates were first cleaned in an ultrasonic bath of acetone, followed by scrubbing with sodium dodecyl sulphate (Acros, 99%) soap solution in deionized water, sonication in the soap solution, rinsing in deionized water, followed by sonication in 2-propanol. Prior to use, the substrates were exposed to UV-ozone treatment for 30 min after which they were transferred to a N₂-filled glovebox. 2PACz hole transport layer was spin-coated at 3000 rpm for 30 s, followed by thermal annealing at 100 °C for 10 min. The samples were allowed to cool down for 5 – 10 min following which the perovskite film was deposited by spin-coating 150 μL of the precursor at 4000 rpm (5 s to ramp to 4000 rpm) for 35 s. At approx. 25 s from the beginning of the spin-coating, 300 μL of anisole was cast onto the spinning substrate. The substrates were immediately annealed at 100 °C for 30 min. 20 nm C₆₀ and 8 nm BCP were sequentially evaporated at a rate of 0.5 Å s⁻¹ following which 100 nm Ag electrode was thermally evaporated.

Single-junction silicon heterojunction solar cells were prepared using 4-inch Topsis n-type double-side-flat float-zone (FZ) <100> c-Si wafers with a thickness of 280 ± 20 μm and a range of resistivity (3 ± 2 Ω cm). To prepare the single-side-textured substrates for solar cell fabrication, we deposited on one side of polished c-Si wafers with plasma-enhanced chemical vapor deposition (PECVD, Novellus Systems Inc.) grown SiN_x, which is etching-resilient to tetramethylammonium (TMAH) solution. After the texturing of the bare c-Si side that is not covered with SiN_x in diluted TMAH solution, wafers were dipped into buffered-HF (BHF) solution to remove the SiN_x. Then, wafers were cleaned through sequential dipping them in 99% room-temperature nitric acid, 69.5% 110 °C nitric acid and finally 0.55% hydrofluoric acid. The wafers were then loaded into a multi-chamber PECVD cluster tool (Elettrorava S.p.A.) for the depositions of (i) a-Si:H/(n) a-Si:H stack. After a short vacuum break, the wafers were inverted to deposit the (i) a-Si:H/(p)-layer stack ((p) nc-SiOx:H/(p) nc-Si:H).⁴⁴ Thereafter, RF sputtering of ITO

(Polyteknik AS) on the front (75 nm) and the rear sides (150 nm) of the solar cell was done with final depositions of Ag at both sides using screen printing.

Monolithic tandem solar cell fabrication: The SHJ bottom cell was prepared as described before, except that one face of the solar cell (that eventually consists of the (i) a-Si:H/(n) a-Si:H stack) was covered only by 30 nm-thick ITO recombination layer, while the rear side was finished with thermally evaporated Ag. The wafers were diced to 2.5 cm × 2.5 cm sized samples prior to deposition of the perovskite top-cell. Where mentioned, approx. 8 nm NiO was deposited using thermal atomic layer deposition on the ITO recombination layer (30 nm). The deposition was done at a base pressure of 5×10^{-6} mbar in a home-built reactor using nickel bis(*N,N'*-di-*tert*-butylacetamidinate) ($\text{Ni}(\text{tBu-MeAMD})_2$) as the nickel source and water as the co-reactant. The precursor bubbler was maintained at 90 °C and Ar flow was used for bubbling. The substrate temperature approaches 150 °C during the deposition. 2PACz, perovskite, choline chloride, and C_{60} layers were deposited as described before. Following that, spatial atomic layer deposition (sALD) was used to deposit a SnO_2 (20 nm) buffer layer as described previously.⁴⁵ Tetrakis(dimethylamino)tin(IV) was used as the tin source and water as the co-reactant. A nitrogen curtain was used to isolate the two half-reaction steps. A 180 nm-thick ITO layer was deposited using RF sputtering process at a rate of 0.3 \AA s^{-1} . Finally, a 100 nm-thick Ag perimeter contact, and a 120 nm-thick MgF_2 anti-reflective coating were thermally evaporated to complete the tandem device.

Electrochemical Characterization: Galvanostatic polarization curves and steady-state stability were performed using a 2-channel Keithley 2600 SMU controlled by LabVIEW. The first channel was used to apply the current whereas the second channel was used to measure the voltage across the PEM electrochemical cell. Electrochemical impedance spectroscopy (EIS) was performed using a potentiostat PGSTAT30 (Autolab) equipped with a frequency analyzer (FRA) module. All measurements were done at room temperature. Water was circulated through the cell for 1 h to allow membrane swelling and equilibration prior to any measurements. The cell was conditioned by applying 10, 20, 50 and 100 mA cm^{-2} for 30 s and then 250 mA cm^{-2} for 30 min, followed by EIS with a frequency of 10 kHz – 1 Hz at 10, 50 and 100 mA cm^{-2} to determine the contact resistance, R_Ω . The galvanostatic polarization curve was recorded from 0.01 to 375 mA cm^{-2} . Each current density step was held for 2 min (5 min for steps < 1 mA cm^{-2} for the 90 h polarization curve) to allow potential stabilization and the average of the last 10 s was taken as the potential value.

Gas chromatography was carried out by a compact gas chromatograph CGC 4.0 (Global Analyzer Solutions–Interscience B.V.) controlled by Chromeleon 7 software (Thermo Fischer Scientific). A EL-FLOW Prestige mass flow controller (Bronkhorst Nederland) was used to control the nitrogen flow ($F_{\text{N}_2} = 135 \text{ mL min}^{-1}$) through the cathode water feeding bottle where the outlet was connected to the CGC 4.0. Once every 3.8 min, a sample is taken into the gas chromatograph for analysis. A thermal conductivity detector (TCD) was used to measure the H_2 content of the flowing gas. The gas chromatograph was calibrated at 3 points using calibration bottles with 5, 100, and 1000 ppm of hydrogen in a nitrogen balance. The faradaic efficiency was calculated using the following equation:

$$\eta_{\text{far}} = \frac{\int_0^t \frac{C_{\text{H}_2} F_{\text{N}_2}}{10^6 - C_{\text{H}_2}} dt}{60It} \quad (3.2)$$

$$\frac{2000F}{2000F}$$

Efficient continuous light-driven water electrolysis using an electrochemical flow cell and a perovskite/silicon tandem solar cell

where C_{H_2} is the concentration of H_2 measured with CGC 4.0 in ppm, I is the applied current in mA, F is the Faraday constant (96485 C mol^{-1}) and t is total time of the analysis in min.

Scanning electron microscopy was carried out using a Phenom ProX desktop SEM at an acceleration voltage of 15 kV. The MEA was embedded in epoxy resin (Epofix Cold-setting Embedding resin, Electron Microscopy Sciences) for 24 h before being cryo-fractured in liquid nitrogen.

Solar cell characterization: Current density versus voltage scans of the perovskite single-junction solar cell (electrode overlap area 0.16 cm^2) were done using a tungsten-halogen illumination source filtered by a UV filter (Schott GG385) and a daylight filter (Hoya LB120) with intensity adjusted to 100 mW cm^{-2} . A shadow mask with an aperture area 0.1296 cm^2 was used. For the tandem solar cell, a 1 cm^2 shadow mask was used. The solar cells were operated under reverse or forward sweeps (between $+1.5 \text{ V}$ and -0.5 V for single-junction perovskite solar cell, and between $+2.0 \text{ V}$ and -0.5 V for tandem solar cell) at a rate of 0.25 V s^{-1} using a Keithley 2400 source meter. The silicon single-junction solar cell was measured using a AAA class WACOM WXS-90S-L2 solar simulator using standard test conditions.

External quantum efficiency (EQE) measurements of the perovskite single-junction and perovskite-silicon tandem solar cell were done using a modulated monochromatic probe light (Philips focusline, 50 W) through a 1 mm radius aperture. The response was recorded and converted to EQE using a calibrated silicon reference cell. EQE of the silicon single-junction solar cell (without the front metal grid) was measured using an in-house developed setup. For the perovskite-silicon tandem solar cell, light- and voltage-biasing was used to isolate the EQE of the individual sub-cells; 530 nm (perovskite) or 940 nm (silicon) bias light and a forward bias close to the open-circuit voltage of the single-junction solar cell was used.

X-ray photoelectron spectroscopy was conducted using a Thermo Scientific KA1066 spectrometer. The excitation source was monochromatic Al $K\alpha$ (1486.6 eV) X-rays. The measurements were done without any pre-sputtering and the layers were in contact with air briefly during the loading. A gold clamp and an electron flood gun were used to reduce sample charging. The data were analyzed using commercial software Avantage with Shirley background subtraction. To avoid possible peak shifts due to charging, the binding energies of the XPS spectra were corrected by setting the maximum of the adventitious carbon peak in the $C1s$ spectrum to 284.4 eV .

Solar water splitting experiments: Solar water splitting was performed using a homebuilt solar simulator with a tungsten-halogen illumination source filtered by a UV filter (Schott GG385) and a daylight filter (Hoya LB120) with intensity adjusted to obtain the operating point current at approx. 1-Sun equivalent light intensity. The resulting irradiance, P_{in} , was calculated from:

$$P_{in} = \frac{I_{op}}{I_{op,1-sun}} P_{in,1-Sun} \quad (3.3)$$

where I_{op} is the average operating current of the solar assisted water splitting system (18.0 mA), $I_{op,1-Sun}$ the operating point current (17.5 mA) and $P_{in,1-Sun}$ the irradiance at 1-Sun equivalent light intensity of the AM1.5G solar irradiance (100 mW cm^{-2}).

All experiments took place outside the glove-box environment, and for that reason, the solar cell was kept inside a N_2 -filled box and connected to the PEM electrochemical cell via external cabling. A Keithley 2600 SMU controlled by code written in the LabVIEW environment

was used for simultaneous measurement of the current and the voltage across the electrochemical cell. Diurnal cycling experiments were carried by using a programmable time electric plug (Theben) to switch the lamp on and off every 12 h.

3.7. References

1. DOE Technical Targets for Hydrogen Production from Photoelectrochemical Water Splitting. <https://www.energy.gov/eere/fuelcells/doe-technical-targets-hydrogen-production-photoelectrochemical-water-splitting>. (Accessed on October 2nd, 2022)
2. Walter, M. G., Warren, E. L., McKone, J. R., Boettcher, S. W., Mi, Q., Santori, E. A. & Lewis, N. S. Solar water splitting cells. *Chem. Rev.* **110**, 6446–6473 (2010).
3. Godula-Jopek, A. *Hydrogen Production: by Electrolysis*. (Wiley-VCH Verlag GmbH & Co., 2015).
4. Koper, M. T. M. Thermodynamic theory of multi-electron transfer reactions: Implications for electrocatalysis. *J. Electroanal. Chem.* **660**, 254–260 (2011).
5. Rau, S., Vierrath, S., Ohlmann, J., Fallisch, A., Lackner, D., Dimroth, F. & Smolinka, T. Highly Efficient Solar Hydrogen Generation—An Integrated Concept Joining III-V Solar Cells with PEM Electrolysis Cells. *Energy Technol.* **2**, 43–53 (2014).
6. Nakamura, A., Ota, Y., Koike, K., Hidaka, Y., Nishioka, K., Sugiyama, M. & Fujii, K. A 24.4% solar to hydrogen energy conversion efficiency by combining concentrator photovoltaic modules and electrochemical cells. *Appl. Phys. Express* **8**, 107101 (2015).
7. Jia, J., Seitz, L. C., Benck, J. D., Huo, Y., Chen, Y., Ng, J. W. D., Bilir, T., Harris, J. S. & Jaramillo, T. F. Solar water splitting by photovoltaic-electrolysis with a solar-to-hydrogen efficiency over 30%. *Nat. Commun.* **7**, 13237 (2016).
8. Kuang, Y., Kenney, M. J., Meng, Y., Hung, W. H., Liu, Y., Huang, J. E., Prasanna, R., Li, P., Li, Y., Wang, L., Lin, M. C., McGehee, M. D., Sun, X. & Dai, H. Solar-driven, highly sustained splitting of seawater into hydrogen and oxygen fuels. *Proc. Natl. Acad. Sci. U. S. A.* **116**, 6624–6629 (2019).
9. Luo, J., Im, J. H., Mayer, M. T., Schreier, M., Nazeeruddin, M. K., Park, N. G., Tilley, S. D., Fan, H. J. & Grätzel, M. Water photolysis at 12.3% efficiency via perovskite photovoltaics and Earth-abundant catalysts. *Science*. **345**, 1593–1596 (2014).
10. Min, H., Lee, D. Y., Kim, J., Kim, G., Lee, K. S., Kim, J., Paik, M. J., Kim, Y. K., Kim, K. S., Kim, M. G., Shin, T. J. & Il Seok, S. Perovskite solar cells with atomically coherent interlayers on SnO₂ electrodes. *Nature* **598**, 444–450 (2021).
11. Masi, S., Gualdrón-Reyes, A. F. & Mora-Seró, I. Stabilization of Black Perovskite Phase in FAPbI₃ and CsPbI₃. *ACS Energy Lett.* **5**, 1974–1985 (2020).
12. Green, M. A. & Bremner, S. P. Energy conversion approaches and materials for high-efficiency photovoltaics. *Nat. Mater.* **16**, 23–34 (2017).
13. Martí, A. & Araújo, G. L. Limiting efficiencies for photovoltaic energy conversion in multigap systems. *Sol. Energy Mater. Sol. Cells* **43**, 203–222 (1996).
14. Di Carlo Rasi, D. & Janssen, R. A. J. Advances in Solution-Processed Multijunction Organic Solar Cells. *Adv. Mater.* **31**, 1806499 (2019).

Efficient continuous light-driven water electrolysis using an electrochemical flow cell and a perovskite/silicon tandem solar cell

15. Datta, K. Mixed-Halide Perovskite Semiconductors for Multijunction Photovoltaics. (Eindhoven University of Technology, 2022).
16. New world records: perovskite-on-silicon-tandem solar cells. <https://actu.epfl.ch/news/new-world-records-perovskite-on-silicon-tandem-sol/> (2022). (Accessed on October 11th, 2022)
17. Park, H., Park, I. J., Lee, M. G., Kwon, K. C., Hong, S.-P., Kim, D. H., Lee, S. A., Lee, T. H., Kim, C., Moon, C. W., Son, D.-Y., Jung, G. H., Yang, H. S., Lee, J. R., Lee, J., Park, N.-G., Kim, S. Y., Kim, J. Y. & Jang, H. W. Water Splitting Exceeding 17% Solar-to-Hydrogen Conversion Efficiency Using Solution-Processed Ni-Based Electrocatalysts and Perovskite/Si Tandem Solar Cell. *ACS Appl. Mater. Interfaces* **11**, 33835–33843 (2019).
18. Gao, J., Sahli, F., Liu, C., Ren, D., Guo, X., Werner, J., Jeangros, Q., Zakeeruddin, S. M., Ballif, C., Grätzel, M. & Luo, J. Solar Water Splitting with Perovskite/Silicon Tandem Cell and TiC-Supported Pt Nanocluster Electrocatalyst. *Joule* **3**, 2930–2941 (2019).
19. Pan, S., Li, R., Zhang, Q., Cui, C., Wang, M., Shi, B., Wang, P., Zhang, C., Zhang, B., Zhao, Y. & Zhang, X. An over 20% solar-to-hydrogen efficiency system comprising a self-reconstructed NiCoFe-based hydroxide nanosheet electrocatalyst and monolithic perovskite/silicon tandem solar cell. *J. Mater. Chem. A* **9**, 14085–14092 (2021).
20. Chen, H., Song, L., Ouyang, S., Wang, J., Lv, J. & Ye, J. Co and Fe Codoped WO_{2.72} as Alkaline-Solution-Available Oxygen Evolution Reaction Catalyst to Construct Photovoltaic Water Splitting System with Solar-To-Hydrogen Efficiency of 16.9%. *Adv. Sci.* **6**, 1900465 (2019).
21. Lee, M., Turan, B., Becker, J. P., Welter, K., Klingebiel, B., Neumann, E., Sohn, Y. J., Merdzhanova, T., Kirchartz, T., Finger, F., Rau, U. & Haas, S. A Bias-Free, Stand-Alone, and Scalable Photovoltaic–Electrochemical Device for Solar Hydrogen Production. *Adv. Sustain. Syst.* **4**, 2000070 (2020).
22. Li, Z., Wu, S., Zhang, J., Lee, K. C., Lei, H., Lin, F., Wang, Z., Zhu, Z. & Jen, A. K. Y. Y. Hybrid Perovskite–Organic Flexible Tandem Solar Cell Enabling Highly Efficient Electrocatalysis Overall Water Splitting. *Adv. Energy Mater.* **10**, 2000361 (2020).
23. Wang, Y., Sharma, A., Duong, T., Arandiyani, H., Zhao, T., Zhang, D., Su, Z., Garbrecht, M., Beck, F. J., Karuturi, S., Zhao, C. & Catchpole, K. Direct Solar Hydrogen Generation at 20% Efficiency Using Low-Cost Materials. *Adv. Energy Mater.* **11**, 2101053 (2021).
24. Song, S., Zhang, H., Ma, X., Shao, Z., Baker, R. T. & Yi, B. Electrochemical investigation of electrocatalysts for the oxygen evolution reaction in PEM water electrolyzers. *Int. J. Hydrogen Energy* **33**, 4955–4961 (2008).
25. Cherevko, S., Geiger, S., Kasian, O., Kulyk, N., Grote, J.-P., Savan, A., Shrestha, B. R., Merzlikin, S., Breitbach, B., Ludwig, A. & Mayrhofer, K. J. J. Oxygen and hydrogen evolution reactions on Ru, RuO₂, Ir, and IrO₂ thin film electrodes in acidic and alkaline electrolytes: A comparative study on activity and stability. *Catal. Today* **262**, 170–180 (2016).
26. Zheng, X., Chen, B., Dai, J., Fang, Y., Bai, Y., Lin, Y., Wei, H., Zeng, X. C. & Huang, J. Defect passivation in hybrid perovskite solar cells using quaternary ammonium halide anions and cations. *Nat. Energy* **2**, 17102 (2017).
27. Datta, K., Wang, J., Zhang, D., Zardetto, V., Remmerswaal, W. H. M. M., Weijtens, C. H. L. L., Wienk, M. M. & Janssen, R. A. J. Monolithic All-Perovskite Tandem Solar Cells

- with Minimized Optical and Energetic Losses. *Adv. Mater.* **34**, 2110053 (2022).
28. Liu, Y., Li, Y., Wu, Y., Yang, G., Mazzarella, L., Procel-Moya, P., Tamboli, A. C., Weber, K., Boccard, M., Isabella, O., Yang, X. & Sun, B. High-Efficiency Silicon Heterojunction Solar Cells: Materials, Devices and Applications. *Mater. Sci. Eng. R Reports* **142**, 100579 (2020).
 29. Al-Ashouri, A., Magomedov, A., Roß, M., Jošt, M., Talaikis, M., Chistiakova, G., Bertram, T., Márquez, J. A., Köhnen, E., Kasparavičius, E., Levenco, S., Gil-Escrig, L., Hages, C. J., Schlattmann, R., Rech, B., Malinauskas, T., Unold, T., Kaufmann, C. A., Korte, L., *et al.* Conformal monolayer contacts with lossless interfaces for perovskite single junction and monolithic tandem solar cells. *Energy Environ. Sci.* **12**, 3356–3369 (2019).
 30. Phung, N., Verheijen, M., Todinova, A., Datta, K., Verhage, M., Al-Ashouri, A., Köbler, H., Li, X., Abate, A., Albrecht, S. & Creatore, M. Enhanced Self-Assembled Monolayer Surface Coverage by ALD NiO in p-i-n Perovskite Solar Cells. *ACS Appl. Mater. Interfaces* **14**, 2166–2176 (2022).
 31. Bonke, S. A., Wiechen, M., MacFarlane, D. R. & Spiccia, L. Renewable fuels from concentrated solar power: towards practical artificial photosynthesis. *Energy Environ. Sci.* **8**, 2791–2796 (2015).
 32. Temburne, S., Nandjou, F. & Haussener, S. A thermally synergistic photo-electrochemical hydrogen generator operating under concentrated solar irradiation. *Nat. Energy* **4**, 399–407 (2019).
 33. Poudel, S., Zou, A. & Maroo, S. C. Thermal Management of Photovoltaics Using Porous Nanochannels. *Energy & Fuels* **36**, 4549–4556 (2022).
 34. Esiner, S., Willems, R. E. M. M., Furlan, A., Li, W., Wienk, M. M. & Janssen, R. A. J. Photoelectrochemical water splitting in an organic artificial leaf. *J. Mater. Chem. A* **3**, 23936–23945 (2015).
 35. Cox, C. R., Lee, J. Z., Nocera, D. G. & Buonassisi, T. Ten-percent solar-to-fuel conversion with nonprecious materials. *Proc. Natl. Acad. Sci.* **111**, 14057–14061 (2014).
 36. Schüttauf, J.-W., Modestino, M. A., Chinello, E., Lambelet, D., Delfino, A., Dominé, D., Faes, A., Despeisse, M., Bailat, J., Psaltis, D., Moser, C. & Ballif, C. Solar-to-Hydrogen Production at 14.2% Efficiency with Silicon Photovoltaics and Earth-Abundant Electrocatalysts. *J. Electrochem. Soc.* **163**, F1177–F1181 (2016).
 37. Hsu, S.-H., Miao, J., Zhang, L., Gao, J., Wang, H., Tao, H., Hung, S.-F., Vasileff, A., Qiao, S. Z. & Liu, B. An Earth-Abundant Catalyst-Based Seawater Photoelectrolysis System with 17.9% Solar-to-Hydrogen Efficiency. *Adv. Mater.* **30**, 1707261 (2018).
 38. Karuturi, S. K., Shen, H., Sharma, A., Beck, F. J., Varadhan, P., Duong, T., Narangari, P. R., Zhang, D., Wan, Y., He, J., Tan, H. H., Jagadish, C. & Catchpole, K. Over 17% Efficiency Stand-Alone Solar Water Splitting Enabled by Perovskite-Silicon Tandem Absorbers. *Adv. Energy Mater.* **10**, 2000772 (2020).
 39. Young, J. L., Steiner, M. A., Döscher, H., France, R. M., Turner, J. A. & Deutsch, T. G. Direct solar-to-hydrogen conversion via inverted metamorphic multi-junction semiconductor architectures. *Nat. Energy* **2**, 17028 (2017).
 40. Verlage, E., Hu, S., Liu, R., Jones, R. J. R. R., Sun, K., Xiang, C., Lewis, N. S. & Atwater,

Efficient continuous light-driven water electrolysis using an electrochemical flow cell and a perovskite/silicon tandem solar cell

- H. A. A monolithically integrated, intrinsically safe, 10% efficient, solar-driven water-splitting system based on active, stable earth-abundant electrocatalysts in conjunction with tandem III–V light absorbers protected by amorphous TiO₂ films. *Energy Environ. Sci.* **8**, 3166–3172 (2015).
41. Shi, Y., Hsieh, T.-Y. Y., Hoque, M. A., Cambarau, W., Narbey, S., Gimbert-Surināch, C., Palomares, E., Lanza, M., Llobet, A., Gimbert-Suriñach, C., Palomares, E., Lanza, M. & Llobet, A. High Solar-to-Hydrogen Conversion Efficiency at pH 7 Based on a PV-EC Cell with an Oligomeric Molecular Anode. *ACS Appl. Mater. Interfaces* **12**, 55856–55864 (2020).
42. Messmer, C., Goraya, B. S., Nold, S., Schulze, P. S. C., Sittinger, V., Schön, J., Goldschmidt, J. C., Bivour, M., Glunz, S. W. & Hermle, M. The race for the best silicon bottom cell: Efficiency and cost evaluation of perovskite–silicon tandem solar cells. *Prog. Photovoltaics Res. Appl.* **29**, 744–759 (2021).
43. Roger, I., Shipman, M. A. & Symes, M. D. Earth-abundant catalysts for electrochemical and photoelectrochemical water splitting. *Nat. Rev. Chem.* **1**, 0003 (2017).
44. Zhao, Y., Procel, P., Han, C., Mazzarella, L., Yang, G., Weeber, A., Zeman, M. & Isabella, O. Design and optimization of hole collectors based on nc-SiO_x:H for high-efficiency silicon heterojunction solar cells. *Sol. Energy Mater. Sol. Cells* **219**, 110779 (2021).
45. Wang, J., Zardetto, V., Datta, K., Zhang, D., Wienk, M. M. & Janssen, R. A. J. 16.8% Monolithic all-perovskite triple-junction solar cells via a universal two-step solution process. *Nat. Commun.* **11**, 5254 (2020).

Chapter 4

All-perovskite tandem solar cells for solar-driven water electrolysis

Abstract

All-perovskite tandem solar cells represent a promising cost-effective route to achieve high efficiency photovoltaics. Additionally, the large V_{oc} provided by such cells potentially enables the use of less efficient catalysts in a water electrolysis without a major solar-to-hydrogen efficiency (STH) loss. In this chapter, the scale up of an all-perovskite tandem solar cell is demonstrated from 0.09 to 1 cm² active area without efficiency loss. This allows it to be coupled with a continuous electrochemical flow cell and achieve an initial STH of 18.6%. This represents the first time that such system is demonstrated. To potentially increase the efficiency of all-perovskite tandem solar cells and the STH of the coupled system, an one-step deposition procedure for the narrow-bandgap perovskite sub-cell was adopted and optimized. This optimization involved testing different bulk additives and top surface treatments, which allowed to reach a maximum power conversion efficiency (PCE) of 18.6%, a 3.1% increase over the previous procedure. This optimization combined with further improvements on the wide-bandgap sub-cell might elevate the PCE of all-perovskite tandems to above 26% and STH to almost 20%.

The wide-bandgap perovskite single-junction and sub-cell were fabricated by Kunal Datta, PhD.

4.1. Introduction

Monolithic all-perovskite tandem solar cells can potentially provide a cost-effective route for high power conversion efficiency (PCE) photovoltaics. In contrast to the c-Si/perovskite tandem described in chapter 3, in all-perovskite tandem cells, both photoabsorbers are easily processed as thin films by a variety of solution-based processes, conformal coating techniques such as co-evaporation, or a combination of both. Most of these processes are easily scalable, inexpensive and, in addition, are suitable for flexible substrates, opening a wide range of applications, e.g. building integrated systems or wearables, that cannot be made with the commonly used rigid c-Si.¹⁻³

Metal halide perovskite semiconductors are notably suitable for multijunction photovoltaic applications due to their bandgap engineering done by tuning the perovskite composition. For instance, mixed lead-tin (Pb-Sn) perovskites have shown bandgaps of 1.2–1.6 eV, depending on the Pb/Sn ratio. Similarly, in mixed-halide lead perovskites, by tuning the ratio of iodide to bromide (I/Br ratio), bandgaps in the 1.5–2.4 eV range are attainable.^{4,5} All-perovskite tandems commonly combine a wide-bandgap mixed-halide lead perovskite (~ 1.8 eV) with a narrow-bandgap Pb-Sn perovskite (1.2–1.5 eV) solar cells, resulting in open-circuit voltages (V_{oc}) of about ~2 V.⁶ The higher V_{oc} compared to c-Si/perovskite is followed by a shift in the maximum power point potential (V_{mpp}) to higher voltages as well, which enables a wider range of materials to be used as catalysts in a coupled water electrolysis cell. For example, earth abundant catalysts that have associated larger overpotentials will evidently push the water electrolysis to higher potentials. By using an all-perovskite tandem, the expected operating potential of a solar water electrolysis system can still be below the V_{mpp} , where the operating current (I_{op}) is still close to the short-circuit current (I_{sc}) of the tandem solar cell, maximizing the solar-to-hydrogen (STH) given by **Eq. 4.1**.

$$STH = \frac{1.23 I_{op} \eta_{far}}{A_{sc} P_{in}} \times 100 \quad (4.1)$$

where η_{far} is the (dimensionless) faradaic efficiency, A_{sc} the solar cell area in m^2 , and P_{in} the irradiance in $W m^{-2}$.

When using an all-perovskite tandem solar cell, the expected STH will be obviously lower than of c-Si/perovskite tandem, simply because the current density output is lower. Nonetheless, $STH > 20\%$ can be a reality.⁷ Despite the advantages of all-perovskite tandem solar cells, so far, no study has reported their use in solar-driven water electrolysis (Figure 1.4, chapter 1). Work involving

perovskite-based photovoltaic components commonly use c-Si/perovskite tandems (described in chapter 3) or several perovskite single-junctions connected in series instead. The complexity of making a monolithic all-perovskite tandem solar cell that has at least 14 different layers, especially with high PCE, might be one of the few reasons for the lack of use in solar-driven water electrolysis.

Mixed Pb-Sn perovskites are the most commonly used narrow-bandgap perovskite for tandem applications. However, such Pb-Sn perovskite have been considered the limiting factor in the development of all-perovskite tandem cells, due to issues related to its heterogeneous nucleation, fast crystallization, and readily oxidation of Sn^{2+} to Sn^{4+} .⁸⁻¹⁰ Precursor engineering has been one of the main strategies to overcome these issues. For example, the use of reducing agents and antioxidants, such as SnF_2 and metallic Sn powder, have been explored to suppress such oxidation events and hence, also reduce the associated defect density. Thiocyanate salts are also commonly used to control crystal growth, enabling more homogeneous films and less defective grain surfaces.^{8,9,11} Another promising class of molecules that has resulted in improved performance are zwitterionic salts. The double functionality of such salts is reportedly able to passivate both electron-donating (e.g. formamidinium or methylammonium vacancies) as well as electron-accepting defects (e.g. halide vacancies) on the film.^{7,8,11} Post-treatments of the film surface are often used to decrease surface defects and enhance the perovskite/charge collection layer, resulting in lower non-radiative losses at that interface.¹¹⁻¹³ Highly efficiency narrow-bandgap Pb-Sn perovskite (PCE > 20%) are typically obtained by a combination of these strategies and, often, the precursor solution contains several of the mentioned salts and molecules. Recently, a record efficiency of 23.6% was reported by Hu et al. when they added SnF_2 , NH_4SCN , and glycine hydrochloride (GlyHCl) in the precursor solution and surface treated the perovskite films with ethylenediammonium diiodide (EDAI_2).¹¹

In this chapter, the use of an all-perovskite tandem solar cell to power a water electrolysis flow cell is described for the first time. This system reached an initial STH of 18.6%. Further work involved the development of large area tandem cells (1 cm^2) to ensure an appropriate operating point with the water electrolysis cell and the optimization of a one-step procedure for narrow-bandgap perovskite processing.

4.2. All-perovskite tandem solar cells: 1 cm^2 active area

The monolithic all-perovskite tandem solar cell (SC) (**Figure 4.1a**) was based on the work developed by Datta et al.¹⁴ Briefly, the wide-bandgap (WBG) mixed halide lead perovskite top-cell ($E_g \sim 1.77 \text{ eV}$) was fabricated using a self-

assembled monolayer (SAM) that consists of [2-(9*H*-carbazol-9-yl)ethyl]phosphonic acid (2PACz) as hole-transport layer (HTL) and a thermally evaporated C₆₀ layer as electron-transport layer. The SAM was deposited on hydrogenated indium oxide (IOH). IOH was chosen as transparent conductive oxide (TCO) instead of the common indium tin oxide (ITO) as the former is more transparent in the near infrared region, enhancing the photocurrent of the narrow-bandgap (NBG) sub-cell. Furthermore, choline chloride was used on top of the wide-bandgap perovskite layer to reduce V_{oc} losses by improving the perovskite/C₆₀ interface.^{14,15} Subsequently, a SnO₂ layer was deposited by atomic layer deposition to complete the electron transport stack but also, to function as an impermeable layer enabling the processing of the NBG perovskite sub-cell via solution processing. For the intermediate contact layer (ICL) that connects both sub-cells, electrically and optically, a 1 nm layer of gold (Au) that was thermally evaporated, followed by a 20 nm layer of poly(3,4-ethylenedioxythiophene):polystyrene sulfonate (PEDOT:PSS) as HTL for the NBG sub-cell.

The narrow-bandgap ($E_g \sim 1.23$ eV) mixed Pb-Sn perovskite (FA_{0.66}MA_{0.34}Pb_{0.5}Sn_{0.5}I₃) layer was prepared using a two-step solution process where an inorganic precursor solution consisting of SnI₂, PbI₂, and SnF₂ is firstly deposited on the HTL, dried at room temperature and then treated with a FAI/MAI (where FA is formamidinium and MA is methyl ammonium) solution and immediately annealed to obtain a polycrystalline film. The perovskite layer is then treated with a CdI₂ solution to passivate the perovskite/C₆₀ interface. Datta et al. found that CdI₂ did not significantly affect the crystallinity, morphology, and energy-level diagram, but the presence of Cd and higher iodide concentration helped to reduce atomic vacancies at the perovskite film surface, resulting in a reduction of non-radiative recombination losses.^{14,16} The all-perovskite tandem cells were completed with thermally evaporated layers of C₆₀ and bathocuproine (BCP) as ETL and silver as back electrode.

For a successful integration of an all-perovskite tandem solar cell with an electrochemical flow cell, the current and voltage outputs of the two components must match. The tandem cells described above have an active area of 0.09 cm² with the champion device reaching a J_{sc} of 15.8 mA cm⁻² (PCE = 23.1%, V_{oc} = 1.95 V, and FF = 0.75). Thus, the I_{sc} ($I_{sc} = A \times J_{sc}$) is 1.422 mA and is considerably lower than the current output of the flow electrochemical cell as seen in chapter 3. A new cell layout (Figure 4.1b) was designed with an active area of 1 cm² (with mask) to increase the current output of the all-perovskite tandem solar cells.

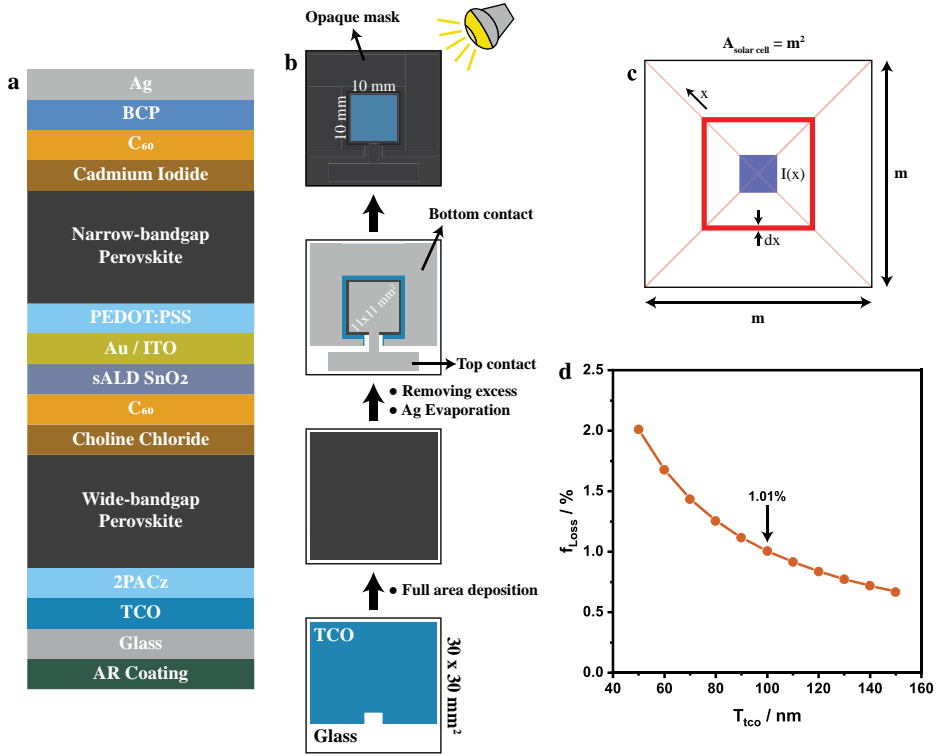


Figure 4.1: Monolithic all-perovskite tandem solar cell. a) Schematic of the monolithic tandem device. b) Large area (1 cm^2) solar cell layout. c) Schematic used for TCO resistance calculation. d) Power loss (f_{loss}) dependence on the IOH thickness for a $m^2 = 1 \text{ cm}^2$ cell. Arrow points to the f_{loss} value at 100 nm of IOH.

In larger area devices, the increasing TCO resistance may lead to a drop mainly in FF, limiting the cell performance.⁸ Hence, for the device layout shown in Figure 4.1b, the PCE loss (f_{loss}) due to the TCO was calculated following Eq. 4.2 – 4.6 according to Figure 4.1c:

$$I(x) = J_{\text{mpp}} A(x) = J_{\text{mpp}} (2x \sin 45^\circ)^2 = 2J_{\text{mpp}} x^2 \quad (4.2)$$

$$R_{\text{tco}}(x) = \frac{\rho_{\text{tco}}}{8T_{\text{tco}} x \sin 45^\circ} dx = \frac{\rho_{\text{tco}}}{4\sqrt{2}T_{\text{tco}} x} dx \quad (4.3)$$

$$P_{\text{tco}}(x) = \frac{I(x)^2 R_{\text{tco}}(x)}{1000} = \frac{J_{\text{mpp}}^2 x^3 \rho_{\text{tco}}}{4000\sqrt{2}T_{\text{tco}}} dx \quad (4.4)$$

$$P_{\text{tco, total}} = \int_0^{\frac{m}{2 \cos 45^\circ}} \frac{J_{\text{mpp}}^2 x^3 \rho_{\text{tco}}}{4000\sqrt{2}T_{\text{tco}}} dx = \frac{J_{\text{mpp}}^2 m^4 \rho_{\text{tco}}}{16000\sqrt{2}T_{\text{tco}}} \quad (4.5)$$

$$f_{\text{loss}} = \frac{P_{\text{tco,total}}}{P_{\text{mpp}}} \times 100 \quad (4.6)$$

where I is the current in mA, J the current density in mA cm⁻², A the active area in cm², R_{tco} the differential TCO resistance in Ω , ρ_{tco} the TCO resistivity in Ω cm, T_{tco} the TCO thickness in cm, P_{tco} and $P_{\text{tco,total}}$ are the differential and total power loss in mW, respectively. Using $J_{\text{mpp}} = 14.5$ mA cm⁻², $P_{\text{mpp}} = 23.1$ mW, $m = 1$ cm, and the IOH resistivity ($\rho_{\text{tco}} = 2.5 \times 10^{-4}$ Ω cm), the f_{loss} calculated as function of the IOH thickness is shown in Figure 4.1d. It is found that for the same IOH thickness used by Datta et al. (100 nm), f_{loss} is about 1.01%.¹⁴ This represents a small drop of PCE from 23.1% to 22.9%. Further increasing the IOH thickness may actually be detrimental for device performance as optical losses may increase and these have been excluded from the f_{loss} calculation above. Therefore, for the large area devices, 100 nm of IOH as TCO was maintained.

The large area (1 cm²) device had comparable cell performance to the small area (0.09 cm²) devices (**Figure 4.2a**). **Table 4.1** shows the photovoltaic parameters of the single-junctions and tandem solar cells. The large area champion device reached a PCE of 23.7% with a high V_{oc} of 1.97 V and current density of 15.7 mA cm⁻². The tandem cell exhibits a V_{oc} loss of only 20 mV when compared to the added V_{oc} s of the two sub-cells. Such loss is expected because in the tandem, charge generation in the NBG is reduced by a factor of roughly 2, resulting in a V_{oc} loss of ~20 mV, calculated from ($\Delta V_{\text{oc}} = -(kT/q) \times \ln 2$, with k the Boltzmann constant, T the absolute temperature, and q the elementary charge). The small area cell had a slightly lower PCE because of a small additional voltage loss (**Figure 4.2a**), which might be due to the individual cell processing. In **Figure 4.2b**, the external quantum efficiency (EQE) spectrum of the 1 cm² all perovskite tandem solar cell shows some current mismatch, with the WBG sub-cell being the current-limiting cell. Nonetheless, the device layout proposed in **Figure 4.1b** does not present significant resistance losses, in contrast to other all-perovskite tandem solar cells studies where a cell scale up (few mm² to cm²) led to a drop in PCE. This work also represents the lowest PCE loss found for such cell scale up as seen in **Figure 4.2c**. The successful scale up of the tandem solar without loss of performance enables then the appropriate integration with the electrolysis cell for solar-driven water electrolysis.

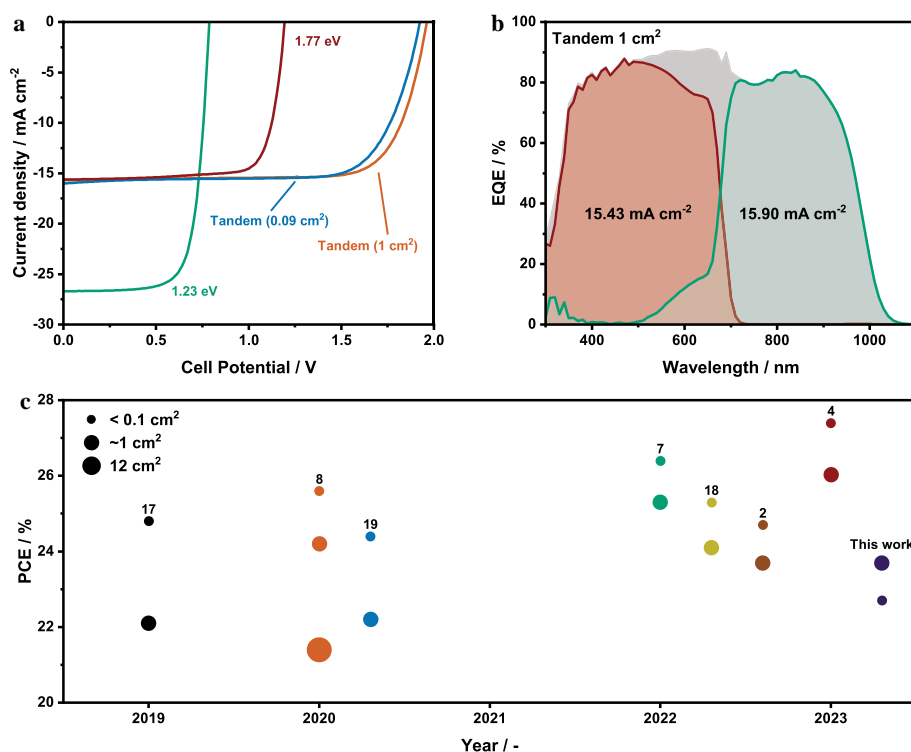


Figure 4.2: Photovoltaic performance of all-perovskite tandem solar cells with different areas. a) Current density versus voltage (J - V) curves of the tandem and single-junction solar cells. b) External quantum efficiency (EQE) spectrum of the large area (1 cm^2) all-perovskite tandem solar cell. For each sub-cell the integrated short-circuit current density (J_{sc}) is indicated. c) Power conversion efficiency (PCE) comparison between small ($< 0.1 \text{ cm}^2$) and large area ($> 1 \text{ cm}^2$) all-perovskite tandem solar cells. The color of the marker distinguishes each small/large area device pair. The numbers above the markers are the reference number associated to each pair.^{2,4,7,8,17-19}

Table 4.1: Photovoltaic parameters (reverse scan) of the single-junctions and all-perovskite tandem solar cells shown in Figure 4.2a.

Devices	$J_{sc} / \text{mA cm}^{-2}$	V_{oc} / V	FF / -	PCE / %
1.23 eV	26.7	0.79	0.73	15.5
1.77 eV	15.6	1.20	0.77	14.6
Tandem (0.09 cm^2)	16.0	1.92	0.74	22.7
Tandem (1 cm^2)	15.7	1.97	0.76	23.7

4.3. Solar-driven water electrolysis with all-perovskite tandem solar cell

Following the tandem cell scale up, the next step was to combine the large area tandem solar cell to the electrochemical flow cell (EC) in a similar manner

to chapter 3. In short, the electrochemical flow cell consisted of a Nafion NRE-212 membrane spray coated with 1.1 mg cm^{-2} Pt and 2.0 mg cm^{-2} RuO₂ on opposite sides. The membrane-electrode assembly (MEA), as well as titanium (anode) and carbon (cathode) porous transport layers (PTLs), is compressed between two titanium flow fields. The polarization curve of the electrochemical flow carried out at room temperature (**Figure 4.3a**) is consistent with previous results (chapter 3), and will not be further discussed. For this study, the 1 cm^2 tandem solar cell (same cell stack as mentioned above) was combined with the electrochemical flow cell.

The polarization curve of the EC and the current versus voltage (J - V) curve of the tandem cell overlap at 1.40 V and 15.1 mA, which represents the operating point of the solar-driven water splitting system at 1-sun equivalent light intensity (Figure 4.3b). The expected STH (Eq. 4.1) of the system is then 18.6%. The system was operated over 1 h of continuous illumination at 1-Sun equivalent light intensity (Figure 4.3c). For the first 15 min, the output voltage and STH were seemingly stable, however, afterwards the operating current I_{op} drops from 15.0 mA to 11.6 mA (STH drop from 18.5% to 14.4%, respectively). The decrease of operating voltage V_{op} is not as noticeable as the loss in I_{op} due to the electrochemical cell polarization characteristics. The polarization curve of the EC after 1 h continuous operation is virtually identical to the first measurement (Figure 4.3a), indicating that no degradation took place in this timespan. In contrast, the J - V curve of the tandem solar cell (Figure 4.3b) shows a decrease in I_{sc} from 15.5 mA to 14.9 mA, while FF and V_{oc} are retained. Such current decrease would imply a drop in I_{op} of the solar-driven water splitting system to 14.6 mA, and not the observed 11.6 mA.

To further understand this current loss, the external quantum efficiency (EQE) spectrum of tandem solar cell after 1 h of operation was also analyzed (Figure 4.3d). The EQE of the WBG sub-cell suffered a red-shift, resulting in the NBG sub-cell becoming the current limiting cell and in a drop of the $J_{\text{sc,eqe}}$ of the tandem cell from 15.43 mA cm^{-2} to 15.33 mA cm^{-2} . The red-shift observed for the WBG sub-cell is most probably associated with photoinduced halide segregation. Photoinduced halide segregation involves the segregation of iodide and bromide ions in mixed-halide perovskites under illumination (Figure 4.3e). This is typically observed for high bromide content perovskite films with an optical bandgap above 1.7 eV as it is the case of the WBG sub-cell used in this work.^{20,21}

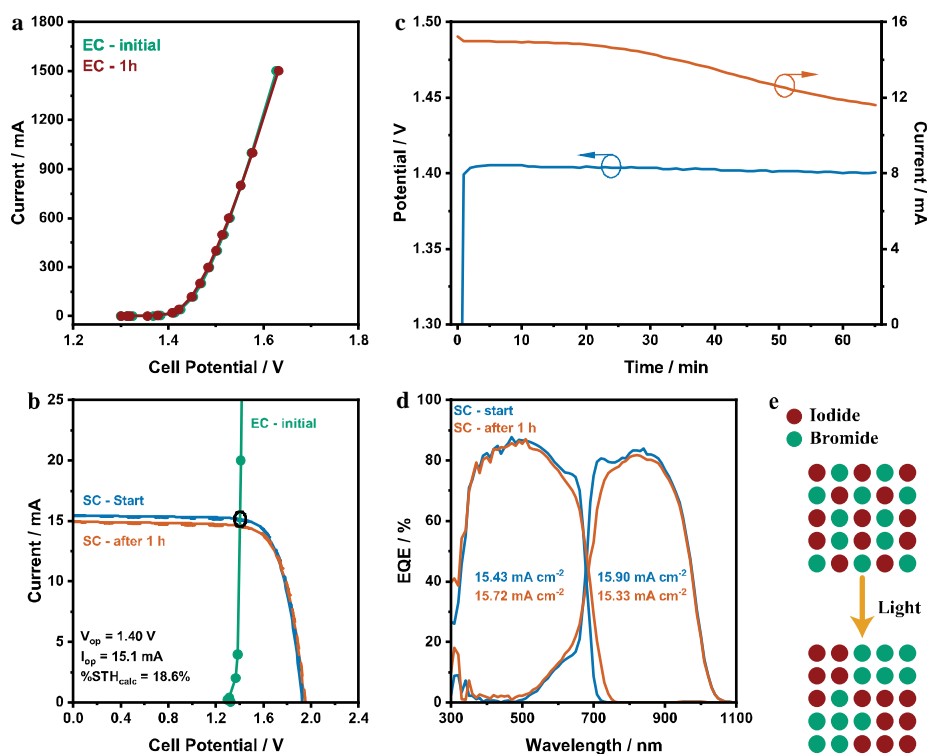


Figure 4.3: Solar-driven water electrolysis with an all-perovskite tandem solar cell. a) Polarization curve of the electrochemical flow cell (active area = 4 cm², Pt/Nafion NRE-212/RuO₂). b) Overlap of the J - V curve of the all-perovskite tandem solar cell with the polarization curve of the electrochemical flow cell. c) Current and voltage as a function of time using integrated PV-EC system over 1 h continuous operation at approx. 1-Sun equivalent light intensity. d) EQE spectra of the all-perovskite solar cell before and after 1 h of operation. For each sub-cell the integrated J_{sc} is indicated. e) Schematics of light-induced halide segregation in mixed halide perovskites.

The impact of the light-induced instability of the solar cell was further studied by operating the tandem solar cell under continuous illumination (~ 1 -Sun equivalent light intensity) and a bias voltage of 1.45 V over 20 h, mimicking the conditions of the solar-driven water splitting experiment (Figure 4.4a). The J - V curves (Figure 4.4b) and EQE (Figure 4.4c) were measured at 0 h and at about 1.5, 14, and 20 h. For this study, a 1 cm² tandem solar cell with an ICL made of ITO/PEDOT:PSS instead of Au/PEDOT:PSS was used and the illuminated area was delimited by 0.0314 cm². Similarly to the water splitting experiment, the current density had a steep decrease, reaching a minimum at 8.94 mA cm⁻² after 1.5 h. Then, it started to increase again continuously until the end of the experiment, reaching 12.4 mA cm⁻², which is actually higher than the initial current density.

The abrupt current density decrease at this voltage bias at 1.5 h was related to a major decrease in the FF and also, a decrease in $J_{sc,JV}$ as seen in the J - V curve taken at 1.5 h (Figure 4.4b). At this time, the EQE spectrum of the WBG sub-cell shows again a red-shift attributed to halide segregation, accompanied by a decrease of the EQEs of both sub-cells. The $J_{sc,EQE}$ drops only marginally, which is attributed to a higher EQE of the NBG sub-cell at wavelengths between 300 and 700 nm that should have been filtered/absorbed by the WBG sub-cell. The reason for such was not further investigated.

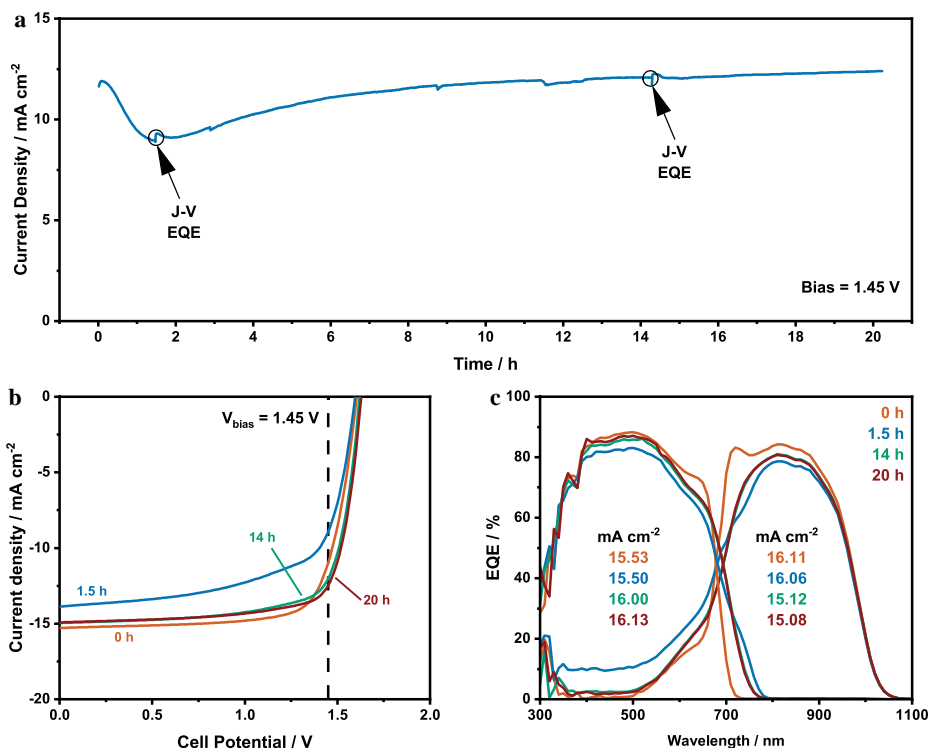


Figure 4.4: Stability of the all-perovskite tandem solar cells under 1-Sun equivalent light intensity and a voltage bias. a) Continuous operation under irradiation and a bias of 1.45 V for over 20 h. b) J - V curves before, during, and after 20 h under operation. c) EQE spectra before, during, and after 20 h under operation.

Interestingly, after 14 h, the EQE of the WBG sub-cell shows a small blue shift, which was retained until the 20 h. The blue shift suggests that the segregated halides (iodide and bromide) partially remixed, causing the increase in bandgap. The J - V curves also show some recovery in comparison to 1.5 h (Figure 4.4b), but do not reach the initial J_{sc} . Additionally, the FF actually

improved in comparison to $t = 0$ h, which explains the higher current density obtained at the end of continuous illumination experiment.

Light-induced halide segregation in single-junction solar cells has been shown to be reversible, but only after storing the cells in dark. The iodide- and bromide-rich domains in the perovskite film tend to remix after storage in the dark over several hours or even days, causing the emission to blue-shift to the original energy, i.e., the original bandgap. However, in the tandem solar cells presented in this chapter, the halide segregation appears to be partially reversible also during illumination. Tong et al. observed a PCE drop, followed by recovery in the 1500 h stability measurement, resembling what is observed in Figure 4.4a, but the authors do not discuss this further.²²

4.4. One-step procedure for narrow-bandgap perovskite solar cell

The NBG perovskite solar cell used for the tandem solar cell lags the most in terms of PCE when comparing to literature where typical PCE for NBG perovskite solar cells are above 20% with J_{sc} and V_{oc} s above 30 mA cm^{-2} and 0.80 V, respectively.^{11,13,18,22,23} To increase the PCE of the tandem solar cell, the photocurrent of the NBG perovskite sub-cell requires first improvement, after which the WBG cell can be matched by shifting its bandgap via adjusting the iodide/bromide ratio. Additionally, achieving high STH, depends on the current density of the photovoltaic component at the operating point of the solar-driven water splitting system and, therefore, high current density output is important. As mentioned previously, Hu et al. reported a 1.25 eV lead-tin iodide perovskite solar cell, nominally $\text{Cs}_{0.1}\text{FA}_{0.6}\text{MA}_{0.3}\text{Pb}_{0.5}\text{Sn}_{0.5}\text{I}_3$, that reached a record PCE of 23.6% ($V_{oc} = 0.89$, $\text{FF} = 0.82$, and $J_{sc} = 32.5 \text{ mA cm}^{-2}$) based on a one-step (antisolvent) procedure.¹¹ In this work, the precursor solution consisted of SnI_2 , PbI_2 , SnF_2 , CsI , FAI , MAI , and NH_4SCN in a mixture of DMF/DMSO with volume ratio of 3:1. The best reported cells also contain glycine hydrochloride (GlyHCl) as bulk additive. This solution is deposited on a PEDOT:PSS HTL and a few seconds before the end of spin coating, chlorobenzene (antisolvent) is deposited on the perovskite film that is subsequently annealed. The perovskite layer is then treated with an EDAI_2 solution to improve the perovskite/ETL interface. The devices are completed with thermally evaporated layers of C_{60} /BCP as ETL and Ag as back electrode.

This one-step procedure, without any passivation agents (GlyHCl and EDAI_2) was tested for all-perovskite tandem solar cells using Au/PEDOT:PSS as ICL and compared with the two-step NBG process. **Figure 4.5a–b** show the

J - V curves and EQE measured for the tandem and single-junction solar cells using either the two-step or one-step NBG process. **Table 4.2** shows the photovoltaic parameters of the NBG single-junctions and tandem solar cells.

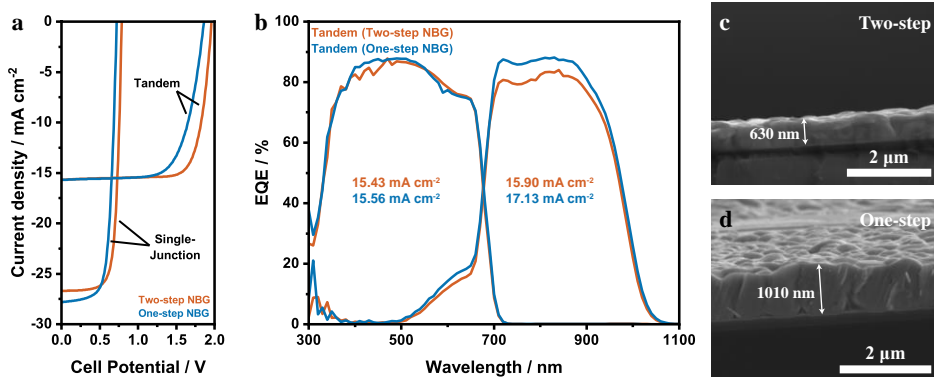


Figure 4.5: Comparison of the two and one-step NBG perovskite procedures. a) J - V curves of the all-perovskite tandems and NBG single-junctions. b) EQE spectra of the two tandems using the two different NBG procedures. For each sub-cell the integrated J_{sc} is indicated. c) Scanning electron microscopy (SEM) picture of a perovskite film prepared with the two-step procedure and d) SEM picture of a perovskite film prepared with either the two-step or one-step procedures.

Table 4.2: Photovoltaic parameters of NBG single-junction and all-perovskite tandem solar cell prepared with either the two-step or one-step procedure.

Devices	$J_{sc} / \text{mA cm}^{-2}$	V_{oc} / V	FF / -	PCE / %
Two-step SJ	26.7	0.79	0.75	15.5
One-step SJ	27.8	0.72	0.70	14.0
Tandem (two-step NB)	15.7	1.97	0.76	23.7
Tandem (one-step NB)	15.7	1.86	0.69	20.9

Both the single-junction and the tandem made with the one-step NBG layer show lower V_{oc} , as expected due to the absence of any passivation agent. The EQE and J - V curves of the single-junctions show, nonetheless, a J_{sc} increase of 2 mA cm^{-2} for the one-step NBG cells, which is partially attributed to a thicker perovskite film ($\sim 1 \mu\text{m}$) as shown in Figure 4.5c and d. For the two-step NBG deposition, Datta et al. have demonstrated that increasing the thickness from 600 to 840 nm, would minimally increase the J_{sc} , while reducing both V_{oc} and FF, which was attributed to the limited carrier diffusion lengths in mixed Pb-Sn perovskite films.^{7,14,17} The increase in current density when using the one-step NBG layer was also observed in the EQE of the NBG sub-cell in the tandem solar cell. This resulted in a larger current mismatch between the two sub-cells since the WBG sub-cell is the current limiting cell in each case and thus, the J_{sc} of the tandem solar cell remains obviously unaffected. Lowering the bandgap of the WBG perovskite cell is a way to reduce the current mismatch between the two

sub-cells. The sum of the $J_{sc,eqe}$ of the two sub-cells for the tandem with the one-step NBG is 32.69 mA cm^{-2} . Assuming current matched cells, the tandem J_{sc} increases to $16.345 \text{ mA cm}^{-2}$ and with similar V_{oc} and FF, the tandem PCE can potentially go up to 24.4%.

4.4.1. Additives in the perovskite precursor solution

In recent literature on NBG perovskite solar cells, there is an increasing trend in using additives, or bulk passivation agents, in the precursor solution that provide many functionalities/functions. Herein, two bulk additives for the one-step NBG procedure were studied: GlyHCl as reported by Hu et al. and BaI_2 based on the work by Yu et al.^{11,18} GlyHCl reportedly stabilizes the formation of larger particles that deposit at the bottom interface, acting as nucleation centers for film growth, resulting in increased crystallinity and reduced defect density. Furthermore, the GlyH^+ cation was mainly found at the bottom of the film where the carboxyl group faces the HTL and the ammonium group faces the perovskite, creating an electric field that enhances charge collection at the HTL. In the case of BaI_2 , Yu et al. found that the incorporation of a small amount of BaI_2 (0.1 mol% to Pb) reduces the defect density by filling in interstitial sites, compensating the p-doping caused by Sn vacancies.¹⁸ This enabled a decreased non-radiative recombination and higher V_{oc} . The authors also experimented with other divalent metal cations such as cadmium, ytterbium, and samarium but found the best results with Ba^{2+} .

The perovskite precursor solution without any additives was prepared as described previously for the one-step NBG procedure. To prepare the solutions with additives, either 2 mol% GlyHCl with respect to the total amount of $\text{SnI}_2/\text{PbI}_2$ or 0.1 mol% BaI_2 with respect to PbI_2 were added to the precursor mixture. The single-junction solar cells were prepared following the cell stack shown in **Figure 4.6a**. The J - V curve and respective photovoltaic parameters (Figure 4.6b and **Table 4.3**) show that GlyHCl has a major effect on the V_{oc} , increasing it from 0.70 to 0.77 V while the FF remains almost constant independently of the additive. BaI_2 does not seem to affect the photovoltaic parameters, but it seemingly decreases the observed hysteresis (Figure 4.6c) in comparison to the control and GlyHCl samples.

The low J_{sc} obtained in the J - V curve for the cells with GlyHCl was initially correlated with the presence of small white crystals at the glass side (Figure 4.6d) that only formed when GlyHCl was used as an additive, which supports the idea that GlyHCl accumulates at the bottom interface. Despite such crystals, the device with GlyHCl actually has the highest EQE (Figure 4.6e), and consequently, the highest integrated J_{sc} from the EQE spectrum. The discrepancy

between the J_{sc} measured by the two methods can be assigned to the light source used for the J - V curve measurement which has low emission at low wavelengths.

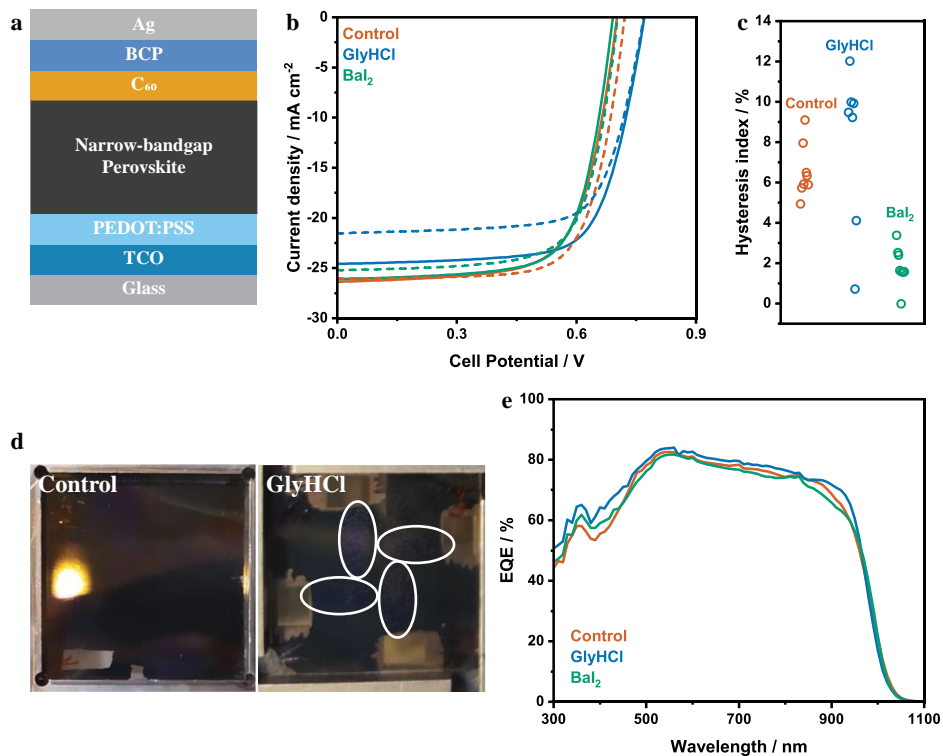


Figure 4.6: Additives in the perovskite precursor solution. a) Schematic of the single-junction stack. b) J - V curves of the solar cells with and without additives. Solid and dashed lines represent the reverse and forward voltage scans, respectively. c) Hysteresis index obtained for at least 8 cells with and without each additive. d) Pictures (glass side) of representative samples without any additive and with GlyHCl. e) EQE spectra of the solar cells with and without additives.

Table 4.3: Photovoltaic parameters (reverse scan) of the solar cells with and without additives in the perovskite precursor solution.

Devices	$J_{sc} / \text{mA cm}^{-2}$	V_{oc} / V	FF / -	PCE / %	$J_{sc,EQE} / \text{mA cm}^{-2}$	$\text{PCE}_{EQE} / \%$
Control	26.4	0.70	0.69	12.6	27.71	14.4
GlyHCl	24.6	0.77	0.70	13.3	28.41	15.5
BaI ₂	26.1	0.70	0.70	12.7	27.42	13.6

Hu et al. also found that such crystals would form when GlyHCl was used in the precursor solution and that, similarly, the effect on the current density was negligible.¹¹ Remarkably, these crystals only form when the TCO was ITO, as in the case of the cells presented in this work, whereas for fluorine-doped tin oxide

(FTO) as TCO and using the same thermal annealing procedure for the perovskite, no obvious crystals were visible. The authors attributed this crystal formation to a faster crystallization process that results in residual GlyH⁺ deposits at the bottom of the film. The authors additionally prepared perovskite films on FTO using preheated antisolvent (45 °C) and they observed the formation of the crystals once again, further suggesting that fast crystallization is the main cause for the crystals.¹¹ This suggests that a slower annealing procedure might be more adequate to ensure that all GlyHCl works as nucleation center for perovskite only and avoid the formation of such crystals.

The influence of the GlyHCl additive on the perovskite films and solar cells was further studied by determining the quasi-Fermi level splitting (QFLS) through absolute photoluminescence (APL) spectroscopy (**Figure 4.7**). The QFLS was calculated by fitting the generalized Planck equation to the high energy edge of the APL spectra.²⁴ The GlyHCl additive increases the intensity of the photoluminescence emission of the perovskite films on glass (Figure 4.7a), implying less non-radiative recombination. Consequently, the QFLS of the perovskite film increases from 0.873 V to 0.892 V (Figure 4.7b). For this bandgap (1.25 eV), the detailed balanced limit of V_{oc} is about 0.98 V and thus, this QFLS represents a loss of ~90 mV. The loss in QFLS upon adding the remaining layers (HTL and ETL) amount to 133 mV and 121 mV without and with the GlyHCl additive, respectively. Therefore, the GlyHCl mainly enhances the QFLS of the perovskite itself while also slightly minimizing the losses at both interfaces, consistent with the work developed by Hu et al.¹¹

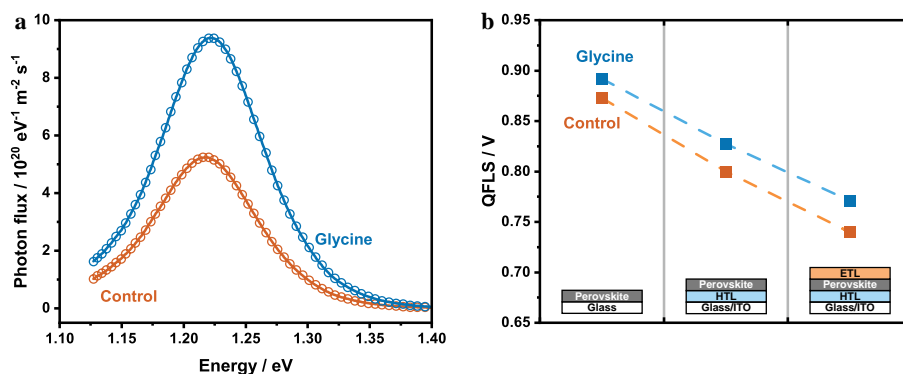


Figure 4.7: Non-radiative losses using GlyHCl as bulk additive. a) Absolute photoluminescence spectra of bare perovskite films deposited on glass. b) Quasi-Fermi level splitting based on absolute photoluminescence for different stacks.

X-ray diffraction (XRD) measurements (**Figure 4.8**) show that the intensity of the (100) peak increases with the use of GlyHCl. Additionally, the

presence of GlyHCl reduces the intensity of the peak at $2\theta = 12.7^\circ$, which is attributed to unreacted PbI_2 or degraded perovskite. The enhanced crystallinity of the perovskite film and the lower amount of PbI_2 suggest that the GlyHCl aids the crystal growth phase of the perovskite as proposed by Hu et al.¹¹ The higher crystallinity can also be correlated to the higher photoluminescence intensity due to the possibly decreased defect density.

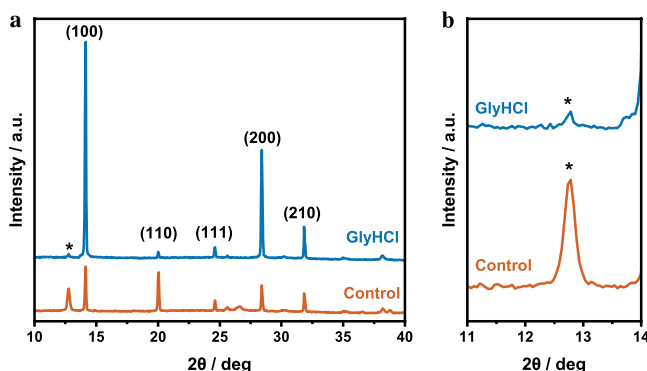


Figure 4.8: X-ray diffractograms (XRD) of perovskite films with and without GlyHCl. a) Complete diffractograms. b) Zoomed in diffractogram around the PbI_2 peak.

4.4.2. Top surface treatment

The top surface of the perovskite films is commonly treated with a passivation agent to reduce surface defects and improve the interface between the perovskite and the charge transport layer on top. As an example, for the WBG perovskite used in the tandems, choline chloride was the passivation agent whereas for the two-step NBG perovskite, it was CdI_2 . In the paper by Hu et al., the authors used 0.5 mg mL^{-1} EDAI_2 in a mixture of isopropanol and toluene.¹¹ In this section, the effect of different concentrations of EDAI_2 (0.25 and 0.5 mg mL^{-1}) and CdI_2 (0.25 , 0.5 , and 1 mg mL^{-1}) on the device performance was investigated. CdI_2 was also chosen since it has been shown to have a positive effect when used in the two-step NBG procedure. It is important to point out that 0.5 mg mL^{-1} EDAI_2 does not fully solubilize in the isopropanol/toluene mixture, and thus, after filtering, the solution is considered to be saturated. Herein, GlyHCl was used as a bulk additive for every device and the device with only GlyHCl and without any surface treatment is denominated “control sample”.

The J - V curves of a series of devices treated with EDAI_2 and CdI_2 and photovoltaic parameters are shown in **Figure 4.9a–e** and **Table 4.4**. The 0.25 mg mL^{-1} EDAI_2 has a detrimental effect on device performance as V_{oc} and FF are, on average, lower than the control sample. For all the other variations, some

improvement on V_{oc} and FF is observed, which consequently increase the PCE of the solar cells. $0.5 \text{ mg mL}^{-1} \text{ CdI}_2$ presents the largest improvement of the V_{oc} in about 41 mV, on average. Moreover, all tested concentrations of CdI_2 resulted in better performance in comparison to EDAI_2 . The effect of the surface treatments on the EQE spectra (Figure 4.9f) appears negligible, except between 830 and 930 nm where a slightly thicker film might have increased the absorption. Ultimately, the combination of GlyHCl in the bulk perovskite and $0.5 \text{ mg mL}^{-1} \text{ CdI}_2$ as top surface treatment resulted in a large improvement on V_{oc} and FF, enabling a PCE of 18.6% (Figure 4.9g). This PCE still lags behind the most efficient NBG perovskite solar cells reported, but it represents an increase of $\sim 3\%$ compared to the best two-step NBG perovskite prepared in this work.

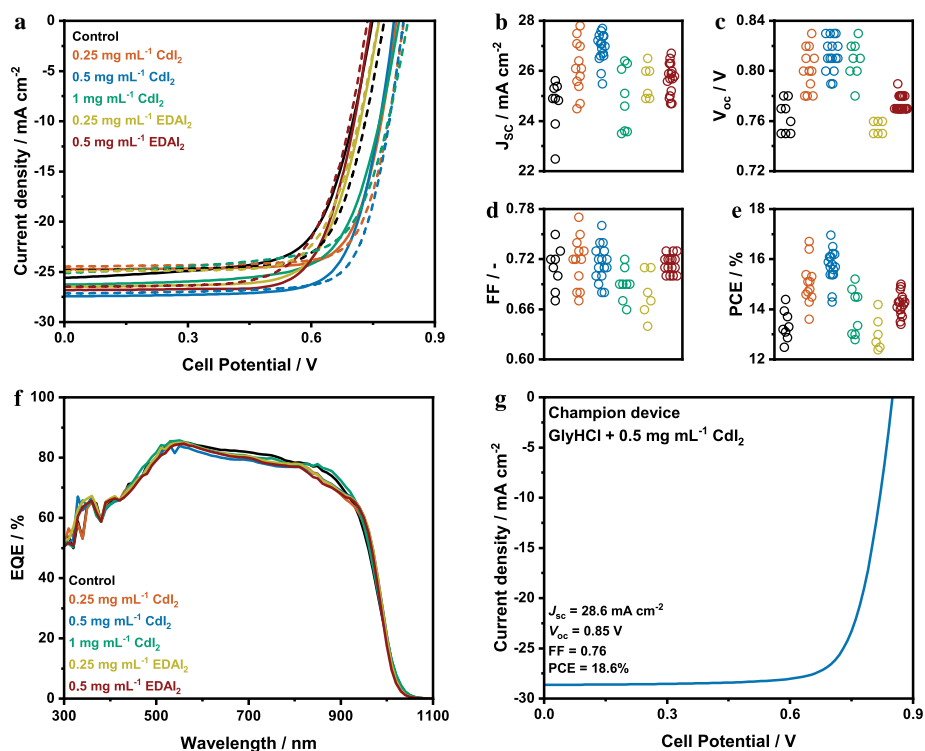


Figure 4.9: Top surface treatment with different concentrations of CdI_2 and EDAI_2 . a) $J-V$ curves of the solar cells with and without surface treatment. Solid and dash lines represent the reverse and forward voltage scans, respectively. b–e) Photovoltaic parameters of 8 devices with each concentration of surface treatment agent. f) EQE spectra of the solar cells with and without surface treatment. g) $J-V$ curves of the champion device prepared with $0.5 \text{ mg mL}^{-1} \text{ CdI}_2$ as surface treatment and GlyHCl as bulk additive.

Table 4.4: Photovoltaic parameters (reverse scan) of the solar cells without and with surface treatment.

Devices	$J_{sc} / \text{mA cm}^{-2}$	V_{oc} / V	FF / -	PCE / %	$J_{sc,EQE} / \text{mA cm}^{-2}$	$\text{PCE}_{EQE} / \%$
Control	25.6	0.75	0.67	12.9	28.94	16.25
0.25 CdI ₂	24.7	0.81	0.75	15.1	28.54	18.02
0.5 CdI ₂	27.4	0.8	0.74	16.2	28.43	17.71
1 CdI ₂	26.3	0.81	0.69	14.8	28.98	16.59
0.25 EDAl ₂	25.2	0.73	0.68	12.5	28.71	14.46
0.5 EDAl ₂	26.8	0.75	0.71	14.4	28.36	15.1

APL spectroscopy and calculation of the QFLS were used to analyze the effect of the surface treatment on the non-radiative recombination of the surface treated perovskite films and devices (**Figure 4.10**). Figure 4.10a–b show the APL spectra for the control sample compared to 0.5 mg mL⁻¹ CdI₂ and EDAl₂ used here as representative samples.

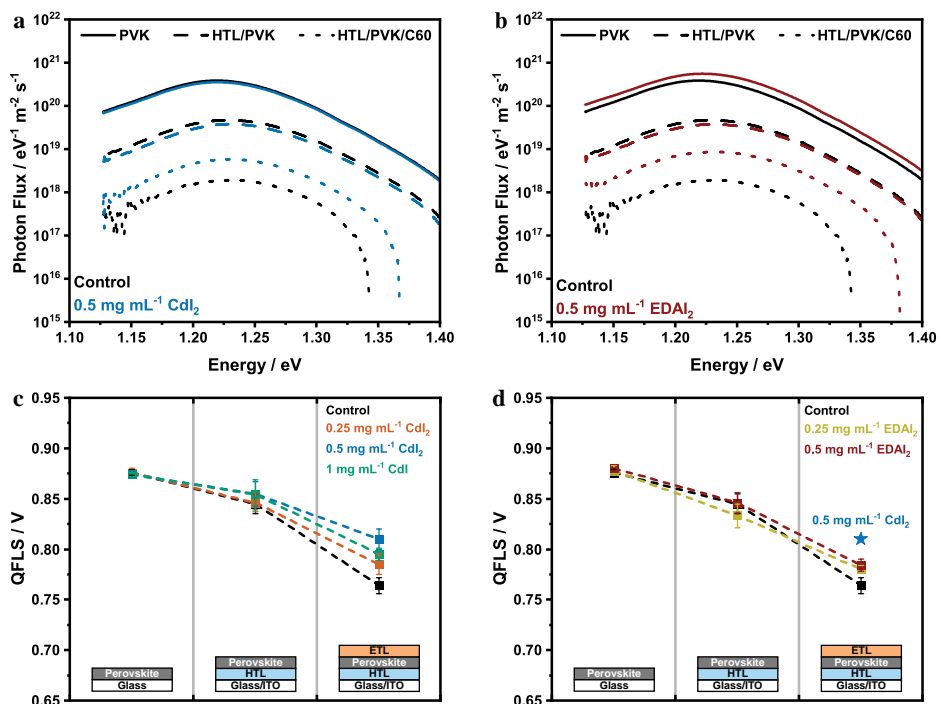


Figure 4.10: Non-radiative losses using top surface treatment. a–b) Absolute photoluminescence spectra of perovskite films with and without surface treatment deposited on glass, glass/ITO/HTL with and without C60 on top. c–d) Quasi-Fermi level splitting based on absolute photoluminescence for the different stacks and concentrations of CdI₂ and EDAl₂.

When the perovskite layers are deposited on PEDOT:PSS instead of on glass, the APL drops identically for the samples without and with surface treatment. Contrastingly, following the addition of C₆₀ on top of the perovskite films, the emission intensity drops much more for the control sample than for the surface-treated samples, indicating a steep reduction in non-radiative recombination losses at that interface. This is reflected on the QFLS values (Figure 4.10c–d) calculated from the APL. Without any surface treatment, the QFLS loss upon depositing C₆₀ is around 81 mV whereas, when using 0.5 mg mL⁻¹ CdI₂ for example, this loss is reduced to about 45 mV.

Moreover, CdI₂ (at all concentrations) seems to have a larger effect on enhancing the perovskite/C₆₀ interface, further reducing non-radiative recombination, than EDAI₂. The 0.5 mg mL⁻¹ CdI₂ resulted in the highest QFLS and device V_{oc} of all variations. The intermediate concentration of CdI₂ might be enough to adequately fill the atomic vacancies on the perovskite film surface but sufficiently low to avoid creating an insulating layer between the perovskite film and the C₆₀ ETL. For this reason, 0.5 mg mL⁻¹ CdI₂ was chosen as surface treatment for subsequent experiments.

4.4.3. Self-assembled monolayers for hole transport layers

The additives and surface treatment employed mainly improved the V_{oc} and the FF of the NBG perovskite solar cells while the current density was fairly similar between the control sample and the treated samples. The V_{oc} and FF obtained are already comparable to values obtained in literature, however, the current density is lower. Typical current densities range from 30 to 32 mA cm⁻² for similar NBG cells.^{8,12,13,18,22,25} Improving the current density of the NBG sub-cells, together with an improvement of the wide-bandgap sub-cell as well, in the all-perovskite tandem solar cell would not only enhance the PCE but also increase the STH of the solar-water splitting system with such photovoltaic component. Replacing the PEDOT:PSS with a SAM can be a viable pathway to reach higher current density in both the tandem and the single-junction cell. Furthermore, it has also been shown that the use of SAMs has a negligible effect on the QFLS in comparison to other HTLs, allowing to reach higher V_{oc}s. However, the use of a MeO-2PACz ([2-(3,6-dimethoxy-9H-carbazol-9-yl)ethyl]phosphonic acid) SAM in the tandem solar cell led to a loss in V_{oc} and FF, which was not observed for the NBG single-junction cell (Figure 4.11a–c). Here, the MeO-2PACz was deposited on a thin ITO layer instead of Au, as it requires dangling –OH groups to bind the phosphonic acid anchoring groups via a condensation reaction.²⁶ Moreover, the use of ITO instead of Au increases the

transparency of the ICL, enhancing the light transmission to the NBG sub-cell that results in higher current density.

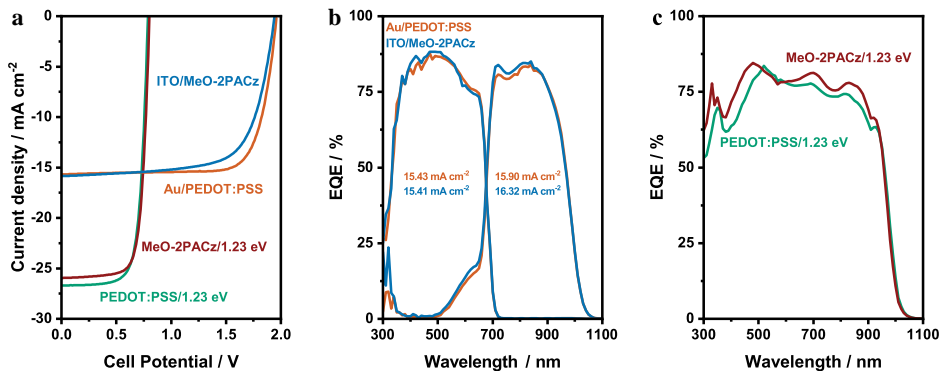


Figure 4.11: Tandem and NBG single-junction solar cells prepared with PEDOT:PSS or MeO-2PACz as HTL. The NBG perovskite sub-cell was prepared using the two-step procedure. a) J - V curves of the NBG single-junctions and all-perovskite tandem solar cells. b) EQE spectra of the tandem solar cells. c) EQE of the NBG single-junctions.

Most publications that report the use of SAMs as HTL instead of PEDOT:PSS in NBG perovskite solar cells, solely focuses on the performance of single-junction cells and not tandems.^{13,27,28} The main goal in those reports was to avoid the hydrophilicity and acidity of the PEDOT:PSS by using such SAM, greatly improve device performance stability and performance. But on tandems, the use of SAMs on NBG sub-cell in tandems is hindered by the roughness of the layers underneath, in particular due to the WBG perovskite. The SAM is not able to planarize the layers below, in contrast to PEDOT:PSS, leaving a rough surface to deposit the NBG perovskite and leading to poorer performance. To solve this issue, Xiao et al. proposed the use of a nickel oxide (NiO) planarization layer deposited before the SAM as illustrated in **Figure 4.12**.²⁹ In this work, the NiO/SAM HTL was used for the middle sub-cell ($E_g = 1.60$ eV) in a triple-junction solar cell but the same principle is valid in the case of NBG sub-cell.

MeO-2PACz has already been shown by Datta et al. as a viable replacement for PEDOT:PSS in single-junctions.¹⁴ 2PACz is more commonly used as HTL for WBG perovskite solar cells, but recently, Kapil et al. have reported the use of a 2PACz/methyl phosphonic acid bilayer as HTL for NBG cells, having achieved a PCE of 23.23%.¹³ Hence, MeO-2PACz and 2PACz (**Figure 4.13**) were used as HTL on ITO or ITO/NiO and compared with PEDOT:PSS.

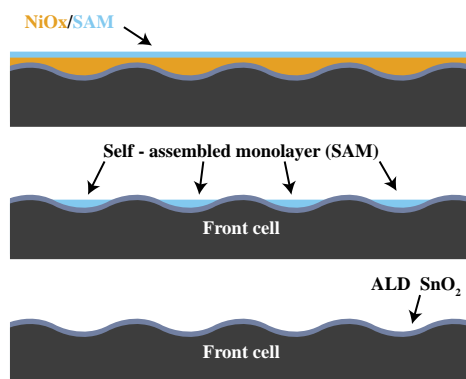


Figure 4.12: Schematic diagram of SAM and NiO/SAM layers spin-coated on the front sub-cell. Based on ref. ²⁹.

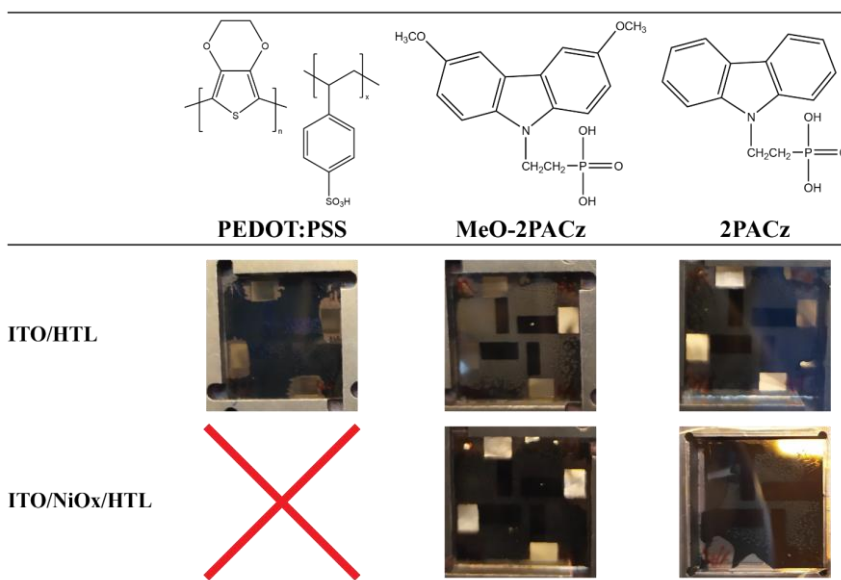


Figure 4.13: Summary of prepared solar cells with different hole transport layers. Pictures (glass/ITO side) of the devices prepared on PEDOT:PSS, MeO-2PACz, 2PACz with and without a NiO layer.

The bottom surface of the device using PEDOT:PSS as HTL has similar appearance as shown before, presenting some white crystals, especially in the ITO bottom electrode area (Figure 4.13). Contrastingly, the samples prepared on SAM and NiO/SAM present a much larger amount of such crystals, seemingly covering most of the bottom surface of the perovskite. Interestingly, on these samples, the crystals appear to have accumulated outside the areas where ITO/NiO/SAM is present. Independently of the HTL used, the perovskite films

show the expected diffraction peaks for a perovskite film with identical intensities (**Figure 4.14a**). Therefore, the formation of those crystals at the bottom did not lead to any significant change of the crystallinity of the perovskite layer.

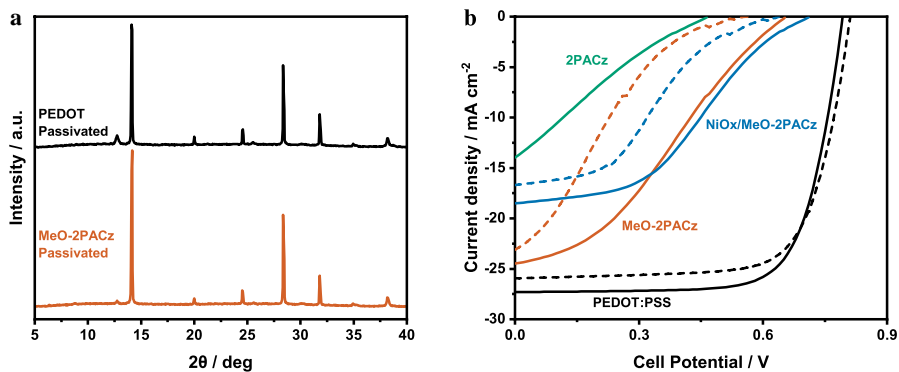


Figure 4.14: Narrow-bandgap perovskite single-junctions prepared on different HTLs. a) XRD of the perovskite films deposited on PEDOT:PSS or MeO-2PACz. b) J - V curves of the narrow bandgap perovskite solar cells with different HTLs. Solid and dash lines represent the reverse and forward voltage scans, respectively.

The photovoltaic performance of the solar cells prepared with SAMs as HTLs (Figure 4.14b) was significantly worse than with PEDOT:PSS, opposed to what was observed for the two-step NBG procedure mentioned earlier. The J - V curves of the devices with SAM or NiO/SAM have strong s-shapes, which is commonly associated with charge transport barriers at the perovskite/charge transport layer interfaces.^{30,31} The existence of a large amount of crystals at the bottom surface may have caused a resistance increase that limits charge transport, resulting in the observed s-shaped J - V curves.³² However, the exact cause was not further investigated.

The optimization of the narrow bandgap perovskite solar cell in this chapter resulted in a PCE of 18.6%, with $V_{oc} = 0.85$ V, FF = 0.76, and $J_{sc} = 28.6$ mA cm⁻². The thicker perovskite absorber layer prepared with this procedure, enabled a higher current density output of this sub-cell in the tandem, resulting in a current mismatch of about 1.57 mA cm⁻². Therefore, for appropriate current matching in the tandem cell, the E_g of the WBG cell can be slightly reduced, e.g., to 1.75 eV, while minimally reducing the V_{oc} . Assuming an identical V_{oc} loss compared to the sum of the V_{ocs} of the two single-junctions (~ 20 mV) observed before and similar FF, the resulting tandem could reach a PCE of 25.1% with $V_{oc} = 2.02$ V ($V_{oc,wbg} = 1.18$ V),³³ FF = 0.76, and $J_{sc} = 16.35$ mA cm⁻², representing a PCE gain of 6.5% and 9.7% in relation to the NBG and WBG sub-cells. Currently, all-perovskite tandem solar cells have reached a PCE of 27.4% ($V_{oc} =$

2.19 V, $J_{sc} = 15.05 \text{ mA cm}^{-2}$ and $FF = 0.831$), and in comparison this has resulted in a PCE gains of 5.9% (1.25 eV) and 7.2% (1.75 eV).⁴ This shows that individual improvements on both sub-cells are still required, but also, that promising performances (PCE > 26% and STH > 20%) are attainable.

4.5. Conclusion

This chapter initially focused on designing and preparing 1 cm² all-perovskite tandem solar cells, with the final aim of carrying out solar-driven water splitting. The performance of the 1 cm² tandem cell (PCE = 23.7%) was consistent with the smaller counterpart and previously reported work. Moreover, the $|\Delta\text{PCE}|$ between the large and small area cells was relatively low when compared to other reports on all-perovskite tandem solar cells. This was enabled by the low resistance losses of the IOH electrode (~1%).

The large area cell was then connected to a water electrolysis flow cell for solar-driven water electrolysis, reaching an initial STH efficiency of 18.6%. However, the current output of the system dropped over time due to photoinduced halide segregation on the WBG sub-cell. It was also found that this is partially reversible under operation at a bias close to maximum power point over extended periods of time. This contrasts with the commonly reported requirement for dark storage of wide-bandgap mixed halide perovskite cells to reverse halide segregation.

In a second part of this chapter, the work focused on testing and improving a different procedure for NBG perovskite solar cell based on a one-step procedure. This procedure allowed obtaining a thicker perovskite film, enabling higher current density, while also promising higher V_{oc} , FF, and PCE than the previous two-step procedure used up to here. The optimization of this procedure was divided into three stages: bulk additives, top surface treatment and replacement of PEDOT:PSS by SAM and NiO/SAMs. GlyHCl as bulk additive and $0.5 \text{ mg mL}^{-1} \text{ CdI}_2$ as surface treatment resulted in the highest V_{oc} (0.85 V) and PCE (18.6%) of all the combinations. GlyHCl increases the overall crystallinity of the perovskite and QFLS of the bare perovskite film, due to the lower non-radiative recombination, while minimally affecting the perovskite interfaces with both the HTL and ETL. CdI_2 , on the other hand, minimizes the losses at the perovskite/ C_{60} interface, further improving the V_{oc} . An optimization of the annealing procedure can lead to minimizing the amount of crystals deposited on HTL/perovskite interface, and reduce losses there as well. The two treatments (bulk and surface) were applied for the study with SAM as HTL, however, this procedure appears to be incompatible with the use of MeO-2PACz and 2PACz. Nonetheless, replacing PEDOT:PSS by a SAM as HTL is possibly a

viable option to improve the performance of the NBG perovskite single-junction and also, the tandem solar cell, and it should be further studied.

The NBG perovskite solar cell saw improvements mainly in V_{oc} and FF, but the J_{sc} was constant, independently of the modifications on the perovskite films. Furthermore, it was fairly low in comparison to literature work where $J_{sc} > 30 \text{ mA cm}^{-2}$ are standard. Enhancing the current density to values above 30.2 mA cm^{-2} would already yield NBG cells with PCEs above 20%. Possible pathways to improve the current density output may involve using a thinner layer of PEDOT:PSS HTL or replace the ITO by an IOH TCO to avoid parasitic absorption and increase light transmission to the perovskite absorber layer. Such developments on the NBG perovskite cell should be obviously followed by an improvement of the WBG cell for all-perovskite tandem applications. A small E_g reduction of the WBG sub-cell might be beneficial for achieving current matched sub-cells in the tandem solar cell. Finally, considering the work developed in this thesis, a successful integration of the two sub-cells can bring the PCE above 26% and STH to almost 20%.

4.6. Experimental Section

Materials and precursor solution preparation: All materials were used as received without purification and stored in inert atmosphere unless stated otherwise. 2PACz (> 98%), PbI_2 (> 99.99%), and PbBr_2 (> 98.0%), and MeO-2PACz were purchased from TCI. Formamminium iodide (FAI, > 99.99%), methylammonium iodide (MAI, > 99.99%) and methylammonium bromide (MABr, > 99.99%), ethylenediammonium diiodide (EDAI_2) were purchased from Greatcell Solar Materials. KI (ultra-dry, 99.999%) was purchased from Fisher Scientific. CsI (beads, 99.999%), choline chloride (> 99%), *N,N*-dimethylformamide (DMF, 99.8%), dimethyl sulfoxide (DMSO, 99.9%), 2-propanol (99.95%, anhydrous), anisole (99.7%), SnI_2 (beads, 99.99%), SnF_2 (99%), CdI_2 (99.999%), GlyHCl ($\geq 99\%$, HPLC), ammonium thiocyanate (NH_4SCN , ACS reagent, $\geq 97.5\%$), and BaI_2 (anhydrobeads, 99.995%) were purchased from Sigma Aldrich. Ethanol (anhydrous) was purchased from Merck Millipore. PEDOT:PSS (PVP Al 4083) was purchased from Heraeus Clevios. 1-propanol (99+%, extra pure) was purchased from Acro Organics. C_{60} (99.95%) was purchased from SES Research and bathocuproine (BCP, 99%) was purchased from Lumtec.

For the wide-bandgap perovskite solar cells, the 2PACz hole transport layer was dissolved in anhydrous ethanol (0.33 mg mL^{-1}) with 30 min of sonication. FAPbI_3 solution was prepared by dissolving 1.5 M PbI_2 and 1.24 M FAI in DMF and DMSO at a volume ratio of 4:1. MAPbBr_3 was prepared by dissolving 1.5 M PbBr_2 and 1.27 M MABr in DMF and DMSO at a volume ratio of 4:1. 1.5 M CsI was dissolved in DMSO and 1.5 M KI was dissolved in DMF/DMSO at a volume ratio of 4:1. The wide-bandgap precursor solution (40% Br, $E_g \sim 1.77 \text{ eV}$) was prepared by mixing the FAPbI_3 and MAPbBr_3 solutions at a volume ratio of 3:2 and 5 vol% of CsI, 5 vol% of KI were subsequently added. The surface treatment agent for this perovskite, choline chloride was dissolved in 2-propanol at 1 mg mL^{-1} . Except for the 2PACz solution, all solutions were prepared in a N_2 -filled glovebox, stirred at $60 \text{ }^\circ\text{C}$ overnight and cooled before use.

For the narrow bandgap perovskite solar cells, the PEDOT:PSS was filtered by a PVDF syringe filter (0.45 μm) before use. For tandems, the PEDOT:PSS was further diluted by drop-wise addition of 1-propanol under vigorous stirring (2:1 v/v). MeO-2PACz was dissolved by 30 min sonication in ethanol at 0.275 mg mL^{-1} . NiO was dispersed in Millipore purified water ($\rho > 18 \text{ M}\Omega \text{ cm}$) at a concentration of 30 mg mL^{-1} and then, the dispersion was filtered by a PVDF syringe filter (0.45 μm) before use. CdI_2 was dissolved in 2-propanol at 0.25, 0.5 and 1 mg mL^{-1} at 60 $^\circ\text{C}$ for 1 h. 0.25 and 0.5 mg mL^{-1} EDAl₂ was dispersed in toluene/2-propanol in a ratio of 58:42 v/v at 70 $^\circ\text{C}$ overnight. The solutions were then cooled down before use and in the case of EDAl₂, the solution was filtered through a PTFE syringe filter (0.22 μm) as well.

For the narrow bandgap perovskite deposited by the two-step procedure, in a first vial, 0.75 M PbI_2 and 0.75 M SnI_2 (with 10 mol% SnF_2 , with the respect to SnI_2) were dissolved in DMF/DMSO at a volume ratio of 10.1:1. In a second vial, 0.413 M FAI and 0.212 MAI were dissolved in 2-propanol. These two solutions were stirred at 60 $^\circ\text{C}$ for 1 h, cooled down and filtered through PTFE syringe filter (0.22 μm) prior to use.

For the one-step procedure, the perovskite precursor solution was prepared by dissolving 0.9 M PbI_2 , 0.9 M SnI_2 , 0.09 M SnF_2 , 0.18 M CsI, 1.08 M FAI, 0.54 M MAI, 0.035 M NH_4SCN in DMF/DMSO in ratio of 3:1 v/v. The solutions with additives, either 2 mol% GlyHCl (with respect to $\text{SnI}_2 + \text{PbI}_2$ amount) or 0.1 mol% BaI_2 (with respected to PbI_2) was added to the precursor solution. The precursor solution was then stirred at 45 $^\circ\text{C}$ for 40 min, cooled down and filtered through PTFE syringe filter (0.22 μm) before use.

Solar cell fabrication: Glass substrates ($3 \times 3 \text{ cm}^2$) with patterned ITO (narrow-bandgap single-junctions) or IOH were cleaned in an ultrasonic bath of acetone, followed by scrubbing with sodium dodecyl sulphate (Acros, 99%) soap solution in deionized water, sonication in the soap solution, rinsing in deionized water, followed by sonication in 2-propanol. Prior to use, the substrates were exposed to UV-ozone treatment for 30 min after which they were transferred to a N_2 -filled glove-box.

For the wide-bandgap perovskite solar cells, 100 μL 2PACz solution was spin coated (with a 5 s delay to allow the solution to spread on the substrate) at 3000 rpm for 30 s and annealed at 100 $^\circ\text{C}$ for 10 min. After cooling down, 120 μL perovskite precursor solution was dynamically spin coated onto the substrate at 1000 rpm for 10 s and 5000 rpm for 18 s. At approx. 23 s from the beginning of the spin-coating, 300 μL of anisole was cast onto the spinning substrate. The substrates were immediately annealed at 100 $^\circ\text{C}$ for 30 min. After cooling down, 70 μL choline chloride was dynamically spin coated at 4000 rpm for 35 s and annealed at 100 $^\circ\text{C}$ for 30 min. 20 nm C_{60} was then thermally evaporated, and subsequently transferred in the air to a home-built spatial atomic layer deposition (sALD) reactor as described previously.³⁴ Tetrakis(dimethylamino)tin(IV) was used as the tin source while H_2O was used as co-reactant. The deposition process was carried out at 100 $^\circ\text{C}$, and the final thickness of the SnO_x layer was 45 nm. To complete the device, 100 nm Al was thermally evaporated onto the substrate under high vacuum ($\sim 3 \times 10^{-7}$ mbar).

For the two-step narrow-bandgap perovskite, 150 μL diluted PEDOT:PSS was spin coated onto the ITO substrate at 3000 rpm for 60 s and annealed at 140 $^\circ\text{C}$ (100 $^\circ\text{C}$ for tandems) for 15 min under ambient conditions. After cooling down, the substrates were transferred to a N_2 -filled glovebox where 70 μL of $\text{PbI}_2/\text{SnI}_2$ precursor solution was spin coated onto the HTL at 3000 rpm (acceleration 2000 rpm s^{-1}) for 30 s. After 10–20 min at room temperature, 70 μL of FAI/MAI solution was dynamically spin coated at 3000 rpm for 60 s, and the substrate was subsequently

annealed at 100 °C for 30 min. After cooling down, 0.5 mg mL⁻¹ CdI₂ was dynamically spin coated onto the perovskite film at 5000 rpm for 30 s without any further annealing. Following this, 20 nm C₆₀ and 8 nm BCP were sequentially evaporated at a rate of 0.5 Å s⁻¹, following which 100 nm Ag electrode was thermally evaporated under a high vacuum (~3 × 10⁻⁷ mbar).

For the one-step narrow-bandgap perovskite, 150 μL PEDOT:PSS (with dilution for tandems and without dilution for single-junctions) was spin coated onto the ITO substrate at 500 rpm for 10 s and then, 4000 rpm for 30 s and annealed at 140 °C for 20 min under ambient conditions. After transferring these substrates into a N₂-filled glovebox, they were further annealed at 140 °C for 30 s to completely dry the PEDOT:PSS. Otherwise, 80 μL NiO was spin coated at 2000 rpm for 30 s and annealed at 100 °C for 10 min. For the SAM deposition, inside a N₂-filled glovebox, 100 μL of either MeO-2PACz or 2PACz were spin coated onto the ITO/NiO or ITO at 3000 rpm for 30 s, followed by annealing at 100 °C for 10 min. After cooling down, 200 μL of perovskite precursor was spin coated onto the substrate at 1000 rpm for 10 s (acceleration 200 rpm s⁻¹) and 4000 rpm for 40 s (acceleration 1000 rpm s⁻¹). At approximately 20 s from the end of the spin-coating, 400 μL of chlorobenzene was cast onto the spinning substrate. The substrates were immediately annealed firstly at 100 °C for 10 min and then, at 65 °C for 10 min. For the surface treatment, the CdI₂ solutions were applied as described above while for the EDAl₂ solutions, 70 μL were dynamically spin coated on the perovskite film at 4000 rpm (acceleration 1333 rpm s⁻¹) for 20 s and immediately annealed at 100 °C for 5 min. The devices were finished by thermal evaporation of C₆₀ (20 nm), BCP (8nm), and Ag (100 nm) under a high vacuum (~3 × 10⁻⁷ mbar).

For all-perovskite tandem solar cells, the same procedures were used to prepare the sub-cells, except with the one-step narrow-bandgap perovskite, where no additives or surface treatment was applied, using glass/IOH substrates. After evaporating 20 nm C₆₀ and 45 nm sALD SnO_x on the wide-bandgap perovskite film, either 1 nm Au was thermally evaporated or 5 nm ITO was deposited using a magnetron sputtering tool over the active cell area using shadow masks. The narrow-bandgap perovskite sub-cell was subsequently deposited.

Solar cell characterization: Current density versus voltage (J - V) and EQE measurements were performed under a N₂ atmosphere at room temperature. The J - V scans were done using a tungsten-halogen illumination source filtered by a UV filter (Schott GG385) and a daylight filter (Hoya LB120) with intensity adjusted to 100 mW cm⁻². A shadow mask with an aperture area smaller than the active area (0.0676 or 0.1296 cm² for single-junctions and 0.09 or 1 cm² for tandems) was used to define the illumination area. Under illumination, the solar cells were operated under reverse (+1.5 V to -0.5 V for the wide-bandgap perovskite single-junctions, +1.0 V to -0.5 V for the narrow-bandgap perovskite single-junctions and +2.5 V to -0.5 V for the tandems) and forward (+1.5 V to -0.5 V for the wide-bandgap perovskite single-junctions, +1.0 V to -0.5 V for the narrow-bandgap perovskite single-junctions and +2.5 V to -0.5 V for the tandems) voltage sweeps at a rate of 0.25 V s⁻¹ controlled by a Keithley 2400 source meter.

External quantum efficiency (EQE) measurements of the perovskite single-junction and all-perovskite tandem solar cell were done using a modulated monochromatic probe light (Philips focusline, 50 W) through a 1 mm radius aperture. The spectral response was recorded and converted to EQE using a calibrated silicon reference cell. During the measurement, LED bias light (that generates a photocurrent close to the J_{sc}) was used to mimic the 1-Sun equivalent light intensity for single-junction solar cells. For tandem solar cells, light- and voltage-biasing was used to isolate the EQE of the individual sub-cells. A 530 nm bias light and a forward voltage bias close to the V_{oc} of the wide-bandgap sub-cell was used to measure the narrow-bandgap sub-cell while a 940 nm

and a forward voltage bias close to the V_{oc} of the narrow-bandgap was used to measure the wide-bandgap sub-cell.

Thin film characterization: Absolute photoluminescence spectroscopy was done using 455 nm LED (Thorlabs, M455F3-455 fiber couple LED) source to excite the perovskite film through an optical fiber placed in an integrating sphere (Avantes, AvaSphere-30-REFL) fitted with a 550 nm short-pass filter (Edmund Optics). The excitation intensity was calibrated to 1-Sun equivalent light intensity. The spectrum is measured through an optical fiber connected to a calibrated AvaSpec-HERO spectrometer (Avantes, AVASPEC-HSC1024X58TEC-EVO) using a 550 nm long-pass filter.

X-ray diffraction (XRD) patterns were recorded by a Bruker 2D phase using $\text{Cu K}\alpha$ ($\lambda = 1.5405 \text{ \AA}$) radiation. An increment step size of 0.05° was used between 10° – 40° .

Scanning Electron Microscopy (SEM) was carried out using a SEM FEI Quanta 3D FEG (Thermo Fisher Scientific, USA) with a secondary electron detector and an acceleration voltage of 5 kV.

Materials and membrane-electrode assembly preparation: All materials were used as received without purification. Nafion membrane NRE-212 was purchased from Ion Power. Pt/C (40 wt%) was purchased from Sigma Aldrich. RuO_2 (anhydrous, 99.9%) and Nafion dispersion (D-521) were purchased from Alfa Aesar. RuO_2 was stored inside inert atmosphere. 2-propanol was purchased from Biosolve. All catalyst inks were prepared using water purified in Millipore system ($\rho > 18 \text{ M}\Omega \text{ cm}$).

The catalyst inks were prepared with 5 wt% solid content, with 3:1 ratio of catalyst to Nafion ionomer in a 2-propanol:water (4:1) mixture. For the RuO_2 ink, Nafion dispersion was first added, followed by 2-propanol:water. For the Pt/C ink, the catalyst power was first mixed with water to avoid combustion of the carbon particles and, subsequently, the Nafion dispersion and 2-propanol were sequentially added. The inks were ultrasonicated for at least 10 min prior to catalyst deposition. The catalyst inks were manually spray-coated using a pneumatic airbrush (Aerotec) through a stainless-steel mask with a $2 \times 2 \text{ cm}^2$ opening on opposite sides of the membrane until the target loadings of 1 and 2 mg cm^{-2} for Pt and RuO_2 were reached, respectively. The catalyst loadings were calculated by weighing the membrane before and after spray coating. The deposition temperature was set to 85°C to evaporate the solvent upon deposition and to avoid excessive membrane swelling.

Proton exchange membrane (PEM) electrochemical cell setup: Water electrolysis tests were carried out in an in-house built PEM-electrolyzer cell ($5 \times 5 \text{ cm}^2$) using high-impact polypropylene (PP) as end plates and titanium current collectors (1 mm thick) with machined parallel flow fields (1 mm wide, channel area: $2.25 \times 2.25 \text{ cm}^2$). Titanium fiber felt ($2.5 \times 2.5 \text{ cm}^2$, 0.2–0.3 mm, porosity: 53–56%, from Fuel Cell Store) and carbon fiber non-woven fabric ($2.5 \times 2.5 \text{ cm}^2$, 255 μm , with MPL, H23 C2, from Quintech) were used as porous transport layers (PTL) at the anode and cathode, respectively. The MEA was pressed between the PTLs and the electrolyzer was sealed with PTFE ($5 \times 5 \text{ cm}^2$, 200 mm, from Polyflour) and closed using a compression force of 0.8 Nm. Polyimide film (50 μm , from Wu Xi Shun Xuan New Materials Co., Ltd) was used between the Ti PTL and the membrane to delimit the active area to 4 cm^2 . Millipore purified water ($\rho > 18 \text{ M}\Omega \text{ cm}$) was circulated using a peristaltic pump (Masterflex® L/S® Digital Miniflex®) into both anodic and cathodic compartment at 10 mL min^{-1} . Independent water lines and feeding bottles were used for each compartment. The water bottles were N_2 -bubbled to prevent oxygen and hydrogen build-up.

Electrochemical Characterization: Galvanostatic polarization curves were measured using a 2-channel Keithley 2600 SMU controlled by LabVIEW. The first channel was used to apply the current whereas the second channel was used to measure the voltage across the PEM electrochemical cell. All measurements were done at room temperature. Water was circulated through the cell for 1 h to allow membrane swelling and equilibration prior to any measurements. The cell was conditioned by applying constant current at 10, 20, 50, and 100 mA cm⁻² for 30 s, and then 250 mA cm⁻² for 30 min. The galvanostatic polarization curve was recorded from 0.01 to 375 mA cm⁻². Each current density step was held for 2 min to allow potential stabilization and the average of the last 10 s was taken as the potential value. This was repeated after the solar-driven water electrolysis experiment.

Solar-driven water electrolysis experiments: Solar-driven water electrolysis was performed using a homebuilt solar simulator with a tungsten-halogen illumination source filtered by a UV filter (Schott GG385) and a daylight filter (Hoya LB120) with intensity adjusted to obtain the operating point current at approx. 1-Sun equivalent light intensity.

All experiments took place outside the glovebox environment, and for that reason, the solar cell was kept inside a N₂-filled box and connected to the PEM electrochemical cell via external cabling. A Keithley 2600 SMU controlled by code written in the LabVIEW environment was used for simultaneous measurement of the current and the voltage across the electrochemical cell.

4.7. References

1. Palmstrom, A. F., Eperon, G. E., Leijtens, T., Prasanna, R., Habisreutinger, S. N., Nemeth, W., Gauling, E. A., Dunfield, S. P., Reese, M., Nanayakkara, S., Moot, T., Werner, J., Liu, J., To, B., Christensen, S. T., McGehee, M. D., van Hest, M. F. A. M., Luther, J. M., Berry, J. J., *et al.* Enabling Flexible All-Perovskite Tandem Solar Cells. *Joule* **3**, 2193–2204 (2019).
2. Li, L., Wang, Y., Wang, X., Lin, R., Luo, X., Liu, Z., Zhou, K., Xiong, S., Bao, Q., Chen, G., Tian, Y., Deng, Y., Xiao, K., Wu, J., Saidaminov, M. I., Lin, H., Ma, C.-Q., Zhao, Z., Wu, Y., *et al.* Flexible all-perovskite tandem solar cells approaching 25% efficiency with molecule-bridged hole-selective contact. *Nat. Energy* **7**, 708–717 (2022).
3. Ernst, M., Herterich, J.-P., Margenfeld, C., Kohlstädt, M. & Würfel, U. Multilayer Blade-Coating Fabrication of Methylammonium-Free Perovskite Photovoltaic Modules with 66 cm² Active Area. *Sol. RRL* **6**, 2100535 (2022).
4. Chen, H., Maxwell, A., Li, C., Teale, S., Chen, B., Zhu, T., Ugur, E., Harrison, G., Grater, L., Wang, J., Wang, Z., Zeng, L., Park, S. M., Chen, L., Serles, P., Awni, R. A., Subedi, B., Zheng, X., Xiao, C., *et al.* Regulating surface potential maximizes voltage in all-perovskite tandems. *Nature* **613**, 676–681 (2023).
5. McMeekin, D. P., Sadoughi, G., Rehman, W., Eperon, G. E., Saliba, M., Hörantner, M. T., Haghighirad, A., Sakai, N., Korte, L., Rech, B., Johnston, M. B., Herz, L. M. & Snaith, H. J. A mixed-cation lead mixed-halide perovskite absorber for tandem solar cells. *Science*. **351**, 151–155 (2016).
6. Wang, C., Song, Z., Li, C., Zhao, D. & Yan, Y. Low-Bandgap Mixed Tin-Lead Perovskites and Their Applications in All-Perovskite Tandem Solar Cells. *Adv. Funct. Mater.* **29**, 1808801 (2019).

7. Lin, R., Xu, J. J., Wei, M., Wang, Y., Qin, Z., Liu, Z., Wu, J., Xiao, K., Chen, B., Park, S. M., Chen, G., Atapattu, H. R., Graham, K. R., Xu, J. J., Zhu, J., Li, L., Zhang, C., Sargent, E. H. & Tan, H. All-perovskite tandem solar cells with improved grain surface passivation. *Nature* **603**, 73–78 (2022).
8. Xiao, K., Lin, R., Han, Q., Hou, Y., Qin, Z., Nguyen, H. T., Wen, J., Wei, M., Yeddu, V., Saidaminov, M. I., Gao, Y., Luo, X., Wang, Y., Gao, H., Zhang, C., Xu, J., Zhu, J., Sargent, E. H. & Tan, H. All-perovskite tandem solar cells with 24.2% certified efficiency and area over 1 cm² using surface-anchoring zwitterionic antioxidant. *Nat. Energy* **5**, 870–880 (2020).
9. Tong, J., Song, Z., Kim, D. H., Chen, X., Chen, C., Palmstrom, A. F., Ndione, P. F., Reese, M. O., Dunfield, S. P., Reid, O. G., Liu, J., Zhang, F., Harvey, S. P., Li, Z., Christensen, S. T., Teeter, G., Zhao, D., Al-Jassim, M. M., van Hest, M. F. A. M., *et al.* Carrier lifetimes of >1 μs in Sn-Pb perovskites enable efficient all-perovskite tandem solar cells. *Science* . **364**, 475–479 (2019).
10. Ke, W., Spanopoulos, I., Tu, Q., Hadar, I., Li, X., Shekhawat, G. S., Dravid, V. P. & Kanatzidis, M. G. Ethylenediammonium-Based “Hollow” Pb/Sn Perovskites with Ideal Band Gap Yield Solar Cells with Higher Efficiency and Stability. *J. Am. Chem. Soc.* **141**, 8627–8637 (2019).
11. Hu, S., Otsuka, K., Murdey, R., Nakamura, T., Truong, M. A., Yamada, T., Handa, T., Matsuda, K., Nakano, K., Sato, A., Marumoto, K., Tajima, K., Kanemitsu, Y. & Wakamiya, A. Optimized carrier extraction at interfaces for 23.6% efficient tin–lead perovskite solar cells. *Energy Environ. Sci.* **15**, 2096–2107 (2022).
12. Kapil, G., Bessho, T., Maekawa, T., Baranwal, A. K., Zhang, Y., Kamarudin, M. A., Hirotsu, D., Shen, Q., Segawa, H. & Hayase, S. Tin-Lead Perovskite Fabricated via Ethylenediamine Interlayer Guides to the Solar Cell Efficiency of 21.74%. *Adv. Energy Mater.* **11**, 2101069 (2021).
13. Kapil, G., Bessho, T., Sanehira, Y., Sahamir, S. R., Chen, M., Baranwal, A. K., Liu, D., Sono, Y., Hirotsu, D., Nomura, D., Nishimura, K., Kamarudin, M. A., Shen, Q., Segawa, H. & Hayase, S. Tin-Lead Perovskite Solar Cells Fabricated on Hole Selective Monolayers. *ACS Energy Lett.* **7**, 966–974 (2022).
14. Datta, K., Wang, J., Zhang, D., Zardetto, V., Remmerswaal, W. H. M. M., Weijtens, C. H. L. L., Wienk, M. M. & Janssen, R. A. J. J. Monolithic All-Perovskite Tandem Solar Cells with Minimized Optical and Energetic Losses. *Adv. Mater.* **34**, 2110053 (2022).
15. Zheng, X., Chen, B., Dai, J., Fang, Y., Bai, Y., Lin, Y., Wei, H., Zeng, X. C. & Huang, J. Defect passivation in hybrid perovskite solar cells using quaternary ammonium halide anions and cations. *Nat. Energy* **2**, 17102 (2017).
16. Saidaminov, M. I., Kim, J., Jain, A., Quintero-Bermudez, R., Tan, H., Long, G., Tan, F., Johnston, A., Zhao, Y., Voznyy, O. & Sargent, E. H. Suppression of atomic vacancies via incorporation of isovalent small ions to increase the stability of halide perovskite solar cells in ambient air. *Nat. Energy* **3**, 648–654 (2018).
17. Lin, R., Xiao, K., Qin, Z., Han, Q., Zhang, C., Wei, M., Saidaminov, M. I., Gao, Y., Xu, J., Xiao, M., Li, A., Zhu, J., Sargent, E. H. & Tan, H. Monolithic all-perovskite tandem solar cells with 24.8% efficiency exploiting comproportionation to suppress Sn(ii) oxidation in precursor ink. *Nat. Energy* **4**, 864–873 (2019).

18. Yu, Z., Chen, X., Harvey, S. P., Ni, Z., Chen, B., Chen, S., Yao, C., Xiao, X., Xu, S., Yang, G., Yan, Y., Berry, J. J., Beard, M. C. & Huang, J. Gradient Doping in Sn–Pb Perovskites by Barium Ions for Efficient Single-Junction and Tandem Solar Cells. *Adv. Mater.* **34**, 2110351 (2022).
19. Yu, Z., Yang, Z., Ni, Z., Shao, Y., Chen, B., Lin, Y., Wei, H., Yu, Z. J., Holman, Z. & Huang, J. Simplified interconnection structure based on C60/SnO_{2-x} for all-perovskite tandem solar cells. *Nat. Energy* **5**, 657–665 (2020).
20. Unger, E. L., Kegelmann, L., Suchan, K., Sörell, D., Korte, L. & Albrecht, S. Roadmap and roadblocks for the band gap tunability of metal halide perovskites. *J. Mater. Chem. A* **5**, 11401–11409 (2017).
21. Datta, K., van Gorkom, B. T., Chen, Z., Dyson, M. J., van der Pol, T. P. A., Meskers, S. C. J., Tao, S., Bobbert, P. A., Wienk, M. M. & Janssen, R. A. J. Effect of Light-Induced Halide Segregation on the Performance of Mixed-Halide Perovskite Solar Cells. *ACS Appl. Energy Mater.* **4**, 6650–6658 (2021).
22. Tong, J., Jiang, Q., Ferguson, A. J., Palmstrom, A. F., Wang, X., Hao, J., Dunfield, S. P., Louks, A. E., Harvey, S. P., Li, C., Lu, H., France, R. M., Johnson, S. A., Zhang, F., Yang, M., Geisz, J. F., McGehee, M. D., Beard, M. C., Yan, Y., *et al.* Carrier control in Sn–Pb perovskites via 2D cation engineering for all-perovskite tandem solar cells with improved efficiency and stability. *Nat. Energy* **7**, 642–651 (2022).
23. Cao, J., Loi, H., Xu, Y., Guo, X., Wang, N., Liu, C., Wang, T., Cheng, H., Zhu, Y., Li, M. G., Wong, W. & Yan, F. High-Performance Tin–Lead Mixed-Perovskite Solar Cells with Vertical Compositional Gradient. *Adv. Mater.* **34**, 2107729 (2022).
24. Braly, I. L., DeQuilettes, D. W., Pazos-Outón, L. M., Burke, S., Ziffer, M. E., Ginger, D. S. & Hillhouse, H. W. Hybrid perovskite films approaching the radiative limit with over 90% photoluminescence quantum efficiency. *Nat. Photonics* **12**, 355–361 (2018).
25. Sahamir, S. R., Kamarudin, M. A., Ripolles, T. S., Baranwal, A. K., Kapil, G., Shen, Q., Segawa, H., Bisquert, J. & Hayase, S. Enhancing the Electronic Properties and Stability of High-Efficiency Tin-Lead Mixed Halide Perovskite Solar Cells via Doping Engineering. *J. Phys. Chem. Lett.* **13**, 3130–3137 (2022).
26. Paniagua, S. A., Hotchkiss, P. J., Jones, S. C., Marder, S. R., Mudalige, A., Marrikar, F. S., Pemberton, J. E. & Armstrong, N. R. Phosphonic Acid Modification of Indium–Tin Oxide Electrodes: Combined XPS/UPS/Contact Angle Studies. *J. Phys. Chem. C* **112**, 7809–7817 (2008).
27. Werner, J., Moot, T., Gossett, T. A., Gould, I. E., Palmstrom, A. F., Wolf, E. J., Boyd, C. C., van Hest, M. F. A. M., Luther, J. M., Berry, J. J. & McGehee, M. D. Improving Low-Bandgap Tin–Lead Perovskite Solar Cells via Contact Engineering and Gas Quench Processing. *ACS Energy Lett.* **5**, 1215–1223 (2020).
28. Han, Q., Wei, Y., Lin, R., Fang, Z., Xiao, K., Luo, X., Gu, S., Zhu, J., Ding, L. & Tan, H. Low-temperature processed inorganic hole transport layer for efficient and stable mixed Pb–Sn low-bandgap perovskite solar cells. *Sci. Bull.* **64**, 1399–1401 (2019).
29. Xiao, K., Wen, J., Han, Q., Lin, R., Gao, Y., Gu, S., Zang, Y., Nie, Y., Zhu, J., Xu, J. & Tan, H. Solution-processed monolithic all-perovskite triple-junction solar cells with efficiency exceeding 20%. *ACS Energy Lett.* **5**, 2819–2826 (2020).
30. Saive, R., Mueller, C., Schinke, J., Lovrincic, R. & Kowalsky, W. Understanding S-shaped

- current-voltage characteristics of organic solar cells: Direct measurement of potential distributions by scanning Kelvin probe. *Appl. Phys. Lett.* **103**, 243303 (2013).
31. Saive, R. S-Shaped Current–Voltage Characteristics in Solar Cells: A Review. *IEEE J. Photovoltaics* **9**, 1477–1484 (2019).
 32. Wang, J., Datta, K., Weijtens, C. H. L., Wienk, M. M. & Janssen, R. A. J. Insights into Fullerene Passivation of SnO₂ Electron Transport Layers in Perovskite Solar Cells. *Adv. Funct. Mater.* **29**, 1905883 (2019).
 33. Datta, K. Mixed-Halide Perovskite Semiconductors for Multijunction Photovoltaics. (Eindhoven University of Technology, 2022).
 34. Illiberi, A., Roozeboom, F. & Poodt, P. Spatial Atomic Layer Deposition of Zinc Oxide Thin Films. *ACS Appl. Mater. Interfaces* **4**, 268–272 (2012).

Chapter 5

Proton exchange membranes for water electrolysis

Abstract

Ionomers based on fluorinated aromatic backbones with sulfonic acid functional groups are a promising group of materials to replace perfluorosulfonic acid proton exchange membranes such as Nafion. Herein, four ionomers based on pentafluorostyrene and poly(arylene thioether)s blended with polybenzimidazole derivatives were compared with Nafion NRE-212, regarding the water electrolysis performance and hydrogen permeability. Despite most of the blend membranes having better ion conductivity and ion exchange capacity than Nafion, Nafion still achieved lower potentials at all tested current densities. The excessive water uptake of the blend membranes, and associated swelling, resulted in increased ohmic losses due to thickening and also, increased mass transfer losses at the electrodes. Steady-state stability and posterior characterization showed a global resistance increase. The best initial performing blend membrane showed the highest performance loss. Regarding hydrogen permeability, it was found that Nafion had the lower permeability, which was also ascribed to higher water uptake of the remaining membranes.

5.1. Introduction

Proton exchange membranes (PEM) typically consist of an inert polymer backbone functionalized with negatively charged functional groups (e.g. SO_3^-). PEMs appeared in the late 1950s/early 1960s, referred to as solid polymer electrolytes at the time, and they have been used for water electrolysis and other electrochemical technologies since then.^{1,2} The continuously growing research interest on PEMs arises from the ability of not only providing ion conduction as well as preventing the mixing of reactants or products, and thus, avoiding the use of corrosive and concentrated liquid electrolytes. For example, in the case of PEM water electrolysis, the porous electrodes are directly in contact with the PEM that serves as permeation barrier for the formed hydrogen (H_2) and oxygen (O_2) and that transports the protons (H^+) formed at the anode to the cathode and deionized water can be used as feed.

PEMs should be designed to be chemically and mechanically stable and have high ion conductivity and low permeability to be employed in real-life applications, ensuring exceptional performance and long-term stability. Perfluorosulfonic acid (PFSA) membranes have been the most widely used material for PEM such as the benchmark Nafion membranes developed by DuPont.³ The polytetrafluoroethylene backbone in PFSA membranes provides excellent mechanical and chemical stability while the vinyl ether side chains functionalized with sulfonic acid groups provide high proton conductivities.⁴ However, the complex synthesis of Nafion leads to high manufacturing costs, further contributing to the large investment required for proton exchange membrane water electrolysis (PEMWE).⁵ Other drawbacks of PFSA membranes include dehydration of the ionic clusters above 80 °C, limiting the operation at high temperatures, and relatively high gas permeability that results in the use of thicker membranes to reduce gas crossover, which will also increase the ohmic resistance. These have been responsible for the significant effort in the last few years to develop membranes based on different polymeric materials that could potentially show similar or better performances than Nafion at lower economic cost.^{2,4,6}

A promising group of polymers that has been extensively studied as possible replacement for PFSA membranes are poly(arylenes) (PA). PAs consist of an aromatic backbone, e.g. poly(phenylene ether) and poly(ether ketones), that is typically functionalized with sulfonic acid groups but phosphonic acid has also been used instead.^{4,7} PA are usually cheaper than PFSA membranes while also presenting excellent mechanical and thermal stability (up to 200 °C) and low gas permeability.² These polymers, depending on the degree of sulfonation, have also

shown excellent ion conductivities and ion exchange capacities (IEC) that are often higher than Nafion. For example, Schuster et al. reported the synthesis of a poly(phenylene sulfone) in which each phenyl ring is monosulfonated, resulting in an IEC of 4.5 mmol g⁻¹ (mmol g⁻¹ is the millimoles of ion-exchange groups in 1 g dry membrane) and ion conductivity slightly above 0.1 S cm⁻¹ (50% relative humidity (RH) and 120 °C) for 100% degree of sulfonation. Furthermore, the water uptake (**Eq. 5.1**) was found to be more than double of Nafion. The high IEC, combined with the high water uptake, caused the polymer to be water soluble, and thus, rendering it unsuitable for water electrolysis.⁸ Furthermore, the high water uptake leads to excessive swelling, negatively impacting the mechanical properties of the membrane, causing loss of mechanical integrity. Takamaku et al. observed similar issues for their tetrasulfonated poly(phenylene sulfone) (IEC = 8.02 mmol g⁻¹ and proton conductivity at 50% RH and 120 °C was 0.09 S cm⁻¹).⁹ In both reports, the main target was to obtain a PEM that would provide high proton conductivities at low RH conditions for fuel cells and thus, having a water soluble polymer is not as an issue as in water electrolysis. The water uptake is therefore a very important parameter which is defined in the following equation:

$$WU = \frac{w_{\text{wet}} - w_{\text{dry}}}{w_{\text{dry}}} \quad (5.1)$$

where w_{wet} and w_{dry} are the wet membrane weight and the dry weight membrane.

Reducing the water uptake and swelling of poly(arylene)-based PEMs while maintaining high ion conductivity has driven researchers to introduce other functional groups such as fluorine.^{4,10-12} The fluorine functional groups increase the hydrophobicity of the polymer, reducing the water uptake while their high electronegativity, by increasing the electron withdrawing effect, helps to stabilize the dissociation of the sulfonic acid groups to sulfonate (SO₃⁻). In addition, the C-F bonds are far stronger than C-H bonds, further enhancing the overall stability of the polymer.¹³ Miyatake et al.¹⁰ varied the amount of trifluoromethyl groups in a sulfonated polyimide between 0 and 60 mol%. They found that despite a water uptake decrease from 68 wt% (at 10 mol%) to around 50 wt% (at 30 mol%), the proton conductivity would be just slightly lower at temperatures below 100 °C (100% RH), possibly due to an almost constant hydration number λ (mol H₂O/mol SO₃H, **Eq. 5.2**). Nonetheless, above 100 °C, the polymer with 30 mol% of trifluoromethyl groups would actually show two orders of magnitude higher conductivity. Without any trifluoromethyl groups, the water uptake is 102 wt%, but no proton conductivity data is shown.

$$\lambda = 1000 \frac{\text{WU}}{18 \times \text{IEC} (\text{mmol g}^{-1})} \quad (5.2)$$

Atanasov and Kerres introduced in 2011 a new class of polymers suitable for proton exchange membranes based on fluorinated polystyrene.¹⁴ In that report, the authors showed the phosphonation of polypentafluorostyrene (PFS) on the para position. The phosphonated polymer, named PWN in the report, reached a $\text{IEC} = 7 \text{ mmol g}^{-1}$ ($\text{IEC}_{\text{theoretical}} = 7.8 \text{ mmol g}^{-1}$) and ion conductivity slightly higher than Nafion at $110 - 160 \text{ }^\circ\text{C}$ and $P_{\text{H}_2\text{O}} = 1 \text{ atm}$. The water uptake of PWN is a few times higher than of Nafion but due to the high IEC, both ionomers have similar hydration numbers, i.e., number of water molecules per functional groups (PO_3^{2-} or SO_3^-). The relatively high hydration number of PWN is ascribed to the enhanced acidity of phosphonic acid group, due to the fluorine groups, in PWN in comparison to the corresponding phosphonated polystyrene. PFS shows an already high decomposition temperature ($T_{\text{decomp}} = 285 \text{ }^\circ\text{C}$) but PWN had an even higher decomposition temperature at around $340 \text{ }^\circ\text{C}$, showing the excellent thermal stability of this polymer. However, similarly to what is observed in Nafion, the conductivity drops abruptly at higher temperatures ($T > 100 \text{ }^\circ\text{C}$), likely due to a steep decrease in water uptake and thus, hydration number at lower RH.

In a later paper, Atanasov et al. reports the synthesis and characterization of the sulfonated equivalent of PWN, poly(4-vinyl-2,3,5,6-tetrafluorophenylsulfonic acid), also referred to as sulfonated polypentafluorostyrene (sPFS).¹⁵ Due to the higher acidity of the sulfonic acid group ($\text{p}K_{\text{a}} = -1.99 \pm 0.5$, according to the authors) in comparison to the phosphonic acid ($\text{p}K_{\text{a}} = 0.47 \pm 0.36$, for $\text{PO}_3\text{H}_2 \rightarrow \text{PO}_3\text{H}^-$), the ion conductivity of sPFS is higher than PWN, and thus, higher than Nafion. In addition, the ion conductivity of sPFS appears to be less affected by the water content than for PWN, Nafion, and the sulfonated poly(phenylene sulfone) described by Schuster et al.⁸ referred earlier in this section. This is especially advantageous for fuel cells, but also, for higher temperature water electrolysis. The sPFS ionomer reached an IEC of 3.2 mmol g^{-1} ($\text{IEC}_{\text{theoretical}} = 3.9 \text{ mmol g}^{-1}$), which is lower than the IEC of PWN, due to having only one exchangeable proton instead of two. The water uptake and hydration number were similar for both ionomers, suggesting that there is little dependence of these parameters on the functional group. However these polymers, PWN and sPFS, show weak mechanical stability and poor film-forming properties due to their high functionalization degree that leads to water-soluble polymers.^{7,15,16}

Alternatively, the mechanical stability of these ionomers can be improved via copolymerization or simply by mixing them with other polymers, also called blending agents.^{5,7,16–18} The addition of such polymeric structures constitutes a trade-off between ionic transport properties (conductivity and IEC) and chemical and mechanical properties. The co-monomer or blending agent are typically not ion conductive and therefore, an appropriate ratio between these polymers is required. Bülbül et al. prepared blend membranes consisting of PWN (degree of phosphonation of 74%) and poly(hexafluoroisopropylidene benzimidazole) (F6PBI) with different PWN/F6PBI weight ratios.⁷ It was shown that by decreasing the ratio from 9:1 to 7:3, the ion conductivity dropped readily from 22.2 to 5.1 mS cm⁻¹ and it was similar for the other ratios, 5:5 and 1:9. It is also mentioned that the blend membrane with 9:1 ratio reached a similar water uptake and ion conductivity to Nafion 112 in the same measuring conditions, despite having an IEC of 4.66 mmol g⁻¹. Furthermore, all tested blend membranes showed degradation temperatures above 400 °C, higher than for the sole PWN (100% phosphonated) mentioned earlier, which is attributed to higher thermal resistance of the F6PBI. Earlier, Wei et al.¹⁷ had also prepared a blend membrane but based on partially sulfonated poly(ether ether ketone) (SPEEK) and polyether sulfone (PES) in a ratio of 70:30 in weight and evaluated the ionic conductivity, swelling ratio and water electrolysis performance. They found that by increasing the degree of sulfonation from 62% to 68%, the swelling ratio would increase from roughly 10% to 20% at 60 °C while the conductivity would increase an order of magnitude. These reports show that blend membranes are an excellent strategy to achieve mechanically stable membranes based on many highly ion conductive polyelectrolytes that otherwise would be unsuitable for use.

In the present chapter, PEMWE is carried out using different blend membranes based on sPFS and sulfonated poly(octofluorobiphenyl-alt-thiobisbenzene) and the results are compared with state-of-the-art Nafion NRE-212. The membranes were prepared by blending the ionomers with either F6PBI or poly(1-(4,4'-diphenylether)-5-oxybenzimidazole)-benzimidazole)) (PBI-OO) to improve film-formation properties and mechanical stability. Moreover, the hydrogen permeability of each membrane during operation was also measured by connecting the anode outlet to a gas chromatograph. The synthesis and membrane preparation were outside of the scope of this chapter and they will be reported by the early-stage researchers who developed them in their respective PhD theses.

5.2. Ionomers and their blend membranes

The ionomers and the membranes used in this chapter were synthesized by fellow early-stage researchers of the eSCALED project and their structures are shown in **Figure 5.1**. The ionomers shown in Figure 5.1a, b and c are based on poly(pentafluorostyrene) while the ionomer in Figure 5.1d is based on poly(octofluorobiphenyl-*alt*-thiobisbenzene). sPFS-s-BuAc was 35 – 40 mol% of sPFS whereas sPFS-s-OcAc was 75 mol% sPFS. These ionomers, when fully sulfonated, are water soluble and/or show large swelling ratios and thus, it was required to blend them with water insoluble polymers, referred herein as blending agents, to prepare more mechanically stable membranes. sPFS and sPFS-s-BuAc were blended with F6PBI while sPFS-s-OcAc and PSAT were blended with PBI-OO.^{7,16,19} The ionomer to PBI weight ratios are shown in Figure 5.1 next to each ionomer name.

The PBI-based polymers improve the stability by ionic cross-linking through a proton exchange between the sulfonic acid group of the ionomers and the imine nitrogen of benzimidazole (**Figure 5.2**) as firstly proposed by Kerres et al.¹⁸ It is claimed that the acid-base blend membranes enhance the membrane stability with minimal flexibility losses due to the ionic polymer interaction while, for example, covalently cross-linked blend membranes are highly brittle due to the inflexibility of the covalent network.^{7,20}

Table 5.1 summarizes a few key parameters of these blend membranes that have direct impact on their water electrolysis efficiency. The ion conductivity was measured in 0.5 M H₂SO₄ or 0.5 M HCl at room temperature. These membranes show improved ion conductivity and ion exchange capacity when compared to the standard Nafion membrane (NRE-212), suggesting that they could be a viable replacement. However, these membranes had to be stored in MilliQ water because otherwise they would become quite brittle if fully dry. The brittleness of the dried membranes made handling more difficult and hindered the preparation of the membrane-electrode assemblies (MEAs) by the usual approach described in chapter 2. In contrast, the MEAs were prepared using a catalyst-coated substrate (CCS) approach, i.e., the catalyst inks were spray coated directly on the porous transport layers (PTLs). This was followed by a hot-press step of the PTLs and the wet membranes, also to prevent breaking the membranes during this step. The CCS approach typically results in lower electrochemical performance than catalyst-coated membrane (CCM), because it leads to a worse membrane-catalyst layer interface, affecting the electrochemical surface area and the charge transfer resistance.^{21–23} The hot-press step was included to improve the membrane-catalyst layer interface and minimize this performance reduction.

Moreover, since the blend membranes were stored in MilliQ water, they were immersed in 0.5 M H₂SO₄ for at least one day to ensure full protonation. It is important to note that the catalyst inks were prepared with Nafion ionomer except for the MEA with sPFS blend membrane, where sPFS ionomer (1 wt% in DMSO) was used.

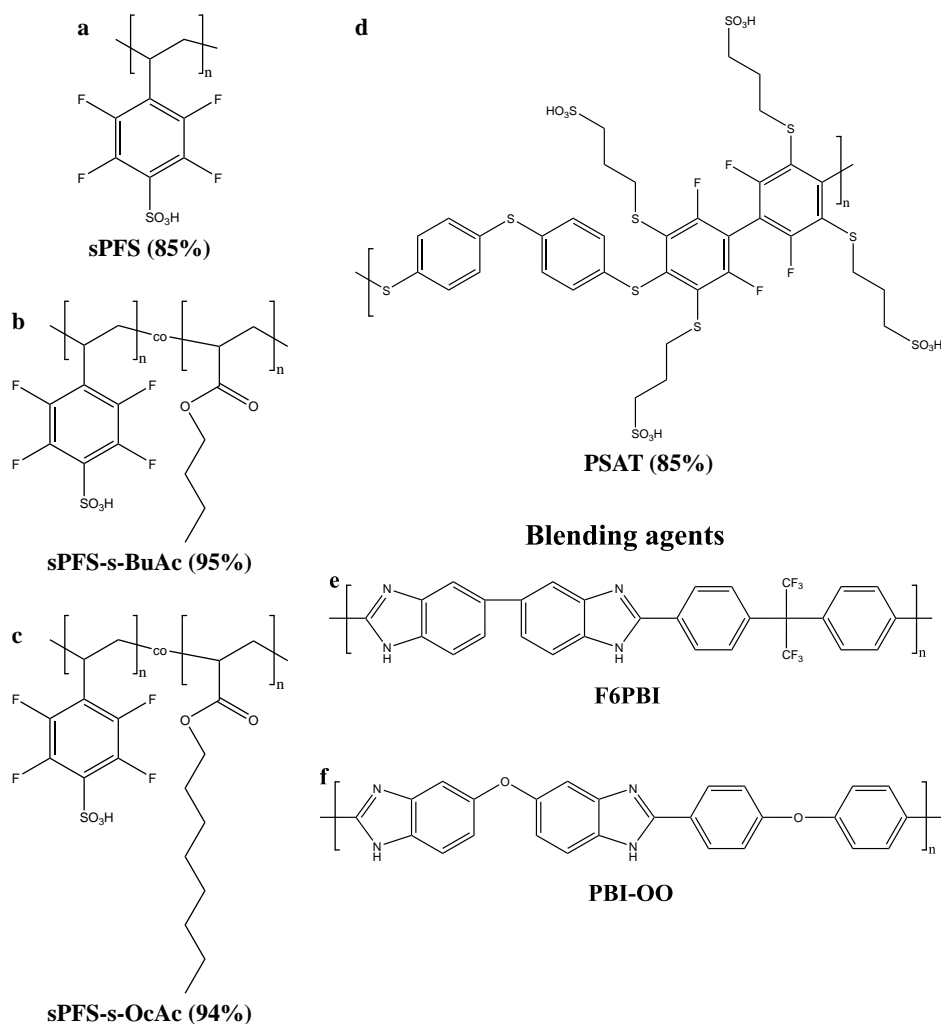


Figure 5.1: Ionomer and blending agent structures. a) sPFS: sulfonated polypentafluorostyrene. b) sPFS-s-BuAc: sulfonated poly(pentafluorostyrene-s-butylacrylate). c) sPFS-s-OcAc: sulfonated poly(pentafluorostyrene-s-octylacrylate). d) PSAT: poly(fluorinated sulfonated propanethiobiphenyl-alt-thiobisbenzene). e) F6PBI: poly(hexafluoropropylidene benzimidazole). f) PBI-OO: poly(1-(4,4'-diphenyl ether)-5-oxybenzimidazole-benzimidazole).

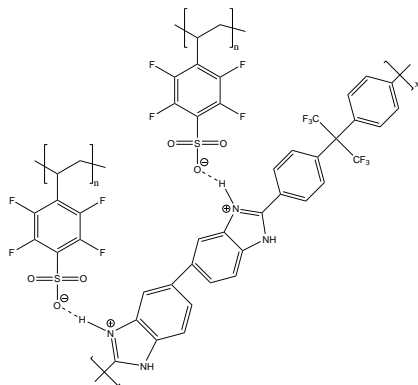


Figure 5.2: Schematic representation of ionic cross-linking between sPFS and F6PBI. Based on ref. ⁷.

Table 5.1: Blend membrane parameters.

	$t_{\text{wet}} / \mu\text{m}$	$\sigma_m / \text{mS cm}^{-1}$	IEC / mmol g^{-1}	WU _{60 °C} / %	$\lambda_{60 °C} / -$
Nafion NRE-212*	84	97.7	0.909	34.36	21.00
sPFS	50 ± 1 (used)	130	1.093	79.34	40.30
sPFS-s-BuAc	81 ± 3	36.8	0.5911	150.2	141.5
sPFS-s-OcAc	125 ± 16	145	2.67**	570.0	171.39**
PSAT	91 ± 34	179	1.09	105.3	53.66

*values from ref. ²⁴, **theoretical value

5.3. Water electrolysis with blend membranes

Figure 5.3 shows the electrochemical characterization performed at ~ 60 °C for each new fluorinated membrane and the benchmark Nafion NRE-212 membrane as comparison. The electrochemical cell follows the same assembly method and materials described in chapter 2, except for the PEM. In the polarization curves (Figure 5.3a), the sPFS-s-BuAc MEA reaches the highest cell potential at all current densities, reaching 2.041 V at 1 A cm⁻². This could be expected since this membrane also has the lowest ion conductivity out of all tested membranes. PSAT and sPFS-s-OcAc reached cell potentials of 1.784 V and 1.792 V at 1 A cm⁻², respectively, that are just slightly higher than the cell potential of 1.741 V at 1 A cm⁻² obtained with the Nafion membrane. Moreover, both membranes fulfilled the goal set in chapter 2 of reaching a current density of 1 A cm⁻² at a cell potential below 1.8 V.

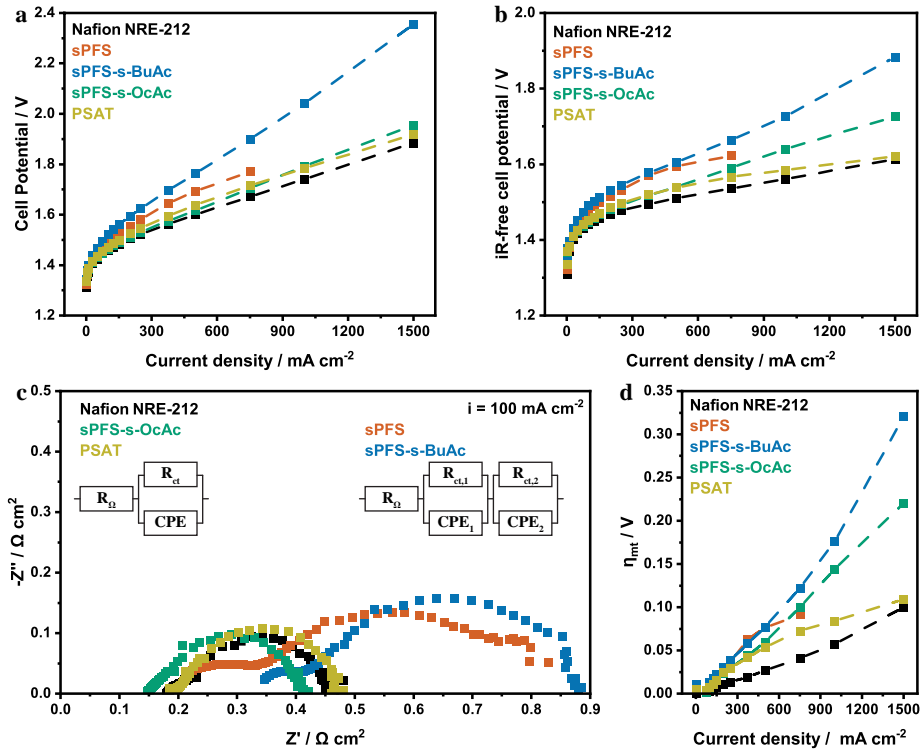


Figure 5.3: Electrochemical characterization of the new blend membranes compared with Nafion NRE-212. a) Polarization curves. b) iR_{Ω} -free polarization curves c) Electrochemical impedance spectroscopy (EIS) carried out before the polarization curves at 100 mA cm^{-2} . The shown EIS of sPFS-s-BuAc was performed after recording the polarization curves. Inset: Equivalent electrical circuits used to fit the EIS data. d) Mass transfer overpotential η_{mt} calculated by subtracting the kinetic overpotential (η_{kin}) and ohmic losses (iR_{Ω}) from the cell potential (E_{cell}).

Table 5.2: Fitted resistance parameters from electrochemical impedance spectroscopy before and after 18 h steady-state stability (in brackets).

	$R_{\Omega} / \Omega \text{ cm}^2$	$R_{ct,1} / \Omega \text{ cm}^2$	$R_{ct,2} / \Omega \text{ cm}^2$
Nafion NRE-212	0.190 ± 0.002 (0.207 ± 0.002)	0.286 ± 0.008 (0.255 ± 0.004)	–
sPFS	0.197 ± 0.007 (0.055 ± 0.013)	0.110 ± 0.013 (0.148 ± 0.013)	0.542 ± 0.014 (0.624 ± 0.030)
sPFS-s-BuAc	0.314 ± 0.008 (0.324 ± 0.006)	0.117 ± 0.013 (0.094 ± 0.010)	0.458 ± 0.008 (0.453 ± 0.008)
sPFS-s-OcAc	0.151 ± 0.002 (0.147 ± 0.003)	0.271 ± 0.006 (0.424 ± 0.01)	–
PSAT	0.199 ± 0.001 (0.372 ± 0.03)	0.280 ± 0.004 (5.00 ± 0.05)	–

It was expected that the sPFS membrane would reach the lowest potential of all membranes, since it showed the best area conductance $\frac{\sigma}{t_{\text{wet}}}$ (S cm^{-2}), but this was not the case. In contrast to the other membranes, the catalyst inks used for the sPFS blend membrane were prepared with sPFS ionomer instead of Nafion to favor an adequate catalyst layer–membrane interface. However, the sPFS ionomer had to be first solubilized in DMSO (1 w/v%) prior to be mixed with the catalyst powder, 2–propanol and water. It is known that DMSO can deactivate the Pt catalyst, by replacing the adsorbed hydrogen during the reaction and thus, the lower performance of this membrane may suggest an incomplete evaporation of the DMSO, leaving some leftover solvent on the catalyst layer.^{25,26} This is further supported by the ohmic resistance corrected polarization curves (Figure 5.3b), especially at low current densities where the reaction kinetics are the limiting factor. The sPFS and the sPFS–s–BuAc curves are quite similar, suggesting similar kinetics, in spite of the supposedly better catalyst layer–membrane interface due to the use of same ionomer for the catalyst ink and membrane and higher IEC for the sPFS blend membrane.

The electrochemical impedance spectroscopy (EIS) at 100 mA cm^{-2} is shown in Figure 5.3c. The EIS data were fitted to the two equivalent electrical circuits shown in the inset of Figure 5.3c where R_{Ω} is the ohmic resistance, R_{ct} is charge transfer resistance and CPE is a constant phase element. The R_{Ω} and R_{ct} results are summarized in **Table 5.2**. The ohmic resistance R_{Ω} is related to the membranes' resistance while the charge transfer resistance R_{ct} is associated with the charge transfer within the catalyst layer–membrane interface. Thus, R_{ct} is connected with membrane IEC since the number of H^{+} will affect charge transfer at that interface. For sPFS and sPFS–s–BuAc, two semicircles are clearly present, which may be associated with the hydrogen ($R_{\text{ct},1}$ and CPE_1 at high frequency) and oxygen evolution reaction ($R_{\text{ct},2}$ and CPE_2 at low frequency) at the measured current density.^{23,27}

The sPFS–s–BuAc shows the highest R_{Ω} of all membranes, in agreement with reaching the highest potentials within the tested current density range. The sPFS and PSAT blend membranes have the highest area conductances at room temperature (Table 5.1) but show higher R_{Ω} than Nafion. The thickness increase associated to the membrane swelling is the most likely reason responsible for the higher resistance of PSAT and sPFS. In contrast, sPFS–s–OcAc has the lowest R_{Ω} . After the hot–press step during the membrane–electrode assembly preparation of this membrane, the edges of the membrane would be easily teared, alluding to excessive thinning of membrane, weakening it. This thinning could

not be ascertained after disassembling the cell as the membrane would easily break and tear while delaminating the PTLs.

The sPFS and sPFS–s–BuAc blend membrane show similar R_{ct} s but much larger than the remaining PEMs. For sPFS–s–BuAc, this might be attributed to a low IEC as less protons are readily available.³ While for sPFS, the high R_{ct} s may arise due to the use of DMSO in the catalyst ink as referred previously, causing the deactivation of the catalyst. The remaining membranes have R_{ct} between 0.271 and 0.286 $\Omega\text{ cm}^2$ with the Nafion membrane actually showing the higher value, suggesting that the catalyst layer–membrane interface is improved, which can be an effect of the higher IEC of PSAT and sPFS–s–BuAc. The higher water uptake of these membranes can also affect the R_{ct} because it leads to higher compression between the membrane and the catalyst–coated PTLs, improving this interface. However, such membrane swelling might also cause the membrane to infiltrate the pores of PTLs, also having an adverse effect on the performance of these membranes since the polarization curves (Figure 5.3a) and the iR -free polarization curves (Figure 5.3b) of PSAT and sPFS–s–BuAc are still worse than of Nafion. The filled pores may result in less space for the evolved gas to escape and thus, increased mass transfer losses η_{mt} occur (Figure 5.3d).

Subsequently, the stability of the MEAs with each membrane were evaluated by applying 250 mA cm^{-2} for 18 h (Figure 5.4a). The degradation rates increase in the order of sPFS–s–BuAc < sPFS < Nafion < sPFS–s–OcAc < PSAT, ranging from 0.339 to 12.2 mV h^{-1} . Overall, these rates are considerably high as typical values are around a few $\mu\text{V h}^{-1}$ instead and this was attributed in chapter 2 to the oxide formation on the titanium flow fields surface. Hence, only the rate increase order shall be discussed. After the 18 h, the polarization curves and EIS with each membrane was remeasured (Figure 5.4b–d and Table 5.2). In general, a potential increase in the polarization curves of every membrane was observed related to an overall increase in ohmic resistance, except for sPFS and sPFS–s–OcAc. The increase in R_{Ω} most probably arises from the oxide passivation layer on the titanium flow fields of the electrochemical cell. Instead, the R_{Ω} of sPFS decreased, but the origin of such decrease was not further studied. Nonetheless, at low current densities, this effect was surpassed by an increase in R_{ct} s ($R_{ct,1}$ and $R_{ct,2}$), resulting in an increase in activation losses in the polarization curves.²⁸ For sPFS–s–OcAc, the R_{ct} also suffered the largest change, reaching similar values to sPFS, while the R_{Ω} remained roughly constant, which could explain the similar polarization curves observed for these two membranes. For PSAT, the R_{Ω} almost doubled but, the highest increase was in the R_{ct} , in agreement with a major

increase in activation losses observed at low current densities in the polarization curves.

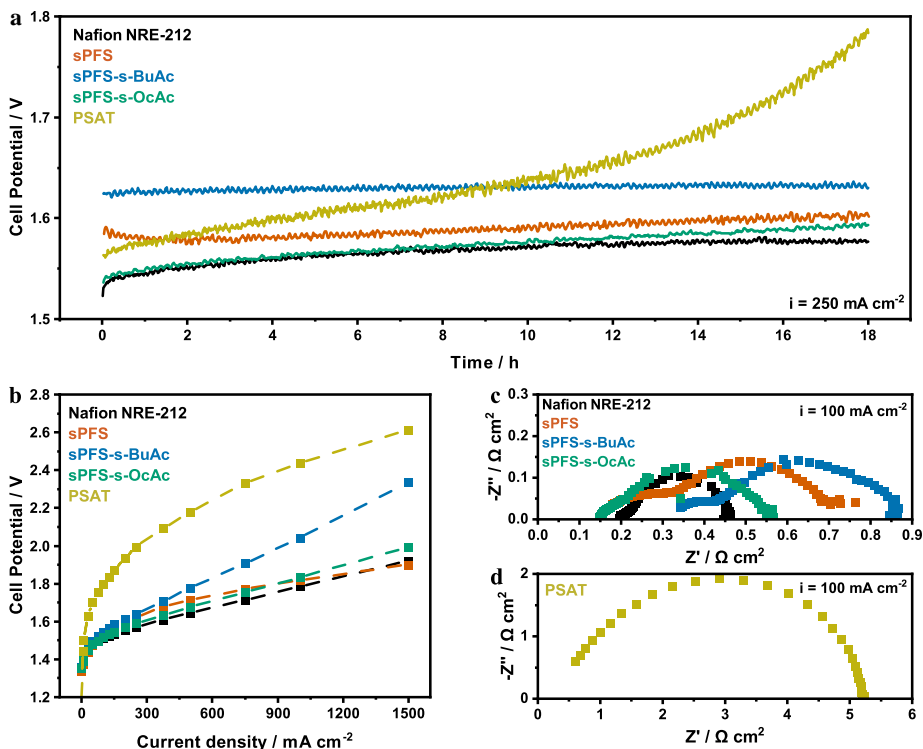


Figure 5.4: Steady-state stability and subsequent electrochemical characterization. a) Constant current density (250 mA cm^{-2}) for 18 hours. b) Polarization curves after 18 h of steady-state stability. c) and d) Electrochemical impedance spectroscopy carried out after 18 h of steady-state stability at 100 mA cm^{-2} .

During the 18 h stability measurement, the H_2 present in the anode compartment was simultaneously measured by gas chromatography to evaluate the H_2 crossover and faradaic efficiency (Figure 5.5a). The amount of hydrogen crossing over the membranes and faradaic efficiency were calculated according to Eqs. 5.3 and 5.4, respectively. Eq. 5.4 assumes that only hydrogen evolution takes place at the cathode and the loss of faradaic efficiency is completely due to hydrogen crossover.

$$n_{\text{H}_2} = \int_0^{t_f} \frac{C_{\text{H}_2} F_{\text{N}_2}}{10^6 - C_{\text{H}_2}} dt \quad (5.3)$$

$$\eta = 1 - \frac{2000Fn_{\text{H}_2,t_f}}{60It_f} \quad (5.4)$$

where C_{H_2} is the concentration of H_2 measured by gas chromatography in ppm, F_{H_2} the nitrogen volumetric flow in mL min^{-1} , t the analysis time in min, t_f the total analysis time, F the Faraday constant (96485 C mol^{-1}), n_{H_2,t_f} the total permeated H_2 amount in mol and I the applied current in mA.

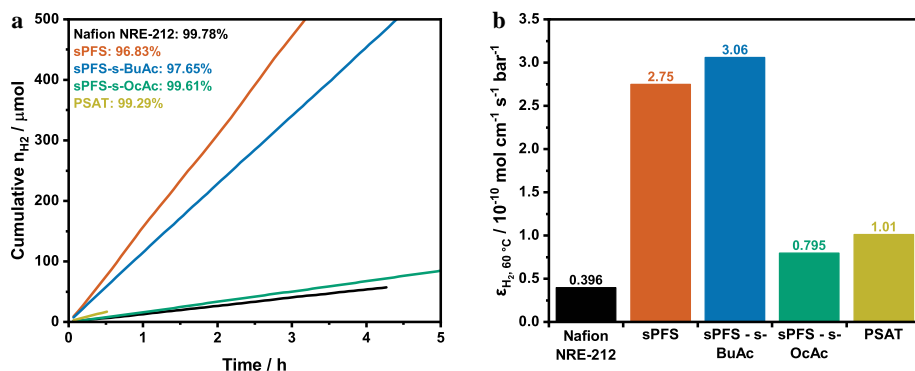


Figure 5.5: Hydrogen permeability of PEMs. a) Cumulative hydrogen amount detected at the anode compartment by gas chromatography. b) Hydrogen permeability at 60°C and atmospheric pressure (balanced pressure approach) calculated for each membrane.

The considerable hydrogen crossover across the sPFS and sPFS-s-BuAc membranes results in a hydrogen concentration at the anode of 6.34% and 4.7% which are above the lower explosivity limit of a H_2/O_2 mixture ($> 4 \text{ mol H}_2\%$), raising a safety issue regarding the use of these membranes. This issue could be avoided if the membranes were thicker, however, that would also increase the ohmic resistance. The other two membranes, which are slightly thicker, sPFS-s-OcAc and PSAT, show faradaic efficiencies approximate similar to that of Nafion NRE-212. Nonetheless, for large scale operation, i.e., several kA, these lower η_f can represent large hydrogen losses.

Since the membrane thickness plays an important role in the hydrogen crossover, the H_2 permeability was calculated as well for a better comparison between all tested membranes. Assuming that H_2 permeation across the membranes occurs only by diffusion according to Fick's law and that the H_2 concentration across the membrane varies linearly with the membrane thickness, the permeability ϵ_{H_2} can be calculated from **Eqs. 5.5 – 5.7** and are shown in Figure 5.5b:

$$\frac{F_{\text{H}_2,\text{anode}}}{A} = -D \frac{\Delta c}{d} \quad (5.5)$$

$$c_{\text{H}_2} = P_{\text{H}_2} S_{\text{H}_2} \quad (5.6)$$

$$\varepsilon_{\text{H}_2} = DS_{\text{H}_2} = -\frac{F_{\text{H}_2,\text{anode}}}{A(P_{\text{H}_2,\text{anode}} - P_{\text{H}_2,\text{cathode}})} d \quad (5.7)$$

where $F_{\text{H}_2,\text{anode}}$ is the hydrogen molar flow through the membrane in mol min^{-1} , A is the active area in cm^2 , D the H_2 diffusion coefficient in the membranes in $\text{cm}^2 \text{s}^{-1}$, c_x and P_x are the concentration and partial pressure of H_2 in the compartment x in mol cm^{-3} and bar, respectively. d is the membrane thickness in cm and S_{H_2} the Henry's constant in $\text{mol cm}^{-3} \text{bar}^{-1}$. It was assumed all permeated hydrogen would leave the cell immediately, and thus, $P_{\text{H}_2,\text{anode}}$ was considered 0 bar.

The hydrogen permeability of the new membranes is much higher than Nafion, as expected from the faradaic efficiencies and respective membrane thicknesses. A possible explanation for such values could be the water uptake values of these membranes. Schalenbach et al. suggest that the membranes' water uptake, and thus, swelling directly influence their gas permeability, with higher values, resulting in higher gas permeabilities. They suggest that gas permeation occurs via a mixed pathway, i.e., both through the solid ionomer phase and through the water-filled pores. Thus, larger swelling values, which imply larger pore sizes, can lead to increased gas permeabilities since permeation is easier through the aqueous phase than through the solid ionomer phase. This highlights the importance of designing new ionomers, not only to reach high ion conductivities and ion exchange capacities but also that have low gas permeabilities, at full hydration, to increase faradaic efficiencies and avoid dangerous gas mixtures.

Recently, a restriction proposal on per- and polyfluoroalkyl substances (PFAS), which also includes PFSA and fluorinated membranes, has been submitted to the European Chemicals Agency (ECHA).²⁹ This proposal submitted under the European Union's Registration, Evaluation, Authorization, and Restriction of Chemicals (REACH) regulation aims to ban the production and use of PFAS due to their health and environmental risks. PFAS-compounds degrade very slowly, ending up in the atmosphere or the ocean for possibly thousands of years and they can lead to health issues such as cancer, liver damage and many others.^{30,31} Before this ban comes into force, research on proton exchange membranes for electrolysis applications therefore needs to focus on non-fluorinated polymers to avoid the use of PFAS-compounds.

5.4. Conclusion

Four sulfonated ionomers based on polypentafluorostyrene and poly(octafluorobiphenyl-*alt*-thiobisbenzene) synthesized within the eSCALED project were tested in a water electrolysis cell and compared with state-of-the-art Nafion NRE-212. To prepare the PEMs, the ionomers were mixed with poly(benzimidazole) derivatives to improve film-formation properties and mechanical stability. The area ion conductance of the membranes (at room temperature) increased in the following order: sPFS > PSAT > Nafion NRE-212 > sPFS-*s*-OcAc > sPFS-*s*-BuAc. In addition to good ion transport properties, PEMs should have a low gas permeability to avoid gas crossover that would result in a drop in faradaic efficiency and a dangerous gas mixture in one of the cell compartments. Hence, the hydrogen permeability of each membrane was measured during continuous operation at 250 mA cm⁻² and 60 °C. The membrane-electrode assemblies were prepared by spray coating the catalysts directly onto the titanium (anode) and carbon (cathode) PTLs, followed by hot-pressing the PTLs and the wet membrane together at 80 °C and 5 MPa for 5 min. This approach was used instead of the typical CCM to avoid drying the membranes as they would become highly brittle and easily break. The electrochemical characterization of all membranes was done in the same electrochemical cell described in chapter 2.

The sPFS-*s*-BuAc membrane had the poorer performance of all membranes, reaching much higher potentials in the polarization curves. EIS showed that both R_{Ω} and R_{ct} were higher than for the other membranes, which was attributed to this membrane's low ion conductivity and ion exchange capacity. The sPFS membrane was expected to have the best overall performance, due to its high ion conductivity, high IEC and also, the MEA with this membrane was prepared with the same ionomer whereas the remaining MEAs were prepared with Nafion ionomer instead. However, the MEA with sPFS showed large activation losses at low current densities which agreed with the high R_{ct} measured by EIS. This was mainly ascribed to an incomplete evaporation of the DMSO used to dissolve the sPFS ionomer for the catalyst inks. The DMSO tends to adsorb on the Pt surface, rendering the active sites unusable for the hydrogen evolution reaction. The other two membranes, PSAT and sPFS-*s*-OcAc, showed better polarization curves than the other two membranes but they were still outperformed by the Nafion membrane. Nonetheless, these membranes had marginally lower R_{ct} s than Nafion and in the case of sPFS-*s*-OcAc, the R_{Ω} was also lower. The lower R_{ct} is most probably an effect of the higher IEC of PSAT and sPFS-*s*-OcAc. In addition, the large water uptake of these membranes might press them against the PTLs, simultaneously improving the R_{Ω} and R_{ct} , but it can

also have a detrimental effect. The excessively swollen membrane by occupying the PTLs' pores, hinders the evolved gas escape, leading to increased mass transfer losses.

Subsequently, the membranes were submitted to a constant current density for 18 h to evaluate their stability, followed by measuring the polarization curves and EIS. The increase in ohmic resistance, related to the increase in potential at higher current densities in the post-stability polarization curves, was partially ascribed to the oxide passivation layer on the titanium flow fields of the electrochemical cell. The largest degradation rate and resistances increase, both R_{Ω} and R_{ct} , was observed for PSAT, causing this membrane to reach much higher potentials in the polarization curves than the remaining membranes. For sPFS, a decrease in R_{Ω} resulted in approximate potentials to Nafion at higher current densities, however, at low current densities, the activation losses were still higher than most membranes, associated to a large increase in R_{ct} .

Ultimately, the hydrogen crossover was evaluated during the continuous operation experiment, with the thinner membranes, sPFS and sPFS-s-BuAc, having the highest crossover values and the others having comparable values to Nafion. The H_2 concentration at the anode with these two membranes were, in fact, above the lower explosivity limit for a H_2/O_2 , indicating that these blend membranes should be thicker to avoid this issue, at the expense of increasing the ohmic resistance. Using the hydrogen crossover values, it was possible to calculate the hydrogen permeability for each membrane. All membranes had permeabilities a few times higher than Nafion. These permeability values are most probably associated with the large water uptake, and consequently, the swelling of these membranes since the hydrogen permeability is higher in the aqueous phase of the membranes. This result further emphasizes the need to design ionomers and therefore, membranes that have excellent ionic transport properties but, have low gas permeabilities while fully hydrated and under operation.

Lastly, all membranes described here are based on fluorinated polymers. With the most recent proposal on the ban of PFAS, the production of PFSA (e.g. Nafion) and fluorinated polymers may be restricted or even completely stopped. Hence, from this point forward, research needs to turn their focus onto non-fluorinated polymers and develop environmentally acceptable and efficient options to avoid the use of PFAS.

5.5. Experimental Section

Materials and membrane–electrode assembly preparation: All materials were used as received without purification. Nafion membrane NRE–212 was purchased from Ion Power. Pt/C (40 wt%) was purchased from Sigma Aldrich. RuO₂ (anhydrous, 99.9%) and Nafion dispersion (D–521) were purchased from Alfa Aesar. RuO₂ was stored inside inert atmosphere. 2–Propanol was purchased from Biosolve. All catalyst inks were prepared using water purified in Millipore system ($\rho > 18 \text{ M}\Omega \text{ cm}$).

The catalyst inks with Nafion ionomer were prepared with 5 wt% solid content, with 3:1 ratio of catalyst to Nafion ionomer in a 2–propanol:water (4:1) mixture. For the inks with sPFS, the solid content was 3 wt% instead, with the same catalyst to ionomer ratio in a 2–propanol:water (4:1) mixture. For the RuO₂ ink, Nafion dispersion or sPFS (1 w/v% in DMSO) was first added to RuO₂ powder, followed by 2–propanol:water. For the Pt/C ink, the catalyst power was first mixed with water to avoid combustion of the carbon particles and, subsequently, the Nafion dispersion and 2–propanol were sequentially added. The inks were ultrasonicated for at least 10 min prior to catalyst deposition. The catalyst inks were manually spray–coated using a pneumatic airbrush (Aerotec) through a stainless–steel mask with a $2 \times 2 \text{ cm}^2$ opening on the respective porous transport layers (PTL) until the target loadings of 1 and 2 mg cm^{-2} for Pt and RuO₂ were reached, respectively. The catalyst loadings were calculated by weighing the PTLs before and after spray coating. The deposition temperature was set to 85 °C (for Nafion) or 105 °C (for sPFS ionomer) to evaporate the solvent upon deposition.

The membranes, except for Nafion NRE–212, were immersed in 0.5 M H₂SO₄ overnight to ensure full protonation of the ionomers and then, washed in Millipore purified water to remove the excess acid. Subsequently, the wet membranes, including Nafion, were hot–pressed between the PTLs at 80 °C and 5 MPa for 5 min.

Water uptake and hydration number measurements: The blend membranes were firstly dried at 50 °C under vacuum for 24 h before weighing (w_{dry}), followed by immersing the membranes in MilliQ water at 60 °C for 5 h and weighed again (w_{wet}). The water uptake was calculated according to Eq. 5.1.

PEM electrochemical cell setup: Water electrolysis tests were carried out in an in–house built PEM – electrolyzer cell ($5 \times 5 \text{ cm}^2$) using high–impact polypropylene (PP) as end plates and titanium current collectors (1 mm thick) with machined parallel flow fields (1 mm wide, channel area: $2.25 \times 2.25 \text{ cm}^2$). Titanium fiber felt ($2 \times 2 \text{ cm}^2$, 0.2 – 0.3 mm, porosity: 53 – 56 %, from Fuel Cell Store) and carbon fiber non–woven fabric ($2 \times 2 \text{ cm}^2$, 255 μm , with MPL, H23 C2, from Quintech) were used as PTLs at the anode and cathode, respectively. The electrolyzer was sealed with PTFE ($5 \times 5 \text{ cm}^2$, 200 mm, from Polyfluor) and closed using a compression force of 0.8 Nm. Polyimide film (Kapton 100HN, 25 μm , from DuPont) was used between the Ti PTL and the membrane to delimit the active area to 1 cm^2 . Millipore purified water ($\rho > 18 \text{ M}\Omega \text{ cm}$) was circulated using a peristaltic pump (Masterflex® L/S® Digital Miniflex®) into both anodic and cathodic compartment at 10 mL min^{-1} . Independent water lines and feeding bottles were used for each compartment. The water bottles were N₂–bubbled to prevent oxygen and hydrogen build–up.

Electrochemical Characterization: Galvanostatic polarization curves and steady–state stability were performed using a 2–channel Keithley 2600 SMU controlled by LabVIEW. The first channel was used to apply the current whereas the second channel was used to measure the voltage across the PEM electrochemical cell. Electrochemical impedance spectroscopy (EIS) was

performed using a potentiostat PGSTAT30 (Autolab) equipped with a frequency analyzer (FRA) module. All measurements were done at 60 °C. Water was circulated through the cell for 1 h to allow membrane swelling and equilibration prior to any measurements. The cell was conditioned by applying 10, 20, 50 and 100 mA cm⁻² for 30 s and then 250 mA cm⁻² for 30 min, followed by EIS with a frequency of 10 kHz–100 mHz at 10, 50 and 100 mA cm⁻². The galvanostatic polarization curve was recorded from 1 to 1500 mA cm⁻². Each current density step was held for 2 min to allow potential stabilization and the average of the last 10 s was taken as the potential value. The first two polarization curves were considered part of the conditioning process and thus, not included here. All polarization curves shown in this work represent an average of the last three polarization curves. Steady – state stability was recorded while applying a current density of 250 mA cm⁻² for 18 h. After the steady–state stability, EIS and three polarization curves were carried out as before.

Gas chromatography was carried out by a compact gas chromatograph CGC 4.0 (Global Analyzer Solutions–Interscience B.V.) controlled by Chromeleon 7 software (Thermo Fischer Scientific). A EL–FLOW Prestige mass flow controller (Bronkhorst Nederland) was used to control the nitrogen flow ($F_{N_2} = 135 \text{ mL min}^{-1}$) through the anode water feeding bottle where the outlet was connected to the CGC 4.0. Once every 3.8 min, a sample was taken into the gas chromatograph for analysis. A thermal conductivity detector (TCD) was used to measure the H₂ content of the flowing gas. The gas chromatograph was calibrated at 3 points using calibration bottles with 5, 100 and 1000 ppm of hydrogen in a nitrogen balance.

5.6. References

1. Grubb, W. T. Ionic Migration in Ion-exchange Membranes. *J. Phys. Chem.* **63**, 55–58 (1959).
2. Ge, X., Zhang, F., Wu, L., Yang, Z. & Xu, T. Current Challenges and Perspectives of Polymer Electrolyte Membranes. *Macromolecules* **55**, 3773–3787 (2022).
3. Siracusano, S., Baglio, V., Stassi, A., Merlo, L., Moukheiber, E. & Arico', A. S. Performance analysis of short-side-chain Aquivion® perfluorosulfonic acid polymer for proton exchange membrane water electrolysis. *J. Memb. Sci.* **466**, 1–7 (2014).
4. Chae, J. E., Lee, S. Y., Baek, S. Y., Song, K. H., Park, C. H., Kim, H.-J. & Lee, K.-S. High-performance multiblock PEMs containing a highly acidic fluorinated-hydrophilic domain for water electrolysis. *J. Memb. Sci.* **638**, 119694 (2021).
5. Bosson, K., Marcasuzaa, P., Bousquet, A., Tovar, G. E. M., Atanasov, V. & Billon, L. para fluoro-thiol clicked diblock-copolymer self-assembly: Towards a new paradigm for highly proton-conductive membranes. *J. Memb. Sci.* **659**, 120796 (2022).
6. Cruz, J. C., Baglio, V., Siracusano, S., Ornelas, R., Ortiz-Frade, L., Arriaga, L. G., Antonucci, V. & Aricò, A. S. Nanosized IrO₂ electrocatalysts for oxygen evolution reaction in an SPE electrolyzer. *J. Nanoparticle Res.* **13**, 1639–1646 (2011).
7. Bülbül, E., Atanasov, V., Mehlhorn, M., Bürger, M., Chromik, A., Häring, T. & Kerres, J. Highly phosphonated polypentafluorostyrene blended with polybenzimidazole: Application in vanadium redox flow battery. *J. Memb. Sci.* **570–571**, 194–203 (2019).
8. Schuster, M., de Araujo, C. C., Atanasov, V., Andersen, H. T., Kreuer, K.-D. & Maier, J. Highly Sulfonated Poly(phenylene sulfone): Preparation and Stability Issues. *Macromolecules* **42**, 3129–3137 (2009).

9. Takamuku, S., Wohlfarth, A., Manhart, A., Räder, P. & Jannasch, P. Hypersulfonated polyelectrolytes: preparation, stability and conductivity. *Polym. Chem.* **6**, 1267–1274 (2015).
10. Miyatake, K., Zhou, H., Matsuo, T., Uchida, H. & Watanabe, M. Proton Conductive Polyimide Electrolytes Containing Trifluoromethyl Groups: Synthesis, Properties, and DMFC Performance. *Macromolecules* **37**, 4961–4966 (2004).
11. Kim, D. S., Robertson, G. P., Guiver, M. D. & Lee, Y. M. Synthesis of highly fluorinated poly(arylene ether)s copolymers for proton exchange membrane materials. *J. Memb. Sci.* **281**, 111–120 (2006).
12. Kim, D. S., Robertson, G. P., Kim, Y. S. & Guiver, M. D. Copoly(arylene ether)s Containing Pendant Sulfonic Acid Groups as Proton Exchange Membranes. *Macromolecules* **42**, 957–963 (2009).
13. Lee, K.-S., Jeong, M.-H., Lee, J.-P. & Lee, J.-S. End-Group Cross-Linked Poly(arylene ether) for Proton Exchange Membranes. *Macromolecules* **42**, 584–590 (2009).
14. Atanasov, V. & Kerres, J. Highly Phosphonated Polypentafluorostyrene. *Macromolecules* **44**, 6416–6423 (2011).
15. Atanasov, V., Bürger, M., Lyonnard, S., Porcar, L. & Kerres, J. Sulfonated poly(pentafluorostyrene): Synthesis & characterization. *Solid State Ionics* **252**, 75–83 (2013).
16. Atanasov, V., Gudat, D., Ruffmann, B. & Kerres, J. Highly phosphonated polypentafluorostyrene: Characterization and blends with polybenzimidazole. *Eur. Polym. J.* **49**, 3977–3985 (2013).
17. Wei, G., Xu, L., Huang, C. & Wang, Y. SPE water electrolysis with SPEEK/PES blend membrane. *Int. J. Hydrogen Energy* **35**, 7778–7783 (2010).
18. Kerres, J., Ullrich, A., Meier, F. & Häring, T. Synthesis and characterization of novel acid–base polymer blends for application in membrane fuel cells. *Solid State Ionics* **125**, 243–249 (1999).
19. Cho, H., Krieg, H. & Kerres, J. Performances of Anion-Exchange Blend Membranes on Vanadium Redox Flow Batteries. *Membranes (Basel)*. **9**, 31 (2019).
20. Kerres, J. A. Development of ionomer membranes for fuel cells. *J. Memb. Sci.* **185**, 3–27 (2001).
21. Thanasilp, S. & Hunsom, M. Effect of MEA fabrication techniques on the cell performance of Pt–Pd/C electrocatalyst for oxygen reduction in PEM fuel cell. *Fuel* **89**, 3847–3852 (2010).
22. Tang, H., Wang, S., Jiang, S. P. & Pan, M. A comparative study of CCM and hot-pressed MEAs for PEM fuel cells. *J. Power Sources* **170**, 140–144 (2007).
23. Liu, C., Wippermann, K., Rasinski, M., Suo, Y., Shviro, M., Carmo, M. & Lehnert, W. Constructing a Multifunctional Interface between Membrane and Porous Transport Layer for Water Electrolyzers. *ACS Appl. Mater. Interfaces* **13**, 16182–16196 (2021).
24. Bernt, M. P. Analysis of Voltage Losses and Degradation Phenomena in PEM Water Electrolyzers. (Technische Universität München, 2019).

25. Franklin, T. C. & Kagawa, H. Poisoning of platinumized platinum electrodes by hydrogen in dimethylsulphoxide. *Electrochim. Acta* **17**, 1213–1217 (1972).
26. Zhao, G., Sanchez, S., Schmidt, O. G. & Pumera, M. Poisoning of bubble propelled catalytic micromotors: the chemical environment matters. *Nanoscale* **5**, 2909–2914 (2013).
27. Siracusano, S., Baglio, V., Van Dijk, N., Merlo, L. & Aricò, A. S. Enhanced performance and durability of low catalyst loading PEM water electrolyser based on a short-side chain perfluorosulfonic ionomer. *Appl. Energy* **192**, 477–489 (2017).
28. Pantò, F., Siracusano, S., Briguglio, N. & Aricò, A. S. Durability of a recombination catalyst-based membrane-electrode assembly for electrolysis operation at high current density. *Appl. Energy* **279**, 115809 (2020).
29. European Chemicals Agency (ECHA). ECHA publishes PFAS restriction proposal. <https://echa.europa.eu/-/echa-publishes-pfas-restriction-proposal> (2023). (Accessed on March 8th, 2023)
30. Evich, M. G., Davis, M. J. B., McCord, J. P., Acrey, B., Awkerman, J. A., Knappe, D. R. U., Lindstrom, A. B., Speth, T. F., Tebes-Stevens, C., Strynar, M. J., Wang, Z., Weber, E. J., Henderson, W. M. & Washington, J. W. Per- and polyfluoroalkyl substances in the environment. *Science*. **375**, eabg9065 (2022).
31. Cousins, I. T., DeWitt, J. C., Glüge, J., Goldenman, G., Herzke, D., Lohmann, R., Miller, M., Ng, C. A., Scheringer, M., Vierke, L. & Wang, Z. Strategies for grouping per- and polyfluoroalkyl substances (PFAS) to protect human and environmental health. *Environ. Sci. Process. Impacts* **22**, 1444–1460 (2020).

Chapter 6

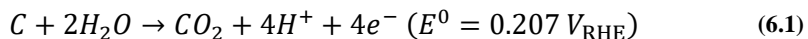
Analysis of the challenges in preparing membrane–electrode assemblies by screen printing

Abstract

The use of titanium as base material for porous transport layers and bipolar plates in proton exchange water electrolysis results in high capital cost, which may hamper implementation of this technology on large scale. The emerging field of printed electronics can provide a suitable answer for high throughput and low-cost manufacturing of electrodes. In this chapter, graphite-based screen-printed electrodes were manually printed on both sides of a proton exchange membrane (Nafion NRE-212) as substitute of the porous transport layers and bipolar plates. The used ink is only electron conductive and to also allow proton conduction, two patterns were designed where the membrane has uncoated areas. Water electrolysis activity was observed with both screen-printed patterns despite the large resistances and graphite oxidation. This shows that the patterns are successful in conducting protons from the anode to the cathode.

6.1. Introduction

The porous transport layers (PTLs) and bipolar plates (BPPs) used in proton exchange membrane (PEM) water electrolysis need to resist the highly acidic environment due to the PEM and the high applied bias at high current densities.¹ These conditions hinder the use of carbon materials, especially at the anode side of the electrolysis cell, where oxygen and water are present, further promoting the corrosive environment and oxidation of carbon to CO₂ according to **Eq. 6.1**.²



Titanium is the most widely used material for BPPs and PTLs because of its excellent strength, low electrical resistance, and low permeability.³ However, it is also prone to oxidize at the anode side, forming a passivation layer that increases the resistance, and on the cathode, hydrogen embrittlement can also occur. Noble metal coatings such as Au and Pt are commonly applied to overcome these issues.⁴ This increases the costs of PEM water electrolysis even further as titanium itself is also highly expensive (ca. 4977 € kg⁻¹ Ti foil, 99.7% purity from Sigma Aldrich),⁵ contributing to the high cost of the electrolysis cell stack – i.e. membrane, catalysts, PTL, BPP. The system cost for PEM water electrolysis is around 900 € kW⁻¹ (for 100 MW hydrogen plant) while for its alkaline counterpart, this cost is about 600 € kW⁻¹ due to the use of nickel-based catalysts, low cost electrolyte, and stack materials.⁶ This large cost difference hinders the implementation of PEM water electrolysis (PEMWE), despite the higher efficiency when compared to alkaline water electrolysis.^{7,8}

The PEM electrolysis cell stack is the major contributor for the capital expenditures of PEMWE. A report by the US National Renewable Energy Laboratory (NREL) in 2019 shows that the BPP and PTL represent roughly 50% of the total PEM stack cost.⁹ This contribution is explained by the large amounts of titanium required in comparison to the amount of platinum group metal catalysts, despite their much higher price. Hence, the cost reduction of PEMWE greatly depends on replacing Ti as core material and on the development and application of alternative cost-effective manufacturing routes. A possible alternative route is the use of printing methodologies.

Printed electronics (PE) is an emerging field that merges the fabrication of electronic components with traditional printing techniques like screen printing,^{10–12} inkjet printing,^{13–15} gravure printing,^{16–18} flexographic printing,^{19,20} and offset printing.^{21,22} This allows high throughput manufacture of thin electronic components that can be flexible, lightweight, wearable, cost-effective

and environmentally friendly, making this technology complementary to traditional electronics.^{12,23–26} The production of many distinct electrical devices – e.g. displays,^{27–29} sensors,³⁰ RFID,^{10,31,32} capacitors,³³ light–emitting diodes,^{34,35} and solar cells^{36–38} – already involves PE, either partially or totally.

The functional inks are based on organic and inorganic materials that can be conductive, semiconductive, luminescent, electrochromic, or dielectric. The inks are formulated depending on the target application and the printing method adopted. Controlling ink properties as viscosity and wetting on the substrate is essential to obtain high quality printed devices.

A major advantage of PE is the seemingly endless variety of substrates that can be employed. The substrates can be not only the typical rigid materials but also flexible. For example, an 80 m length polymeric flexible foil has been used to fully print a module of 16000 organic solar cells.³⁸ Another flexible substrate becoming very popular is paper. Reports have shown that paper is a suitable substrate to manufacture batteries¹¹ and RFID tags¹⁰. This myriad of substrates contributes for the low–cost manufacturing of PE, helping to compete with Si–based electronics, especially for low–end applications.

The choice of printing method for high–quality PE depends on the type of device, required ink, substrate, target thickness, device structure and geometry, manufacturing speed and yield. Typically, these methods are combined to overcome their disadvantages and improve the printability and quality of PE devices.^{24,26,39} A comparison between the printing methods is shown in **Table 6.1**. Some of these techniques have already reached sufficient maturity level at the laboratory scale and the upscaling for faster processing is the next development step. For upscaling, printing can be adapted to a roll–to–roll (R2R) processing where flexible and cheap substrates can be easily used.⁴⁰

Table 6.1: Comparison of most common printing techniques. Adapted from²⁴.

	Flexography	Gravure	Offset	Screen	Inkjet
Resolution / lines mm⁻¹	13 – 33	13 – 50	20 – 50	10 – 20	20 – 50
Print speed / m min⁻¹	50 – 500	20 – 1000	15 – 1000	10 – 100	1 – 100
Wet film thickness / μm	0.5 – 8	0.1 – 5	0.5 – 2	3 – 100	0.3 – 20
Viscosity / Pa s	0.05 – 0.5	0.05 – 0.2	20 – 100	0.500 – 50	0.001 – 0.040

6.1.1. Screen Printing

Screen printing (**Figure 6.1**) is widely considered as one of the most mature printing methodologies as it has been used for many years in electronics production. It provides an inexpensive and rapid approach for mass production

with adequate control of the deposition area and it is compatible with a wide range of substrates and functional inks.^{11,35,41}

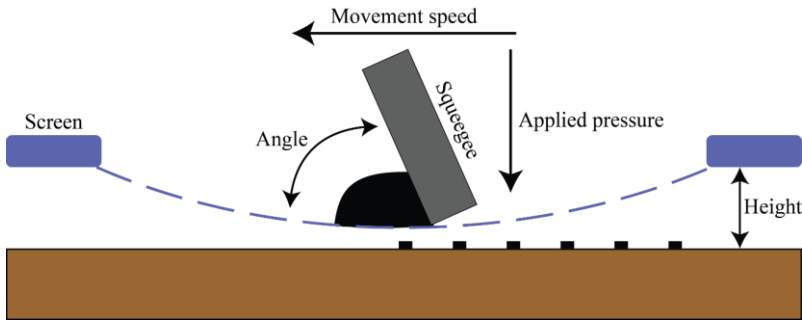


Figure 6.1: Schematics of screen printing and the key parameters. The parameters are: screen height, squeegee angle, applied pressure and speed.

Screen printing consists in transferring the ink through a mesh screen onto the substrate with a squeegee. The mesh screen supports a stencil that forms a negative image of the desired pattern.^{24,42,43} The squeegee is moved relatively to the screen, subsequently forcing the ink through the open areas of the mesh screen onto the substrate. Screen printing requires high viscosity inks (Table 6.1) since otherwise the ink would just flow through the mesh and spread over the substrate.^{44,45} This high viscosity is achieved by adding binders and surfactants to the ink. Such materials have typically low conductivities which makes the formulation a critical step to form a film with good electrical properties.

Screen printing offers the highest obtained thickness in comparison to the other printing techniques.^{12,41} Screen printing can easily yield thick films in the μm range in a single pass, which reduces processing times when high conductivities are required.⁴⁶ The dry film thickness δ can be empirically calculated by **Eq. 6.2**.⁴⁷

$$\delta = V_{\text{screen}} k_p \frac{c}{\rho} \tag{6.2}$$

where V_{screen} is the volume between the threads of the screen in $\text{cm}^3 \text{m}^{-2}$ and it depends on the thread diameter and thread number, c is the concentration of solid material in the ink in g cm^{-3} , ρ is the density of the material in the final film in g cm^{-3} and k_p is the pick-out ratio. The pick-out ratio k_p can be defined as the percentage of ink in the screen that is actually transferred onto the substrate. This ratio is influenced by the force applied on the squeegee, squeegee angle, printing speed, substrate-to-screen distance and ink viscosity.⁴⁸

In this chapter, the use of graphite screen printed electrodes (gSPEs) in membrane–electrode assemblies for PEMWE is discussed as a replacement of PTLs and BPPs. The gSPE were manually printed directly on the PEM and next, the catalysts were spray–coated on the gSPE. The graphite ink is not proton conductive, so the gSPEs were printed using two patterns where the membrane has uncovered areas, providing proton conduction between the catalyst layers during the PEMWE experiments.

6.2. Screen Printing patterns

Ideally, the gSPE electrode would be porous, promoting water flow through them and to the catalyst layer and PEM, similarly to the PTLs. However, the electrodes prepared in this work are not porous, and for that reason, the MEA had the following stack: hydrogen evolution catalyst (HEC) / gSPE / PEM / gSPE / oxygen evolution catalyst (OEC) where the catalyst layers have direct contact with the feed water. The placement of the catalyst layers over the electrode instead of the membrane raises another issue for the implementation of gSPE for water electrolysis. An insulating co–polymer of methyl methacrylate–butyl acrylate–methyl methacrylate (MBM) is used as binder in the graphite ink, and hence these electrodes are only electron conductive. To provide the required ionic conductivity and enable protons to move from the anodic catalyst layer through the membrane to the cathodic catalyst layer, the membrane must not be completely covered with graphite.

Two patterns for the printed electrodes where the PEM was partially uncovered (**Figure 6.2**) were created to facilitate proton conduction. The printed electrodes were encapsulated within polyimide film coated with a fluoro elastomer with an open area of 5.0625 cm^2 , and the covered graphite area was set to 4 cm^2 . In the *Slit* pattern (Figure 6.2a–c), 9 uncovered spaces ($2.1 \times 0.055\text{ cm}^2$), hereinafter referred as slits, were evenly spaced by 2 mm of graphite. Instead, in the *Small* pattern (Figure 6.2d–f), there was a continuous graphite film, followed by an uncovered space ($2.25 \times 0.462\text{ cm}^2$).

The gSPE are expected to work without the aid of BPPs but they still require an electrical connection to the power source. For this reason, a small graphite strip is included at the top of the electrode patterns and double–sided conductive tape can be used over it to obtain electrical connection. However, for initial tests, this graphite strip was not printed to understand the viability of the patterns in terms of proton conduction (Figure 6.2b and e). For no–contact gSPE, the flow fields of the 3D–printed electrochemical cell were coated with Cu, Ni and Au by electrodeposition (**Figure 6.3a**) while for gSPE with graphite contacts, the flow fields were not coated to ensure that all current was collected by the

graphite contact – Figure 6.3b. Only gSPE with the *Slit* pattern were tested with both configurations.

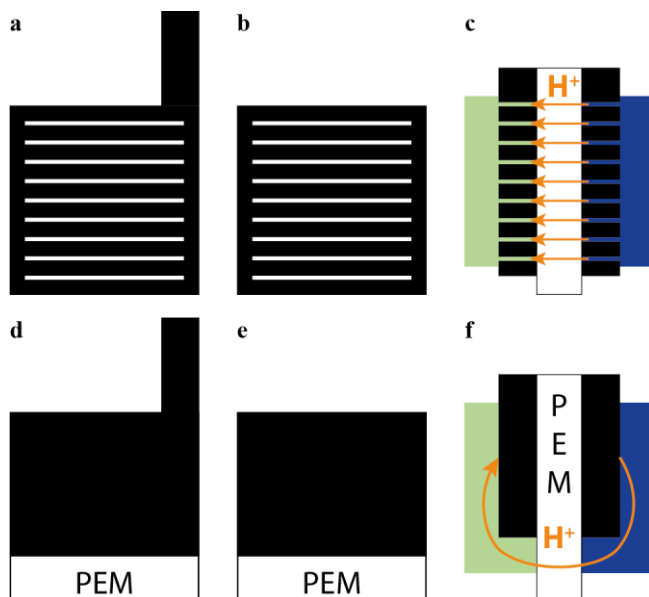


Figure 6.2: Screen printing patterns for MEA. a) and d) *Slit* and *Small* pattern, respectively. The top graphite strip in a) and d) is used to connect the gSPE to the potentiostat. b) and e) *Slit* and *Small* patterns without top graphite contact, respectively. c) and f) Cross-section of MEA with *Slit* and *Small* patterns and illustrative proton conduction lines. The green and the blue rectangles represent the Pt and RuO₂ catalysts, respectively, and the white rectangle is the PEM. The catalyst layers are in direct contact with the PEM through the uncovered spaces on the patterns.

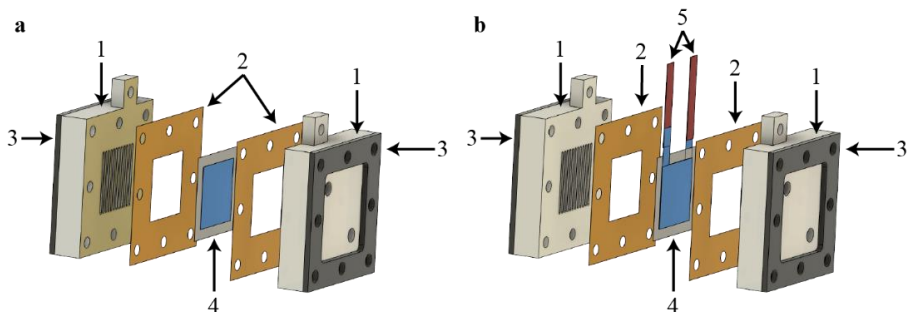


Figure 6.3: Electrochemical Cell assembly used for gSPE. a) Gold-coated fluid diffusers for gSPE without top graphite contacts (gSPE-NC). b) Bare fluid diffusers for gSPE with top graphite contacts (gSPE-C). (1) Fluid diffusers coated with a gold layer (a) or uncoated (b), (2) Polyimide films, (3) Stainless steel metal frames, (4) Membrane-electrode assembly with gSPE, (5) Copper tape.

A summary of the prepared MEA with gSPE and the main results is presented in **Table 6.2**. The variation in catalyst coatings results from the manual spray coating deposition.

Table 6.2: Summary of PEMWE with printed electrodes. Slit: *Slit* pattern, Small: *Small* pattern, C: top graphite contact, NC: no graphite top contact.

Method	Pt Loading / mg cm ⁻²	RuO ₂ Loading / mg cm ⁻²	R _Ω / Ω cm ²	R _{ct} / Ω cm ²	J _{1.6V} / mA cm ⁻²
Slit–NC_1	1.18	1.24		Short Circuit	
Slit–NC_2	0.94	0.98	1.46	23.5	5.49
Slit–C_1	1.04	2.00		High resistance	
Slit–C_2	1.15	2.00		High resistance	
Small–NC_1	1.09	1.36	1.07	11.7	20.7
Small–NC_2	1.00	0.97	0.96	25.7	8.66
Small–NC_3	0.64	1.00	1.34	20.2	11.3

All samples were manually screen printed and therefore, screen printing key parameters like applied force on the squeegee, printing speed, squeegee angle and screen–to–substrate height were not easily controlled. These parameters easily influence the properties of the printed electrodes and the lack of control of these parameters has induced some reproducibility issues within this work. Such issue though can be avoided when using an automatic screen printer that is able to control the key parameters in a potential scale–up as SPE are currently used in diverse applications as solar cells and biosensor where reproducibility is a key parameter.^{40,49}

6.3. *Slit* screen printed graphite electrodes

Figure 6.4 shows representative MEA with gSPE on opposite sides of the PEM with and without the top graphite contact. For the gSPE with contact (Slit–C), the copper tape was glued onto the graphite contact prior to encapsulation. The linear sweep voltammetry (LSV) of two no–contact gSPEs (Slit–NC) are completely dissimilar as shown in **Figure 6.5a**, indicating the low reproducibility of the gSPE. The absence of a reaction onset combined with the linear increase of the current density, reaching the maximum current output of the equipment ($I_{max} = 3 A$), suggests that Slit–NC_1 has an ohmic short, that can possibly be assigned to the presence of holes in the membrane, that would contact both electrodes through it. In contrast, Slit–NC_2 has a well–defined reaction onset at around 1.43 V, reaching a current density of 3 mA cm⁻² at 1.6 V and 8.4 mA cm⁻² at 1.8 V.

Further characterization of Slit–NC_2 was carried out by electrochemical impedance spectroscopy (EIS) (Figure 6.5b). The ohmic resistance (1.46 Ω cm²) and the charge transfer resistance (23.5 Ω cm²) were calculated by fitting the EIS

spectrum to a modified Randles circuit (inset in Figure 6.5c). Printed electrodes are usually less conductive than common electrodes, and thus, the ohmic resistance (R_{Ω}) was expected to be high in comparison to typical values found in literature.²⁵

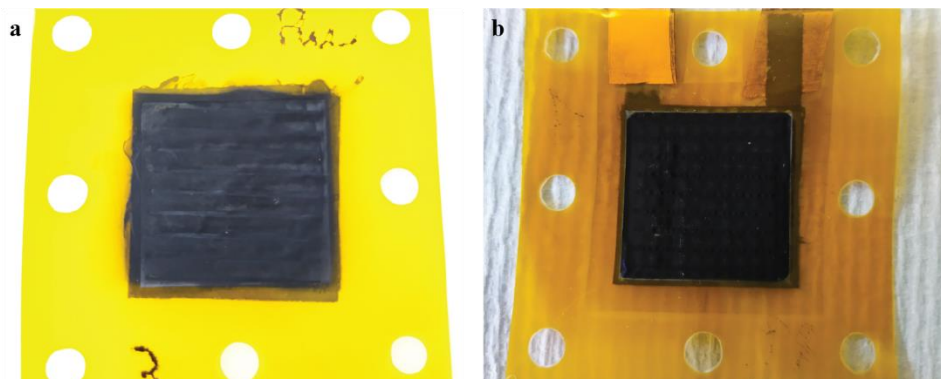


Figure 6.4: MEA with *Slit* patterned gSPE. a) Slit-NC_3. b) Slit-C1. The black area is (a) RuO₂ and (b) Pt over the graphite ink. The yellow foil is the polyimide foil used to encapsulate the Nafion membrane.

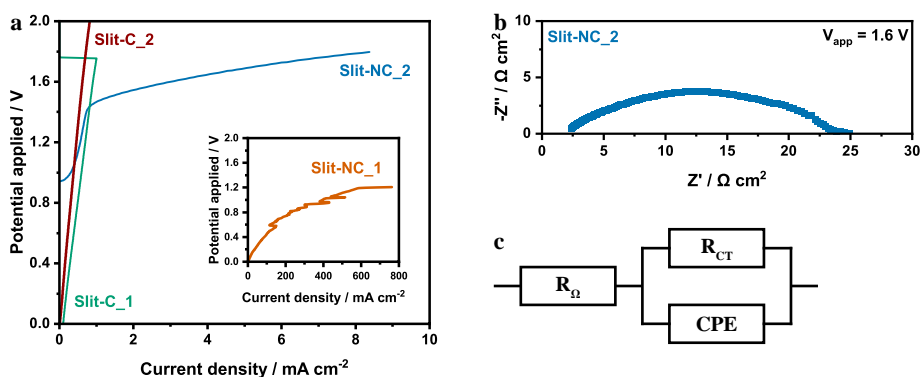


Figure 6.5: Water electrolysis performance of gSPE with *Slit* pattern. a) Linear sweep voltammetry. b) Electrochemical impedance spectroscopy (EIS) of Slit-NC_2 at a bias voltage of 1.6 V. c) Equivalent electrical circuit used to fit the EIS data. R_{Ω} is the ohmic resistance, R_{ct} is the charge transfer resistance, and CPE is the constant phase element.

The catalyst layer in the gSPE is mostly in contact with the non-H⁺ conductive graphite layer. Most catalyst is therefore electrochemically inactive, and the formed protons can only reach the cathode through the uncovered spaces in the gSPEs. This poor catalyst–membrane interface leads to a large charge transfer resistance (R_{ct}).⁵⁰ Nevertheless, these results show that proton conduction is possible through the slits of the graphite electrode, allowing water splitting to

occur, despite large resistances. This is further supported by the presence of gas bubbles in both water lines during the experiment.

Graphite electrodes containing the top graphite strip (Figure 6.2a) were subsequently printed to test the feasibility of removing the BPP, which would result in a large cost advantage for such approach. The Slit–C samples were highly resistive, represented by the linear rise of current density with cell potential as shown in Figure 6.5a. The worse behavior can be ascribed to a bad contact between the conductive tape and the graphite top strip. A few ways to improve such contact would be by widening the graphite strip, printing more graphite layers, or increasing the bolt torque used to assemble the cell. A wider top strip increases its cross section resulting in lower resistance. The printed graphite particles form a random network after solvent evaporation and by increasing the number of layers, graphite particles are more likely to contact and create more electron pathways.⁵¹ Finally, higher bolt torque can promote better contact as the surfaces of the conductive tape and the graphite become more compressed against each other.

6.4. Small screen printed graphite electrodes

Figure 6.6 shows a representative sample of a MEA with *Small* pattern gSPE after encapsulation. This pattern was only tested without the graphite top strip.

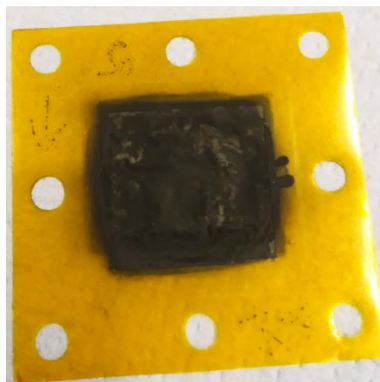


Figure 6.6: MEA with *Small* patterned gSPE (Small–NC_2). The black area is RuO₂ side over the graphite ink. The yellow foil is the polyimide foil used to encapsulate the Nafion membrane.

All the Small–NC samples showed water electrolysis activity. Nevertheless, LSV and EIS indicate a lack of reproducibility of the current printing process as can be seen in **Figure 6.7**. Gas bubbles were observed on both cell outlets. This indicates that indeed H₂ and O₂ are being formed, but these may

not be the only reaction products. A small peak at about 1.3 V arises in the linear sweep voltammetry of Small-NC_1 and Small-NC_3, which suggests the presence of a side reaction to water splitting. Yi et al.⁵² reported such increase in current around 1.2 V, assigning it to the oxidation of the glassy carbon electrode that was later supported by an increase of the electrode roughness and FTIR data. In the case of these electrodes, there is also the presence of carbon in the form of graphite and thus, it is plausible that this faradaic process is graphite oxidation at the anode. The side reaction seems to occur in larger extent in Small-NC_1, due to larger faradaic peak, which might explain the higher currents and earlier reaction onset obtained for this sample. Moreover, the faradaic peak appears to increase with the number of scans while the current density decreases as shown in Figure 6.7b for Small-NC_1, implying poor stability of the gSPEs. Similar behavior arises in the other two Small gSPEs as well.

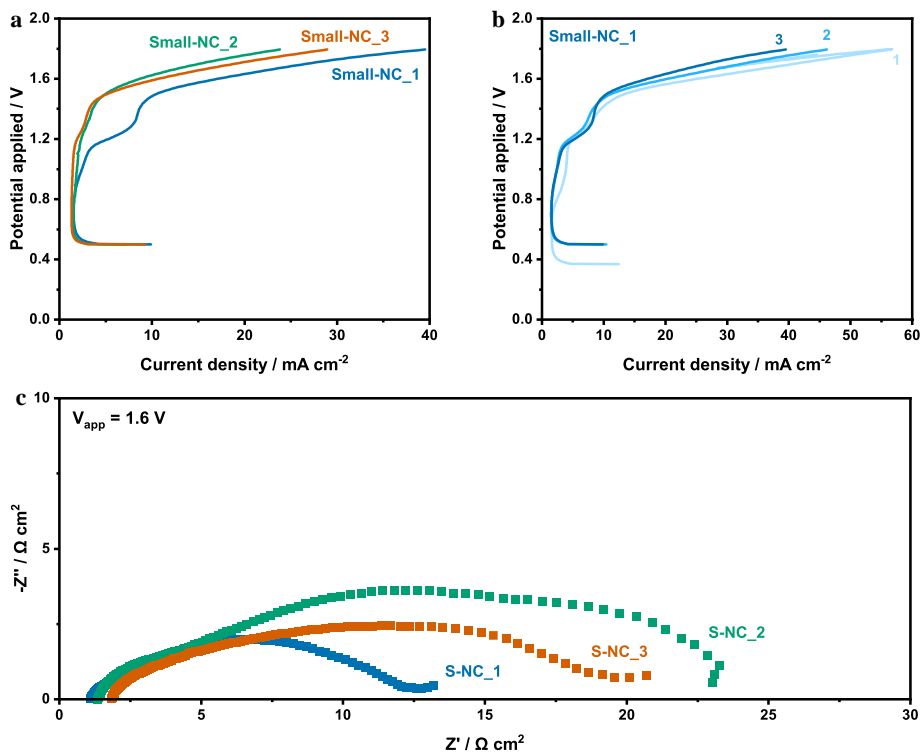


Figure 6.7: Water electrolysis performance of gSPE with *Small* pattern. a) 3rd (2nd for Small-NC_3) scan of linear sweep voltammetry of printed MEAs with *Small* pattern without top contact. b) All three scans of linear sweep voltammetry of Small-NC_1. c) Electrochemical impedance spectroscopy of MEAs with *Small* pattern without top contact.

The ohmic resistance is comparable between samples, $0.96 - 1.34 \Omega \text{ cm}^2$. In contrast, the charge transfer resistance largely varies as observed by the increase in the semicircle radius (Figure 6.7c). A possible reason for this inconsistency is the slightly different catalyst loadings. The catalyst loading influences the number of active sites, and thus it directly affects the magnitude of the charge transfer resistance, especially the oxygen evolution catalyst at the anode.⁵³ The lowest charge transfer resistance is found for Small–NC_1 which corresponds to the larger RuO₂ loading (Table 6.2) and to the highest current density in Figure 6.7a.

The RuO₂ loading might also be connected to the graphite oxidation previously mentioned. The intensity of the faradaic peak at 1.3 V in Figure 6.7a increases with the RuO₂ loading. This suggests that RuO₂ not only catalyzes the water oxidation but also, to some extent, graphite oxidation. Consequently, the observed charge transfer resistance is an overall product of the water oxidation and graphite oxidation reactions.

A direct comparison between the two patterns is only possible through sample Small–NC_2 since it has similar RuO₂ loading to Slit–NC_2 and does not clearly show any graphite oxidation as the remainder samples with the same pattern. The *Small* pattern shows improved ohmic resistance and current density. A plausible reason for this is the difficult manual alignment of the different layers in *Slit* pattern gSPE. A misalignment of the layers decreases the free area of PEM available for proton conduction, thus negatively influencing its activity.

6.5. Conclusion

Printed electrodes arise as a possible replacement for the expensive electrodes currently used in water electrolysis. The fast and easy large area production of PE would contribute to reduce the general cost of water electrolysis and possibly facilitate the implementation of this technology at large scale. This work focused on screen printing graphite electrodes on both sides of a proton exchange membrane, Nafion NRE–212 using RuO₂ and Pt as OEC and HEC, respectively, as a replacement for titanium bipolar plates and porous transport layers. As the graphite ink is not proton conductive, the electrodes were manually screen printed using two patterns – *Slit* and *Small* – that had graphite-free zones to allow proton conduction from the anode to the cathode. The *Slit* pattern MEAs were tested with and without a graphite top contact whereas all *Small* pattern had no top contact. The top contact serves as current collector and hence, avoids the usage of large and expensive current collectors made of, for example, Ti or Au.

Without top graphite contact, both screen printed patterns displayed water electrolysis activity verified by the presence of gas bubbles, presumably H₂ and O₂, in the water lines and the large current density increase only above the thermodynamic water splitting potential, $E^0 = 1.23$ V. The gSPE, independently of the pattern, showed similar ohmic resistance, but as expected for graphite, a much higher resistance is found than for common current collecting materials used in water electrolysis. The largest voltage losses, however, come from the charge transfer resistance, indicating a poor catalyst–membrane interface, because most catalyst is in contact with the graphite layer instead. In addition, an increased RuO₂ loading enhanced the graphite oxidation side–reaction that contributed to the high current observed with the *Small* pattern MEA. Moreover, the intensity from the graphite oxidation reaction increased with the number of scans while the catalytic current density at $E_{\text{cell}} = 1.8$ V decreased. The current density decrease indicates poor stability of the graphite electrode and thus, a more suitable material is required as screen printed electrode at the anode.

Despite the limitation at the anode, the results suggest that the uncoated areas in the gSPE result in proton conduction as intended and that the printed patterns influence the overall performance. Optimizing the SPE should primarily involve testing patterns with different position, geometry and number of uncoated membrane areas that could preferably reduce the charge transfer resistance issue observed in this work. The ohmic resistance is greatly impacted by the ink formulation, so optimizing it would clearly boost the performance of the SPEs. In addition, including a proton conductive binder in the ink formulation could benefit the SPE by providing proton conduction through the layer and improving the adhesion of the catalyst layer to the SPE.

6.6. Experimental section

Materials: All materials were used as received without purification. Nafion™ perfluorinated membrane NRE–212 was purchased from Ion Power. RuO₂ (anhydrous, 99.90%), Pt/C (HISPEC 4000 – 40 wt% Pt on carbon), graphite powder (natural, microcrystal grade, APS 2–15 micron, 99.9995% (metals basis)) and Nafion™ solution (D521CS, alcohol based 1100 EW at 5 wt%) were purchased from Alfa Aesar. Methyl methacrylate – n–butyl acrylate – methyl acrylate (MBM) block copolymer pellets (LA2250) were purchased from Kurarity. All solvents were obtained from Sigma–Aldrich. Nafion NRE–212 was pre–treated before any MEA preparation by immersing the membrane in 30 wt% H₂O₂ at 80 °C for 1 h, 8 wt% H₂SO₄ at 80 °C for 1 h and again, in deionized water at 80 °C for 1 h.

Graphite ink preparation: The MBM pellets (10 wt%) were dissolved in p–xylene for 1 h at 750 rpm using a RCT basic IKAMAG™ (IKA®). After complete dissolution, the solution was added to the graphite powder (23 wt%) and stirred for 1 h at 750 rpm. The stirring was carried out in a closed vial to avoid solvent evaporation.

Analysis of the challenges in preparing membrane–electrode assemblies by screen printing

Graphite Screen printing: All screen printing work was carried out using a manual screen printing setup (CPL Fabbrika) as shown in **Figure 6.8**. The membrane was cut into $15 \times 5 \text{ cm}^2$ pieces and the edges of the membrane were taped to the support to hold it in place. In pre–printing position (Figure 6.8a), the graphite ink is distributed over the desired patterns in the opposite direction of printing. In printing position (Figure 6.8b), the squeegee is pressed against the screen and moved in the printing direction to print the pattern and subsequently, the screen is lifted to pre–printing position to let the electrodes dry at room temperature. The process was repeated until 3 layers were printed. After printing 3 layers, the membrane was placed in an oven at $85 \text{ }^\circ\text{C}$ for 5 min to evaporate the remaining solvent. The same approach was used to print the graphite electrodes on the opposite side of the membrane.

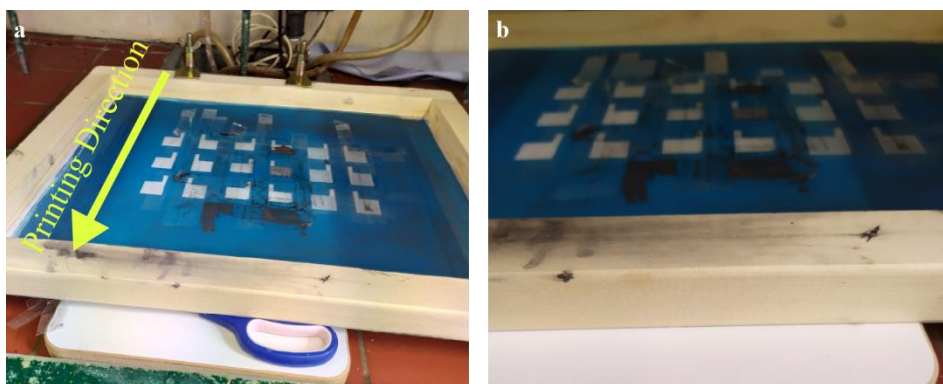


Figure 6.8: Manual Screen printing setup. (a) Pre–printing position: large space between screen and substrate. Used to distribute the ink on the target pattern mesh prior to printing. (b) Printing position: screen is close to the substrate.

Catalyst ink preparation: The catalyst inks were prepared with 5 wt% solid content, with 3:1 ratio of catalyst to Nafion ionomer in 2–propanol:water (4:1). For RuO_2 ink, Nafion dispersion is added first and subsequently, a 2–propanol:water is added. For Pt/C ink, the catalyst power is first mixed with water to avoid combustion of the carbon particles and subsequently, the Nafion dispersion and 2–propanol are sequentially added. The inks were ultrasonicated for at least 10 min between each solvent addition and prior to catalyst deposition. All catalyst inks were prepared using water purified in Millipore system ($18 \text{ M}\Omega \text{ cm}$).

Membrane–electrode assembly (MEA) preparation: The PEM with graphite screen printed electrodes were encapsulated between two polyimide films ($50 \mu\text{m}$, from Wu Xi Shun Xuan New Materials Co., Ltd) coated with FKM (FOR 9381, from Solvay) to delimit the active area to 4 cm^2 . The catalyst inks were manually spray–coated using a pneumatic airbrush (Act Air Color Technik) through a stainless–steel mask with a $2 \times 2 \text{ cm}^2$ opening on top of the graphite electrodes or membrane until the target loadings for Pt and RuO_2 were reached, respectively. The catalyst loadings were calculated by weighing the membrane before and after coating. The deposition temperature was set to $85 \text{ }^\circ\text{C}$ to evaporate the solvent upon deposition and to avoid excessive membrane swelling.

PEM electrochemical cell setup: Water electrolysis tests were carried out in an in–house built PEM – electrolyser cell ($5 \times 5 \text{ cm}^2$) using acrylonitrile butadiene styrene (ABS) as end plates with parallel flow fields (1 mm wide, channel area: $2.25 \times 2.25 \text{ cm}^2$). The flow field side of the ABS plates was sequentially spray coated with CuO and then coated with Cu, Ni, and Au by

electrodeposition to make it conductive. No extra sealing was used. For gSPE with the graphite top strip, double-sided conductive copper tape (RS Components Deutschland) was fixed on the top contact and the ABS endplates were uncoated to ensure that current collection occur only through the conductive tape. Millipore purified water ($>18\text{ M}\Omega\text{ cm}$) was circulated using membrane pumps (mp-6 hyb from Microtechnik) into both anodic and cathodic compartment at $\sim 6\text{ mL min}^{-1}$. Independent water lines and feeding bottles were used for each compartment.

Electrochemical Characterization: All electrochemical characterization was performed using an electrochemical workstation Zahner Elektrik IM6 in a 2-electrode configuration. All measurements were done at room temperature. Linear sweep voltammetry was recorded at a scan rate of 10 mV s^{-1} between open circuit potential and 1.8 or 2.1 V with a resolution of 5 mV for 5 scans, unless otherwise specified. The two first scans were used for activation of the catalyst. Electrochemical impedance spectroscopy was carried out in a frequency range of 50 or 100 mHz to 100 kHz at 1.6 V with an amplitude of 50 mV.

6.7. References

1. Carmo, M., Fritz, D. L., Mergel, J. & Stolten, D. A comprehensive review on PEM water electrolysis. *Int. J. Hydrogen Energy* **38**, 4901–4934 (2013).
2. Kim, T. & Popov, B. N. Development of highly-active and stable Pt/C catalyst for polymer electrolyte membrane fuel cells under simulated start-up/shut-down cycling. *Int. J. Hydrogen Energy* **41**, 1828–1836 (2016).
3. Millet, P. Degradation Processes and Failure Mechanisms in PEM Water Electrolyzers. in *PEM Electrolysis for Hydrogen Production* 219–242 (CRC Press/Taylor & Francis, 2016).
4. Jung, H.-Y., Huang, S.-Y., Ganesan, P. & Popov, B. N. Performance of gold-coated titanium bipolar plates in unitized regenerative fuel cell operation. *J. Power Sources* **194**, 972–975 (2009).
5. Sigma-Aldrich. Titanium foil, thickness 0.25mm, 99.7 trace metals 7440-32-6. <https://www.sigmaaldrich.com/NL/en/product/aldrich/267503>. (Accessed on August 29th, 2022)
6. Dolci, F., Gryc, K., Eynard, U., Georgakaki, A., Letout, S., Kuokkanen, A., Mountraki, A., Ince, E., Shtjefni, D., Joanny, G., Eulaerts, O. & Grabowska, M. *Clean Energy Technology Observatory, Water electrolysis and hydrogen in the European Union: status report on technology development, trends, value chains and markets: 2022*. (Publications Office of the European Union, 2022). doi:doi/10.2760/7606.
7. Schmidt, O., Gambhir, A., Staffell, I., Hawkes, A., Nelson, J. & Few, S. Future cost and performance of water electrolysis: An expert elicitation study. *Int. J. Hydrogen Energy* **42**, 30470–30492 (2017).
8. Bessarabov, D. & Millet, P. *PEM water electrolysis*. vol. 1 (Academic Press, 2018).
9. Mayyas, A., Ruth, M., Pivovar, B., Bender, G. & Wipke, K. *Manufacturing Cost Analysis for Proton Exchange Membrane Water Electrolyzers*. <https://www.nrel.gov/docs/fy10osti/72740.pdf>. (2019).
10. Kavčič, U., Pivar, M., Dokić, M., Svetec, D. G., Pavlovič, L. & Muck, T. UHF RFID tags with printed antennas on recycled papers and cardboards. *Mater. Tehnol.* **48**, 261–267 (2014).

11. Garcia, D. M. E. E., Pereira, A. S. T. M., Almeida, A. C., Roma, U. S., Soler, A. B. A., Lacharmoise, P. D., Das Mercês Ferreira, I. M., Simão, C. C. D. & Simaõ, C. C. D. Large-Area Paper Batteries with Ag and Zn/Ag Screen-Printed Electrodes. *ACS Omega* **4**, 16781–16788 (2019).
12. He, P., Cao, J., Ding, H., Liu, C., Neilson, J., Li, Z., Kinloch, I. A. & Derby, B. Screen-Printing of a Highly Conductive Graphene Ink for Flexible Printed Electronics. *ACS Appl. Mater. Interfaces* **11**, 32225–32234 (2019).
13. Klingele, M., Breitwieser, M., Zengerle, R. & Thiele, S. Direct deposition of proton exchange membranes enabling high performance hydrogen fuel cells. *J. Mater. Chem. A* **3**, 11239–11245 (2015).
14. Dodoo-Arhin, D., Howe, R. C. T., Hu, G., Zhang, Y., Hiralal, P., Bello, A., Amaratunga, G. & Hasan, T. Inkjet-Printed Graphene Electrodes for Dye-Sensitized Solar Cells. *Carbon N. Y.* **105**, 33 (2016).
15. He, P. & Derby, B. Inkjet Printing Ultra-Large Graphene Oxide Flakes. *2D Mater.* **4**, 21021 (2017).
16. Secor, E. B., Lim, S., Zhang, H., Frisbie, C. D., Francis, L. F. & Hersam, M. C. Gravure Printing of Graphene for Large-Area Flexible Electronics. *Adv. Mater.* **26**, 4533 (2014).
17. Hu, Q., Wu, H., Sun, J., Yan, D., Gao, Y. & Yang, J. Large-area perovskite nanowire arrays fabricated by large-scale roll-to-roll micro-gravure printing and doctor blading. *Nanoscale* **8**, 5350–5357 (2016).
18. Montanino, M., Sico, G., De Girolamo Del Mauro, A. & Moreno, M. LFP-Based Gravure Printed Cathodes for Lithium-Ion Printed Batteries. *Membranes (Basel)*. **9**, 71 (2019).
19. Lepak-Kuc, S., Wasilewska, K., Janczak, D., Nowicka, T. & Jakubowska, M. Conductive Layers on a Shrinkable PET Film by Flexographic Printing. *Materials (Basel)*. **15**, 3649 (2022).
20. Hübler, A. C., Bellmann, M., Schmidt, G. C., Zimmermann, S., Gerlach, A. & Haentjes, C. Fully mass printed loudspeakers on paper. *Org. Electron.* **13**, 2290–2295 (2012).
21. Shin, S., Kim, S. & Cho, Y. T. Tunable Reverse Offset Printing with a Stretchable Blanket for Fabricating Flexible Printed Electronics. *Adv. Eng. Mater.* **23**, 2001537 (2021).
22. Kikkawa, T., Kumaki, D., Tokito, S., Fukuda, N. & Kusaka, Y. Nickel oxide-based flexible thin-film NTC thermistors by using reverse offset printing. *Flex. Print. Electron.* **7**, 015003 (2022).
23. Keskinen, M. End-of-life options for printed electronics. in *Waste Electrical and Electronic Equipment (WEEE) Handbook* 352–364 (Elsevier, 2012).
24. Tobjörk, D. & Österbacka, R. Paper Electronics. *Adv. Mater.* **23**, 1935–1961 (2011).
25. Gregor-Svetec, D. Intelligent Packaging. in *Nanomaterials for Food Packaging* 203–247 (Elsevier, 2018).
26. Suganuma, K. *Introduction to Printed Electronics*. vol. 74 (Springer New York, 2014).
27. Li, S., Peele, B. N., Larson, C. M., Zhao, H. & Shepherd, R. F. A Stretchable Multicolor Display and Touch Interface Using Photopatterning and Transfer Printing. *Adv. Mater.* **28**, 9770 (2016).

28. Choi, M., Jang, B., Lee, W., Lee, S., Kim, T. W., Lee, H.-J., Kim, J.-H. & Ahn, J.-H. Stretchable Active Matrix Inorganic Light-Emitting Diode Display Enabled by Overlay-Aligned Roll-Transfer Printing. *Adv. Funct. Mater.* **27**, 1606005 (2017).
29. Coleman, J. P., Lynch, A. T., Madhukar, P. & Wagenknecht, J. H. Printed, flexible electrochromic displays using interdigitated electrodes. *Sol. Energy Mater. Sol. Cells* **56**, 395–418 (1999).
30. He, P., Brent, J. R., Ding, H., Yang, J., Lewis, D. J., O'Brien, P. & Derby, B. Fully Printed High Performance Humidity Sensors Based on Two-Dimensional Materials. *Nanoscale* **10**, 5599 (2018).
31. Huang, X., Leng, T., Zhang, X., Chen, J. C., Chang, K. H., Geim, A. K., Novoselov, K. S. & Hu, Z. Binder-Free Highly Conductive Graphene Laminate for Low Cost Printed Radio Frequency Applications. *Appl. Phys. Lett.* **106**, 203105 (2015).
32. Perelaer, J., de Gans, B.-J. & Schubert, U. S. Ink-jet Printing and Microwave Sintering of Conductive Silver Tracks. *Adv. Mater.* **18**, 2101–2104 (2006).
33. Xu, Y., Schwab, M. G., Strudwick, A. J., Hennig, I., Feng, X., Wu, Z. & Müllen, K. Screen-Printable Thin Film Supercapacitor Device Utilizing Graphene/Polyaniline Inks. *Adv. Energy Mater.* **3**, 1035–1040 (2013).
34. Kim, B. H., Onses, M. S., Lim, J. B., Nam, S., Oh, N., Kim, H., Yu, K. J., Lee, J. W., Kim, J.-H., Kang, S.-K., Lee, C. H., Lee, J., Shin, J. H., Kim, N. H., Leal, C., Shim, M. & Rogers, J. A. High-Resolution Patterns of Quantum Dots Formed by Electrohydrodynamic Jet Printing for Light-Emitting Diodes. *Nano Lett.* **15**, 969 (2015).
35. Pardo, D. A., Jabbour, G. E. & Peyghambarian, N. Application of Screen Printing in the Fabrication of Organic Light-Emitting Devices. *Adv. Mater.* **12**, 1249–1252 (2000).
36. Zhang, D. W., Li, X. D., Li, H. B., Chen, S., Sun, Z., Yin, X. J. & Huang, S. M. Graphene-based counter electrode for dye-sensitized solar cells. *Carbon N. Y.* **49**, 5382–5388 (2011).
37. Zhang, C., Luo, Q., Wu, H., Li, H., Lai, J., Ji, G., Yan, L., Wang, X., Zhang, D., Lin, J., Chen, L., Yang, J. & Ma, C. Roll-to-Roll Micro-Gravure Printed Large-Area Zinc Oxide Thin Film as the Electron Transport Layer for Solution-Processed Polymer Solar Cells. *Org. Electron.* **45**, 190 (2017).
38. Sommer-Larsen, P., Jørgensen, M., Søndergaard, R. R., Hösel, M. & Krebs, F. C. It is all in the Pattern-High-Efficiency Power Extraction from Polymer Solar Cells through High-Voltage Serial Connection. *Energy Technol.* **1**, 15–19 (2013).
39. Sousa, R. E., Costa, C. M. & Lanceros-Méndez, S. Advances and Future Challenges in Printed Batteries. *ChemSusChem* **8**, 3539–3555 (2015).
40. Roth, B., Søndergaard, R. R. & Krebs, F. C. Roll-to-roll printing and coating techniques for manufacturing large-area flexible organic electronics. in *Handbook of Flexible Organic Electronics* 171–197 (Elsevier, 2015).
41. Arapov, K., Rubingh, E., Abbel, R., Laven, J., de With, G. & Friedrich, H. Conductive Screen Printing Inks by Gelation of Graphene Dispersions. *Adv. Funct. Mater.* **26**, 586–593 (2016).
42. Kantola, V., Kulovesi, J., Lahti, L., Lin, R., Zavodchikova, M. & Coatanéa, E. *Bit Bang Rays to the Future. Bit Bang - Rays to the Future* (Helsinki University Print, 2009).

43. Hyun, W. J., Secor, E. B., Hersam, M. C., Frisbie, C. D. & Francis, L. F. High-Resolution Patterning of Graphene by Screen Printing with a Silicon Stencil for Highly Flexible Printed Electronics. *Adv. Mater.* **27**, 109–115 (2015).
44. Kipphan, H. *Handbook of Print Media. Handbook of print media: technologies and production methods* (Springer Berlin Heidelberg, 2001).
45. Søndergaard, R., Hösel, M., Angmo, D., Larsen-Olsen, T. T. & Krebs, F. C. Roll-to-roll fabrication of polymer solar cells. *Mater. Today* **15**, 36–49 (2012).
46. Huang, Q. & Zhu, Y. Printing Conductive Nanomaterials for Flexible and Stretchable Electronics: A Review of Materials, Processes, and Applications. *Adv. Mater. Technol.* **4**, 1800546 (2019).
47. Krebs, F. C. Fabrication and processing of polymer solar cells: A review of printing and coating techniques. *Sol. Energy Mater. Sol. Cells* **93**, 394–412 (2009).
48. Riemer, D. E. The Theoretical Fundamentals of the Screen Printing Process. *Microelectron. Int.* **6**, 8–17 (1989).
49. Yoon, H., Kang, S. M., Lee, J.-K. & Choi, M. Hysteresis-free low-temperature-processed planar perovskite solar cells with 19.1% efficiency. *Energy Environ. Sci.* **9**, 2262–2266 (2016).
50. Siracusano, S., Baglio, V., Stassi, A., Merlo, L., Moukheiber, E. & Arico', A. S. Performance analysis of short-side-chain Aquivion® perfluorosulfonic acid polymer for proton exchange membrane water electrolysis. *J. Memb. Sci.* **466**, 1–7 (2014).
51. Tortorich, R. & Choi, J.-W. Inkjet Printing of Carbon Nanotubes. *Nanomaterials* **3**, 453–468 (2013).
52. Yi, Y., Weinberg, G., Prenzel, M., Greiner, M., Heumann, S., Becker, S. & Schlögl, R. Electrochemical corrosion of a glassy carbon electrode. *Catal. Today* **295**, 32–40 (2017).
53. Liu, C., Wippermann, K., Rasinski, M., Suo, Y., Shviro, M., Carmo, M. & Lehnert, W. Constructing a Multifunctional Interface between Membrane and Porous Transport Layer for Water Electrolyzers. *ACS Appl. Mater. Interfaces* **13**, 16182–16196 (2021).

Chapter 7

Life cycle assessment of an artificial leaf: new and standard materials

Abstract

The current transition to sustainable production and consumption is leading to the creation of new environmental policies. Together with these policies comes the growing importance of objectively quantifying the environmental impacts of these new sustainable technologies. It is then important to analyze new materials during the development phase to understand where environmental limitations can occur. Here, the environmental impacts and energy demand of two artificial leaves were analyzed and compared using LCA methodology. One artificial leaf is based on state-of-the-art (SOA) water electrolysis materials while the other is based on the materials developed during the eSCALED project. The artificial leaves have solar-to-hydrogen efficiencies of 12% (eSCALED) and 14% (SOA). It was found that the eSCALED device has a much higher environmental impact and energy demand than the SOA one. The eSCALED membrane had the largest environmental impact of all materials due to the use of pentafluorostyrene as main monomer. Finally, the devices had an expected energy payback time of 476 years (eSCALED) and 90 years (SOA) assuming an operating current density similar to what is described in chapter 3. The eSCALED project is a low technology readiness level (TRL) project and commonly, lower TRLs project have worse environmental profiles when compared to more mature technologies. These results also indicate where future work should focus to reach lower environmental impacts at higher TRLs.

7.1. Introduction

Proton exchange membrane water electrolysis (PEMWE) is considered as a key technology for the energy transition. The energy surplus from renewable energy sources can be used to power PEMWE and thus, store energy in molecular hydrogen.^{1,2} However, PEMWE is currently limited by a narrow range of usable materials. For instance, the most common electrocatalysts are Pt, RuO₂, and IrO₂, which are some of the rarest metals and metal oxides on Earth. For instance, ruthenium and iridium are only minor by-products of nickel and copper mining, resulting in high prices. Titanium is typically used to fabricate the thick bipolar plates and, despite being less expensive than the electrocatalysts, large quantities are required.³ As PEM, perfluorinated sulfonic acid (PFSA) compounds are usually used, and as result of the complex synthesis process, are also very expensive.⁴ But cost is not the only issue of this set of materials.

Another issue raised by this set of materials is their environmental impact. A study in 2010 by Glaister et al. showed that the mining and refining of platinum group metals (PGM), such as Ru, Ir, and Pt had CO₂ emissions around 39 t kg_{pgm}⁻¹.⁵ More recent studies have shown that this value might be lower (33 t kg_{pgm}⁻¹) but it amounts to a very large impact.⁶ In addition, perfluorinated membranes like Nafion also have high CO₂ emissions, associated with the use of fluorinated compounds such as tetrafluoroethylene and perfluoro alkyl vinyl ethers with sulfonyl fluoride end groups. These fluorinated and perfluorinated compounds can also stay in the atmosphere for thousands of years.

This has inspired an extensive effort to research and develop new materials that can replace state-of-the-art materials, not only in terms of efficiency but also, in terms of cost and environmental impact. Frequently, such new systems are immediately regarded as solutions for some of the previously mentioned issues, especially environmentally. Generally, when new materials are reported, there is no environmental analysis and comparison that would point to that. Hence, there is a growing interest in studying the environmental impacts of new technologies, as well as well-established ones, to ensure that they are indeed better than their predecessors.

Industrial partners, together with researchers, are especially interested in understanding where the environmental impacts lie in their processes and activities.⁷ The environmental assessment of the raw material extraction (cradle) through manufacture (gate), maintenance and finally, to the end of life (grave) can be used to support decisions on how and where to improve the products. The most established method to estimate the environmental performance is life cycle

assessment (LCA).⁸ LCA is an iterative process aimed to provide continuous improvement of the environmental profile of the product as illustrated in **Figure 7.1**.⁹ The environmental burden described by LCA covers a broad range of impacts upon the environment, such as extraction of natural resources, emissions of toxic and hazardous compounds and different types of land use.¹⁰ LCA plays a useful role in environmental management regarding products as it may include comparison between already existing products and development of new ones, for instance, the eSCALED project artificial leaf.¹¹ LCA helps to understand and locate the environmental limitations, in order to improve the product, and consequently, decrease the negative environmental effects.¹²

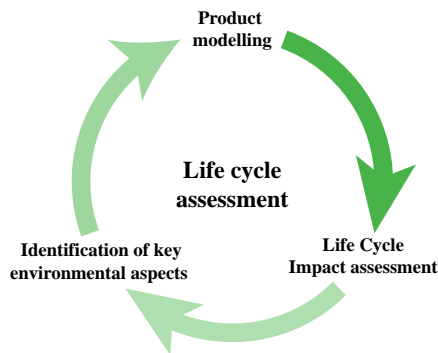


Figure 7.1: Schematics of the iterative nature of life cycle assessment. Based on ref. ¹³.

LCA has a few limitations. Large amounts of data need to be collected and often, certain data is unavailable. Hence, the processes need to be frequently simplified, which can lead to uncertainties in the analysis. There are large databases being developed and standardised to include a broader scope of processes and even country dependence, but they require regular updates to avoid old and incomparable data.¹⁴ LCA cannot provide the framework for a local or temporal risk assessment. For instance, the impacts cannot be related to the functioning of a facility in a certain location or point in time. Finally, the LCA is solely focused on the physical characteristics of the activities, and it excludes market mechanisms, secondary effects on technological development or social effects.¹¹

LCA methodology has been applied several times to study PEMWE. For example, a study by Bareiß et al in 2019 on hydrogen production by PEMWE in Germany has shown that the global warming potential (GWP), associated to CO₂ emissions, is mainly affected by the electricity grid mix. The authors have shown the GWP would decrease from about 29.5 to 3 kg CO₂ eq. for each kg of produced

H₂ when PEMWE is operated for 3000 h of excess power in a year from wind (65%) and solar energy (35%) instead of the current electricity grid mix based on fossil fuels.¹⁵ Additional studies have reached similar conclusions, further supporting the necessity for an energy transition from fossil fuels to renewable energy sources.^{16,17} Despite the lower impact of the electrolysis stack relative to the electricity grid mix, in the study by Schropp et al., it was stated that the environmental impacts of the electrolysis cell components start to have higher relative contribution when renewable energies are used, with the bipolar plates having the largest environmental impacts.¹⁶ Few other studies have focused instead on the material requirements and their impacts.^{6,18} It was found that the anode materials, namely iridium or ruthenium, account for most of the environmental impacts, closely followed by the titanium bipolar plates. They attribute most of these impacts to the mining processes required to produce these materials. The PFSA membranes, such as Nafion, also have large contributions, especially for ozone depletion potential, as mentioned previously. These previous studies only included state-of-the-art materials, most probably because they are focused on industrial scale. However, with the increasing amount of materials reported every day to substitute the SOA materials, there is no detailed environmental reports on such new materials. One of the reasons might be that most of them are still at lab-scale and thus, most material and energy requirements are not optimized. Nonetheless, LCA can be carried out for any scale.

In this chapter, the environmental impacts and energy demand of two artificial leaves, i.e. two different PEMWE cells, each coupled to a solar cell are analyzed and compared using LCA methodology. The artificial leaves differ in their PEMWE electrochemical cells. One is based on state-of-the-art water electrolysis materials such as RuO₂, Pt, Nafion, and titanium and it is named state-of-the-art artificial leaf (SOA a-leaf). The other is based on printed electrodes, and new electrocatalysts, and a PEM developed by early-stage researchers from the eSCALED project, and it is named eSCALED artificial leaf (eSCALED a-leaf). For both a-leaves, two perovskite single-junction solar cells as reported by Jiang et al. were used.¹⁹ The LCA of these solar cells has been previously studied by Tian et al.²⁰ The power conversion efficiency of the perovskite single-junction solar cell was 21.6%, the open-circuit voltage was 1.13 V, the short-circuit current density was 23.69 mA cm⁻², and the fill factor was 0.8061.

7.2. Objectives

This LCA study aims to determine the environmental performance of the eSCALED artificial leaf that combines a fully printed membrane–electrode assembly (pMEA) and perovskite solar cells. Finally, the eSCALED artificial leaf shall be compared with an artificial leaf that comprises the same solar cell and a membrane–electrode assembly (MEA) prepared with state–of–the–art materials. The LCA was conducted according to the ISO 14040 and ISO 14044 standards.^{9,10}

7.3. Products

The eSCALED project intends to develop an artificial leaf manufactured partially by up–scalable process techniques such as screen printing. The artificial leaf from eSCALED is composed of two perovskite solar cells connected in series and a fully printed membrane–electrode assembly. The catalyst and membrane materials were prepared by an eSCALED early–stage researcher. The second product of this study is an artificial leaf that combines the same perovskite solar but with a membrane–electrode assembly prepared with standard water electrolysis catalysts, membrane, and porous transport layers as described in chapter 3.

7.4. Life Cycle Assessment

7.4.1. Methodology

Life Cycle Assessment is defined by ISO 14040:2006 as a compilation and evaluation of the inputs, outputs, and potential environmental impacts of a product system throughout its life cycle. The inputs and outputs refer to the raw material, products, and energy required and to the emissions and solid waste produced by the product system, respectively. ISO 14040:2006 divides the LCA methodology into four phases:

a) Goal and Scope definition phase: the first phase of LCA is the goal and scope definition. In the Goal section, the intended application should be described, the reasons to carry out this type of study, the target audience of the study – i.e. to whom the results of the study may interest – and finally, whether the results of the LCA are supposed to be used in comparative assertions which are to be disclosed to the general public. The Scope section should include the product system in the study, the function of the product system, the functional unit, the system boundaries, limitations of the study, allocation procedures, methodology, and interpretation methods to determine the impacts of the study, assumptions made, data requirements and limitations, and the type of report

needed for the study, e.g. confidential, open to the public, open to the consortium and closed to the public.

b) Inventory Analysis phase: in this phase, data regarding the materials and energy requirements are collected and subsequently, interpreted to calculate the different impacts. The material, energy flows and emissions are calculated for every unit process comprised in the system boundaries and the results are related to the reference flow of the functional unit previously defined in the Goal and Scope phase.

c) Impact Assessment phase: the Impact Assessment phase aims to assess the potential environmental impacts by relating the results of the life cycle inventory (LCI) to the chosen impact categories, and thus, providing information for the next phase, the Interpretation phase.

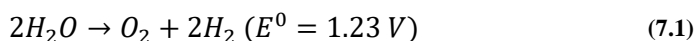
d) Interpretation phase: the last phase of LCA is the Interpretation phase, which considers both the results from the inventory analysis and the life cycle impact assessment (LCIA). Furthermore, the interpretation should be consistent with the goal and scope defined earlier, provide conclusions and recommendations, and explain the limitations.

7.4.2. Goal and Scope definition

7.4.2.1. Goal

7.4.2.1.1. Purpose of the study

This study intends to evaluate the environmental impacts of the manufacture of the eSCALED artificial leaf and an artificial leaf with state-of-the-art (SOA) water splitting materials considering every stage of their manufacture. The eSCALED device will be based on printed electrodes, earth-abundant materials for catalysts, and two perovskite solar cells that provide the necessary energy to drive the water splitting reaction – **Eq. 7.1**. The SOA device consists of the same solar cell but the electrochemical cell comprises RuO₂ and Pt as oxygen evolution catalysts and hydrogen evolution catalysts, respectively, and titanium and carbon-based porous transport layers.



A list of objectives for this study is given below:

- Assess the integration of the innovative materials developed in the eSCALED project such as the electrocatalysts, polymeric membranes, electrodes, and solar cells in an artificial leaf.

- Evaluate up-scalable processing technologies for the preparation of membrane-electrode assemblies such as screen printing.
- Compare these innovations to state-of-the-art artificial leaf, i.e. a flow electrochemical cell that works with state-of-the-art materials for water electrolysis.

7.4.2.1.2. *Reasons to carry out the study*

The LCA will provide a detailed analysis of the environmental impacts of the manufacture of the eSCALED artificial leaf. This study will help to identify improvable “hot spots” during the development and production of the artificial leaf to minimize the environmental impacts and also, the energy payback time (EPBT) as calculated from **Eq. 7.2**. The identification of these hot spots will help to target research effort to specific processes or materials, improving the future viability of such device.

$$\text{EPBT} = \frac{E_{\text{manufacture}}}{E_{\text{LeafOutput}}} \quad (7.2)$$

where $E_{\text{LeafOutput}}$ is the energy output rate of the artificial leaf and $E_{\text{manufacture}}$ is the energy required to manufacture the artificial leaf.

7.4.2.1.3. *Target Audience*

This study is targeted primarily at researchers involved in the eSCALED project, governmental and legislative bodies such as the European Commission (EC), academic partners and private commercial beneficiaries that are part of the eSCALED consortium. It is intended that the results of this study are disseminated in potential congresses and scientific journals for the wider scientific community.

7.4.2.1.4. *Type of critical review*

This study has been reviewed by LCA experts from Eurecat Technological Centre in Catalunya who are part of the eSCALED consortium. In addition, other partners and early-stage researchers have been involved in the improvement of this LCA, in compliance with the iterative nature of the LCA methodology.

7.4.2.2. *Scope*

7.4.2.2.1. *Function and Functional Unit*

The function of this LCA study has been defined as the amount of material or energy required per area of the artificial leaf with a solar-to-hydrogen efficiency (STH) of at least 10%. Hence, the functional units have been defined

as g cm^{-2} and MJ cm^{-2} . The area of the artificial leaf is considered equal to the area of the solar cell used in the device. This consideration is carried out as the STH is typically calculated with the area of the solar cell – **Eq. 7.3**.

$$\text{STH} = \frac{1.23J_{\text{op}}\eta_{\text{far}}}{P_{\text{in}}} \quad (7.3)$$

where J_{op} is the operating current density, η_{far} is the faradaic efficiency of the water splitting reaction and P_{in} is the irradiance, here considered as the standard AMG 1.5G spectral irradiance that corresponds to 100 mW cm^{-2} , also referred to as 1-sun equivalent light intensity.

7.4.2.2.2. System Boundaries

This LCA study considers the environmental impacts of raw material extraction to produce all the required components of an artificial leaf up to the integration of such materials into a device. This approach is commonly regarded as a cradle-to-gate approach. The analysis of the use and the end-of-life phases are excluded from this study as it would lead to greater uncertainties in the study due to the lack of primary data on processes such as the maintenance of the artificial leaf, disassembling and disposal of the materials at the end of their lifetime. This can be attributed to the low technology readiness level (TRL) of the eSCALED project which is more focused on lab-scale material design and process rather than commercial and industrial scale.

Figure 7.2 shows the system boundaries considered in the present study defined by the “*blue*” (dashed) rectangle. The “*red*” rectangle defines the manufacturing stage that includes the raw material acquisition, energy consumption, and waste produced by each synthesis. In the case of the eSCALED a-leaf, this stage involves the processes modelled by other eSCALED early-stage researchers (ESRs). The “*green*” rectangle comprises the assembly processes for the electrochemical cell that includes spray coating and screen printing and for the a-leaf, which consists of the integration of the solar cell and the electrochemical cell.

7.4.2.2.3. Data Sources and collection

The LCA models included in this study are based on primary data collected by the ESRs through their lab experience during the past 4 years. Other project partners and technology providers with their own expertise have also contributed to data collection. Processes that could not be collected by the aforementioned methods were based on patents, scientific communications, and the Ecoinvent v3.3 database included in the SimaPro software.

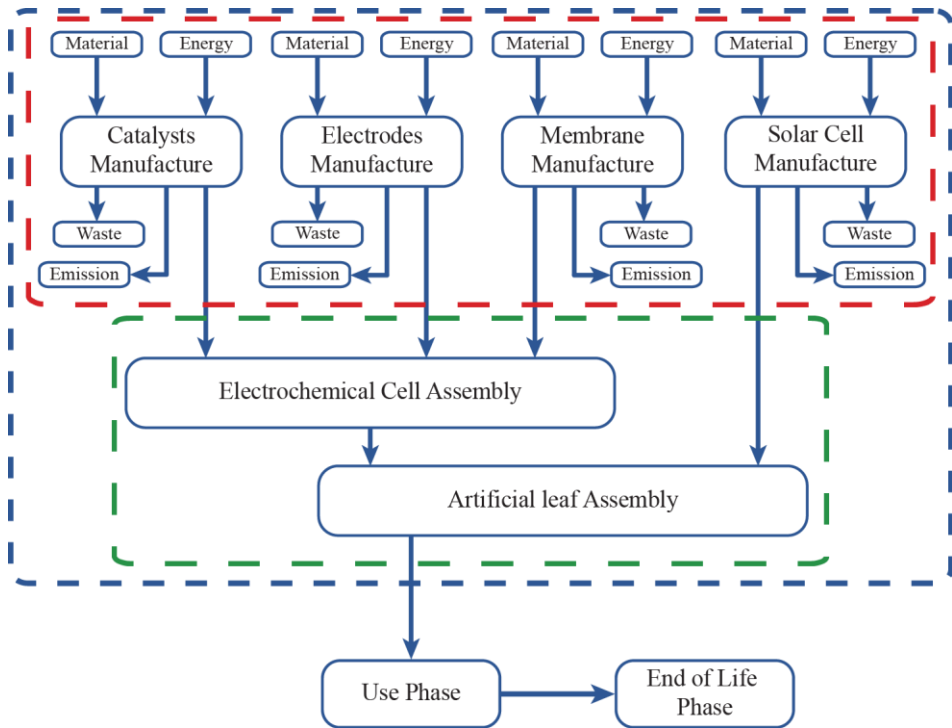


Figure 7.2: System boundaries for the LCA study of both a-leaves are defined by the “blue dashed” rectangle. For the eSCALED a-leaf, the processes inside the “red” rectangle were modelled by the respective early-stage researcher of the eSCALED project whereas in the “green” rectangle are the processes modelled only in the present study. For the state-of-the-art a-leaf, all processes were modelled for the present study.

7.4.2.2.4. Data quality requirements

The data collected in this study were analyzed regarding the completeness of the processes at each stage to ensure the utmost accuracy in reflecting the real processes; the geographical coverage as all processes were modelled as an average for Europe since the individual materials have all come from different parts of Europe; the time-related coverage to make sure that all data gathered is the most updated possible. When a shortage of data was encountered, public databases were employed using the most updated version of that database; the reproducibility by clearly identifying and referencing every data source so that anyone willing to perform this study can reproduce it and obtain equal results.

7.4.2.2.5. Cut-off criteria

As stated in ISO14040:2006, the “cut-off” criteria specify the amount of material, energy flow or the level of environmental significance associated with

unit processes or product system to be excluded from a study.⁹ This LCA study has not developed any cut-off based on mass or energy or environmental relevance. Therefore, all inputs to processes are considered in all stages.

7.4.2.3. Assumptions

The following assumptions and hypotheses are currently considered for the implementation of the LCA in the Excel spreadsheet and SimaPro software:

- All solvents used for the preparation of the inks are considered to evaporate into the air (Emissions to Air);
- Printing conditions and energy requirements were estimated based on prior experience for similar tests at the Functional Printing & Embedded Devices Unit at Fundació Eurecat;
- Energy requirements were estimated based on experimental work held at the Eindhoven University of Technology;
- All waste was considered as hazardous waste, and its treatment was considered as 85% landfill and 15% incineration, according to Eurostat as an average for Europe;²¹
- The lifetime of screen printing screens is assumed to be much larger than the lifetime of the device and therefore, they were not included in the modelling;
- The energy for milling the flow cell pieces was estimated assuming a milling speed of $60 \text{ cm}^2 \text{ h}^{-1}$;
- It is assumed that 30 % of all ink is lost during the coating and printing procedures;
- The energy used to evaporate the solvent during spray coating was calculated assuming an average evaporation time of 2 h;
- The density of CRP-PPFS-*b*-PBuAc (eSCALED membrane) was considered equal to Nafion (2.2 g cm^{-3});²²
- The required amount of isopropanol and acetone to clean the screen printing screens was assumed to be 200 mL each, estimated according to the experimental work held at the Eindhoven University of Technology;
- The nitrogen flowrate during spray coating and spray coating duration are estimated as 100 mL min^{-1} and 20 min, respectively;
- Ethanol (EtOH) is used as proxy material for trifluoroethanol (TFE). It is assumed that $1 \text{ mL TFE} = 1 \text{ mL EtOH}$, meaning that 1.39 g TFE corresponds to $7.84 \times 10^{-1} \text{ g EtOH}$;
- *Tert*-butylamine is used as proxy material for 4-*tert*-butylpyridine used in the perovskite solar cell preparation.

7.4.3. Inventory Analysis

The materials and energy requirements for the assembly of the electrochemical cell and the SOA MEA were modelled according to chapter 3 of this PhD thesis. The process to print graphite electrodes, printed pattern and graphite ink formulation were based on chapter 6 of this thesis. The inventory data for these processes is shown in **Table 7.1 – Table 7.3**. The inventory data for the Pt supported on carbon catalyst, the Nafion membrane and carbon porous transport layer were based on ref. ²². The inventory data for the eSCALED membrane, hydrogen and oxygen evolution catalysts were collected by the respective eSCALED early-stage researcher and are available elsewhere.^{13,23,24} The perovskite solar cell was modelled according to literature data.^{19,20}

Table 7.1: Life cycle inventory of the artificial leaves.

	Process	Amount	Unit	Remarks
SOA Artificial leaf: 1 cm²				
Inputs	Perovskite solar cell	1.00	cm ²	From ref. ²⁰
	Electrochemical cell	2.62	cm ²	
eSCALED Artificial leaf: 1 cm²				
Inputs	Perovskite solar cell	1.00	cm ²	From ref. ²⁰
	Electrochemical cell	2.44	cm ²	
Electrochemical cell: 1 cm²				
Inputs	Flow cell	12.5	cm ²	
	MEA (SOA or eSCALED)	1.00	cm ²	
	Gasket	4.67×10^{-1}	g	PTFE
	Metal frame	10.8	g	Support parts
	Screws	25.4	g	Support parts
	Nuts	4.16	g	Support parts
	Metal rings	2.88	g	Support parts
	Flow cell: 12.5 cm²			
Inputs	Polypropylene	11.2	g	
	Titanium bipolar plates	2.25	g	
	Energy – Milling	7.50×10^{-2}	kWh	

Table 7.2: Life cycle inventory of the SOA membrane–electrode assembly and respective processes.

	Process	Amount	Unit	Remarks
SOA MEA: 1 cm²				
Inputs	Nafion membrane	6.88×10^{-2}	g	$t = 50 \mu\text{m}$, $d = 2.2 \text{ g cm}^{-2}$ / From ref. ²²
	RuO ₂ electrode	1.00	cm ²	
	Pt electrode	1.00	cm ²	
	Titanium porous transport layer	1.56	cm ²	
	Carbon porous transport layer	1.56	cm ²	From ref. ²²
RuO₂ electrode: 1 cm²				

	Process	Amount	Unit	Remarks
Inputs	RuO ₂ ink	7.62×10^{-2}	g	
	Nitrogen flow	5.70×10^{-1}	g	
	Isopropanol (Cleaning)	39.3	g	
	Energy – heat	8.50×10^{-2}	kWh	
Outputs	Waste – Landfill	33.3	g	
	Waste – Incineration	5.97	g	
	Isopropanol	4.34×10^{-2}	g	Emission to air
	Water	1.99×10^{-2}	g	Emission to air
	1-Propanol	9.05×10^{-3}	g	Emission to air
	Nitrogen	5.70×10^{-1}	g	Emission to air
RuO₂ ink: 7.62×10^{-2} g				
Inputs	RuO ₂ powder	2.86×10^{-3}	g	
	Nafion solution (5 wt%)	1.90×10^{-2}	g	
	De-ionized water	1.09×10^{-2}	g	
	IPA	4.34×10^{-2}	g	
	Energy – Ultrasonication	1.65×10^{-3}	kWh	
Pt electrode: 1 cm²				
Inputs	Pt ink	9.52×10^{-2}	g	
	Nitrogen flow	5.70×10^{-1}	g	
	Isopropanol (Cleaning)	39.3	g	
	Energy – heating	8.50×10^{-2}	kWh	
Outputs	Waste – Landfill	33.4	g	
	Waste – Incineration	5.97	g	
	Isopropanol	5.43×10^{-2}	g	Emission to air
	Water	2.49×10^{-2}	g	Emission to air
	1-Propanol	1.13×10^{-2}	g	Emission to air
	Nitrogen	5.70×10^{-1}	g	Emission to air
Pt ink: 9.52×10^{-2} g				
Inputs	Pt/C powder	3.57×10^{-3}	g	From ref. ²²
	Nafion solution (5 wt%)	2.38×10^{-2}	g	
	De-ionized water	1.36×10^{-2}	g	
	IPA	5.43×10^{-2}	g	
	Energy – Ultrasonication	2.06×10^{-3}	kWh	
Nafion solution (5 wt%): 1 g				
Inputs	Nafion ionomer	5.00×10^{-2}	g	From ref. ²²
	1-Propanol	4.75×10^{-1}	g	
	Water	4.75×10^{-1}	g	
Ti PTL: 1.56 cm²				
Inputs	Titanium powder	8.00×10^{-1}	g	

Table 7.3: Life cycle inventory of the eSCALED membrane–electrode assembly and respective processes.

	Process	Amount	Unit	Remarks
eSCALED MEA: 1 cm²				
Inputs	Printed electrodes	2.63	cm ²	
	Membrane eSCALED	6.25	cm ²	From ref. ¹³

Life cycle assessment of an artificial leaf: new and standard materials

	Process	Amount	Unit	Remarks
	HER electrode	1.00	cm ²	
	WOC electrode	1.00	cm ²	
Printed electrodes: 2.63 cm²				
Inputs	Graphite ink	1.16×10^{-1}	g	
	Acetone	157	g	
	Energy – Pre-treatment	1.05×10^{-1}	kWh	
	Energy – Curing	2.23×10^{-1}	kWh	
	Energy – Screen printing	2.00×10^{-5}	kWh	
Output	Hazardous Waste – landfill	133	g	
	Hazardous Waste – Incineration	23.8	g	
Graphite ink: 1.16×10^{-1} g				
Inputs	Graphite powder	2.67×10^{-2}	g	
	Xylene	7.79×10^{-2}	g	
	Energy – Stirring	3.98×10^{-2}	kWh	
	Polymethyl methacrylate beads	1.14×10^{-2}	g	Binder
Output	Xylene	1.51×10^{-2}	g	Emission to air
HER electrode: 1 cm²				
Inputs	HER ink	1.36×10^{-1}	g	
	Nitrogen flow	5.70×10^{-1}	g	
	Dimethylformamide (Cleaning)	1.34×10^{-1}	g	
	Isopropanol (Cleaning)	39.3	g	
	Energy – Heat	8.5×10^{-2}	kWh	
Outputs	Hazardous Waste – Landfill	33.5	g	
	Hazardous Waste – Incineration	6.00	g	
	Dimethylformamide	1.34×10^{-1}	g	Emission to air
	Ethanol	1.10×10^{-1}	g	Emission to air
	Nitrogen	5.70×10^{-1}	g	Emission to air
HER ink: 1.36×10^{-1} g				
Inputs	HER catalyst	2.14×10^{-3}	g	From ref. ²³
	Dimethylformamide (DMF)	1.34×10^{-1}	g	
	MWCNTs suspension	4.29×10^{-4}	g	From ref. ²³
	Energy – Stirring	3.51×10^{-2}	kWh	
	Energy – Ultrasonication	8.87×10^{-3}	kWh	
WOC electrode: 1 cm²				
Inputs	WOC ink	2.97×10^{-2}	g	
	Nitrogen flow	5.70×10^{-1}	g	
	Isopropanol (Cleaning)	39.3	g	
	Energy – Heat	8.50×10^{-2}	kWh	
Outputs	Hazardous Waste – Landfill	33.3	g	
	Hazardous Waste – Incineration	5.97	g	
	Trifluoroethanol	2.97×10^{-2}	g	Emission to air
	Nitrogen	5.70×10^{-1}	g	Emission to air
WOC ink: 2.97×10^{-2} g				
Inputs	WOC catalyst	2.13×10^{-5}	g	From ref. ²⁴
	Trifluoroethanol	2.97×10^{-2}	g	
	Energy – Stirring	7.63×10^{-3}	kWh	

7.4.4. Life Cycle Impact assessment and evaluation

7.4.4.1. Impact characterization method selection

The impact assessment has been determined by the European ReCiPe 2016 midpoint method, hierarchist version 1.01 and the Cumulative Energy Demand version 1.10 as included in SimaPro software version 9.1.0.8. Two impact assessment methods must be used for this study since the ReCiPe method does not include an impact category regarding the embodied energy consumed throughout the life cycle of the used processes and materials. Midpoint indicators were chosen instead of endpoint indicators due to their lower uncertainty. **Table 7.4** summarizes all the impact categories considered for this project and their respective abbreviation and units.^{25–27} The choice of these impact categories was based on similar studies in literature. A brief explanation for the selection of each impact category is carried out below.

Table 7.4: Impact categories considered in the life cycle impact assessment.

Impact Category	Abbreviation	Unit / cm ⁻²
Cumulative Energy Demand	CED	MJ
Global Warming Potential	GWP	kg CO ₂ eq
Stratospheric Ozone Depletion	SOD	kg CFC–115 eq
Terrestrial Acidification	TA	kg SO ₂ eq
Freshwater Eutrophication	FE	kg P eq
Marine Eutrophication	ME	kg N eq
Terrestrial Ecotoxicity	TEC	kg 1,4–DCB eq
Freshwater Ecotoxicity	FEC	kg 1,4–DCB eq
Marine Ecotoxicity	MET	kg 1,4–DCB eq
Human Toxicity	HT	kg 1,4–DCB eq
Fossil Fuel Depletion	FFD	kg oil eq
Metal Depletion	MD	kg Fe eq
Water Consumption	WC	m ³

For energy-related devices such as an artificial leaf, the comparison between the manufacture energy and the energy produced – e.g. from the fuel produced by the artificial leaf – is an important assessment of its viability. Hence, the cumulative energy demand (CED) impact category was selected to calculate the EPBT according to **Eqs. 7.2 – 7.5**.

$$E_{\text{manufacture}} = \text{CED} \quad (7.4)$$

$$E_{\text{LeafOutput}} = \Delta G^0 \times N_{\text{H}_2} \quad (7.5)$$

where N_{H_2} is the hydrogen production rate in kg cm⁻² year⁻¹, and ΔG^0 is the standard Gibbs free energy in J kg⁻¹.

The purpose of solar cells and artificial leaves is to produce energy while providing a route to reduce the amount of anthropogenic CO₂ emissions. Therefore, one of the major impact categories required to evaluate the environmental performance of the a-leaves is the Global Warming Potential (GWP) which yields the amount of CO₂ produced and emitted by the analyzed processes.

Lead has been a major concern since the early days of perovskite solar cells. The use of this toxic substance has been restricted by the European Restriction of Hazardous Substances Directive.²⁵ Thus, in the case of the artificial photosynthesis device, the toxicity emerges as an important impact category to be evaluated. This impact category was divided into four: Terrestrial Ecotoxicity (TEC), Freshwater Ecotoxicity (FEC), Marine Ecotoxicity (MET), and Human Toxicity (HT). The latter includes both cancerous and non-cancerous effects.

The consumption of mineral resources, and energy via fossil fuels and water are evaluated by the impact category of abiotic depletion potential (ADP). ADP can then be divided into three sub-categories: fossil fuel depletion (FFD), metal depletion (MD), and water consumption (WC).

Lastly, due to the consumption of halogenated solvents, acids, nitrogen oxides (NO_x), and phosphate-containing compounds during the synthesis of the individual materials of the device, the stratospheric ozone depletion (SOD), terrestrial acidification (TA), freshwater eutrophication (FE), and marine eutrophication (ME) also arise as important impact categories.

7.4.4.2. Life cycle impact assessment

The studied a-leaves differ in two particular ways: solar cell to electrochemical cell ratio and materials and preparation methods used for the membrane-electrode assemblies. The solar cell (A_{sc}) to electrochemical cell (A_{ec}) active area ratio was obtained by first defining the operating current I_{op} , followed by operating voltages V_{op} for the solar cell and for the electrochemical cell. The I_{op} was defined as 17.5 mA for both a-leaves. the V_{op} of the SOA a-leaf was set to 1.41 V, assuming an electrochemical cell area of 4 cm² ($J_{op,ec} = 4.375 \text{ mA cm}^{-2}$) based on the work from chapter 3. For the eSCALED a-leaf, the electrochemical cell was assumed to be 70% less efficient than the SOA electrochemical cell, which results in a V_{op} of 2.01 V, which is close to maximum power point voltage (V_{mpp}) of the perovskite solar cells. The operating current density of the series-connected perovskite solar cells ($J_{op,sc}$) were based on the current density – voltage (J - V) curve obtained for the single-junction described in ref.¹⁹. This resulted in estimated STHs of 14.1% and 12.1% for the SOA and the eSCALED

a–leaf. Subsequently, the active area ratio between the solar cell and electrochemical cell (r_{area}) was calculated as:

$$r_{area} = \frac{A_{sc}}{A_{ec}} = \frac{J_{op,ec}}{J_{op,sc}} \quad (7.6)$$

Thus, the r_{area} for the eSCALED device was 0.41 and for SOA device is 0.38. This suggests from the start that the environmental impact of the solar cell will have larger relative impact for the SOA device.

Figure 7.3a shows the impact analysis of the two a–leaves. The environmental impacts of the perovskite solar cell are the same in both cases as the solar cell area was defined as 1 cm^2 for both devices. The environmental impact of the electrochemical cells outweighs by far the solar cell as it represents 98% or more in all impact categories in each a–leaf. The negligible contribution of the solar cell derives from being a thin–film technology, on order of hundreds of nanometers, where material expenditure is minimized in comparison to the electrochemical cells.

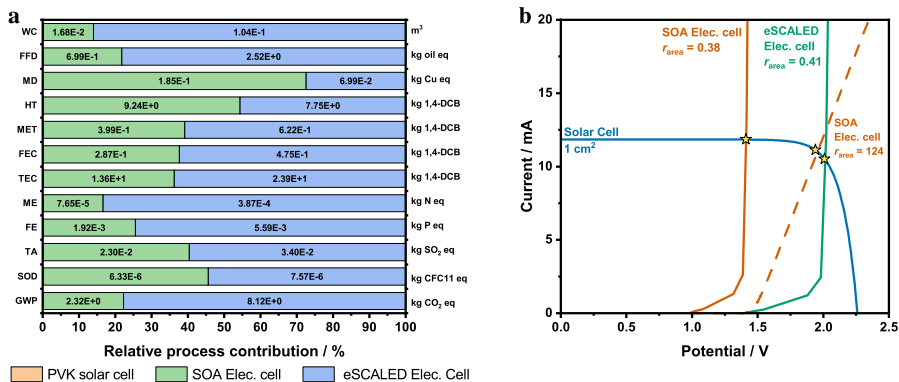


Figure 7.3: Analysis of the artificial leaf devices. a) Environmental impact analysis of 1 cm^2 a–leaves. The values for each impact category and cell are written in each bar. Values representing a relative contribution of less than 2% are not shown and hence the contributions of the PVK solar cell are not visible. b) Current versus voltage curves of the solar cells and the electrochemical cells. The dashed orange line represents the SOA electrochemical cell with smaller area. The star markers represent the operating point for each solar cell – electrochemical cell combination.

To minimize the environmental impact of the devices and balance the contributions of the solar cell in comparison to the electrochemical cell, an increase in the r_{area} would be beneficial, at the expense of some loss in STH. In the SOA a–leaf, the set V_{op} is still quite below the V_{mpp} of the solar cell ($\sim 1.94 \text{ V}$) and thus, a reduction in current density of the solar cell (and STH) is not abrupt (Figure 7.3b). Assuming the $V_{op,SOA}$ would be set to 1.94 V , the r_{area} would be \sim

120, hugely reducing the electrochemical cell material requirements and thus, lowering the environmental impacts and cost while only decreasing the STH from 14.1% to 13.7%. This increase in r_{area} would also further balance the contributions of the solar cell and the electrochemical cell. On the other hand, the eSCALED device already operates close to V_{mpp} , and further increasing the V_{op} would be followed by a large decrease in the current density of the solar cell and STH of the device.

The eSCALED electrochemical cell has higher environmental impact in almost every impact category except from MD and HT. A detailed analysis of each electrochemical cell with 1 cm^2 is done below, describing the origin of these environmental impacts. Equal area was chosen to allow direct comparison between the electrochemical cells, independently of efficiency. The analysis of both electrochemical cells is presented in **Figure 7.4**. The “*Support parts*” process consists of stainless steel screws, frames, nuts, and rings that are used to close the cell. The absolute impacts of the flow cell, gaskets and support parts are the same for both devices as they are independent of the changes in active materials such as catalysts, electrodes, and membranes. Their effect is more noticeable in the SOA electrochemical cell as the overall environmental impact of the SOA MEA is lower.

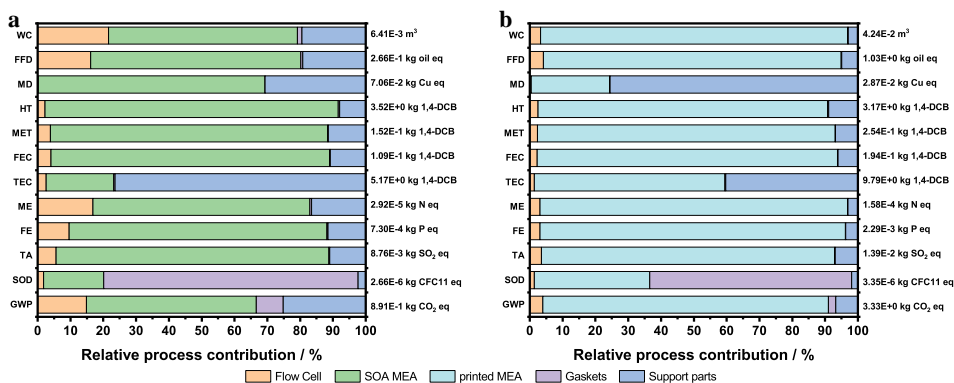


Figure 7.4: Environmental impact analysis of a 1 cm^2 electrochemical cell prepared with different methods. a) SOA electrochemical cell. b) eSCALED electrochemical cell.

The MEAs as major constituent of the electrochemical cell are the primary cause for most impact categories, except for SOD in both systems, TEC in the SOA electrochemical cell and MD in the eSCALED electrochemical cell. The gaskets are made of polytetrafluoroethylene (PTFE), which explains the large impact in the SOD category. The TEC and MD is highly affected by the support parts due to the mining processes of iron and nickel necessary for stainless steel production. The MEAs are the main component that differ most

between the two devices and a direct comparison, regarding the same active area, can be made. The environmental impacts of the SOA MEA and its major impact-causing processes are described and analyzed first, followed by those of the eSCALED MEA.

Most environmental impacts associated with the SOA MEA are mainly influenced by the two electrodes, the RuO₂ and Pt electrodes, as shown in **Figure 7.5a**. Instead, the Nafion membrane is the major contributor for stratospheric ozone depletion, due to the use of perfluorinated compounds for its manufacture such as tetrafluoroethylene – **Figure 7.5b**. Both PTLs (Ti and C) have minimal contributions to the environmental impacts of the SOA MEA and thus, their individual environmental impacts were not further studied here.

The RuO₂ electrode and Pt electrode were individually analyzed to provide further insight on the environmental impacts of these two processes as shown in **Figure 7.5c–d**. As expected, the catalyst inks are the major contributors for most impact categories which is attributed to the catalyst loadings required for optimal water electrolysis activity. These catalysts, RuO₂ and Pt, are known to be among the rarest metals on Earth and therefore, even the mining of a few mg (**Figure 7.5e–f**) largely affects the overall environmental impact of the MEA and lastly, the a-leaf.

The RuO₂ and Pt electrodes are prepared by spray coating the catalyst ink directly onto the membrane at elevated temperatures, followed by cleaning the spray gun with isopropanol and paper. The isopropanol represents the second largest contributor to most impact categories, followed by energy used to heat the membrane. The impact of the cleaning step may possibly be reduced by, for example, introducing a recycling step for the isopropanol, avoiding the use of new isopropanol every time. For the heating step, the heating time influences the most the energy requirements. A slight increase in temperature, e.g. 85°C to 90°C, would decrease the heating time, also representing a decrease in energy requirement for heating. However, it is important to ensure the increase in temperature does not affect the membrane.

The impact analysis of the printed MEA and main components is shown in **Figure 7.6**. For the printed MEA, the eSCALED membrane is clearly the highest contributor to all impact categories, with relative contributions ranging from 38% in MD to 68.4% in FE, followed by the printed electrodes as shown in **Figure 7.6a**. The large impact of the membrane arises primarily from the use of pentafluorostyrene (PFS) as main monomer. The PFS monomer accounts for roughly 90% of the impact of the membrane for almost all categories. One of the solvents used during the synthesis of this monomer is benzonitrile which is

classified as dangerous for the ozone layer and human health.¹³ Metal depletion is more influenced by the treatment of hazardous waste in a landfill which is assigned to the use of steel to build the landfill.

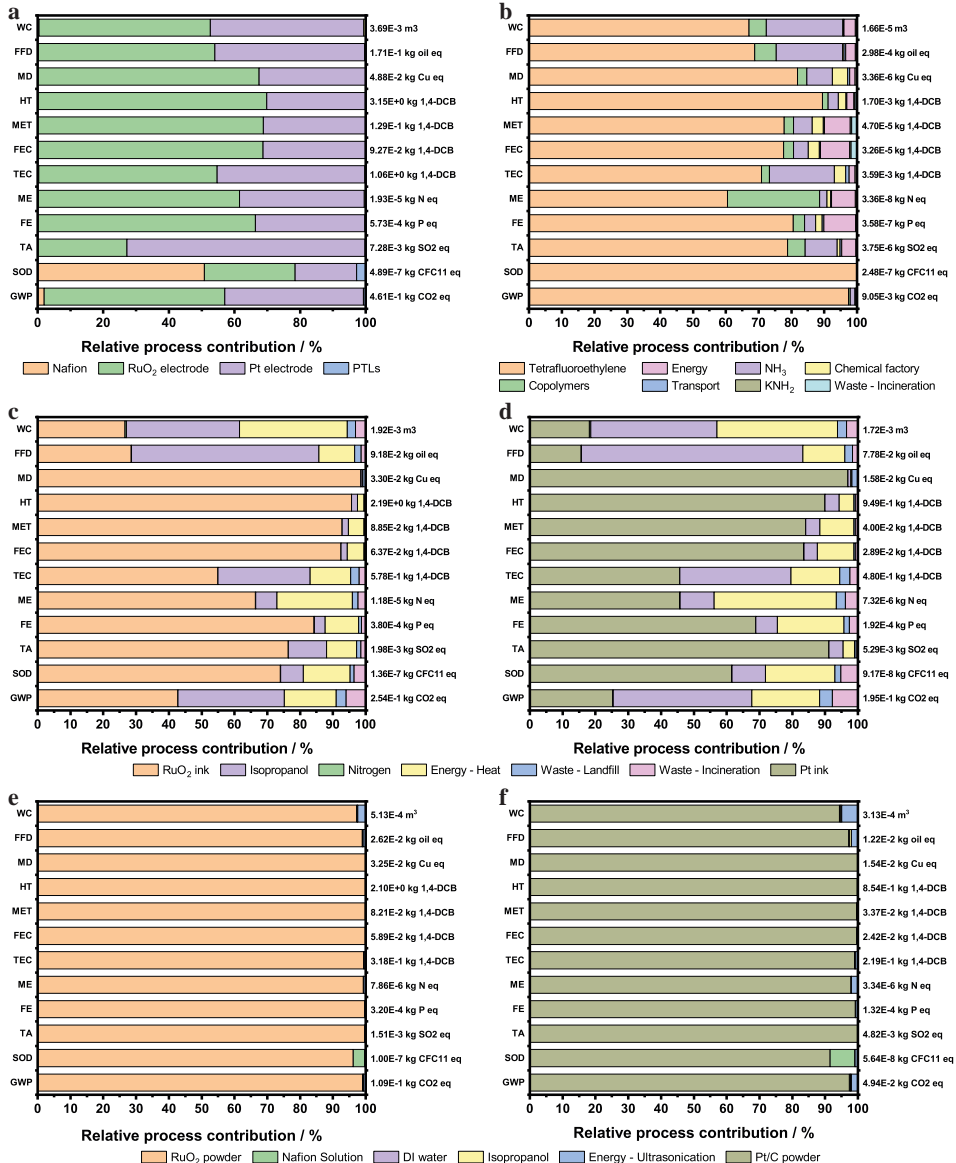


Figure 7.5: Environmental impact analysis of the different components of the SOA MEA. a) 1 cm² MEA prepared with SOA materials, **b)** 6.25 cm² Nafion **c)** 1 cm² RuO₂ electrode and **d)** 1 cm² Pt electrode, **e)** 7.62 × 10⁻² g RuO₂ ink and **f)** 9.52 × 10⁻² g Pt ink.

In the printed electrodes (Figure 7.6b), the energy used for heating, in the form of electricity, has by far the largest impact. This electricity is required to operate the ovens used for pre-treating the substrate and thermally anneal the printed electrodes after printing. The energy requirement for these two steps was modelled assuming that one lab-sized oven was used to pre-treat and cure an electrode with active area of 4 cm^2 , similar to what was done during experiments. Besides, the heating energy is directly proportional to the area of the electrodes. These assumptions immensely affect the impact of the heating energy in this process as the available working area of the oven is much larger than 4 cm^2 . Thus, the impact would be reduced if the total available area of one oven was used to cure more than one electrode at a time.

The lower relative contribution of the electrodes (HER and WOC electrode) only occurs because the eSCALED membrane has much higher environmental impact and therefore, interpretation of solely the relative contributions can be misleading. The absolute contribution of the eSCALED electrodes is actually quite similar to the state-of-the-art electrodes (RuO_2 and Pt) and in the case of HER electrode, it is higher than most impacts of Pt.

For the WOC electrode, it was assumed that the amounts of cleaning solvent, i.e. isopropanol, heating energy, nitrogen and waste treatment would be the same as for the remaining electrodes, even though, the loading is about 100 times lower than for its HER counterpart. This catalyst loading was taken based on the typical loadings used in experimental work with small electrodes and also, it is assumed that similar current output to the HER counterpart is reached. This assumption is considered valid as experimentally, the coating process takes roughly the same time independently of the catalyst loading and the cleaning involves immersing the air gun in isopropanol and sonicating it. For these reasons, the isopropanol and the heating energy have the higher environmental impacts as shown in Figure 7.6c. In the case, the WOC loading is increased to values close to $1\text{--}2 \text{ mg cm}^{-2}$, it will actually outweigh the impact from the isopropanol and heating energy. With loadings similar to RuO_2 , the impact of this electrode will also surpass the impacts for RuO_2 .

Figure 7.6d shows the impact analysis for the HER electrode. The catalyst ink is responsible for most of the impact of the HER electrode, similarly to the remaining electrodes described earlier. In contrast with the other electrodes, the actual catalyst is not the highest contributor to the environmental impacts of the catalyst ink (Figure 7.6f), instead the multiwall carbon nanotubes (MWCNT) are. The HER catalyst has to be anchored on MWCNT to avoid catalyst loss during operation by dissolution in the feed water. The MWCNT production

process is quite energy intensive, leading to the large environmental impacts observed.

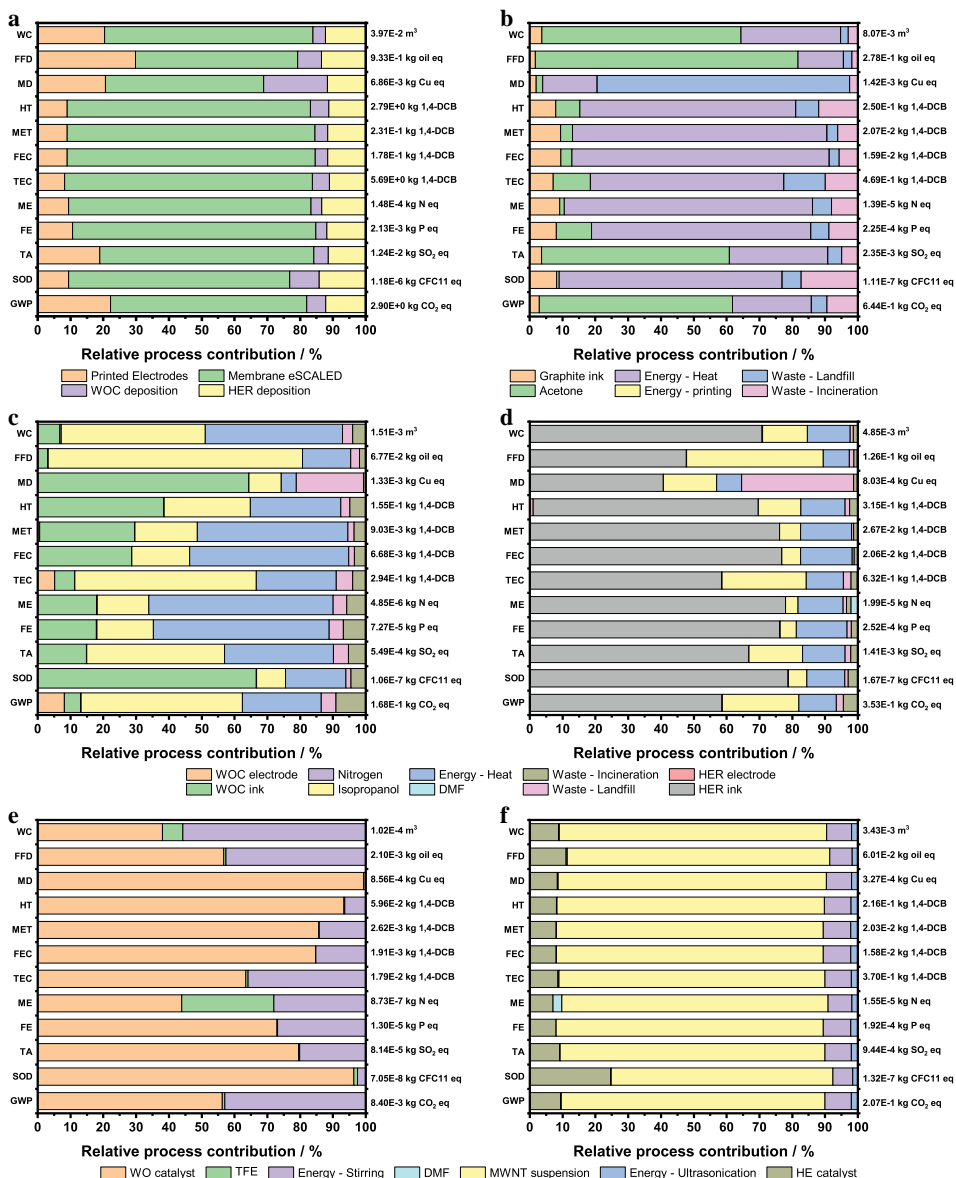


Figure 7.6: Environmental impact analysis of the different components of the eSCALED MEA. a) 1 cm² MEA prepared with eSCALED materials and printed electrodes. b) 2.625 cm² Printed electrodes. c) 1 cm² water oxidation catalyst (WOC) electrode. d) 1 cm² Hydrogen evolution catalyst (HEC) electrode. e) 2.97 × 10⁻² g water oxidation (WO) catalyst ink. f) 1.36 × 10⁻¹ g hydrogen evolution (HE) catalyst ink.

Figure 7.7 shows a comparison of the two studied MEAs as well as a eSCALED MEA where the membrane was replaced by Nafion. The environmental impact of the eSCALED MEA is significantly higher in most impact categories (>60%) except for MD (12.3%) and HT (47.0%). These two impact categories in SOA MEA are mostly affected by the mining processes of Ru (used for RuO₂) and Pt. The slightly higher human toxicity for SOA MEA is assigned to the sulfidic tailings from the ore mining. Nonetheless, the use of harmful chemicals for the synthesis of poly(pentafluorostyrene) has almost the same effect on human toxicity from the eSCALED MEA.

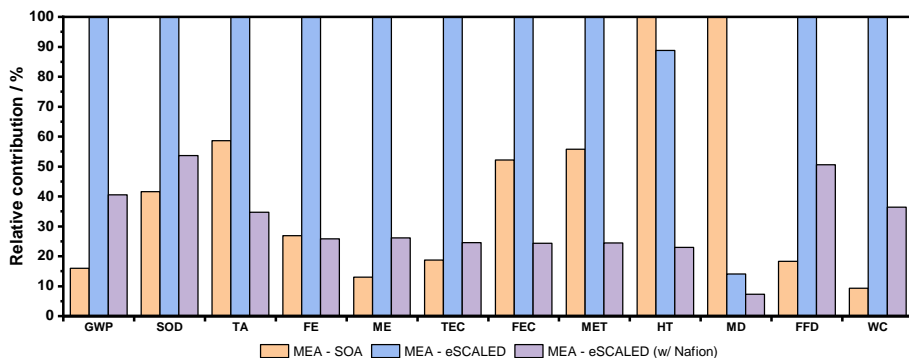


Figure 7.7: Normalized relative contribution to each impact category by each MEA.

As the PPFs–membrane is the most critical material in terms of environmental impacts for the eSCALED MEA, replacing it with Nafion could be beneficial since it has little contribution in comparison to the remaining materials in SOA MEA. This replacement would reduce most environmental impacts to similar or just slightly higher values than the SOA MEA (Figure 7.7). Hence, this change would also result in comparable environmental impacts for both complete artificial leaves.

Lastly, the a–leaves were analyzed regarding the cumulative energy demand (CED), i.e. the energy required to manufacture the devices, as shown in **Figure 7.8**. Similarly to the environmental impacts, the electrochemical cells are significantly more demanding in terms of energy than the solar cells. In the eSCALED device, the PPFs–based membrane represents more than half of the total energy demand at $98.2 \text{ MJ cm}_{\text{sc}}^{-2}$, showing again that is the process that requires the most improvement. For the SOA a–leaf, the most energy demanding processes are the RuO₂ and platinum electrodes with 13.1 and $11.3 \text{ MJ cm}_{\text{sc}}^{-2}$, respectively.

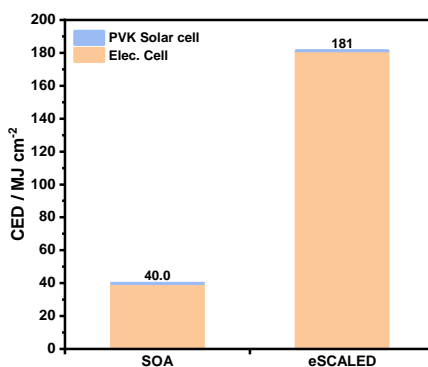


Figure 7.8: Cumulative energy demand of the eSCALED and SOA artificial leaves. The total CED (perovskite (PVK) solar Cell and electrochemical cell (Elec. Cell)) for each a-leaf is shown on top of each bar.

The eSCALED a-leaf (STH = 12%) produces $3.23 \text{ g year}^{-1} \text{ cm}^{-2}$ of hydrogen, which amounts to $3.80 \times 10^{-1} \text{ MJ year}^{-1} \text{ cm}_{\text{sc}}^{-2}$. Therefore, the eSCALED a-leaf would need to operate for 476 years uninterrupted to produce as much energy as it is required to assemble the device. The respective replacement of the PPFS-based membrane with Nafion would reduce it to 218 years. Clearly, these EPBTs are too large and points out that it is crucial to improve the materials' efficiency and energy demand of the eSCALED device. The SOA a-leaf is a slightly more efficient system (STH = 14%) with lower energy fabrication demand and, instead, has a EPBT close to 90 years, which is also far from ideal, but largely better than the eSCALED one. In the case where the V_{op} is moved close to the V_{mpp} and assuming a conservative estimate for r_{area} of 124, the EPBT would be around 0.68 years. This emphasizes once more the importance and influence the operating conditions have in the overall efficiency, environmental impacts and energy demand.

This work has shown that even though the SOA materials, such as Nafion, Pt, and RuO_2 , are highly regarded as the limiting factor of water electrolysis, they still present lower environmental impacts and energy demand than the new materials and approaches envisaged by the eSCALED project. Especially, when the electrochemical cell is operated at very high current densities that allowed to decrease the impacts and energy demand by over two orders of magnitude. The eSCALED a-leaf is mostly influenced by the PPFS-based membrane, in terms of environmental impacts and energy demands. Moreover, the efficiency of the eSCALED materials, particularly of the earth-abundant catalysts, requires a large improvement. Even though often considered environmentally friendly, the insufficient current output of these catalysts

prevents them from being competitive with Pt or RuO₂, both environmentally and energy consumption.

It is important to highlight that these results also reflect the fact that eSCALED is a low TRL project. Lower TRL projects typically have a worse environmental impact than more mature technologies since the materials and processes were only developed at lab-scale. Nonetheless, by showing what are the most environmentally impactful materials/processes, this LCA study provides an initial platform to support the further development of these novel materials at higher TRLs with lower environmental impacts.

7.5. Conclusion

The environmental impacts and primary energy demand of two artificial leaves, based on either state-of-the-art or eSCALED materials, were evaluated using a life cycle assessment methodology following the guidelines and framework provided by the ISO 14040 and 14044 standards. An artificial leaf comprises two separate devices: solar cell and electrochemical cell. The solar cell for both studied artificial leaves was based on a perovskite solar cell described in the literature. The SOA electrochemical cell consists of Nafion as proton exchange membrane, RuO₂, Pt, Ti, and carbon porous transport layers as the key components. In contrast, the electrochemical cell for the eSCALED artificial leaf comprised a polypentafluorostyrene-based proton exchange membrane, graphite screen-printed electrodes, and molecular catalysts. The eSCALED materials were modelled by the respective early-stage researcher of the eSCALED project and integrated here to analyze the overall impact of a working device solely made of eSCALED materials. The SOA electrochemical cell was modelled according to chapter 3 of this thesis. The electrochemical cell consists of a flow cell, supporting parts such as screws, nuts, metal rings and frame, and the membrane-electrode assemblies. The major difference between the two devices lies on the membrane-electrode assemblies where the SOA materials are replaced by the eSCALED ones.

Two important parameters for this integration are the area ratio r_{area} between the solar cell and electrochemical cell and the STH. The r_{area} influences the STH of the devices and the relative contribution of the solar cell on the environmental impacts and cumulative energy demand in comparison to the electrochemical cell. The STH directly affects the EPBT as a higher STH leads to lower EPBT. The material and energy estimations lead to a r_{area} of 0.40 and STH of 12% for the eSCALED a-leaf, while for the SOA a-leaf, the r_{area} was 0.38 and STH was 14%.

All environmental impact categories and energy demand for both devices are primarily caused by the electrochemical cell, which effect is enhanced by the low r_{area} . When comparing both a-leaves, the eSCALED device has clearly larger environmental impacts in all but two impact categories and an energy demand 4.5 times higher than the SOA device. Besides, the relatively good STH of both devices, due to the well-performing solar cell, culminate in an EPBT of 90 and 476 years for the SOA and eSCALED a-leaves, respectively. The EPBT of the SOA a-leaf could be reduced by operating it at higher V_{op} .

Following this, the impact assessment of the electrochemical cell was preferably studied as it provides an easier and direct comparison between the SOA and esCALED materials for the same active area, without considering the materials' efficiency. In both electrochemical cells, the MEA has the highest environmental impact in most categories, except for SOD and TEC. The SOD is more affected by the PTFE gaskets while the TEC is influenced by the stainless steel supporting parts, which is associated to the mining processes of iron and nickel. The environmental impacts of the SOA MEA are mostly related to the mining of Ru, for RuO_2 , and Pt, but the isopropanol used for cleaning the spray gun and heating energy for the electrode preparation also have a large contribution, especially for FFD and WC. Possibly, the impact of the heating energy and isopropanol could be diminished by optimizing the heating time and temperature, and introducing a recycling step for the isopropanol, respectively. For eSCALED MEA, the proton exchange membrane has clearly the highest impact due to the synthesis of PFS, followed by the printed electrodes or the HER electrode. The printed electrodes have a large energy consumption associated to the curing of the electrodes after printing. The main source of environmental impacts of the HER electrode is actually the support material, the MWCNT, and not the catalyst itself.

Overall, the eSCALED a-leaf, in particular the MEA, had larger environmental impact values higher in most impact categories than the SOA device. Despite the typical considerations regarding the high environmental impact of SOA materials and the need for replacement, new materials as the ones developed in the eSCALED project still lag behind in terms of environmental impacts, especially due to the low efficiencies. This further demonstrates that developing materials that can replace the existing ones is an extremely difficult task.

The present study aims to show the importance of performing a LCA of new systems and materials, independently of the TRL, and to provide a comparison with existing systems. LCA methodology should then play an

essential role in driving research and development to higher TRLs in the future with much less environmental impacts and less energy demands.

7.6. References

1. Bernt, M. P. Analysis of Voltage Losses and Degradation Phenomena in PEM Water Electrolyzers. (Technische Universität München, 2019).
2. Wang, Y., Sharma, A., Duong, T., Arandiyani, H., Zhao, T., Zhang, D., Su, Z., Garbrecht, M., Beck, F. J., Karuturi, S., Zhao, C. & Catchpole, K. Direct Solar Hydrogen Generation at 20% Efficiency Using Low-Cost Materials. *Adv. Energy Mater.* **11**, 2101053 (2021).
3. Carmo, M., Fritz, D. L., Mergel, J. & Stolten, D. A comprehensive review on PEM water electrolysis. *Int. J. Hydrogen Energy* **38**, 4901–4934 (2013).
4. Bosson, K., Marcasuzaa, P., Bousquet, A., Tovar, G. E. M., Atanasov, V. & Billon, L. para fluoro-thiol clicked diblock-copolymer self-assembly: Towards a new paradigm for highly proton-conductive membranes. *J. Memb. Sci.* **659**, 120796 (2022).
5. Glaister, B. J. & Mudd, G. M. The environmental costs of platinum–PGM mining and sustainability: Is the glass half-full or half-empty? *Miner. Eng.* **23**, 438–450 (2010).
6. Mori, M., Stropnik, R., Sekavčnik, M. & Lotrič, A. Criticality and Life-Cycle Assessment of Materials Used in Fuel-Cell and Hydrogen Technologies. *Sustainability* **13**, 3565 (2021).
7. Albrecht, S. & Fischer, M. Cooperation of Young Researchers from Science and Industry — Life Cycle Assessment in Theory and Practice. in *Progress in Life Cycle Assessment 2019* 1–4 (2021).
8. European Platform on Life Cycle Assessment (LCA). <https://ec.europa.eu/environment/ipp/lca.htm>. (Accessed on March 3rd, 2023)
9. International Organization for Standardization (ISO). *BS EN ISO 14040:2006 Environmental management - Life Cycle Assessment - Principles and Framework*. (2006).
10. International Organization for Standardization (ISO). *ISO 14044:2006(E) Environmental management - Life cycle assessment - Requirements and guidelines*. (2006).
11. de Bruijn, H. & van Duin, R. *Handbook on Life Cycle Assessment: Operational Guide to the ISO standards*. (Kluwer Academic Publishers, 2002).
12. Baitz, M. *et al.* LCA's theory and practice: like ebony and ivory living in perfect harmony? *Int. J. Life Cycle Assess.* **18**, 5–13 (2013).
13. Bosson, K. N. Proton-conducting membranes for the artificial leaf. (University of Pau and Pays de l'Adour / University of Stuttgart, 2022).
14. Caro, D. Carbon Footprint. in *Encyclopedia of Ecology* 252–257 (Elsevier, 2019).
15. Bareiß, K., de la Rúa, C., Möckl, M. & Hamacher, T. Life cycle assessment of hydrogen from proton exchange membrane water electrolysis in future energy systems. *Appl. Energy* **237**, 862–872 (2019).
16. Schropp, E., Naumann, G. & Gaderer, M. Life Cycle Assessment of a Polymer Electrolyte Membrane Water Electrolysis. in *Progress in Life Cycle Assessment 2019* 53–66 (2021).

17. Gerloff, N. Comparative Life-Cycle Assessment Analysis of Power-to-Methane Plants Including Different Water Electrolysis Technologies and CO₂ Sources While Applying Various Energy Scenarios. *ACS Sustain. Chem. Eng.* **9**, 10123–10141 (2021).
18. Zhao, G., Kraglund, M. R., Frandsen, H. L., Wulff, A. C., Jensen, S. H., Chen, M. & Graves, C. R. Life cycle assessment of H₂O electrolysis technologies. *Int. J. Hydrogen Energy* **45**, 23765–23781 (2020).
19. Jiang, Q., Chu, Z., Wang, P., Yang, X., Liu, H., Wang, Y., Yin, Z., Wu, J., Zhang, X. & You, J. Planar-Structure Perovskite Solar Cells with Efficiency beyond 21%. *Adv. Mater.* **29**, 1703852 (2017).
20. Tian, X., Stranks, S. D. & You, F. Life cycle assessment of recycling strategies for perovskite photovoltaic modules. *Nat. Sustain.* **4**, 821–829 (2021).
21. EU-28 - 2018 Eurostat: <https://appsso.eurostat.ec.europa.eu/nui/submitViewTableAction.do>. (Accessed on September 13th, 2022)
22. Notter, D. A., Kouravelou, K., Karachalios, T., Daletou, M. K. & Haberland, N. T. Life cycle assessment of PEM FC applications: electric mobility and μ -CHP. *Energy Environ. Sci.* **8**, 1969–1985 (2015).
23. Zamader, A., Reuillard, B., Marcasuzaa, P., Bousquet, A., Billon, L., Espí Gallart, J. J., Berggren, G. & Artero, V. Electrode Integration of Synthetic Hydrogenase as Bioinspired and Noble Metal-Free Cathodes for Hydrogen Evolution. *ACS Catal.* **13**, 1246–1256 (2023).
24. Sanjuan, D., Espí, J. J., Grammatico, D., Zamader, A., Branco, B., Bosson, K., Vukovic, O. & Howe, A. *D6.5: Report on LCA and economic costs of the environmental impacts*. (2022).
25. Alberola-Borràs, J. A., Baker, J. A., De Rossi, F., Vidal, R., Beynon, D., Hooper, K. E. A., Watson, T. M. & Mora-Seró, I. Perovskite Photovoltaic Modules: Life Cycle Assessment of Pre-industrial Production Process. *iScience* **9**, 542–551 (2018).
26. Tsang, M. P., Sonnemann, G. W. & Bassani, D. M. A comparative human health, ecotoxicity, and product environmental assessment on the production of organic and silicon solar cells. *Prog. Photovoltaics Res. Appl.* **24**, 645–655 (2016).
27. Alberola-Borràs, J. A., Vidal, R., Juárez-Pérez, E. J., Mas-Marzá, E., Guerrero, A. & Mora-Seró, I. Relative impacts of methylammonium lead triiodide perovskite solar cells based on life cycle assessment. *Sol. Energy Mater. Sol. Cells* **179**, 169–177 (2018).

Summary

The unpredictability and intermittency associated with solar energy render it unsuccessful to fully replace fossil fuels. Expansion of the deployment of renewable energy will also depend on appropriate energy storage methods and water electrolysis arises as one of the most promising of such technologies. However, solar-driven water electrolysis currently relies on noble metal and metal oxide electrocatalysts and bipolar plates, perfluorinated polyelectrolytes, and III–V multijunction solar cells that have high economic and environmental burdens. Developing and implementing zero-carbon and cost-effective solutions is thus fundamental to reduce the global dependence on fossil fuels and achieve carbon-neutrality.

This work focuses on testing proton-exchange membranes based on fluorinated polymers, preparing membrane-electrode assemblies by printing methodologies, and combining a water electrolysis cell with perovskite-based multijunction solar cells to enable high solar-to-hydrogen conversion. The research is part of the eSCALED project that aims at creating new materials and devices to eventually combine into an artificial leaf, mimicking natural photosynthesis.

Firstly, in chapter 2, to ensure reproducible and comparable results with literature work when using state-of-the-art materials, a water electrolysis setup and cell were built and optimized. The optimization process involved the study of the cell clamping torque, cell temperature, flow field's material, porous transport layers (PTLs) materials and sample storage environment. After the improvement of the resistive losses, reaction kinetics, and overall stability, the proton exchange membrane water electrolysis reached current densities as high as 1 A cm^{-2} below 1.70 V. These results established the benchmark for the new electrolysis materials and preparation methodology investigated in later chapters.

In chapter 3, a monolithic two-terminal multijunction solar cell that combined a wide-bandgap perovskite (PVK) semiconductor with a narrow-bandgap crystalline silicon (c-Si) was connected to the water electrolysis cell for solar-driven water electrolysis operation under 1-Sun equivalent light intensity. Two-terminal multijunction solar cells provide an open-circuit voltage (V_{oc}) beyond the standard cell potential for water electrolysis while also increasing the power conversion efficiency (PCE) above the limit of series-connected single-junction cells. The PVK-Si tandem solar cell attains a V_{oc} above 1.75 V, enough to conduct water electrolysis, while reaching high current densities that enable a solar-to-hydrogen efficiency (STH) of 21.5% when using state-of-the-art catalysts and membranes. This STH value is presently the highest reported value

for a system operating without sunlight concentration. The system also represents the first example of a two-terminal PVK–Si multijunction solar cell coupled to a flow electrochemical cell operating in normal sunlight.

In chapter 4, the PVK–Si tandem solar cell is replaced by an all-perovskite tandem solar cell that provides a higher V_{oc} of almost 2 V, widening the operating voltage range at the expense of some current density. The slightly increased V_{oc} is beneficial in case less efficient, but cost-effective electrocatalysts are used as the overpotential for water electrolysis rises. Solar-driven water electrolysis conducted with the all-perovskite tandem solar cell reached a STH close to 19% while using a comparatively inexpensive semiconductor and state-of-the-art catalysts and membranes. Additionally, this chapter describes the optimization of a narrow-bandgap perovskite solar cell to potentially increase the PCE of the all-perovskite tandem solar cell and STH of the coupled system. The use of bulk additives and top surface treatments of the perovskite layer enabled a maximum PCE of 18.6%, a 3.1% increase over the previous procedure. Such optimization combined with further improvements on the wide-bandgap sub-cell might elevate the PCE of the all-perovskite tandems above 26% and STH to almost 20%.

In the next chapter, the water electrolysis performance and hydrogen permeability of different proton exchange membranes (PEMs) made of sulfonated derivatives of polypentafluorostyrene and poly(arylene thioether)s are compared to Nafion as standard membrane. These membranes were developed by other researchers in eSCALED. The ionic transport properties of the new PEMs are mostly better than Nafion, however, Nafion still outperformed them in terms of energy and faradaic efficiency in water electrolysis. This was mainly attributed to the larger water uptake and swelling ratios of the new membranes that increased mass transfer losses at the electrodes and allowed more hydrogen crossover. Hence, the design of new ionomers for PEMs should combine high ion transport properties and low water uptakes to avoid excessive gas permeation and energy losses.

Titanium is widely used to manufacture the porous transport layers and bipolar plates, however, it results in high capital cost, which is higher than the one associated with the noble metal catalysts, decreasing the economic viability of water electrolysis. The growing field of printed electronics may provide a suitable answer to attain high throughput and low-cost manufacturing of electrodes. Graphite-based electrodes printed directly on Nafion with diverse patterns are studied in chapter 6. The patterns allowed proton transport across the membrane that resulted in successful water electrolysis, but also revealed several

Summary

shortcomings in terms of resistive losses, graphite oxidation, reproducibility and overall performance. Additional improvements on the ink formulation and testing other patterns may enhance the efficiency of these electrodes, whilst using minimal amount of materials.

In the last chapter, a life cycle assessment (LCA) of a solar-driven water electrolysis device that integrates the new materials (PEM and molecular catalysts developed in eSCALED project) is conducted. In this LCA, the eSCALED device is further compared with a device employing state-of-the-art materials. The study considers all the environmental impacts from raw material extraction (cradle) to manufacture (gate) of the devices to identify the most environmentally critical processes and materials. Overall, the environmental impact and energy demand of the eSCALED device were larger than of the state-of-the-art device. The low efficiency of the molecular catalysts in particular, prevents operation of the electrochemical cell at high current densities, resulting in larger material and energy consumption in the coupled system (photovoltaics and electrolysis components). Finally, the identification of the most environmentally impactful processes led to a better understanding of the environmental burden of the devices and where to improve them in the future.

Samenvatting

De onvoorspelbaarheid en wisselvalligheid van het aanbod van zonne-energie maakt deze energiebron minder geschikt om fossiele brandstoffen volledig te vervangen. Succesvolle toepassing van hernieuwbare zonne-energie zal mede afhangen van geschikte energieopslagmethoden. Watelektrolyse komt hierbij naar voren als een van de meest veelbelovende technologieën. Elektrolyse van water op basis van zonne-energie is momenteel echter afhankelijk van dure materialen met een hoge ecologische voetafdruk zoals elektrokatalysatoren op basis van edele metalen en metaaloxiden, bipolaire platen, geperfluoreerde polyelektrolyten en III-V-hallegeleider zonnecellen. Het ontwikkelen en implementeren van goedkopere oplossingen met een intrinsiek lage CO₂ uitstoot is van fundamenteel belang om de wereldwijde afhankelijkheid van fossiele brandstoffen te verminderen en koolstofneutraliteit te bereiken.

Dit proefschrift beschrijft het testen van proton-uitwisselingsmembranen op basis van gefluoreerde polymeren, het assembleren van membraan-elektrode combinaties door middel van printmethodologieën en het samenvoegen van een watelektrolyse cel met een perovskiet-silicium tandem zonnecel om een efficiënte omzetting van zonlicht naar waterstof mogelijk te maken. Het onderzoek maakt deel uit van het eSCALED project dat zich richt op het ontwikkelen en analyseren van nieuwe materialen om uiteindelijk een kunstmatig blad te fabriceren dat de natuurlijke fotosynthese nabootst.

In hoofdstuk 2 wordt de bouw van de watelektrolyse opstelling en -cel beschreven. Door middel van optimalisatie van de opstelling zijn reproduceerbare en met de literatuur vergelijkbare resultaten behaald. Het optimalisatieproces omvatte het bestuderen van het klemmoment van de cel, de celtemperatuur, het materiaal van het stromingsveld, de materialen van de poreuze transportlagen (PTL's) en de omgeving voor monsteropslag. Na het verbeteren van de weerstandsverliezen, de reactiekinetiek en de algehele stabiliteit bereikte de watelektrolyse met een proton-uitwisselingsmembraan stroomdichtheden tot 1 A cm⁻² bij een spanning van 1.70 V. Deze resultaten vormden de maatstaf en het startpunt voor de nieuwe elektrolysematerialen en methodes die in latere hoofdstukken zijn beschreven.

Hoofdstuk 3 beschrijft een monolithische, twee-terminal tandem zonnecel, gebaseerd op een perovskiet (PVK) hallegeleider met een brede bandafstand en kristallijn silicium (c-Si) met een smalle bandafstand, aangesloten op de watelektrolyse cel voor door zonlicht aangedreven watelektrolyse bij een lichtintensiteit van 1 zon. Twee-terminal tandem

Samenvatting

zonnecellen bieden een openklemspanning (V_{oc}) die hoger is dan de standaard celpotentialiaal voor waterelektrolyse, terwijl ook energieconversie-efficiëntie (PCE) hoger is dan de limiet van in serie geschakelde enkellaags zonnecellen. De PVK-Si tandemzonnecel bereikte een V_{oc} van meer dan 1.75 V, ruim voldoende om waterelektrolyse uit te voeren. Tegelijkertijd maakten hoge stroomdichtheden een zonlicht-naar-waterstofrendement (STH) van 21.5% mogelijk bij gebruik van geavanceerde katalysatoren en membranen. Deze STH-waarde is momenteel de hoogste gerapporteerde waarde voor een systeem dat werkt zonder concentratie van zonlicht. Het is ook het eerste voorbeeld van een twee-terminal PVK-Si tandem zonnecel gekoppeld aan een elektrochemische doorstroomcel die werkt in normaal zonlicht.

In hoofdstuk 4 wordt de PVK-Si tandemzonnecel vervangen door een volledig-perovskiet tandemzonnecel die een V_{oc} van bijna 2 V levert. Deze hogere spanning gaat ten koste van de stroomdichtheid. De verhoging in V_{oc} is gunstig in combinatie met de goedkopere maar vaak minder efficiënte elektrokatalysatoren waarvan de overpotentialiaal voor waterelektrolyse toeneemt. Waterelektrolyse op zonne-energie met de volledig-perovskiet tandemzonnecel bereikte een STH van bijna 19% bij gebruik van een relatief goedkope halfgeleider en geavanceerde katalysatoren en membranen. Daarnaast beschrijft dit hoofdstuk de optimalisatie van een perovskiet zonnecel met smalle bandafstand om de PCE van de volledig-perovskiet tandemzonnecel en de STH van het gekoppelde systeem te verhogen. Het gebruik van bulkadditieven en oppervlaktebehandelingen voor de perovskietlaag maakte een maximaal rendement (PCE) van 18.6% mogelijk, een stijging van 3.1% ten opzichte van de vorige procedure. Een dergelijke optimalisatie in combinatie met verdere verbeteringen aan de subcel met brede bandafstand zou de PCE van de volledig-perovskiet tandems tot boven de 26% kunnen brengen en de STH tot bijna 20%.

In het volgende hoofdstuk zijn de waterelektrolyseprestaties en waterstofdoorlaatbaarheid van verschillende proton-uitwisselingsmembranen (PEM's) gemaakt van gesulfoneerde derivaten van polypentafluorostyreen en poly(aryleen thioether)s vergeleken met Nafion als standaard membraan. Deze membranen werden ontwikkeld door andere onderzoekers binnen het eSCALED project. De iontransporteigenschappen van de nieuwe PEMs waren meestal beter dan Nafion, maar Nafion presteert beter in termen van energie en faradische efficiëntie in waterelektrolyse. Dit werd voornamelijk toegeschreven aan de grotere wateropname- en zwelratio's van de nieuwe membranen, waardoor de massatransportverliezen bij de elektroden toenamen maar er ook meer permeatie van waterstof naar het zuurstofcompartiment kon plaatsvinden. Daarom moeten bij het ontwerp van nieuwe ionomeren voor PEM's verbeterde iontransport-

Samenvatting

eigenschappen en een lage wateropname worden gecombineerd om overmatige gaspermeatie en energieverliezen te voorkomen.

Titanium wordt veel gebruikt om poreuze transportlagen en bipolaire platen te fabriceren, maar het resulteert in hoge kapitaalkosten die zelfs hoger zijn dan die van edelmetalkatalysatoren. Hierdoor neemt de economische haalbaarheid van water elektrolyse af. Het groeiende gebied van de geprinte elektronica kan mogelijk een geschikt antwoord bieden om een hoge doorvoer en goedkope productie van elektroden te bereiken. In hoofdstuk 6 zijn grafietelektroden bestudeerd die rechtstreeks op Nafion werden gedrukt in verschillende patronen. De patronen maakten protontransport over het membraan mogelijk wat resulteerde in succesvolle water elektrolyse. Er zijn echter ook verschillende tekortkomingen van deze methode, met name op het gebied van weerstandsverliezen, grafietofoxidatie, reproduceerbaarheid en algemene prestaties. Aanvullende verbeteringen aan de inktformulering en het testen van andere patronen zouden de efficiëntie van deze elektroden kunnen verbeteren, terwijl er een minimale hoeveelheid materiaal wordt gebruikt.

In het laatste hoofdstuk is een levenscyclusanalyse (LCA) uitgevoerd van een door zonne-energie ondersteund water elektrolyse apparaat waarin de nieuwe materialen (PEM en moleculaire katalysatoren ontwikkeld in het eSCALED-project) zijn geïntegreerd. Deze LCA is vergeleken met de LCA van een apparaat dat gebruikmaakt van de nieuwste materialen. In de studie werd rekening gehouden met alle milieueffecten van grondstofwinning (wieg) tot fabricage (poort) van de apparaten om de meest-milieukritische processen en materialen te identificeren. In het algemeen waren de milieueffecten en de energiebehoefte van het eSCALED apparaat groter dan die van het state-of-the-art apparaat. Vooral de lage efficiëntie van de moleculaire katalysatoren hinderde de werking van de elektrochemische cel bij hoge stroomdichtheden, wat leidde tot een groter materiaal- en energieverbruik in het gekoppelde systeem (fotovoltaïsche en elektrolysecomponenten). Tot slot zorgde de identificatie van de meest milieubelastende processen voor een beter begrip van de milieubelasting van de apparaten en waar ze in de toekomst verder verbeterd op kunnen worden.

Zusammenfassung

Die Unvorhersehbarkeit und Unbeständigkeit der Solarenergieversorgung macht diese Energiequelle alleine weniger geeignet, um fossile Brennstoffe vollständig zu ersetzen. Der erfolgreiche Einsatz erneuerbarer Solarenergie ist von geeigneten Energiespeichermethoden abhängig. Hier erweist sich die Wasserelektrolyse als eine der vielversprechendsten Technologien. Die solarbetriebene Wasserelektrolyse stützt sich derzeit jedoch auf teure Materialien mit hohem ökologischem Fußabdruck. Beispiele hierfür sind Elektrokatalysatoren auf Basis von Edelmetallen und Metalloxiden, bipolare Platten, perfluorierte Polyelektrolyte und III–V–Halbleitersolarzellen. Die Entwicklung und Umsetzung kostengünstigerer Lösungen mit geringem CO₂–Fußabdruck ist von grundlegender Bedeutung, um die weltweite Abhängigkeit von fossilen Brennstoffen zu verringern und Kohlenstoffneutralität zu erreichen.

Diese Arbeit beschreibt die Testung von Protonenaustauschmembranen auf der Basis fluorierter Polymere, die Entwicklung von Membran–Elektroden–Kombinationen mit Hilfe von Druckverfahren sowie einer Wasserelektrolysezelle mit einer Perowskit–Silizium–Tandemsolarzelle, die eine effiziente Umwandlung von Sonnenlicht in Wasserstoff ermöglicht. Die Forschungsarbeiten sind Teil des eSCALED–Projekts, mit dem neue Materialien entwickelt und analysiert werden sollen, um schließlich ein künstliches Blatt herzustellen, das die natürliche Photosynthese nachahmt.

Kapitel 2 beschreibt die Entwicklung des Wasserelektrolyseaufbaus und der Zelle. Durch Optimierung des Aufbaus konnten reproduzierbare und mit der Literatur vergleichbare Ergebnisse erzielt werden. Der Optimierungsprozess umfasste die Untersuchung des Einspannmoments der Zelle, der Zelltemperatur, des Materials des Strömungsfelds, der Materialien der porösen Transportschichten (PTLs) und der Probenlagerungsumgebung. Nach Verbesserung der Widerstandsverluste, der Reaktionskinetik und der Gesamtstabilität erreichte die Wasserelektrolyse mit einer Protonenaustauschmembran Stromdichten von bis zu 1 A cm⁻² bei einer Spannung von 1,70 V. Diese Ergebnisse bildeten den Maßstab und Ausgangspunkt für die neuen Elektrolysematerialien und –methoden, die in den folgenden Kapiteln beschrieben werden.

Kapitel 3 beschreibt eine monolithische Tandemsolarzelle mit zwei Anschlüssen auf der Basis eines Perowskit–Halbleiters (PVK) mit breiter Bandlücke und kristallinem Silizium (c–Si) mit schmaler Bandlücke, die mit einer Wasserelektrolysezelle für die sonnenlichtgetriebene Wasserelektrolyse bei

Zusammenfassung

einer Lichtintensität von 1 Sonne verbunden ist. Tandem-Solarzellen mit zwei Anschlüssen liefern eine Spannung bei offenem Kreislauf (V_{oc}), die höher ist als das Standardpotenzial für die Wasserelektrolyse, während der Energieumwandlungswirkungsgrad (PCE) ebenfalls höher ist als der Grenzwert für in Reihe geschaltete Einzelschicht-Solarzellen. Die PVK-Si-Tandemsolarzelle erreicht ein V_{oc} von über 1,75 V, was für die Wasserelektrolyse mehr als ausreichend ist. Gleichzeitig ermöglichten hohe Stromdichten einen Solar-to-Hydrogen (STH)-Wirkungsgrad von 21,5 % unter Verwendung fortschrittlicher Katalysatoren und Membranen. Dieser STH-Wert ist derzeit der höchste, der für ein System berichtet wurde, das ohne konzentriertes Sonnenlicht betrieben wird. Es ist auch das erste Beispiel einer PVK-Si-Tandemsolarzelle mit zwei Anschlüssen, die mit einer elektrochemischen Durchflusszelle gekoppelt ist, welche mit normalem Sonnenlicht betrieben wird.

In Kapitel 4 wird die PVK-Si-Tandem-Solarzelle durch eine Voll-Perowskit-Tandem-Solarzelle ersetzt, die ein V_{oc} von fast 2 V liefert. Die höhere Spannung geht jedoch auf Kosten der Stromdichte. Der höhere V_{oc} ist in Kombination mit den billigeren, aber oft weniger effizienten Elektrokatalysatoren von Vorteil, da in jenem Fall das Überpotenzial für die Wasserelektrolyse steigt. Bei der solarbetriebenen Wasserelektrolyse mit der Vollperowskit-Tandemsolarzelle wurde bei Verwendung eines relativ preiswerten Halbleiters und fortschrittlicher Katalysatoren und Membranen eine STH von fast 19 % erreicht. Darüber hinaus wird in diesem Kapitel die Optimierung einer Perowskit-Solarzelle mit schmaler Bandlücke beschrieben, um die PCE der All-Perowskit-Tandemsolarzelle und die STH des gekoppelten Systems zu erhöhen. Durch die Verwendung von Bulk-Additiven und Oberflächenbehandlungen für die Perowskit-Schicht konnte ein maximaler Wirkungsgrad (PCE) von 18,6 % erreicht werden, was einer Steigerung von 3,1 % gegenüber dem vorherigen Verfahren entspricht. Durch diese Optimierung in Verbindung mit weiteren Verbesserungen an der Unterzelle mit breiter Bandlücke könnte der PCE der Vollperowskit-Tandems auf über 26 % und der STH auf fast 20 % gesteigert werden.

Im nächsten Kapitel wurden die Wasserelektrolyseleistung und die Wasserstoffdurchlässigkeit verschiedener Protonenaustauschmembranen (PEM) aus sulfonierten Derivaten von Polypentafluorostyrol und Poly(arylethioether)en mit Nafion als Standardmembran verglichen. Diese Membranen wurden von anderen Forschern im Rahmen des eSCALED-Projekts entwickelt. Die Iontentransporteigenschaften der neuen PEM-Membranen waren meist besser als die von Nafion, welches jedoch bei der Wasserelektrolyse in

Bezug auf die Energie- und Faraday-Effizienz besser abschnitt. Dies war vor allem auf das größere Wasseraufnahme- und Quellungsverhältnis der neuen Membranen zurückzuführen. Dieses erhöht die Massentransportverluste an den Elektroden und ermöglichte eine stärkere Permeation von Wasserstoff in den Sauerstoffspeicher. Bei der Entwicklung neuer Ionomere für PEMs sollten daher verbesserte Ionentransporteigenschaften und eine geringe Wasseraufnahme kombiniert werden, um eine übermäßige Gaspermeation sowie Energieverluste zu vermeiden.

Titan wird häufig für die Herstellung von porösen Transportschichten und bipolaren Platten verwendet, verursacht aber hohe Investitionskosten, die sogar höher sind als die von Edelmetallkatalysatoren. Dies beeinträchtigt die wirtschaftliche Machbarkeit der Wasserelektrolyse. Der wachsende Bereich der gedruckten Elektronik könnte möglicherweise eine geeignete Lösung für die Herstellung von Elektroden mit hohem Durchsatz und zu niedrigen Kosten bieten. In Kapitel 6 wurden Graphitelektroden untersucht, die in verschiedenen Mustern direkt auf Nafion gedruckt wurden. Die Muster ermöglichten den Protonentransport durch die Membran, was zu einer erfolgreichen Wasserelektrolyse führte. Allerdings weist diese Methode auch einige Schwächen auf, insbesondere in Bezug auf Widerstandsverluste, Graphitoxidation, Reproduzierbarkeit und Gesamtleistung. Zusätzliche Verbesserungen der Tintenformulierung und Tests mit anderen Patronen könnten die Effizienz dieser Elektroden bei minimalem Materialeinsatz verbessern.

Im letzten Kapitel wurde eine Lebenszyklusanalyse (LCA) eines solarunterstützten Wasserelektrolysegeräts durchgeführt, das die neuen Materialien (PEM und molekulare Katalysatoren, die im Rahmen des eSCALED-Projekts entwickelt wurden) enthält. Diese Ökobilanz wurde mit der Ökobilanz eines Geräts verglichen, bei dem modernste Materialien verwendet wurden. In der Studie wurden alle Umweltauswirkungen von der Rohstoffgewinnung (Wiege) bis hin zur Herstellung (Tor) der Geräte berücksichtigt, um die umweltkritischsten Prozesse und Materialien zu ermitteln. Insgesamt waren die Umweltauswirkungen und der Energiebedarf des eSCALED-Geräts größer als die des Geräts nach dem Stand der Technik. Insbesondere behinderte die geringe Effizienz der molekularen Katalysatoren den Betrieb der elektrochemischen Zelle bei hohen Stromdichten, was zu einem höheren Material- und Energieverbrauch im gekoppelten System (Photovoltaik- und Elektrolysekomponenten) führte. Schließlich ermöglichte die Identifizierung der umweltschädlichsten Prozesse ein besseres Verständnis der Umweltauswirkungen der Geräte sowie der Bereiche, die in Zukunft weiter verbessert werden könnten.

Resumo

A imprevisibilidade e intermitência associadas à energia solar tornam-na uma alternativa pouco viável para substituir totalmente os combustíveis fósseis. A expansão da rede de energias renováveis dependerá de métodos adequados para armazenamento de energia e a eletrólise da água surge como uma das tecnologias mais promissoras. No entanto, a eletrólise de água que recorre a energia solar como fonte de energia depende, atualmente, de eletrocatalisadores e placas bipolares baseadas em metais nobres e óxidos metálicos, de polieletrólitos perfluorados e de células solares de múltiplas junções com materiais do grupo III-V, que acarretam elevados encargos económicos e ambientais. O desenvolvimento e a implementação de soluções sem emissões de carbono e com uma boa relação custo-eficácia são, por conseguinte, fundamentais para reduzir a dependência global dos combustíveis fósseis e alcançar a neutralidade carbónica.

Este trabalho engloba o teste de membranas de permuta catiónica à base de polímeros fluorados, a preparação de conjuntos membrana-eléctrodo através de tecnologias de impressão, e a integração de uma célula de electrólise de água com células solares de perovskite com múltiplas junções, com o objectivo de obter uma elevada conversão de energia solar em hidrogénio. Este trabalho faz parte do projeto eSCALED que visa desenvolver novos materiais e dispositivos para a criação de uma folha artificial, imitando assim a fotossíntese natural.

Inicialmente, para garantir resultados reproduzíveis e comparáveis com trabalhos previamente reportados e realizados com materiais padrão, é descrito no capítulo 2, a construção e optimização de um sistema e célula de electrólise de água. O processo de optimização consistiu em estudar o efeito do torque aplicado para apertar a célula, da temperatura de operação, do material dos canais fluídicos, do material da camada porosa para transporte de gás e líquido (PTLs) e do ambiente de armazenamento dos conjuntos membrana-eléctrodo. Após a redução das perdas resistivas, a melhoria da cinética e estabilidade global, a electrólise da água com membrana de permuta catiónica atingiu uma densidades de corrente máxima de 1 A cm^{-2} , operando abaixo de 1.70 V. Estes resultados estabeleceram o nível de referência para os novos materiais de eletrólise e metodologias de preparação estudadas nos capítulos seguintes.

No capítulo 3, uma célula solar monolítica de multijunções de dois-terminais (tandem) que combinou um semicondutor de perovskite (PVK) com amplo hiato energético com silício cristalino (c-Si), que possui um hiato energético menor, foi ligada à célula de electrólise de água. Este sistema foi operado com uma intensidade de irradiação equivalente a 1 Sol. Células solares

em tandem permitem obter um potencial elétrico em circuito aberto (V_{oc}) mais elevado que o potencial elétrico padrão de electrólise da água, aumentando simultaneamente a eficiência de conversão de energia (PCE) acima do limite das células solares de junção única ligadas em série. A célula solar em tandem de PVK–Si demonstra um V_{oc} acima de 1.75 V, o que é suficiente para a electrólise da água. O sistema atingiu densidades de corrente suficientemente altas para alcançar uma eficiência de conversão de energia em hidrogénio (STH) de 21.5%, utilizando catalisadores e membranas padrão. Este valor de STH é atualmente o valor mais elevado reportado para um sistema que opera sem concentração solar. Este sistema representa também o primeiro exemplo de uma célula solar monolítica de multijunções de dois–terminais com base em PVK–Si ligada a uma célula electroquímica de fluxo a operar com uma intensidade de luz solar normal.

No capítulo 4, a célula solar em tandem de PVK–Si é substituída por uma célula solar em tandem completamente à base de perovskite, o que proporciona um V_{oc} mais elevado, de quase 2 V, alargando assim o intervalo de potenciais de operação à custa de uma ligeira diminuição da densidade de corrente. O ligeiro aumento do V_{oc} é benéfico, caso se use eletrocatalisadores menos eficientes mas mais baratos, já que o potencial necessário para a electrólise da água aumenta. A electrólise da água combinado com a célula solar em tandem de PVK atingiu uma STH perto de 19%, utilizando semicondutores comparativamente baratos e catalisadores e membranas padrão. Este capítulo descreve também a optimização de uma célula solar de perovskite com um hiato energético pequeno, de forma a potencialmente aumentar a PCE das células solares em tandem completamente à base de perovskite e a STH do sistema combinado. O uso de aditivos e tratamentos da superfície superior da camada de perovskite permitiram atingir um PCE máximo de 18.6%, o que representa um incremento de 3.1% em relação ao procedimento anterior. Esta optimização, combinada com melhorias futuras na sub–célula solar com hiato energético amplo, poderá resultar num aumento de PCE das células solares em tandem de perovskite acima de 26% e a STH para quase 20%.

No capítulo seguinte, o desempenho da electrólise de água e a permeabilidade de hidrogénio de diferentes membranas de permuta catónica (PEMs) à base de derivados sulfonados de polipentafluoroestireno e poli(arileno tioéter)s são comparadas com as de uma membrana de Nafion como referência. Estas membranas foram desenvolvidas por outros investigadores do projecto eSCALED. As propriedades de transporte iónico das novas PEMs são, maioritariamente, melhores que as do Nafion. No entanto, Nafion demonstrou melhor desempenho em termos de eficiência energética e faradaica na electrólise de água. Estes resultados são derivados da uma maior absorção de água e rácio

de dilatação das novas membranas que resultam num aumento das perdas de transferência de massa nos eléctrodos e numa maior permeação de hidrogénio. Consequentemente, o desenho de novos ionómeros para PEMs deve combinar condutividade iónica e capacidade de permuta iónica elevadas com baixa absorção de água para evitar permeação excessiva de gás e perdas de energia.

O titânio é normalmente utilizado para fabricar as PTLs e as placas bipolares, mas o custo capital associado é bastante elevado, sendo superior ao custo dos eletrocatalisadores de metais nobres, o que diminui a viabilidade económica da electrólise da água. A crescente área da eletrónica impressa poderá proporcionar uma resposta adequada para obter elevada produção e um baixo custo de fabrico dos eléctrodos. No capítulo 6 são estudados eléctrodos à base de grafite impressos directamente em Nafion com diversos padrões. Estes padrões permitem transporte de protões através da membrana, o que resultou na electrólise de água. No entanto, revelou também algumas desvantagens em termos de perdas resistivas, oxidação da grafite, reprodutibilidade e desempenho no geral. No futuro, a optimização da formulação da tinta e a utilização de padrões melhorados poderá aumentar a eficiência destes eléctrodos, e reduzir, ao mesmo tempo, a quantidade necessária de materiais.

No último capítulo, é realizada uma avaliação do ciclo de vida (LCA) de um sistema de electrólise de água que utiliza energia solar e integra os novos materiais (PEM e catalisadores moleculares desenvolvidos no projeto eSCALED). Neste LCA, o sistema com materiais desenvolvidos no projeto eSCALED é também comparado com o estado da arte. Este estudo considera todos os impactos ambientais desde a extração de matérias-primas (cradle) até à produção (gate) destes sistemas para identificar os processos e materiais mais críticos. No geral, os impactos ambientais e o requisito energético do sistema eSCALED foram mais elevados em comparação com o sistema padrão. Em particular, a baixa eficiência dos catalisadores moleculares impede a operação da célula eletroquímica a elevadas densidades de corrente, resultando num maior consumo de material e energia no sistema combinado (componentes fotovoltaicos e de electrólise). Por fim, a identificação dos processos com maior impacto ambiental permitiu uma melhor compreensão da carga ambiental destes sistemas e de como os melhorar no futuro.

Curriculum Vitae

Bruno Filipe Pinto Branco was born on February 7th, 1995 in Pragal, Portugal. He finished high school in 2013 at Escola Secundária Emídio Navarro in Portugal. Afterwards, he enrolled in an Integrated Master's in Chemical and Biochemical Engineering at NOVA University of Lisbon, Portugal. In 2018, for his Master thesis project, he joined the Product and Process Engineering group at TU Delft, The Netherlands, as part of the ERASMUS+ Exchange programme. Here, he worked on molecular layer deposition (MLD) of polyester films on titania and protein particles using a fluidized bed reactor.



In January 2019, he started his PhD project in Mataró, Spain, as part of the eSCALED project, funded by a Marie–Curie Skłodowska Actions Innovative Training Network (MSCA–ITN) of the European Union. This PhD project, of which the results are presented in this dissertation, was supervised by prof. dr.ir. René A. J. Janssen (TU Eindhoven, The Netherlands) and prof. dr. rer. nat. K. A. Friedrich (University of Stuttgart, Germany). During his PhD project, he worked at the Eurecat Technology Centre of Catalonia (Spain), the University of Stuttgart (Germany), University of Pau and Pays de l'Adour (France) and lastly, the Eindhoven University of Technology.

Acknowledgements

The last four years have been a crazy journey, living and working in different countries across Europe but, above all, it allowed me to meet and work with remarkable people. Everyone has, scientifically or otherwise, contributed to work described in this thesis, even though, there is a single name in the cover.

I would like to start by thanking my two main supervisors: **René Janssen** and **K. Andreas Friedrich**. **René**, thank you very much for all your inputs, feedback and discussions, especially on a topic that was somewhat different to the rest of the group. You have been a great source of inspiration for me, and I have always admired your seemingly endless knowledge combined with your curiosity and willingness to learn more. I appreciate all the support, and kind words. I am very grateful to have worked in M2N. **Prof. Friedrich**, thank you for accepting me as your PhD student, despite not being deeply involved in the eSCALED project from the start. Your expertise and feedback on my work were highly appreciated.

I also would like to thank the members of my PhD thesis committee – **Elias Klemm**, **Roel van de Krol**, **Thijs de Groot**, **Vladimir Atanasov** and **Željko Tomović** – for accepting to be part of this committee and for reading and provide insightful suggestions to my thesis. Special thanks to **Vladimir** who supervised me during my time in Stuttgart.

My amazing paranymphs, **Kostadin** and **Lana**, thank you for accepting the role of protecting me during my defense. **Kostadin**, this needs to start as always, “*Estou farto de ti*”. Thank you for being such a close friend for so many years. For some strange reason, we have made similar life decisions since high school, even ended up working on similar topics in the PhD. I have admired your scientific acumen, your social skills (only subpar to mine, of course) and your confidence during this time. I wish you the best for finishing your PhD and I am confident you will have a great future afterwards, wherever it is. **Lana**, the youngest but, by far, the wisest person in our office. I am glad you joined the group as a PhD student and ended up in our office. Thank you for surviving our endless complaining the past year, and for always, supporting and comforting us with your wise words. I have really enjoyed our nice and sometimes, “close the door” conversations as well as sharing a similar topic where you are making excellent progress. Also, thank you (and **Nicolas**) for providing random dinners from time to time, during the writing of this thesis, those dinners mattered a lot. Lastly, thank you for such a nice friendship and I wish the best with the remainder of your PhD.

Acknowledgements

To my other officemate for the past almost 2 years and eSCALED fellow, **Olivera**, where do I start? Thank you for always joining me in continuous ranting about life in general, I will actually miss those days. I have always appreciated our time together, particularly our random after work dinners that, sometimes, ended up in Bobby's for the occasional cocktail(s). More importantly, you are a great friend that I could always count on, and I have really enjoyed sharing the office and working with you. Further, I will always be ready to help you with your tech problems, grandma.

The eSCALED project would not be possible without **Laia Francesch** (eSCALED mom), **Antoine Bousquet** and **Laurent Billon**. **Laia**, thank you very much for solving the numerous problems during this project. Lastly, thank you very much for our talks about existential crisis during my short time in Pau, they were deeply appreciated. **Antoine** and **Laurent**, thank you for allowing me to be part of this amazing journey that was eSCALED and for all the support during the project and especially, my time in Pau. Thanks to all my other fellow ESRs, **Andrew H.**, **Andrew B.**, **Afridi**, **Domenico**, **Silvia**, **Karell**, **Ignasi**, **Diogo**, **Saeed**, **Van** and **Robin**. I have enjoyed our time together in and outside the labs, and I am glad to have shared this experience with you. A special thanks to **Karell**, who served as my French translator in Pau, and for all the nice talks we have had.

During the course of this European adventure, I have met and worked with many people. From Eurecat in Mataró, I would like to thank **Cláudia**, **Miguel**, **Ana** and **Alejandra** for teaching me the basics of electrochemistry and showing me the wonderful world of printed electronics. From Eurecat in Manresa, I would like to thank **José** and **Frederic** for introducing me to LCA and for being always available for LCA questions. From ICVT in Stuttgart, I would like to thank **Johannes** and **Hyeongrae** for always beating me in table football. And finally from UPPA in Pau, **Pierre**, thank you for all the help with new practical procedures.

Two years into my PhD, I moved to Eindhoven for the last stay of my project and despite, being the “new” PhD of the group, I quickly felt I was part of the group. I would like to start by thanking **Martijn**, without whom, I would have not been able to assemble my setup and for providing a helping hand whenever it was needed, being with equipment issues, designing masks or guiding students. Also, thank you for the very quick and witty comments during meeting and coffee breaks. To the M2N mom, **Margot**, thank you for the crucial support during this time, being bureaucratic or interpersonal. **Stefan**, thank you for always having time for useful discussions. **Kunal**, thank you for introducing me to the *world* of multijunction solar cells and for the collaboration that resulted

Acknowledgements

in my only paper during this PhD. It was a pleasure to work with you, despite mocking my spicy food tolerance every time you could. **Nicolas**, mein deutscher Freund, du bist super. Vielen Dank für die schönen Abenden mit Gesellschaftsspielen, Abendessen und Nintendo Switch Spielen und danke für deine allgemeine Einstellung zu Wissenschaft und das Leben. **Simone**, thanks for just being the most innocent person I know and eating some tasty snails with me. **Ludo**, my other eSCALED fellow in Eindhoven, thank you for showing and teaching me how to climb and how “small” electrochemistry worked. I enjoyed our time together both in Pau and in Eindhoven. **Alessandro**, thank you for being annoying, but I will excuse you for cooking some amazing pizzas. Your love for Italian food is only rivalled by your love for messing up other people’s food culture. **Bas**, thank you for all the nice dinners, board games and great trash talking ability during those games. **Willie**, thank you for your enthusiasm about Mario Kart and Legend of Zelda and for teaching us how to renovate a house. **Wietse**, thank you for assisting me with assembling my setup and good discussions. **Tom**, thank you for making the daily rounds of calling people for coffee breaks. **Junke**, I will always admire your work ethic and knowledge about perovskites. To the new PhD students that started during my last months as a PhD, **Guus**, **Nick** and **Laura**, I wish you the best and enjoy the PhD journey. **Guus**, small word of advice, try not to smoke any more evaporators, please. The M2N physics: **Lois**, **Christoph**, **Riccardo**, **Xiao**, **Peter**, **Reinder**, **Mahyar**, **Michael**, **Clint**, **Hiroki**, **Niels**, **Wijnand** and **Christian**, thank you for the nice meetings and enjoyable events we had together. Furthermore, thank you to the PhDs and post-docs (**Pieter**, **Bart**, **Haijun**, **Koen**) that still welcomed me in the group but left soon after.

I would like to thank the group of “Dutch”–Portuguese friends: **Catarina** and **Inês** for bringing a bit of Portugal to the Netherlands and for the fun times we had in both countries. To my Portuguese friends **Gonçalo**, **Patrícia**, **Nuno**, **João Alves**, **Teresa**, **Jóia** e **Joinha**, who had four years to visit me, and all decided to do it during the writing of this thesis. I cherished those visits a lot and please, never change. Thank you to all my friends in Portugal who were always ready to meet whenever I went back.

Finally, to my family. Aos meus **pais**, obrigado pelo apoio diário e na minha decisão de fazer um doutoramento fora de Portugal. E por acreditarem sempre em mim e nas minhas decisões, mesmo quando eu não o faço. Ao meu irmão, **Tiago**, mano, obrigado por me perceberes e pelo interesse naquilo que faço. Não chegaria a esta fase sem vocês, mesmo que às vezes não o demonstre. **Daniela**, obrigado pelas gargalhadas e de nada, pela molha no PortAventura. E não podia deixar de agradecer à membra mais recente da família Branco, **Beatriz**,

Acknowledgements

que apesar de ter nascido apenas este ano, serviu como mais uma inspiração nestes curtos meses. Vai ser um prazer ver-te crescer e especialmente, ajudar-te a chatear os teus pais.

Os últimos quatro anos nem sempre foram fáceis, mas **Inês**, obrigado por fazeres com que este duo funcione. O teu apoio foi fundamental e incondicional durante estes anos, apesar do meu bom humor, e de certeza que sem ele, não estaria aqui. Desde fazer 12 h de autocarro por 1 € a apanhar sete comboios, nunca perdeste a oportunidade de vir ter comigo. Isso, além de histórias engraçadas, mostrou que a distância não importa, e que é apenas uma palavra. E prometo que fazemos uma viagem juntos em breve. Mas acima de tudo, obrigado por me fazeres feliz. Se estiver contigo, estou em casa.

Thank you all,

Bedankt allemaal,

Danke euch allen,

Obrigado a todos,

Bruno Filipe Pinto Branco